Lawrence Berkeley National Laboratory
LBL Publications

Title
Seismic Velocities and Attenuation in a Heated Underground Granitic Repository Volume I

Permalink
https://escholarship.org/uc/item/9fw93598

Author
Paulsson, B N P

Publication Date
1983

Copyright Information

SWEDISH-AMERICAN COOPERATIVE PROGRAM ON RADIOACTIVE WASTE STORAGE IN MINED CAVERNS IN CRYSTALLINE ROCK
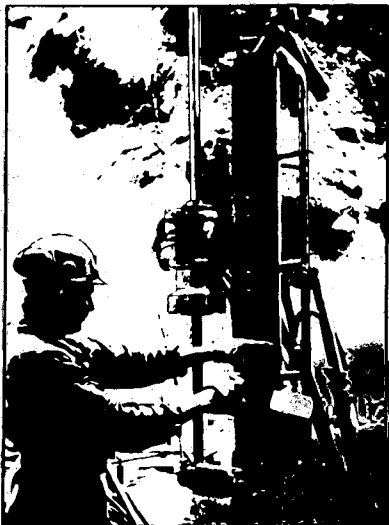
Technical Information Report No. 51

SEISMIC VELOCITIES AND ATTENUATION IN A HEATED UNDERGROUND GRANITIC REPOSITORY

Volume I

B.N.P. Paulsson
ce Berkeley Laboratory
ersity of California
ey, California 94720

January 1983

A Joint Project of

DISCLAIMER

SEISMIC VELOCITIES AND ATTENUATION
IN A HEATED UNDERGROUND GRANITIC REPOSITORY
Volume I

Bjorn Nils Patrick Paulsson

Lawrence Berkeley Laboratory
University of California
Berkeley, California 94720

SEISMIC VELOCITIES AND ATTENUATION IN
A HEATED UNDERGROUND GRANITIC REPOSITORY.

Copyright © 1983

by

Björn Nils Patrick Paulsson

This report is one of a series documenting the results of the Swedish-American cooperative research program in which the cooperating scientists explore the geological, geophysical, hydrological, geochemical, and structural effects anticipated from the use of a large crystalline rock mass as a geologic repository for nuclear waste. This program has been sponsored by the Swedish Nuclear Power Utilities through the Swedish Nuclear Fuel Supply Company (SKBF), and the U.S. Department of Energy (DOE) through the Lawrence Berkeley Laboratory.

The principal investigators are L.B. Nilsson and O. Degerman for SKBF, and N.G.W. Cook, P.A. Witherspoon, and J.E. Gale for LBL. Other participants will appear as authors of the individual reports.

Previous technical reports in this series are listed below.

1. Swedish-American Cooperative Program on Radioactive Waste Storage in Mined Caverns by P.A. Witherspoon and O. Degerman. (LBL-7049, SAC-01).

2. Large Scale Permeability Test of the Granite in the Stripa Mine and Thermal Conductivity Test by Lars Lundstrom and Haken Stille. (LBL-7052, SAC-02).

3. The Mechanical Properties of the Stripa Granite by Graham Swan. (LBL-7074, SAC-03).

4. Stress Measurements in the Stripa Granite by Hans Carlsson. (LBL-7078, SAC-04).

5. Borehole Drilling and Related Activities at the Stripa Mine by P.J. Kurfurst, T. Hugo-Persson, and G. Rudolph. (LBL-7080, SAC-05).

6. A Pilot Heater Test in the Stripa Granite by Hans Carlsson. (LBL-7086, SAC-06).

7. An Analysis of Measured Values for the State of Stress in the Earth's Crust by Dennis B. Jamison and Neville G.W. Cook. (LBL-7071, SAC-07).

8. Mining Methods Used in the Underground Tunnels and Test Rooms at Stripa by B. Andersson and P.A. Halen. (LBL-7081, SAC-08).

9. Theoretical Temperature Fields for the Stripa Heater Project by T. Chan, Neville G.W. Cook, and C.F. Tsang. (LBL-7082, SAC-09).

10. Mechanical and Thermal Design Considerations for Radioactive Waste Repositories in Hard Rock. Part I: An Appraisal of Hard Rock for Potential Underground Repositories of Radioactive Waste by N.G.W. Cook; Part II: In Situ Heating Experiments in Hard Rock: Their Objectives and Design by N.G.W. Cook and P.A. Witherspoon. (LBL-7073, SAC-10).

11. Full-Scale and Time-Scale Heating Experiments at Stripa: Preliminary Results by N.G.W. Cook and M. Hood. (LBL-7072, SAC-11).

12. Geochemistry and Isotope Hydrology of Groundwaters in the Stripa Granite: Results and Preliminary Interpretation by P. Fritz, J.F. Barker, and J.E. Gale. (LBL-8285, SAC-12).

13. Electrical Heaters for Thermo-Mechanical Tests at the Stripa Mine by R.H. Burleigh, E.P. Binnall, A.O. DuBois, D.O. Norgren, and A.R. Ortiz. (LBL-7063, SAC-13).

14. Data Acquisition, Handling, and Display for the Heater Experiments at Stripa by Maurice B. McEvoy. (LBL-7063, SAC-14).

15. An Approach to the Fracture Hydrology at Stripa: Preliminary Results by J.E. Gale and P.A. Witherspoon. (LBL-7079, SAC-15).

16. Preliminary Report on Geophysical and Mechanical Borehole Measurements at Stripa by P. Nelson, B. Paulsson, R. Rachiele, L. Andersson, T. Schrauf, W. Hustrulid, O. Duran, and K.A. Magnussen. (LBL-8280, SAC-16).

17. Observations of a Potential Size-Effect in Experimental Determination of the Hydraulic Properties of Fractures by P.A. Witherspoon, C.H. Amick, J.E. Gale, and K. Iwai. (LBL-8571, SAC-17).

18. Rock Mass Characterization for Storage in Nucler Waste in Granite by P.A. Witherspoon, P. Nelson, T. Doe, R. Thorpe, B. Paulsson, J.E. Gale, and C. Forster. (LBL-8570, SAC-18).

19. Fracture Detection in Crystalline Rock Using Ultrasonic Shear Waves by K.H. Waters, S.P. Palmer, and W.F. Farrell. (LBL-7051, SAC-19).

20. Characterization of Discontinuities in the Stripa Granite--Time Scale Heater Experiment by R. Thorpe. (LBL-7083, SAC-20).

21. Geology and Fracture System at Stripa by A. Okliewicz, J.E. Gale, R. Thorpe, and B. Paulsson. (LBL-8907, SAC-21).

22. Calculated Thermally Induced Displacements and Stresses for Heater Experiements at Stripa by T. Chan and N.G.W. Cook. (LBL-7061, SAC-22).

23. Validity of Cubic Law for Fluid Flow in a Deformable Rock Fracture by P.A. Witherspoon, J. Wang, K. Iwai, and J.E. Gale. (LBL-9557, SAC-23).

24. Determination of In-Situ Thermal Properties of Stripa Granite from Temperature Measurements in the Full-Scale Heater Experiments: Methods and Primary Results by J. Jeffry, T. Chan, N.G.W. Cook and P.A. Witherspoon. (LBL-8424, SAC-24).

25. Instrumentation Evaluation, Calibration, and Installation for Heater Tests Simulating Nuclear Waste in Crystalline Rock, Sweden by T. Schrauf, H. Pratt, E. Simonson, W. Hustrulid, P. Nelson, A. DuBois, E. Binnall, and R. Haught. (LBL-8313, SAC-25)

26. Part I: Some Results From a Field Investigation of Thermo-Mechanical Loading of a Rock Mass When Heater Canisters are Emplaced in the Rock by M. Hood. Part II: The Application of Field Data from Heater Experiments Conducted at Stripa, Sweden for Repository Design by M. Hood, H. Carlsson, and P.H. Nelson. (LBL-9392, SAC-26).

27. Progress with Field Investigations at Stripa by P.A. Witherspoon, N.G.W. Cook, and J.E. Gale (LBL-10559, SAC-27).

28. A Laboratory Assessment of the Use of Borehole Pressure Transients to Measure the Permeability of Fractured Rock Masses by C.B. Forster and J.E. Gale. (LBL-8674, SAC-28).

29. Thermal and Thermomechanical Data for In Situ Heater Experiments at Stripa, Sweden by T. Chan, E. Binnall, P. Nelson, O. Wan, C. Weaver, K. Ang, J. Braley, and M. McEvoy. (LBL-11477, SAC-29).

30. The Effect of Radon Transport in Groundwater Upon Gamma Ray Borehole Logs by P.H. Nelson, R. Rachiele, and A. Smith. (LBL-11180, SAC-30).

31. Strength and Permeability Tests on Ultra-Large Stripa Granite Core by R. Thorpe, D.J. Watkins, W.E. Ralph, R. Hsu, and S. Flexser. (LBL-11203, SAC-31).

32. Ultrasonic and Acoustic Emission Results from the Stripa Heater Experiments. Part I: A Cross-Hole Investigation of a Rock Mass Subjected to Heating by B.N.P. Paulsson and M.S. King. Part II: Acoustic Emission Monitoring During Cool-Down of the Stripa Heater Experiment by R. Rachiele. (LBL-10975, SAC-32).

33. Numerical Modeling to Assess Possible Influence of the Mine Openings on Far-Field In Situ Stress Measurements at Stripa by T. Chan, V. Guvanasen, and N. Littlestone (LBL-12469, SAC-33).

34. A Field Assessment of the Use of Borehole Pressure Transients to Measure the Permeability of Fractured Rock Masses by C.B. Forster and J.E. Gale. (LBL-11829, SAC-34).

35. Water Inflow into Boreholes During the Stripa Experiments by P.H. Nelson, R. Rachiele, J.S. Remer and H.S. Carlsson (LBL-12547, SAC-35).

36. Petrology and Radiogeology of the Stripa Pluton by H. Wollenberg, S. Flexser, and L. Andersson. (LBL-11654, SAC-36).

37. Geohydrological Data from the Macopermeability Experiment at Stripa, Sweden by C.R. Wilson, J.C.S. Long, R.M. Galbraith, K. Karasaki, H.K. Endo, A.O. DuBois, M.J. McPherson, and G. Ramqvist. (LBL-12520, SAC-37).

38. Characterization of Discontinuities in the Stripa Granite--Full-Scale Heater Experiments by B.N.P. Paulsson, P.H. Nelson, and P.J. Kurfurst. (LBL-9063, SAC-38).

39. Application of Borehole Geophysics at an Experimental Waste Storage Site by P.H. Nelson, K.A. Magnusson, and R. Rachiele. (LBL-11982, SAC-39).

40. Laboratory Investigations of Thermomechanical Properties of Stripa Granite by L. Myer and R. Rachiele. (LBL-13435, SAC-40)

41. Petrologic Changes and Damage in the Stripa Quartz Monzonite in Response to Heater Tests by S. Flexser, H. Wollenberg, and D.E. Wedge. (LBL-14929, SAC-41).

42. Fracture Mapping in the Ventilation Drift at Stripa: Procedures and Results by A. Rouleau, J.E. Gale, and J. Baleshta. (LBL-13071, SAC-42).

43. Thermal Analysis of the Stripa Heater Test Data from the Full Scale Drift by I. Javandel and P.A. Witherspoon. (LBL-13217, SAC-43).

44. In Situ Stress Measurements at the Stripa Mine, Sweden by T.W. Doe, K. Ingevald, L. Strindell, B. Leijon, W. Hustrulid, A. Tarikka, M. Holmberg, E. Majer, and H. Carlsson. (LBL-15009, SAC-44).

45. Fracture Detection in Crystalline Rock Using Ultrasonic Reflection Techniques by S.P. Palmer. (LBL-16347, SAC-45).

46. Fracture and Hydrology Data from Field Studies at Stripa, Sweden by J.E. Gale. (LBL-13101, SAC-46).

47. Equipment Design, Installation, and Operation for the Macropermeability Experiment at Stripa, Sweden by R.M. Galbraith, C.R. Wilson, A.O. DuBois, S.A. Lundgren, M.J. McPherson and G.W. West. (LBL-13392, SAC-47).

48. Effects of Sample Size on the Stress Permeability Relationship for Natural Fractures by J.E. Gale and K.G. Raven. (LBL-11865, SAC-48).

49. Progress with Hydrogeological Characterization of the Stripa Site by J.E. Gale, A. Rouleau, P.A. Witherspoon and C.R. Wilson. (LBL-14878, SAC-49).

50. Extensometer Performance During Heater Experiments at Stripa by A.O. DuBois, M. Hood, E.P. Binnall and L. Andersson. (LBL-13531, SAC-50).

Seismic Velocities and Attenuation
in a Heated Underground Granitic Repository

By

Björn Nils Patrick Paulsson

Grad. (University of Gothenburg) 1976
M.S. (University of California) 1979

DISSERTATION

Submitted in partial satisfaction of the requirements for the degree of

DOCTOR OF PHILOSOPHY

in

Engineering

in the

GRADUATE DIVISION

OF THE

UNIVERSITY OF CALIFORNIA, BERKELEY

Approved: .... 12 Jan 83
                        Co-Chair   Date
.... Neville G. W. Cook .... Jan 12, 1983 ..
                        Co-Chair
.... Chi-yuen W-g .... Jan. 12, 1983 ..
.... Jan. 11, 83

SEISMIC VELOCITIES AND ATTENUATION IN
A HEATED UNDERGROUND GRANITIC REPOSITORY.

Björn Nils Patrick Paulsson

Engineering Geoscience

Department of Materials Science and Mineral Engineering

University of California

Berkeley, California 94720

Ph.D

ABSTRACT

The behavior of a rock mass subjected to a thermal load from emplaced canisters with electric heaters simulating high level nuclear waste has been studied using a remote sensing seismic technique in a full-scale drift 340 m below the surface in the Stripa mine facility in Sweden. Travel-times and amplitudes of 20-60 kHz ultrasonic P- and S- waves were measured between four diamond-drilled boreholes around a heater, utilizing a cross-hole seismic technique over the experiment duration, a period of 750 days. A laboratory study of physical properties of the Stripa quartz monzonite was performed on 11 specimens from the full-scale drift using P and S-waves through uniaxially compressed core specimens.

The P and S-wave velocities (V_p and V_s) in the full-scale experiment involving a single heater were obtained by transmitting seismic waves from separate P and S piezoelectric crystals. The attenuation, Q^{-1}, was obtained by a spectral ratio technique. The signals were transmitted in six different directions between four boreholes situated at different distances and at different depths around the heater borehole. Data were collected primarily in two modes. First was the monitor mode, in which the transducers were positioned at the heater midplane depth over a period of time. In the second, or survey, mode the transducers were moved in 0.25 m steps between each measurement from the top of the boreholes to the bottom. Travel time data were measured in the field and waveforms were recorded also on an AM tape recorder. The attenuation analysis was made later in the laboratory. Laboratory tests were performed on both dry and saturated specimens. Two of the specimens were also tested under 12 different saturation levels. The laboratory values thus obtained of V_p, V_s, Q_α and Q_β as functions of different environmental conditions aided in better understanding of the field data.

Zones of low apparent velocity observed for both P- and S-waves correlate well with zones of weak fractures filled with calcite. When the heater was turned on, the P- and S-wave velocities increased rapidly. When the heater was turned off after 398 days of heating, the velocities decreased rapidly and finally reached levels well below those observed prior to the heating of the rock. The P-wave velocities along a particular profile were found to increase linearly with the mean temperature in the profile tested.

In all surveys, the Q-values reveal little of no correlation with temperature or the associated thermal stress. There is, however, a good correlation of decreasing attenuation with the dewatering of the rock mass and the related decrease in the pore pressure.

The most satisfactory model of the observed behavior predicts an effect of heating that decreases permeability because of the thermal expansion of the rock which causes the existing fractures to close. Q-values increased during the heating experiment in the lower, or cooler, end of the cross-section during the dewatering period. However, across the heater level there is little or no increase in Q due to the high pore pressures resulting from fracture closure. The inability of the water to drain becomes a major factor as the thermal expansion of water is 20 times that of the rock, causing hydrofracturing in the heated zone. It was observed in the laboratory tests that samples which came from the heated rock mass exhibited much higher Q-values at high stress than values measured during the test, indicating that the thermal process lowered the fracture average aspect ratio by extending existing fractures. From the experiment on partially-saturated granite, the maximum attenuation was found at a saturation of 65 %. It has been shown that a remote seismic technique can give valuable information of the behavior of a rock mass.

T.V. McEvilly

Co-Chairman of Committee

N.G.W Cook

Co-Chairman of Committee

Till minne av min Morfar och Mormor

Nils och Frida Sundquist

ACKNOWLEDGMENTS

During my absence from Stripa the field experiment was carefully monitored of by Lennart Andersson and Gunnar Ramquist. Their contribution is gratefully acknowledged.

The manager at the Stripa mine, Per-Axel Halen, provided much assistance. Without his help, this project would have been much more difficult.

Margot Harding and Maryilee Bailey did most of the illustrations in this thesis. Their careful work is gratefully acknowledged.

Professor Somerton of the Mechanical Engineering Department at U.C. Berkeley was kind enough to provide help with saturating and drying out the core specimens used for the laboratory tests. Professor Fuerstenau of the Material Science and Mineral Engineering Department at U.C. Berkeley permitted me the use of a mercury porosimeter for the experiment described in Chapter 4, as well as use of other laboratory equipment. This help, which improved the laboratory tests, is gratefully acknowledged.

Frank Morrison in the Engineering Geoscience Group undertook a difficult task in August 1976 when he decided that it is possible to make a Geophysicist out of a Geologist. His help and guidance through the academic jungle at CAL and his encouragement through the years is very much appreciated and gratefully acknowledged.

Finally, I want to thank Karen Ferree for her support, her care and limitless patience which made the time as a graduate student an even more pleasant experience.

TABLE OF CONTENTS

INTRODUCTION

The Swedish-U.S. Cooperative Program to investigate radioactive waste storage in a mined cavern has been conducted at the Stripa mine (Figure 1.1) in central Sweden, (Figure 1.2) since June 1977. The Stripa mine is situated in the Bergslagen mining district, and the mining history of the area and of the Stripa mine is centuries old. However, iron ore production at the mine ceased in early 1977. Since then the mine has been operated as an underground experimental site by the Swedish Nuclear Fuel Safety Program (Karnbranslesakerhet - KBS) under auspices of the parent organization, the Swedish Nuclear Fuel Supply Company (Svensk Karnbransleforsorjning - SKBF), and the U.S. Department of Energy, through the University of California - Lawrence Berkeley Laboratory. The program had several experimental tasks, which have been described by Witherspoon and Degerman (1978), Witherspoon, Cook and Gale (1980), and others.

The main objective at Stripa was to operate three different heater experiments, two full-scale and one time-scale, and to collect information on the behavior of a granitic rock mass when the rock was heated by electric heaters emplaced in large diameter boreholes in the floor of some drifts, as indicated in Figure 1.3. The full-scale electric heaters were intended to simulate radioactive waste cannister with a heat outputs of 3.6 kW (Heater H9) and 5.0 kW (Heater H10). An important part of the radioactive waste research program was concerned with the development and evaluation of geophysical techniques for the investigation of rock masses. One of these was a cross-hole high-frequency seismic technique. This technique was used over a period of two and a half years to survey and monitor the rock mass around a 5.5 m deep, 406

mm diameter borehole (H9) in which a 3.6 kW heater simulating high level nuclear waste had been emplaced. The experiment was performed 340 m below the ground surface in a drift especially excavated for the full scale heater test, as shown in Figure 1.4. The full scale drift is 6 m wide and 5 m high, and a special smooth-wall blasting technique was used to minimize the influence of the blast effect on the experiment, Andersson *et al.* (1979). Figure 1.5 shows the end of the full scale drift where the H9 heater is placed. The heater is in the right lower center of the figure; in the lower center the collars of extensometers placed in a number of vertical boreholes can be seen. In this figure the smoothness of the walls and the the floor is apparent.

Four 10 m long and 56 mm diameter vertical boreholes were drilled in the vicinity of the heater, Figure 1.6. These holes had two purposes: first to investigate the rock mass before the heater was turned on to locate such geological features such as fracture zones, and, second, for the cross hole technique to monitor the behavior of the rock mass during operation of the 3.6 kW electric heater.

In Figure 1.8 a cross section of the full-scale heater drift is shown along the drift centerline. It shows the boreholes and the detailed geology around the H9 heater experiment, with the 406 mm heater borehole in the middle of the array. The left-hand scale indicates depth below the surface datum of the mine. In this figure one should note the large number of diamond-drilled and cored boreholes, as well as the detailed geological mapping. Prominent features include the pegmatite dike (which runs from upper right to lower left), and the thrust faults which have faulted the pegmatite dikes and the quartz veins. Figure 1.7, shows a vertical section perpendicular to the one shown in Figure 1.6, through

the heater hole H9. This section shows the scale and the intensity of the drilling and subsequent instrumentation. The geology has been described in great detail, Paulsson *et al.* (1980); Chan *et al.* (1980) describe the thermal and thermo-mechanical data obtained.

The experiments and extensive logging and mapping provide an unparalleled opportunity to perform a well-controlled seismic field experiment. Similar experiments have been described by Fehler (1982) and by Aki (1982). However, the Stripa experiment is on a smaller scale and is more intensely instrumented.

In the field, the seismic travel times were read from a digital display of the total delay of the signal from the trigger for both P and S waves. The waveforms were also individually recorded on Polaroid film, and by an instrumentation tape recorder for later analysis. The four 56 mm diameter boreholes are 2 to 4 m apart, as indicated in Figure 1.6. This short spacing, together with the detailed investigation of the geology (Paulsson *et al.* 1981) and temperature and stress (Chan *et al.* 1980), provides unique laboratory-type precision and control in an *in situ* cross-hole seismic experiment. Because of this detailed knowledge of the geology, temperature, stress and hydrology, the effectiveness of ultrasonic waves in characterizing a rock mass in field can be evaluated for distances two orders of magnitude larger than commonly employed in a laboratory experiment.

Results from numerous investigations have shown that it is possible to make a quantitative estimate of the quality of a rock from P- and S-wave velocities and P- and S- wave amplitude attenuation in the laboratory. Anisotropic crack distribution causes elastic anisotropy. Non-hydrostatic stress may cause stress induced anisotropy, due to

anisotropic closure of cracks (Nur; 1971). Hadley (1976) has shown that attempts to correlate velocities calculated from the aspect ratio spectrum, obtained with the help of a scanning electron microscope (SEM), with velocities measured on rock samples show that the SEM fails to detect a substantial number of cavities. Nur and Simmons (1969) have shown that the application of uniaxial stress to a sample of granite causes elastic-wave velocity anisotropy. Compressional waves travel fastest in the direction of the applied stress. This behavior is associated with microcracks that exist in granitic rock, as was originally suggested by Adams and Williamson (1923). Nur and Simmons (1969) have shown that at effective (confining pressure minus pore pressure) stress levels below 100 Mpa, the elastic properties of rocks are controlled mainly by the properties of microcracks. Walsh (1965) has indicated that crack shapes in rock are approximated reasonably well by penny-shaped ellipsoids, which makes it possible to describe the effects of cracks with only three parameters: the aspect ratio, porosity, and the distribution of cracks in space. When a non-hydrostatic stress is applied, the effect is that some fractures close while others remain open. The stress necessary to close a penny-shaped crack is proportional to its aspect ratio, defined by

$$\alpha = \frac{c}{a}, \qquad\qquad [1.1]$$

where c is the width and a is the length of the fracture, through

$$\sigma = E_o\, \alpha \qquad\qquad [1.2]$$

where E_o is the intrinsic Young's modulus (Walsh; 1965). A rock which initially has a random distribution of cracks with resulting isotropic

properties will have non-isotropic properties under biaxial or triaxial stress conditions. Seismic velocities, V_p and V_s for both dry and saturated rocks decrease with increasing crack density. The ratio Vp/Vs is a minimum when the cracks in a rock are dry (Hadley; 1976), the ratio increases with increasing saturation. Further more, a plot of (Vp/Vs) versus Vs uniquely specifies the crack density, as shown by O'Connell and Budiansky (1974). Anderson et al. (1974) found that a preferred orientation of open cracks, resulting from intrinsic properties of the rock, or caused by stress-induced anisotropy, has a marked effect on seismic velocities, with the major reduction of velocity observed perpendicular to the planes of open fractures. Cheng and Toksoz (1979) inverted laboratory seismic velocities of various rocks as a function of pressure and saturation to obtain spectra of pore shapes and sizes.

In the fields of geotechnology and mining, high-frequency acoustic techniques are increasingly being employed for site investigation, characterization and evaluation. The classification of rock mass quality and site evaluation by seismic methods have been described by Cratchley et al. (1972), La Porte et al. (1973) and Sjogren et al. (1979). Stephansson et al. (1979) have discussed applications of the seismic method to determine the depth and degree of fracturing of a rock mass near a free surface.

High-frequency acoustic techniques employed within a borehole have been described by Geyer and Myung (1971), Myung and Baltosser (1972) and King et al. (1975,1978). The application of acoustic borehole logs in detecting fractures, for rock classification and in determining the in situ elastic properties of rock have been discussed by these workers and by Carroll (1966,1969) and Coon and Merritt (1970).

The use of acoustic measurements between boreholes for geotechnical purposes has been described by Price *et al.* (1970), McCann *et al.* (1975) and Auld (1977). Recently, Fehler (1982) discussed the dual-well seismic experiment used to determine mechanical properties in a geothermal hot, dry rock experiment at Fenton Hill. Price *et al.* employed the work of their results to determine the optimum rock-bolt pattern to stabilize a rock mass. McCann *et al.* used the between-hole technique to delineate interfaces between homogeneous media and to detect localized, irregular features. They also discussed a means for interpreting their data to estimate the degree of fracturing in the rock mass. Auld has described instrumentation for, and presented field results of, between-borehole acoustic measurements which he then used to determine the elastic properties of the rock mass.

The heater experiments in the Stripa mine had a two-fold objective. The primary objective was to make an assessment of the thermal effect on a rock mass of emplacing electrical heaters simulating cannisters of high-level nuclear waste. The second purpose was to develop instruments and to improve techniques for monitoring a rock mass when a thermal load is applied. The intention with the ultrasonic cross-hole experiment was first, to investigate the possibilities of utilizing a high frequency seismic technique to survey and monitor the effects of stress changes and any changes in physical properties between a pair of boreholes in a rock mass, in conjunction with the heater experiment. The second intention was to investigate the sensitivity of the technique for mapping the physical properties of the rock mass. Cook (1979) has demonstrated the importance of developing a remote sensing technique, both in terms of determining the suitability of a rock mass as a potential

repository for high level nuclear waste and for monitoring the changes in the rock mass, both during excavation and commissioning of a repository. The seismic technique is appealing insofar that it is non-destructive and remote; and that measurements of the rock properties can be performed in boreholes at a suitable distance from the site.

CBB 779-9289

Fig. 1.1 Surface buildings of the Stripa iron ore mine

FORSMARK

STRIPA

STOCKHOLM

RINGHALS

SIMPEVARP

BARSEBÄCK

0 50 100 km

SCALE

Reactor in operation
Reactor under construction
Nuclear power plant
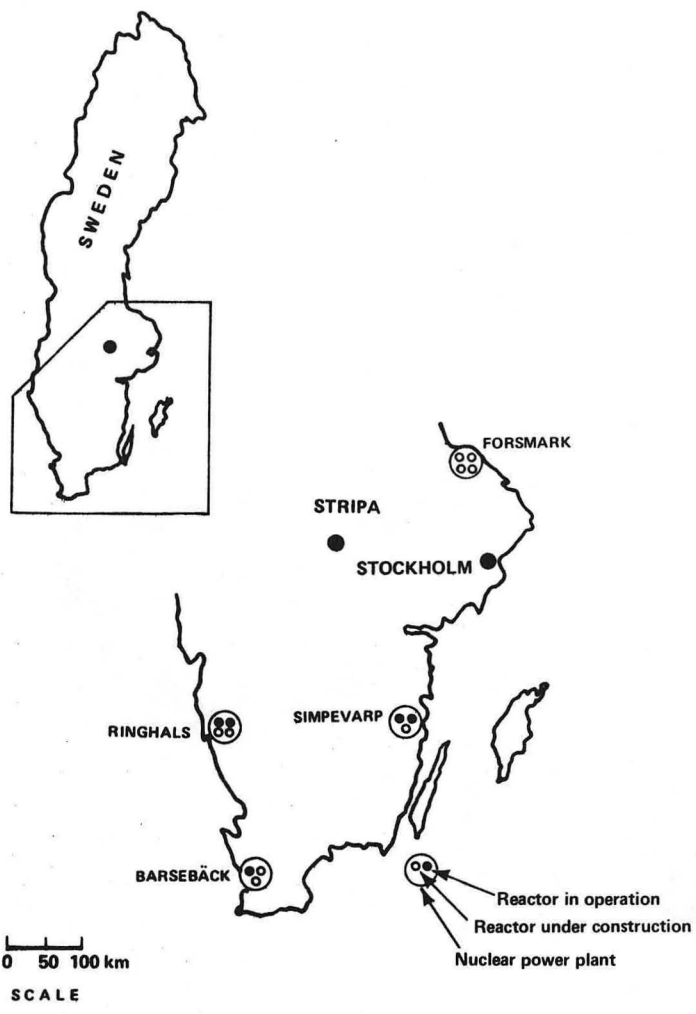
XBL 785-968

Fig. 1.2 **Location** of the Stripa mine

10

Ventilation test (LBL)

Time-scaled heater test (LBL)

Computer building (LBL)

Heating test (KBS)

Full-scale heating test (LBL)

Permeability test (KBS)

Injection test (KBS)
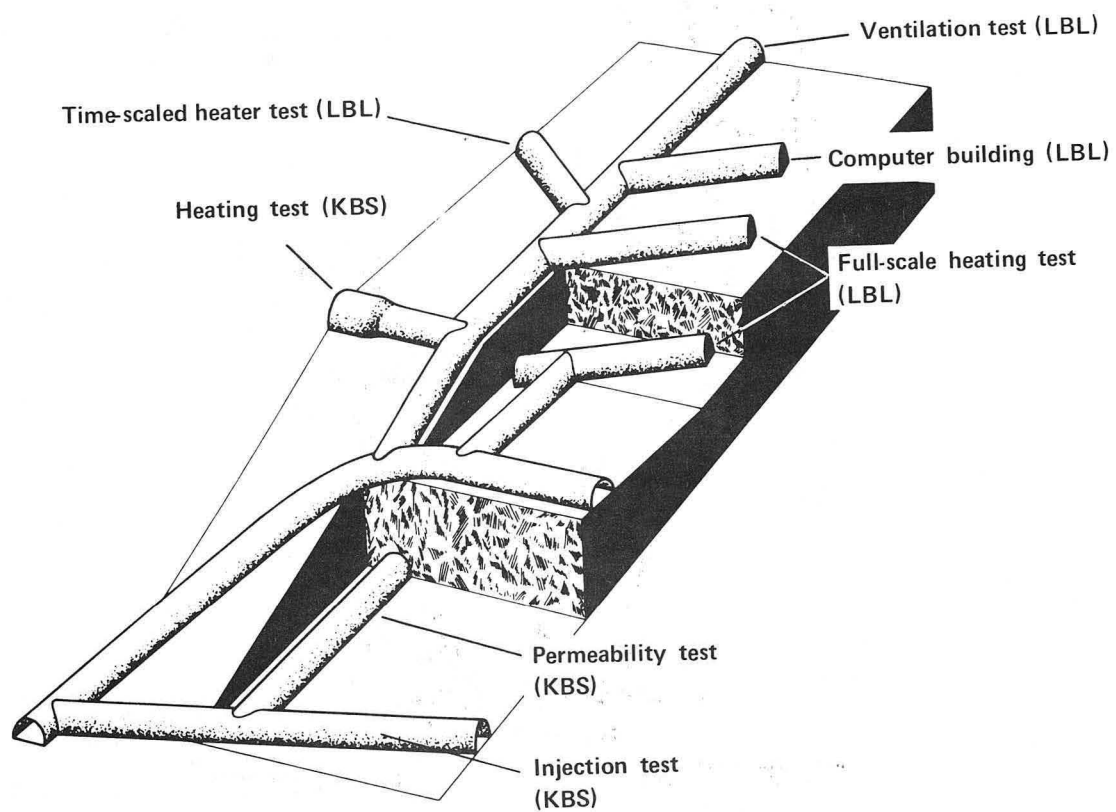
XBL787-2596 A

Fig. 1.3 An isometric sketch showing the location of the experiment rooms at depth of 340 m below surface.

Full scale
heater drift

Full-scale
heater

Instrument
boreholes

Extensometer
drift
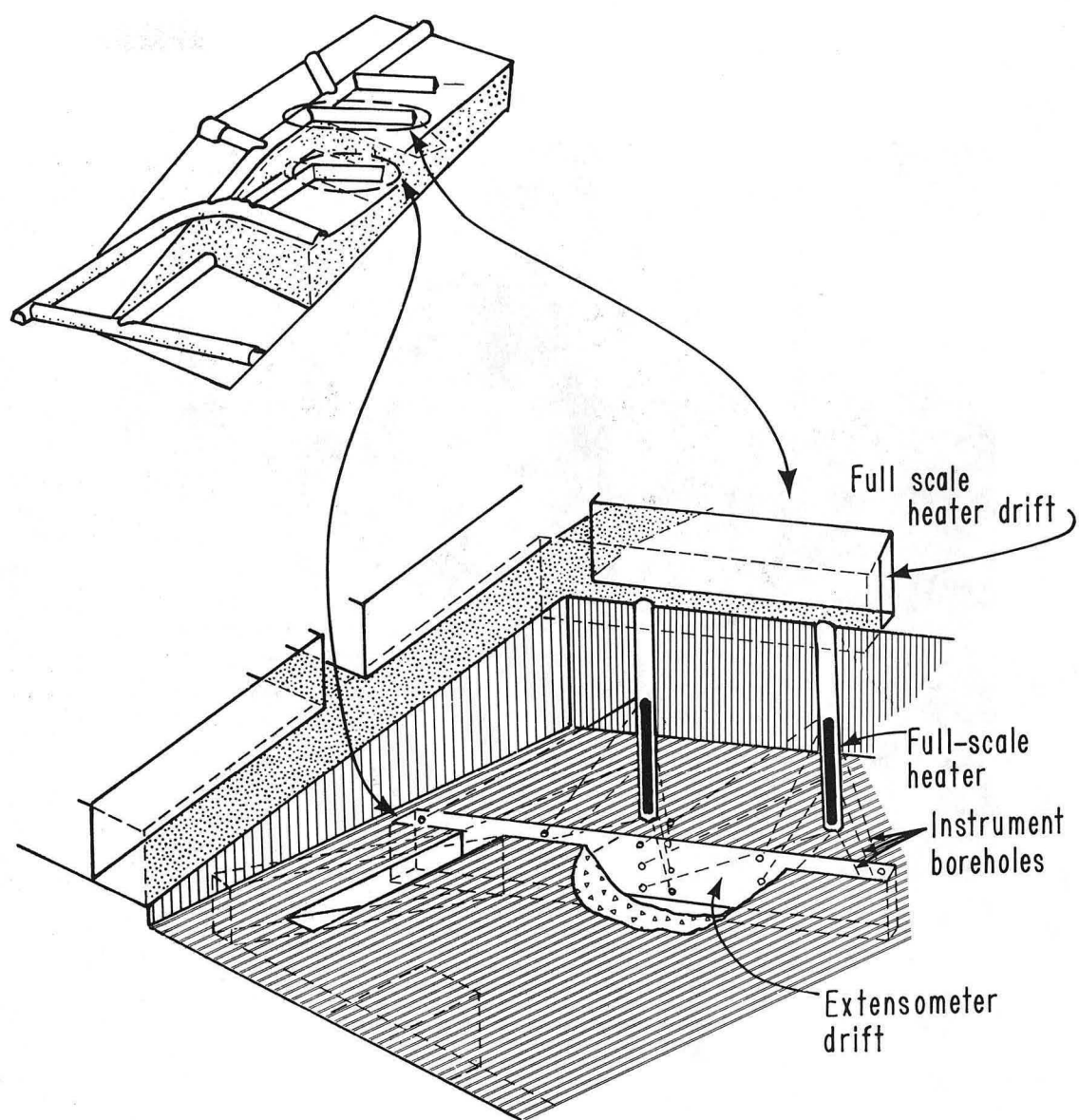
XBL 785-970 A

Fig. 1.4 3-dimensional view of the full scale experiments, showing heater layout and some holes for the horizontal extensometers.
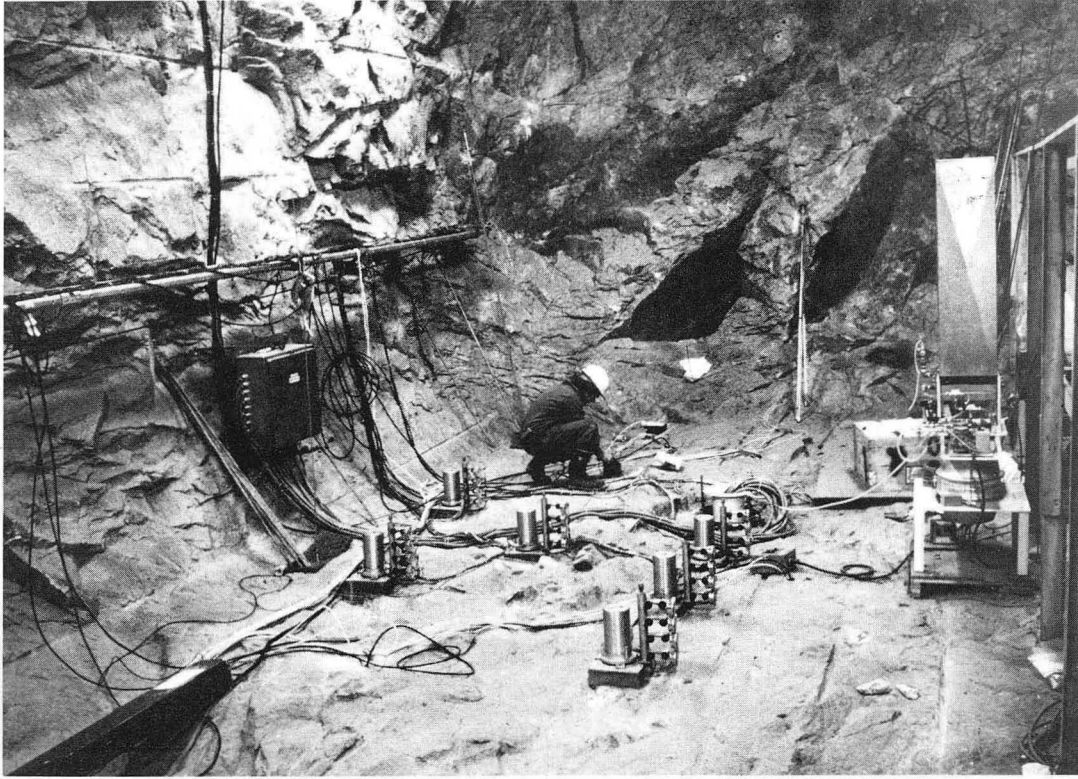
CBB 790-14274

Fig. 1.5 The end of the full-scale drift showing the top of H9 heater and the heads of the vertical extensometer through the H9 heater hole and parallel to the axis of the drift. Also shown are the smooth walls and floor from careful blasting

H9,HIO	Heater holes	406 mm	
E	Extensometer holes	76 mm	
U	US Bureau of Mines guage holes	38 mm	
T	Thermocouple holes	38 mm	
C	Colorado School of Mines cell holes	38 mm	
M	Monitor holes (ultrasonic)	56 mm	
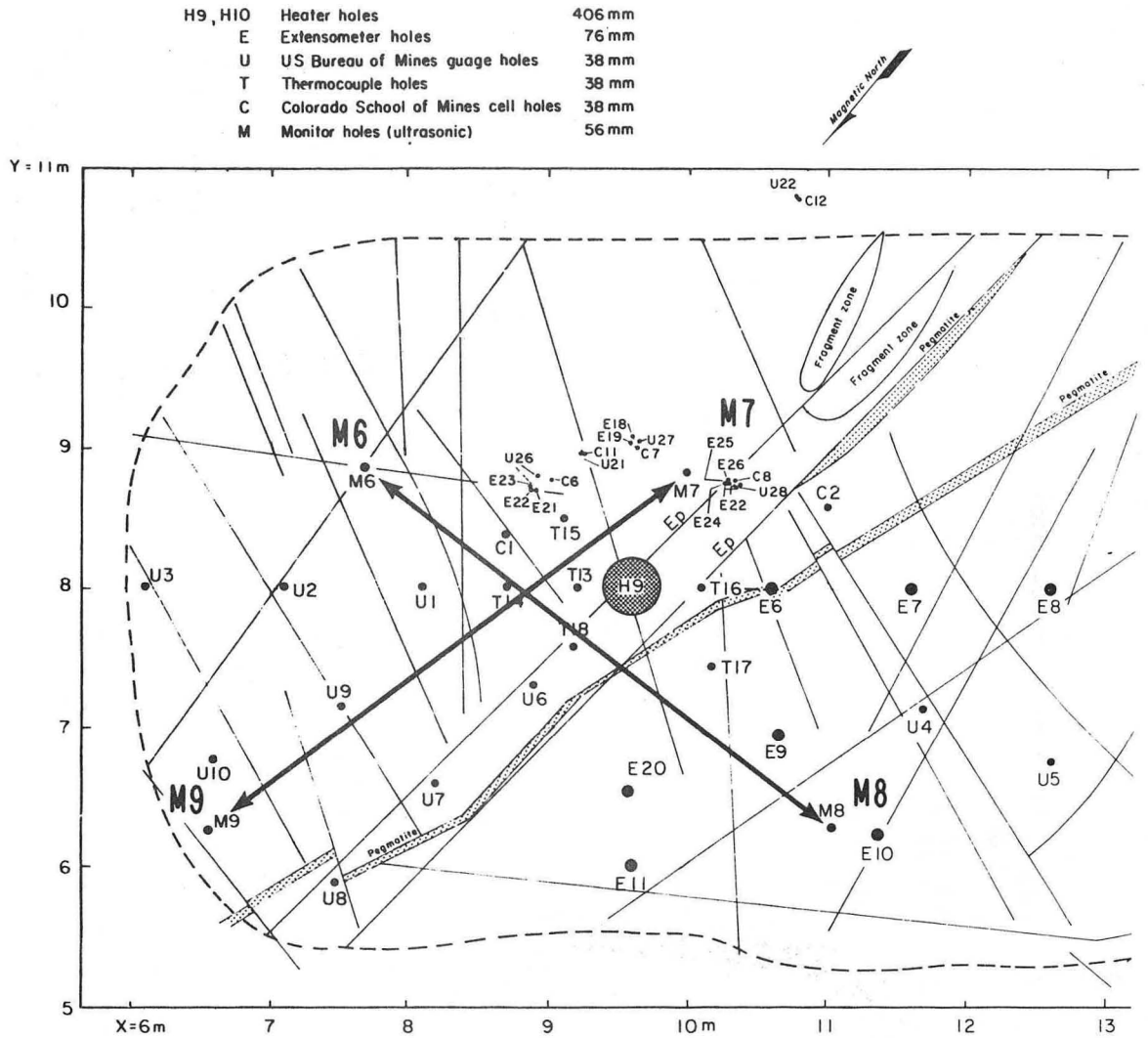
XBL 801-6748

Fig. 1.6 Plan of the drift floor and the boreholes for the H9-heater showing the M6, M7, M8 and M9.
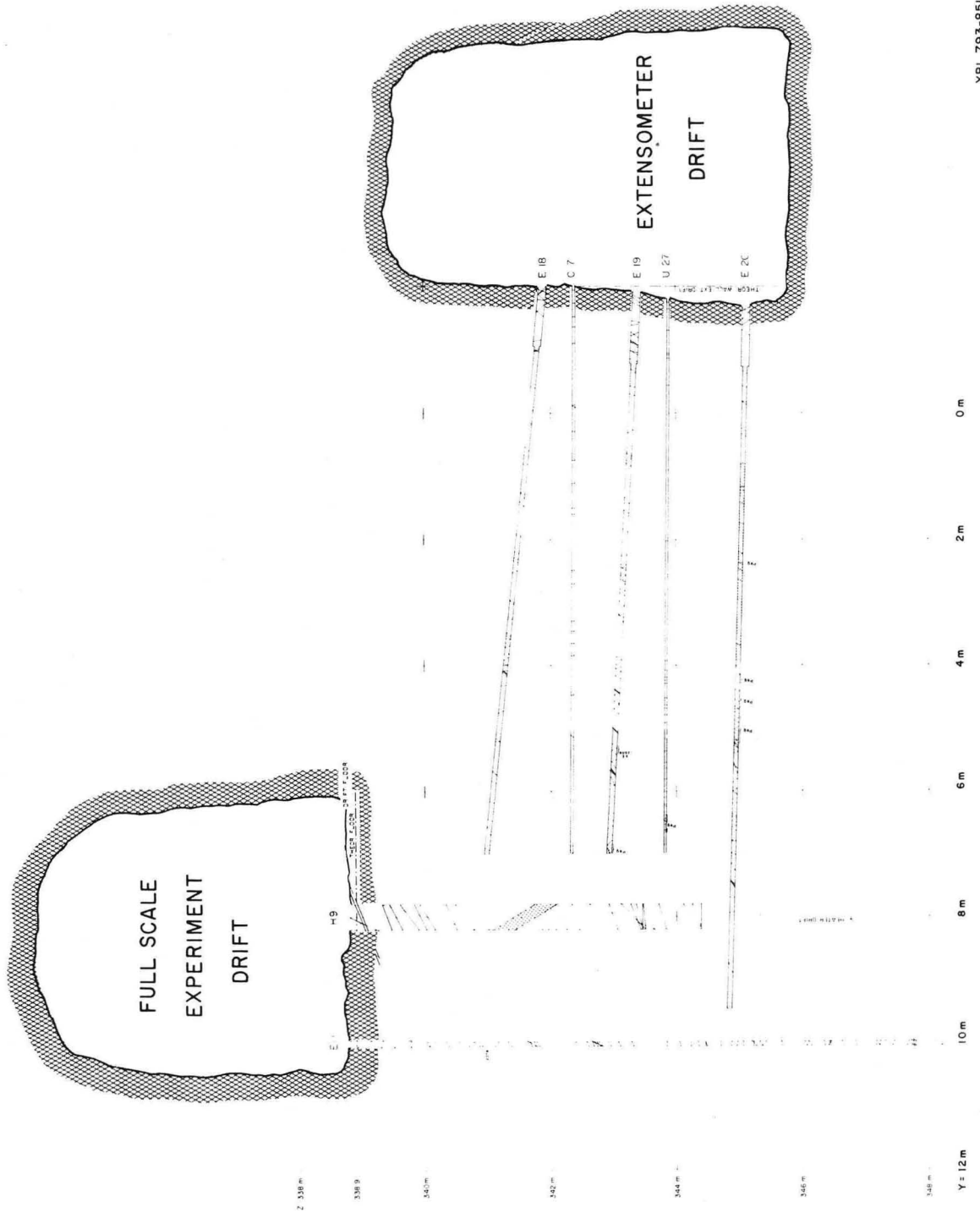
Fig. 1.7 Vertical section of the fullscale and the extensometer drifts and the boreholes. Also shown are the appearent orientations in this cross-section of the logged fractures in each boreholes.
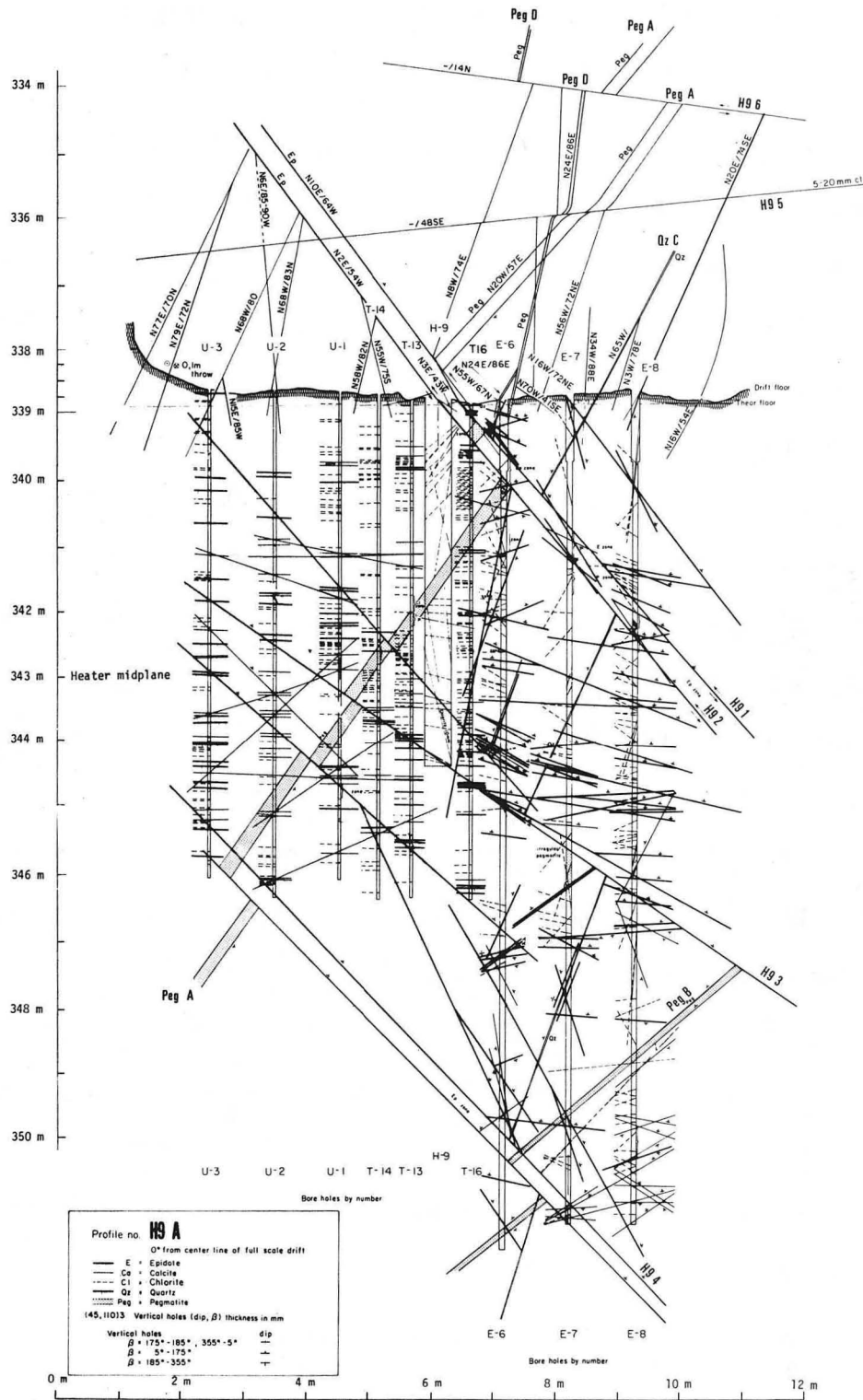
Fig. 1.8 Vertical section through the H9 heater hole and parallel to the axis of the drift, showing drift, boreholes and geology. The lines connecting the boreholes represent fractures found in core from more than one borehole.

2.   GEOLOGY AND FRACTURE MAPPING.

The geology at the Stripa mine has been described by Olkiewicz *et al.* (1979). The ore extracted in the Stripa mine was mainly a quartz-banded hematite, with occasional occurrences of magnetite (Sjustjarne malm). The ore, which has an iron content of 51% and a phosphorus content which is low, is stratiform with the leptite. Leptite is a general term for a predominantly high-grade metamorphic volcanic rock, high in SiO_2 and with a grain size between 0.5 and 0.05 mm. The oldest rock type is the series of grey leptites, which is approximately 2000 million years. The leptite above the main ore is layered, in contrast to the leptite below the main ore which is not layered. The granitic rock in Stripa, predominantly a quartz monzonite, intruded the leptite. There are a number of diabase dikes in the mine which are older than the quartz monzonite in the test area. The age of the quartz monzonite is reported to as 1.69×10^9 years, Wollenberg *et al.* (1981). The quartz monzonite is associated with a series of pegmatite and aplite dikes. The youngest dikes are the steeply dipping diabase dikes with a NNE strike. The test area is dominated by a reddish, medium-grained massive quartz monzonite, with an average grain size of 3 mm. The composition of the reddish quartz monzonite, determined by point counting is indicated in Table 2.1, Wollenberg *et al.* (1981).

The Stripa quartz monzonite is classified as serorogenic. It differs from the pre- or synorogenic granitic rocks because of its apparent homogeneity and its relative lack of foliation. The rock mass at Stripa also contains pegmatites and aplites, the former were found in most boreholes drilled for the full-scale heater experiment. The quartz

Red Stripa quartz monzonite	
Mineral	Volume %
Quartz	37.1
Partly sericitised plagioclase	32.0
Microcline	22.2
Muscovite	7.4
Chlorite	1.3
Accessory minerals	-

Table 2.1

monzonite in the experiment area is less deformed than in other parts of the mine. In places, the rock is strongly fractured and brecciated.

Wollenberg *et al.* (1981), emphasize that the high abundance of fractures extends down to the grain-size scale, stating that "fractures ranging from well under a mm to several cm or more in width, as well as wider ones of brecciation, are readily visible in a hand sample, but only in thin section does the full extent of fracturing and brecciation become apparent". The great majority of fractures have been completely sealed, but in some cases fine openings can be seen in thin sections, and an example of this is shown in Figure 2.1 a. An example of a normal granite from a pluton 1 km from the Stripa pluton is shown in Figure 2.1 b, and here one can see the good contact between the grains. In the thin section from the Stripa pluton one can see that the quartz grains are completely surrounded by fracture infilling material, in this case sericite, but often calcite or chlorite. Even in relatively unfractured samples,

fine discontinuous cracks are very common within primary grains or along grain boundaries.

Although the Stripa quartz monzonite has been severely disrupted mechanically, displaying abundant fracturing and numerous faults, it is evident that most if not all of the discontinuities have been filled with secondary minerals. The majority of the mapped fractures dip steeply to the north, except in the northern part of the drift close to the experimental area where many south-dipping fractures were observed.

In the H9 heater borehole area a total of 4000 open and closed fractures were logged in core obtained from instrumentation holes for the heater experiment. Of these 4000 fractures, 1885 are from cores which were oriented. A total of 224 meters of oriented core was recovered from the 20 boreholes with diameters of 56 mm and 76 mm. These boreholes were drilled from the heater and extensometer drifts. The average distance between these fractures was 0.12 m.

The pole plots of these fractures form two primary clusters, one at N30E/30W and the second at N10E/65W. In Figure 2.2, are shown the plots on a Schmidt lower hemisphere net of the relative distribution of the 1885 open and closed fractures from oriented core from both vertical and horizontal boreholes. However it should be emphasized that the mapped and plotted fractures are major fractures which were clearly visible over the entire circumference of the core; this was necessary in order to get a good estimate of the orientation of the fractures. The frequency of all the fractures, small and large macroscopic, is probably between 20 and 30 fractures/m. This is also what Thorpe (1979) found, (Figure 2.3). The majority of the fractures are filled with chlorite. Epidote also occurs as a fracture-filling mineral and is especially abundant

at the end of the full-scale drift where the cross-hole experiment described in this thesis was conducted. Epidote-filled fractures are associated with faults mapped in the full-scale drift. Calcite, which probably is the youngest fracture set, also occurs frequently. The calcite-filled fractures are the most likely conduits for water, and they have a strong impact on the seismic velocities. In appendix 2 A the pole plots of fractures with different infilling minerals are shown.

Despite the pervasive fracturing, laboratory and field measurements have shown that in many respects the rock does not differ much from other competent igneous rocks. The high values of the attenuation of seismic waves obtained both from the field work and the laboratory work reported in this paper suggest that the monzonite is unusually micro-fractured. Laboratory determinations of porosity are around 0.5-1.0 %, as indicated by Paulsson and Kin (1980) and Nelson $et\ al.$ (1979). In this thesis a porosity of 0.9 % was observed and it is probably a better value for the area where the field work was performed, because the samples on which the measurements were made came from this area. Both field and laboratory measurements of compressional wave velocity V_p at frequencies of the order of 50 kHz yield values of about 5500 to 5700 m/s under ambient conditions. The velocity of compressional waves for a saturated rock are not sensitive to the degree of microfracturing. Micro fractures are much smaller than the wavelength, and are essentially invisible to the ultrasonic velocities. The attenuation measured in the rock reveals the nature of the fracturing as shown in Chapters 6 and 7. The unusually low Q-values found in field are confirmed by the low Q-values obtained in the laboratory.

The pole plots provide a good estimate of the orientation of frac-
tures in the rock mass at large. However, to take full advantage of the
detailed geological mapping, and the temperature and strain measure-
ments around the heater, a 3-dimensional model was found to be very
helpful. This was done with the help of a plexiglas model, Paulsson *et al*.
(1981). The problem is of course to present such data in report form.
Using the 3-dimensional model six cross-sections were constructed.
Each of the six cross sections includes two of the M-holes, used for the
cross-hole seismic measurements. Each fracture logged in the core from
the two boreholes was plotted with its apparent dip at the true depth
from the collar of the borehole in the particular cross section. This in
essence means that the fractures are plotted as they appear in the
actual cross-section intersecting the M-boreholes. In Figure 2.4 the drift
floor at the end of the full scale drift is shown. Figure 2.4 A shows all the
fractures as they were mapped. Only fractures longer than 0.3 meter
were mapped, Paulsson *et al*. (1981). In Figure 2.4 B the major frac-
tures, faults and dikes are shown. The line "A" is the surface expression
of the vertical section shown in Figure 1.6, and the line "E" is the surface
expression of the vertical section shown in Figure 1.7. Figures 2.5 - 2.10
show the six cross-sections used in the ultrasonic between-hole experi-
ment. The fractures shown in these figures have the dip and the strike
in the figure as they would appear to have if the actual cross section
could be observed. The geological strike and dip are provided with each
fracture in each cross section in Appendix 2 B. Despite logging both
open and closed fractures in the core and despite full core recovery, it
proved very difficult to correlate one particular fracture in a borehole
with a fracture in a neighboring borehole only 2-4 meters away, even

though the surface expressions of most fractures show them to be planar. The macroscopic fractures were observed to start and stop in a pseudo-random fashion. It was in some cases possible to perform the correlation, between the boreholes but the only features recognized in all the boreholes in which they appeared were the pegmatite dikes and the epidote faults. The most continuous of the fracture types were the fractures found which had predominantly epidote as infilling material. The epidote fractures were also the fractures which were least prone to break open during the drilling and the core handling process. 80% of the fractures identified as epidote -filled fractures were still intact at time of logging the core. In comparison, of the fractures filled with calcite only 10 % were still intact when the core was logged. This large difference cannot be explained by the relative ease one identifies calcite in fractures with the help of acid: it is clearly a property of the fracture. The calcite fractures belong to a younger set of fractures. This can be seen in Figure 2.11, where it is shown that an old epidote fracture is faulted by a younger fracture filled with calcite. There is, furthermore, a good correlation between low-velocity zones and zones with an abundance of calcite fractures.

In Figure 2.12 the fracture system mapped in the heater midplane is shown. This plane is important insofar as most of the seismic data were collected there. Dominating the picture is the pegmatite dike labeled PEG A, and the fault zones H9-1 and H9-2. Between boreholes M7-M9, there are a few steeply-dipping calcite fractures which are cutting the cross section M7-M9 at an acute angle. These fractures influence the M7-M9 velocity and attenuation data as will be shown in Chapters 5 and 6. Some of the same fractures also cut across the line M8-M6, but the

line and the fracture are nearly perpendicular. Not unexpectedly, the intersection angle between the wave propagation direction and the line of the geological features is very important.
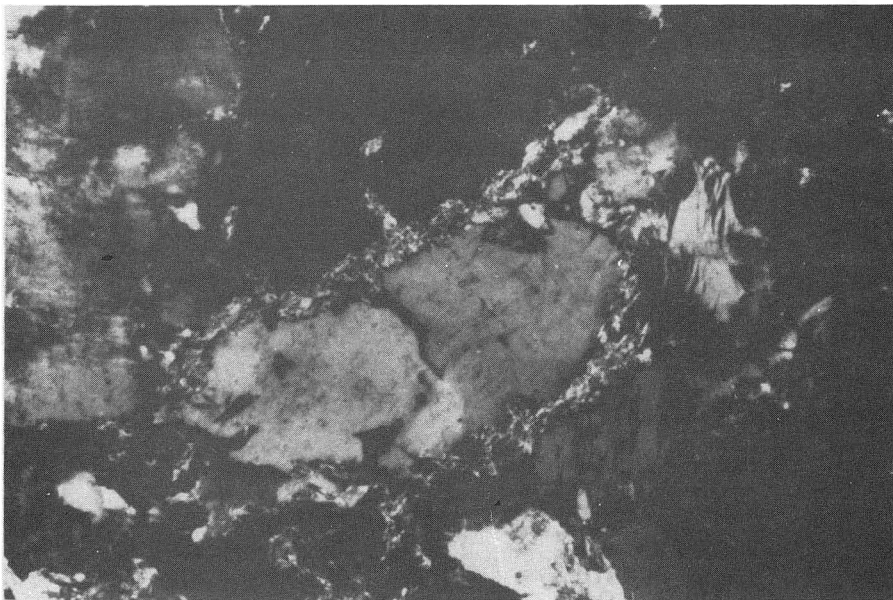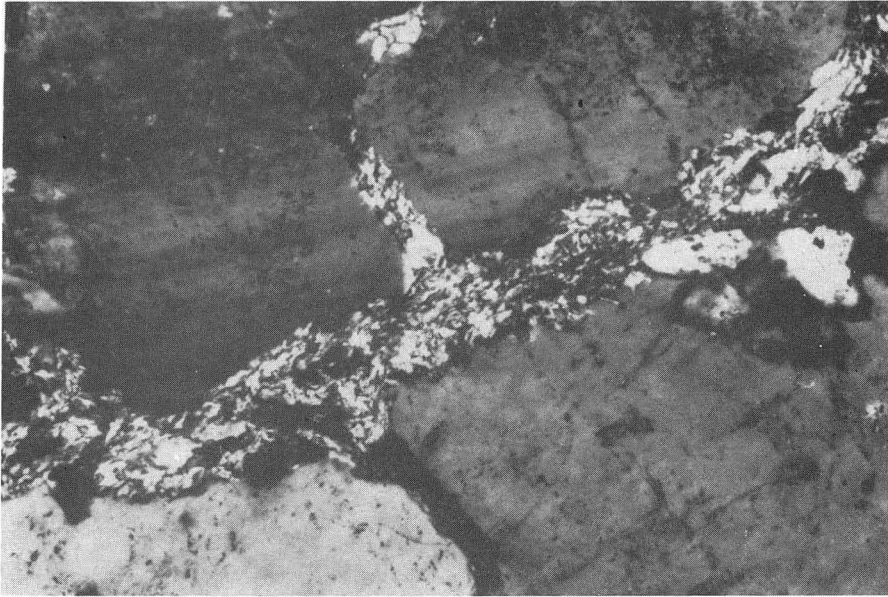
Fig. 2.1 a) Thin section from the fullscale drift in the Stripa pluton. The upper photograph represent 1.32 mm across and the lower 0.66 mm across the long direction. The extensive micro fracturing between each grain is apparent.

XBB 838-6115
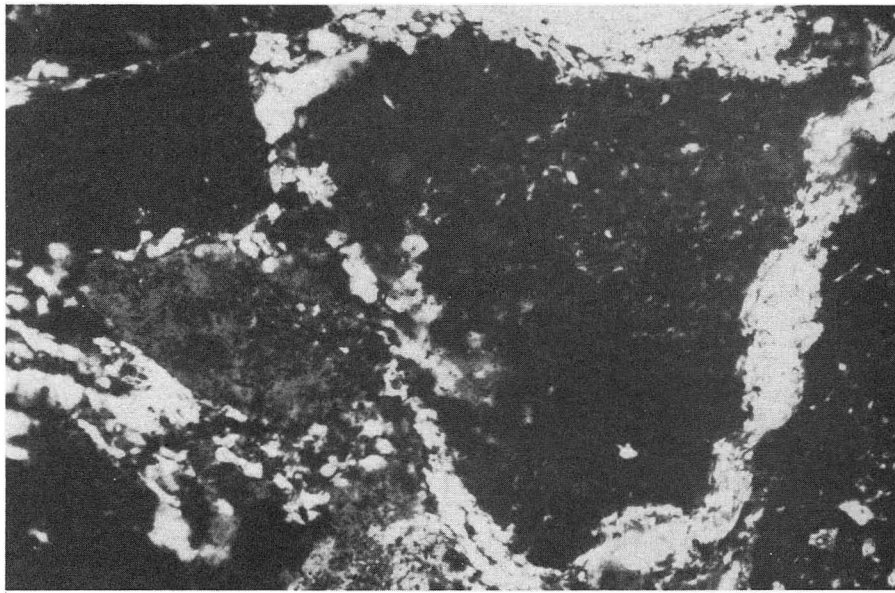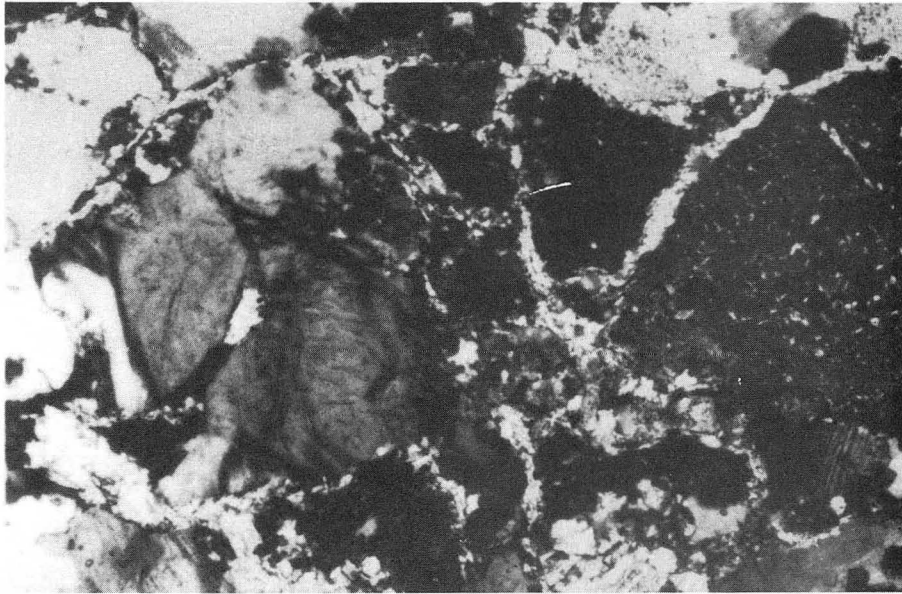
Fig. 2.1 b) Thin section from the fullscale drift in the Stripa pluton. The upper photograph represent 1.32 mm across and the lower 0.66 mm across the long direction. The extensive micro fracturing between each grain is apparent.

XBB 838-6916
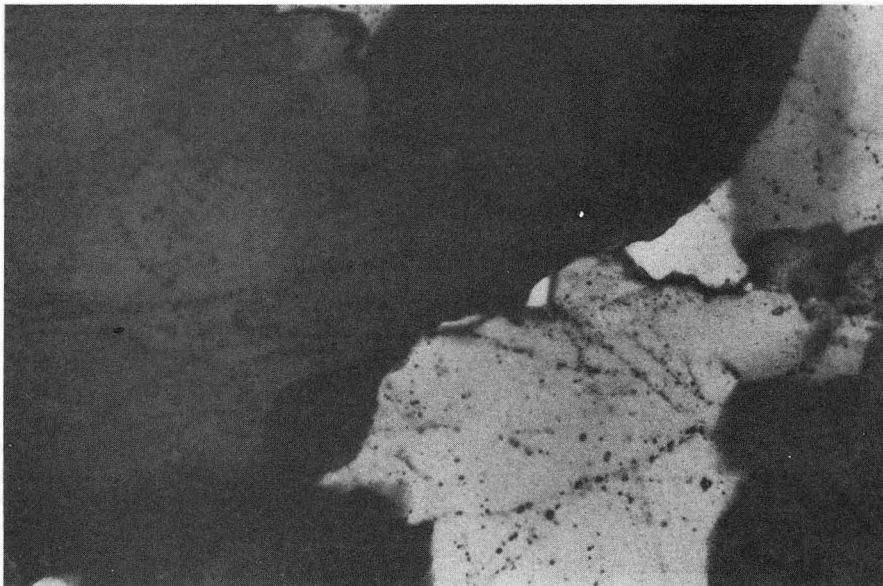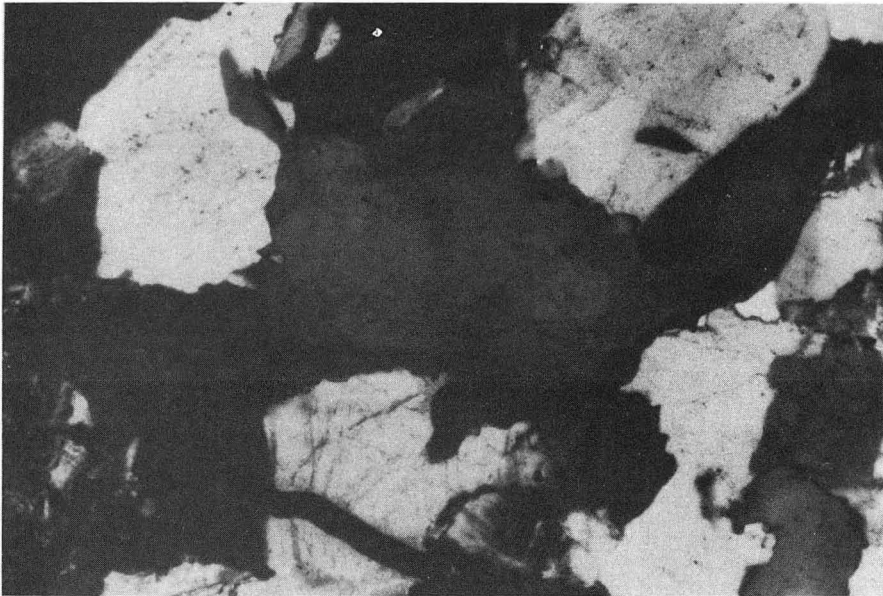
Fig. 2.1 c) Thin section from the fullscale drift in the Stripa pluton. The upper photograph represent 1.32 mm across and the lower 0.66 mm across the long direction. The extensive micro fracturing between each grain is apparent.

XBB 838-6917
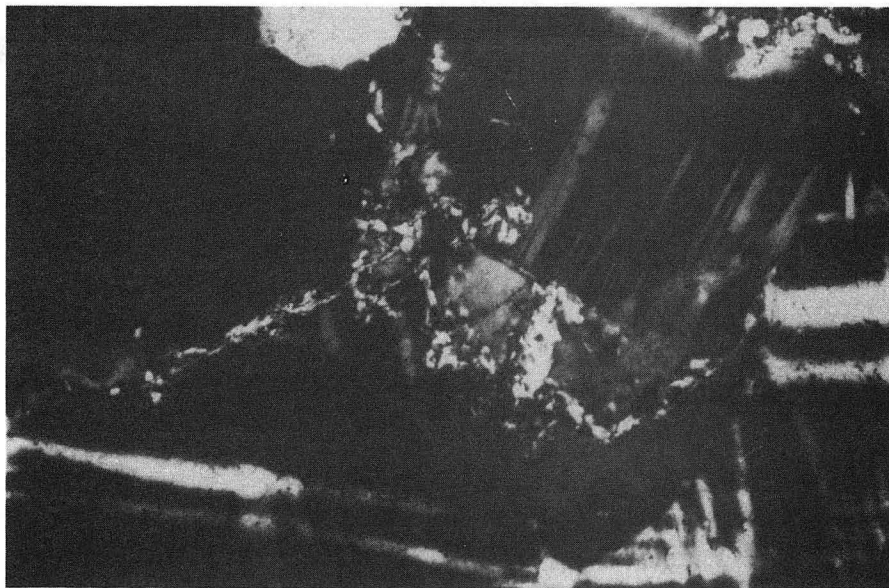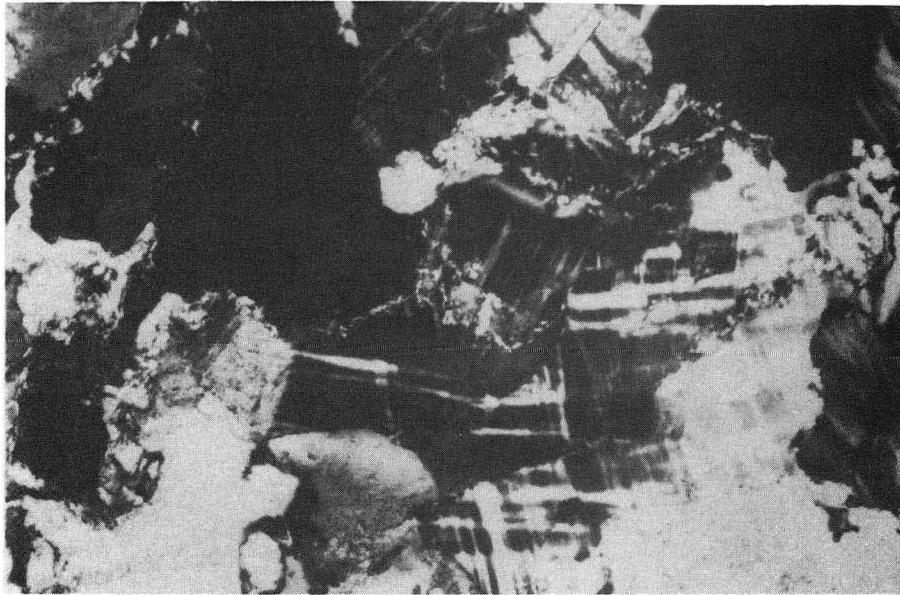
Fig. 2.1 d) Thin section from the fullscale drift in the Stripa pluton. The upper photograph represent 1.32 mm across and the lower 0.66 mm across the long direction. The extensive micro fracturing between each grain is apparent.

XBB 838-6918
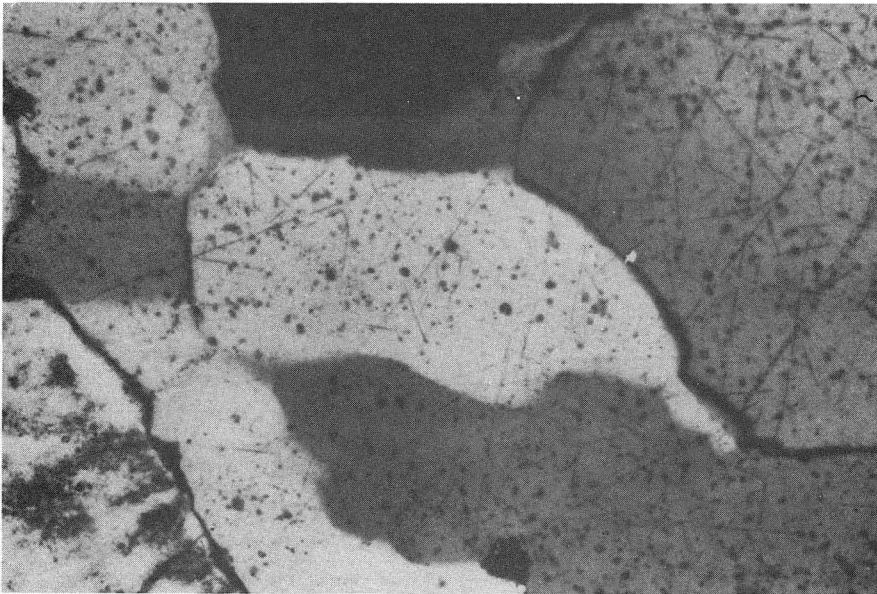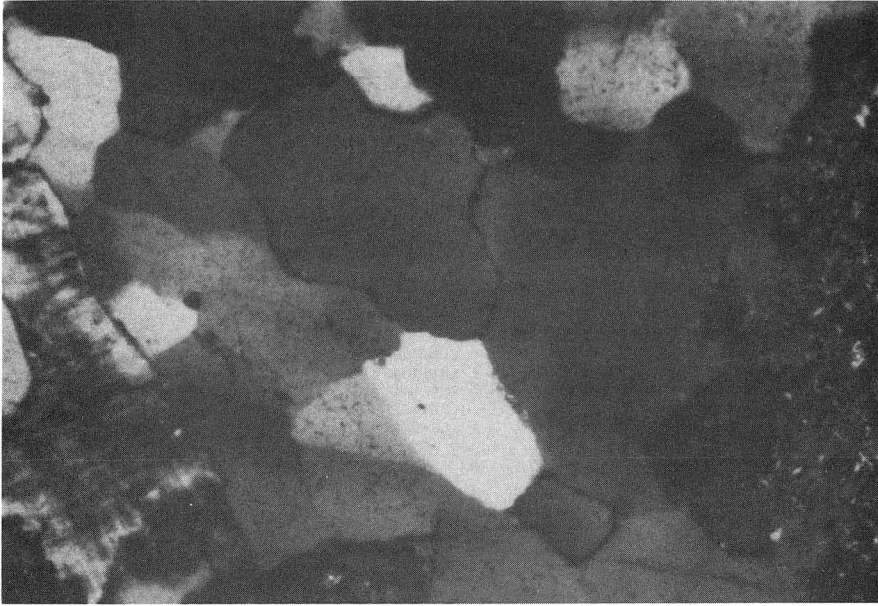
Fig. 2.1 e) Thin section from a granitic pluton adjacent to the Stripa Mine. The upper photograph represent 1.32 mm across and the lower 0.66 mm across the long direction. The micro-fracturing which was so abundant in the Stripa pluton isnot found in this granite.

XBB 838-6919
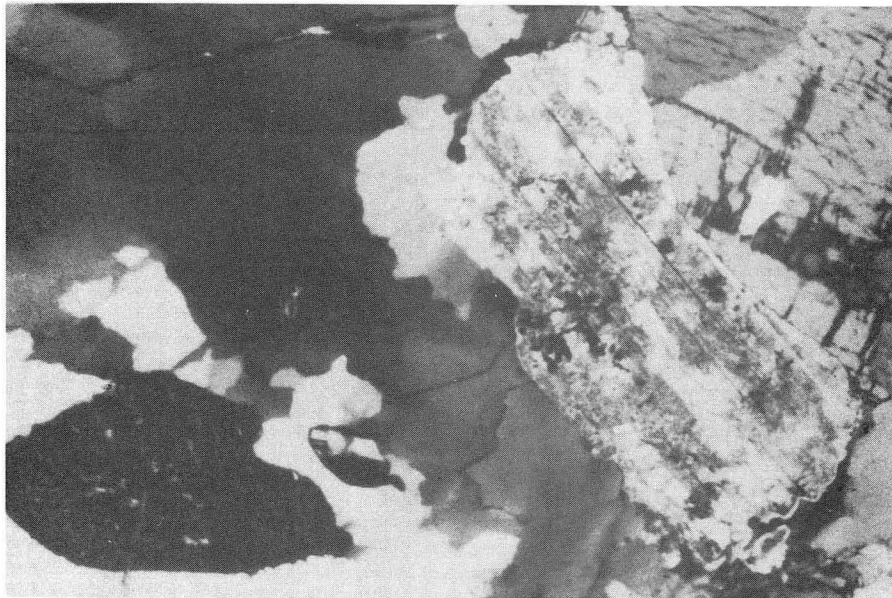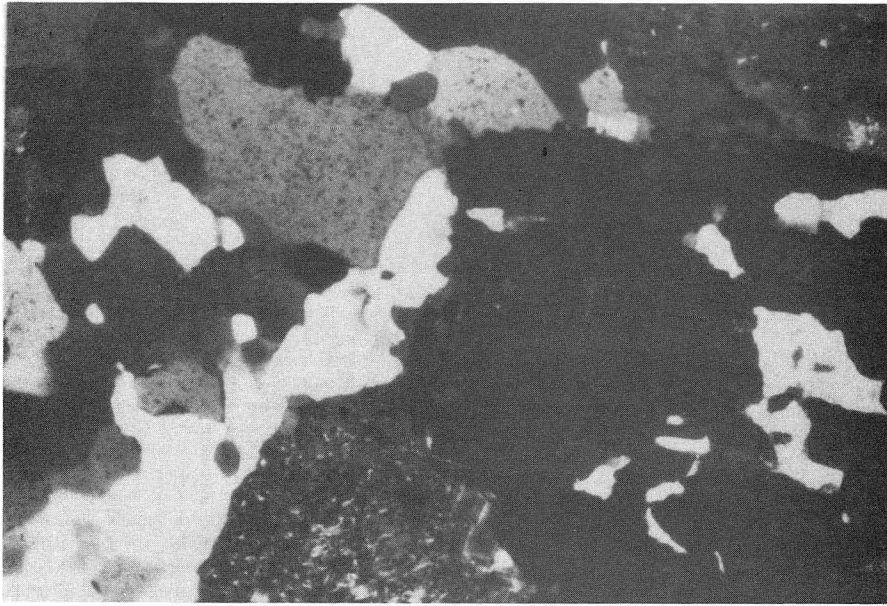
Fig. 2.1 f) Thin section from a granitic pluton adjacent to the Stripa Mine. The upper photograph represent 1.32 mm across and the lower 0.66 mm across the long direction. The micro-fracturing which was so abundant in the Stripa pluton isnot found in this granite.
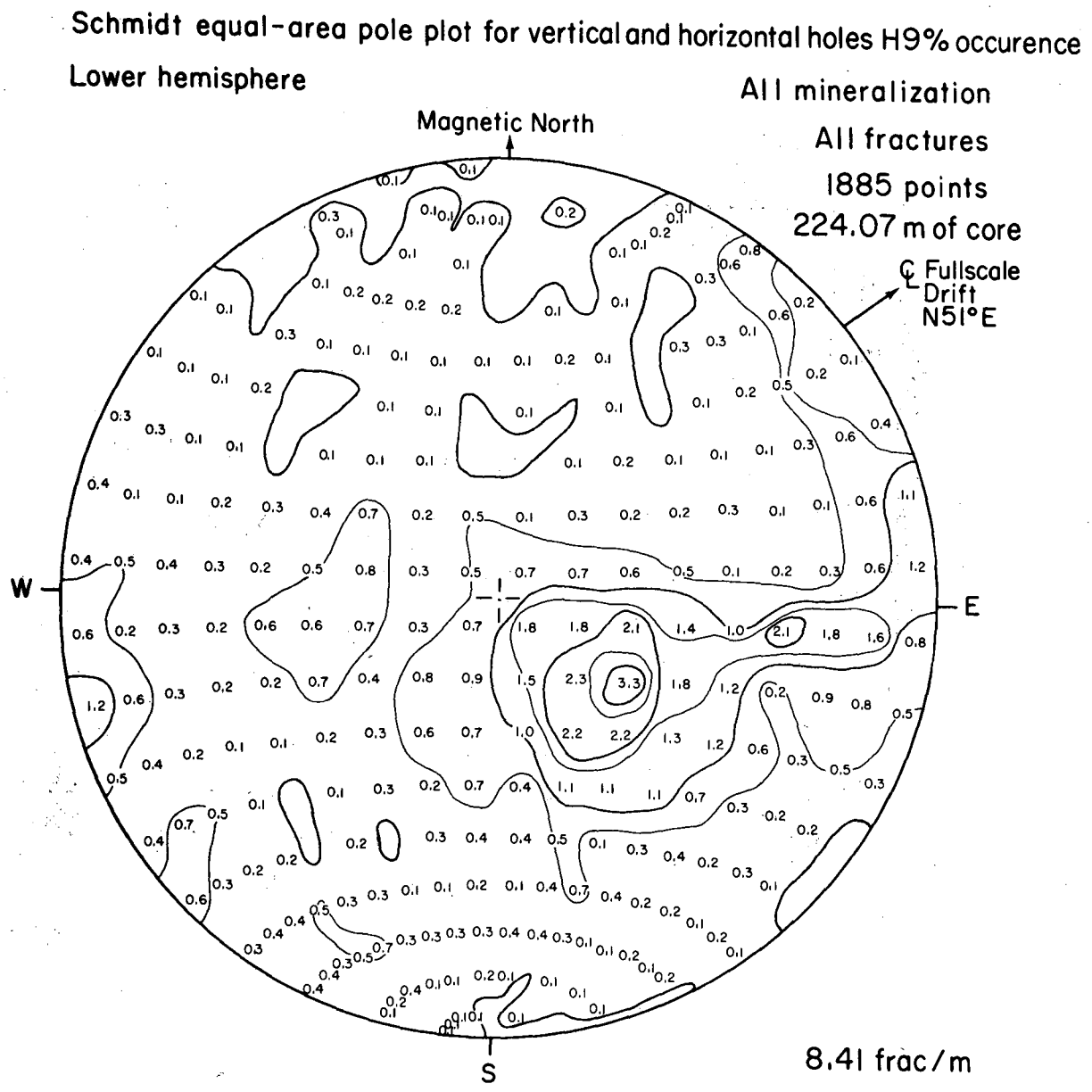
Fig 2.2 Pole plots on a Schmidt equal-area stereo net for all the fractures recorded in oriented core in the H9 heater experiment

XBL 799-11315

Fig 2.3 Fracture frequency in core from time scale drift (after Thorpe, 1979)

XBL 793-659

Fig. 2.4 Surface fracture maps in the full scale drift around the H9 heater.

Fig. 2.5 Vertical cross-section A; M7-M6 showing the boreholes, pegma-tite dikes and logged and projected fractures.

Fig. 2.6 Vertical cross-section B; M7-M8 showing the boreholes, pegmatite dikes and logged and projected fractures.
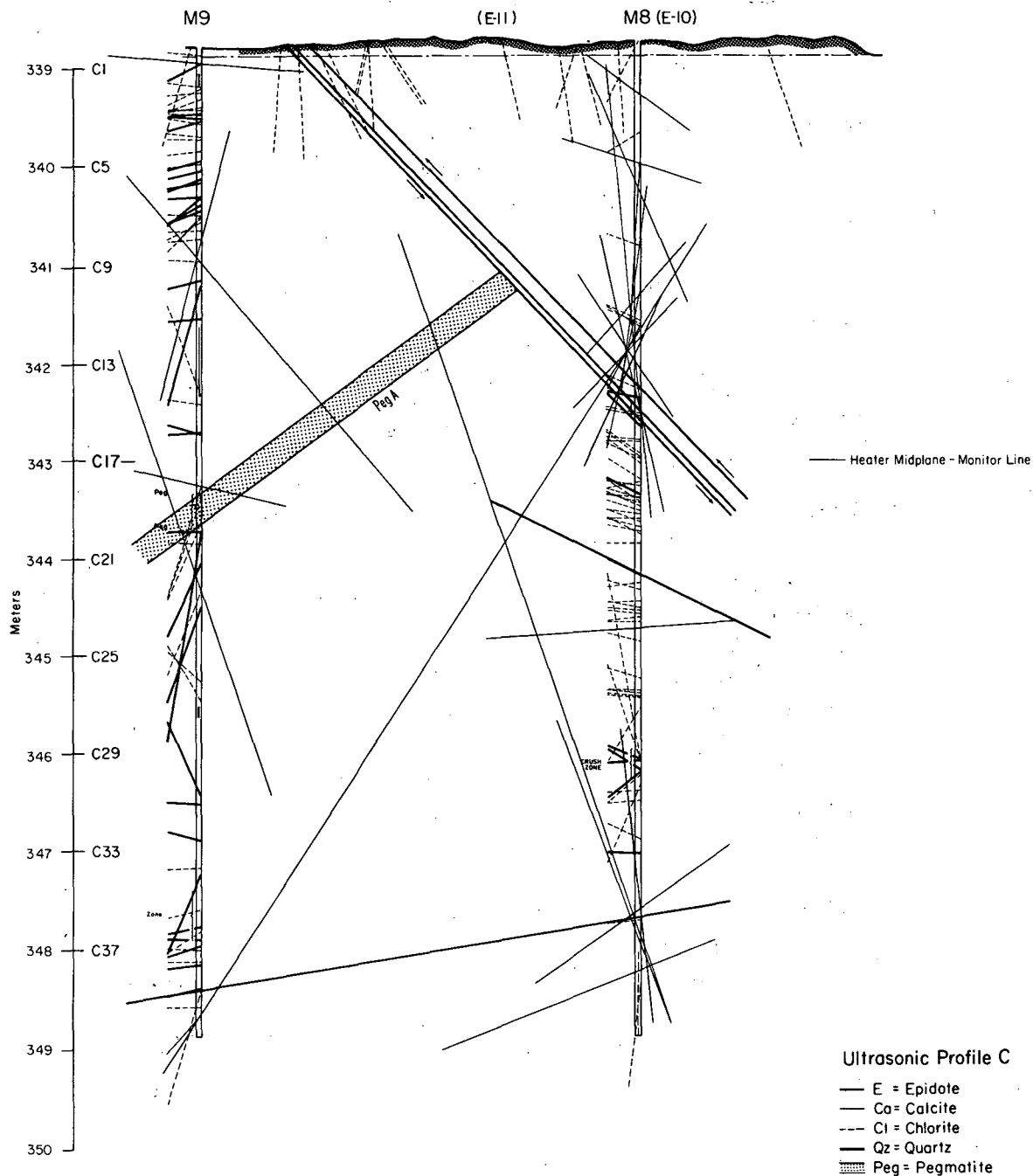
Fig. 2.7 Vertical cross-section C; M8-M9 showing the boreholes, pegmatite dikes and logged and projected fractures.
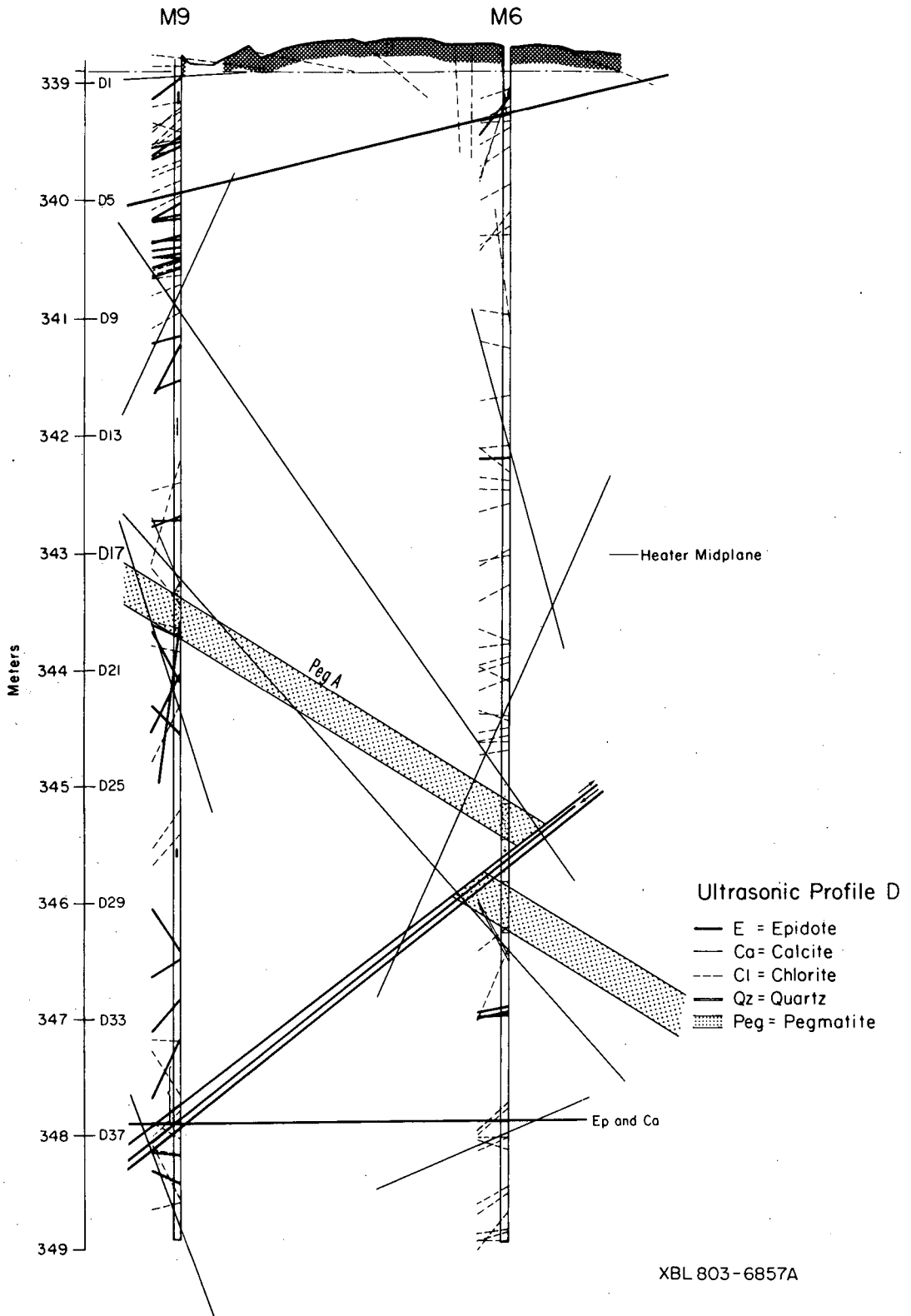
Fig. 2.8 Vertical cross-section D; M6-M9 showing the boreholes, pegma-tite dikes and logged and projected fractures.

Fig. 2.9 Vertical cross-section E; M8-M6 showing the boreholes, pegmatite dikes and logged and projected fractures.

Ultrasonic profile E

| E : Epidote |
| Ca : Calcite |
| Cl : Chlorite |
| Q₂ : Quartz |
| Peg : Pegmatite |

(45.180)= (α=dip, β = strike)
thickness in mm
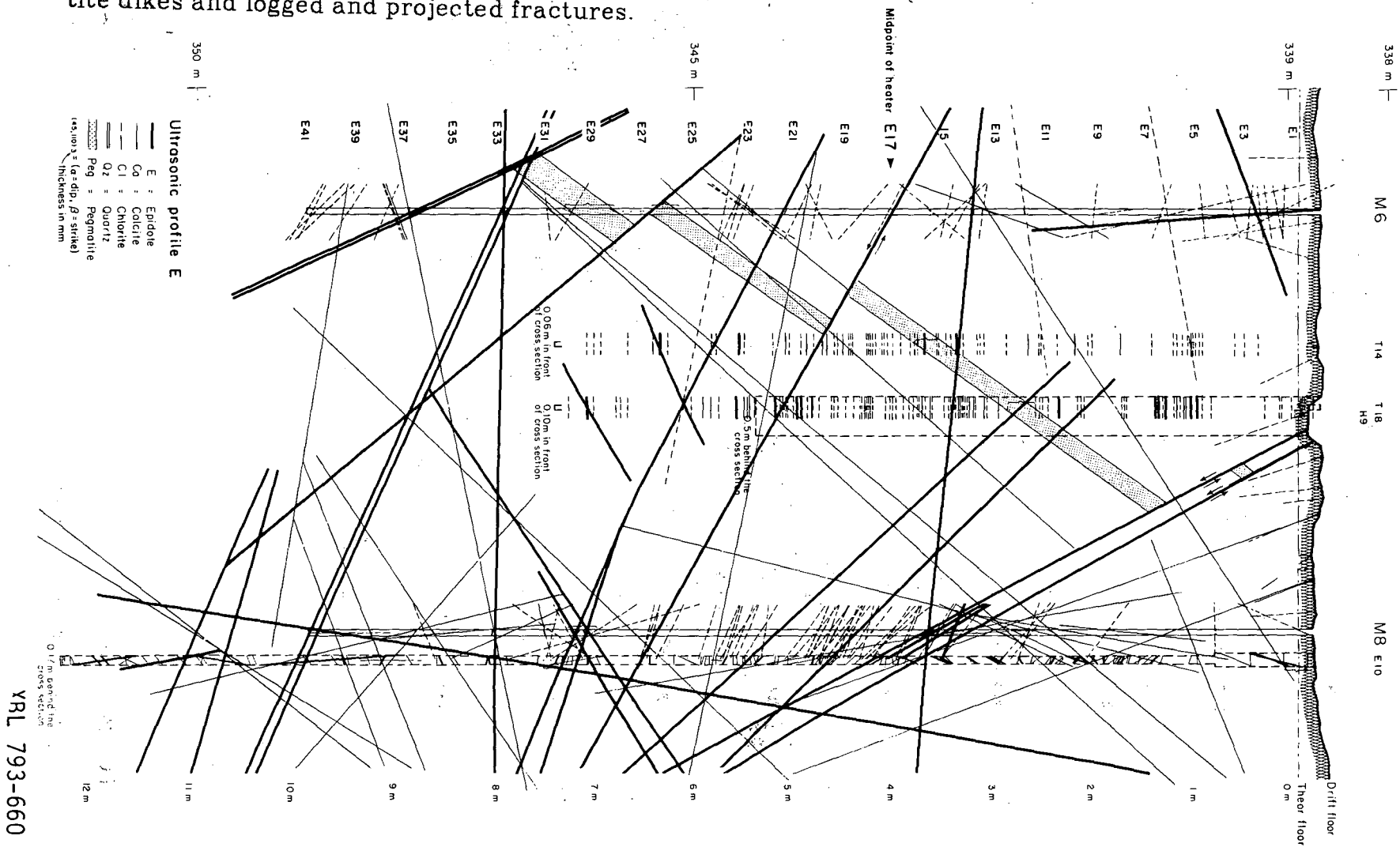
Fig. 2.10 Vertical cross-section F; M7-M9 showing the boreholes, pegmatite dikes and logged and projected fractures.

XBL 793-795
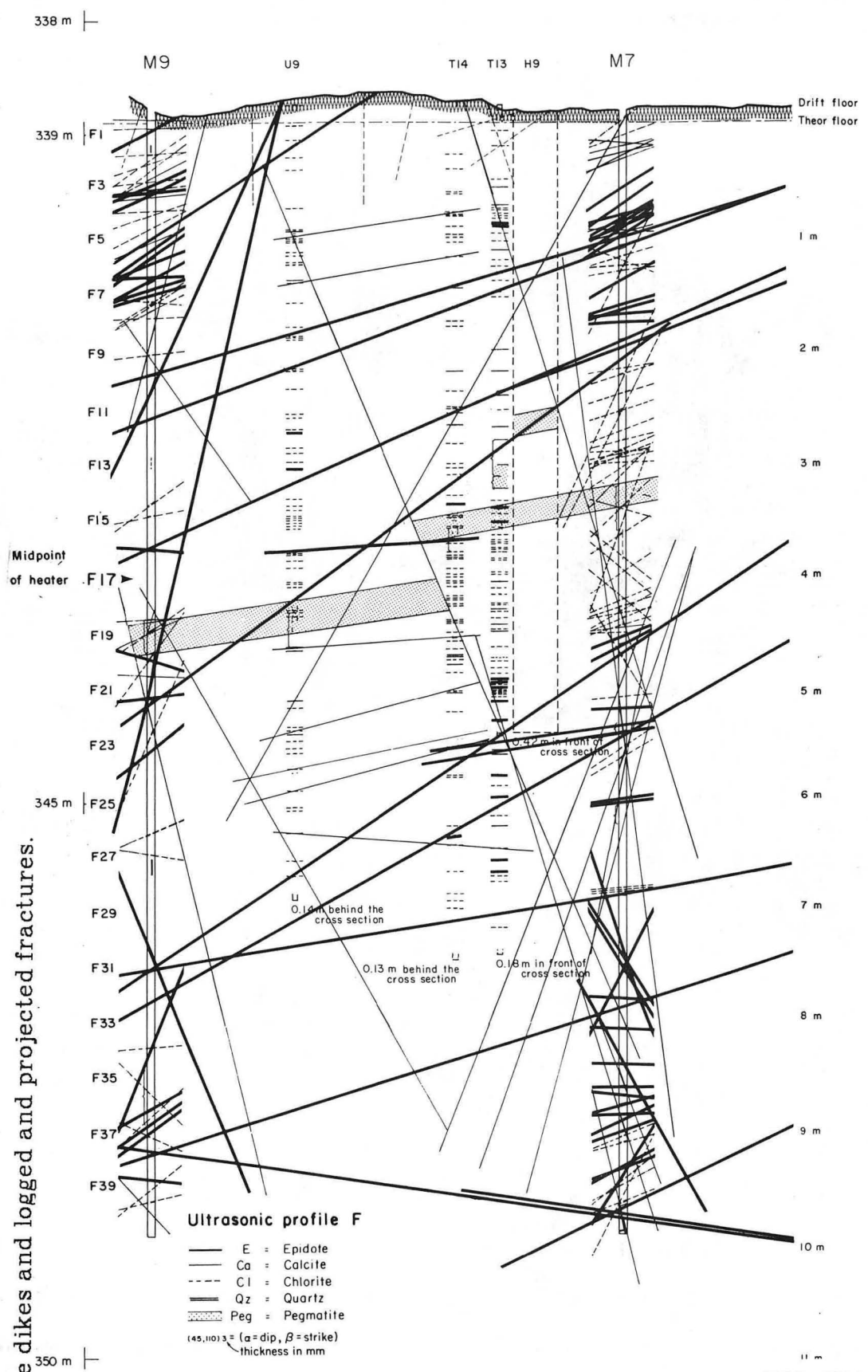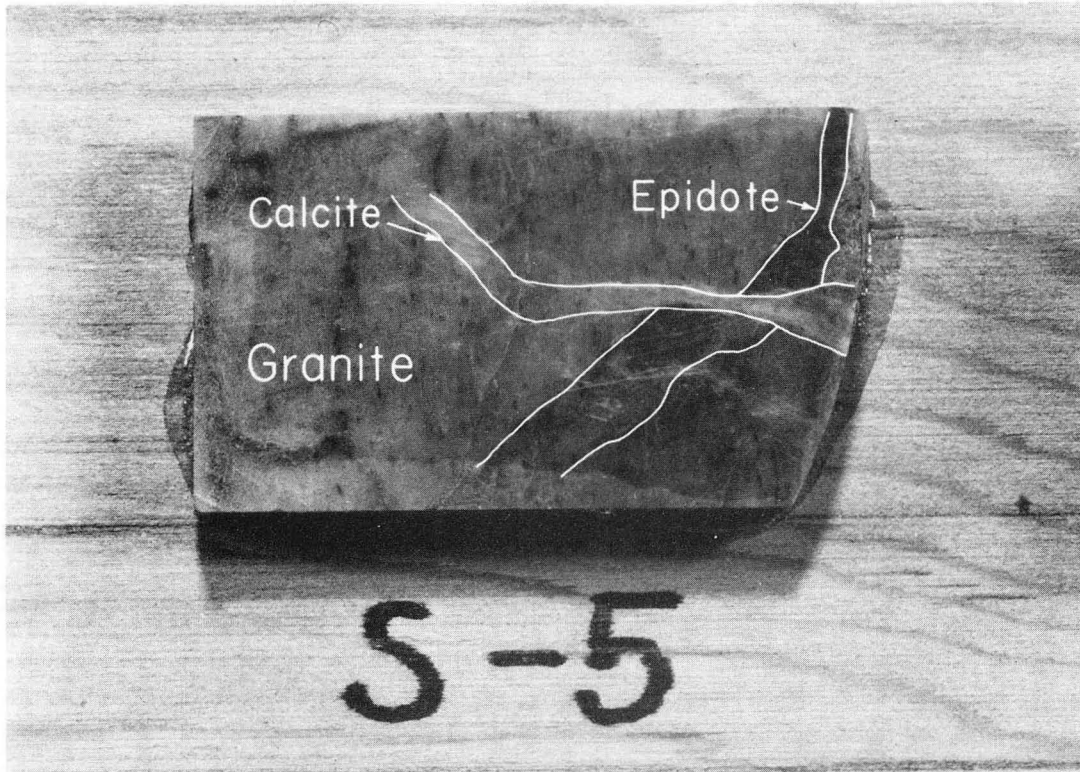
XBB 805-5923A

Fig. 2.11 Calcite fracture faulting an epidote fracture in a specimen from the fullscale drift. The faluting of the epidote filled fracture of the calcite filled give a relative age makin the calcite fracture the younger. The specimen is 20 mm long.
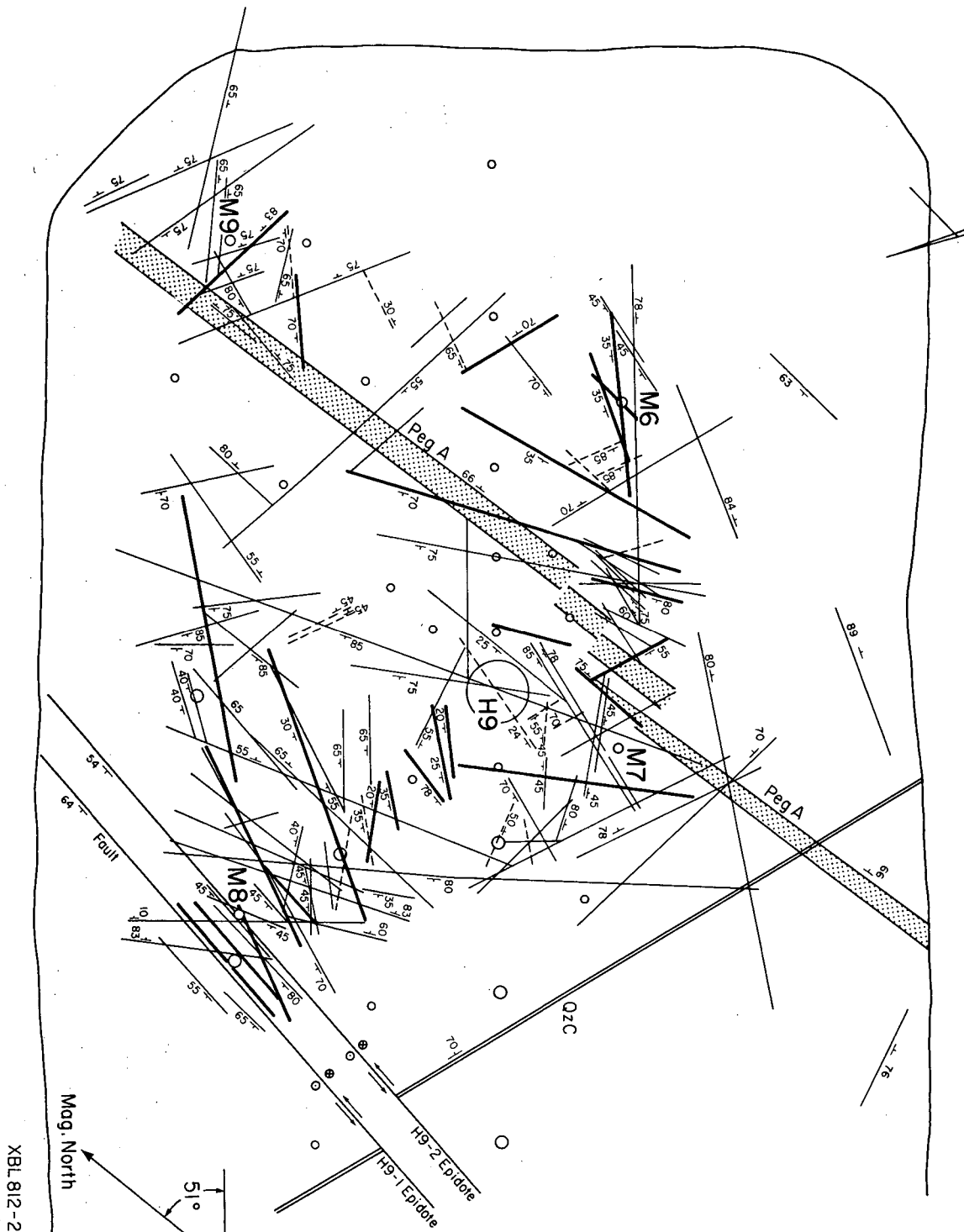
Fig. 2.12 Fracture map of the H9-heater midplane showing faults (H9-1,2), Pegmatite dikes and fractures. The map was constructed from directional fracture data logged in core and projected on the midplane.

3. EXPERIMENTAL PROCEDURES AND DATA PROCESSING

3.1 Drilling, Surveying and Dewatering

The cross-hole experiment was conducted between four empty, dry, vertical boreholes of ten m depth located in the vicinity of the vertical heater borehole H9 shown in Figure 3.1. The four boreholes were drilled with a small Diamec 250 drill rig with a 56 mm thin-wall double-barrel TT-bit which yielded 48 mm core. The drill-rod was also equipped with a reamer to improve the smoothness of the surface of the borehole wall. The quality of the ultrasonic signals received strongly depended on the size of the contact surface between the transducers and the borehole wall.

The boreholes were surveyed at the collar, in the middle, and at the bottom of the hole with an accuracy of ±0.5 mm in the X, Y and Z directions. The survey result is given in appendix 3 A. Forty positions for seismic transmission reception were located along the length of each 10 m long M-borehole. The accuracy with which the coordinates for the positions was established as ±1 mm, or 0.05 % for the shortest line, which is 2.2 m. The coordinates for these positions are given in appendix 3 B. The six cross sections are labeled A-F, with data point A1 being at the same absolute depths as B1, C1, D1, E1 and F1. The depth separation between each data point in the boreholes is 0.25 m.

Small amounts of water were found continually to seep into the four boreholes, but they were blown out regularly to keep the holes dry.

The positions of the pairs of transducers were well defined in each test so it would be easy to go back to the same position over a long

period of time. In sections A through D, not all the points were used: in most cases cross-hole data were collected at points which were 0.5 m apart. For the sections E and F, that is the cross sections M8-M6 and M7-M9, data were collected at points 0.25 m apart. It was a tedious procedure to assemble the transducers, position them in the borehole at the right depth and with the right angular direction and to jack the transducers to the borehole wall. The M8-M6 and the M7-M9 sections were picked as the main sections for three reasons: the time constraints mentioned, that they both pass close to the heater, and finally that they are mutually perpendicular, as shown in Figure 1.7.

3.2 Transducers and data acquisition system

The transducers were jacked to the borehole wall by a mechanical worm-screw jack. The transducers were constructed as two semi-cylinders with the transducers and the jack in the larger of the two parts. The two parts of the transducer were pushed apart towards the walls of the borehole with a worm-screw arrangement, operated by a long rod from the ground surface. In Figure 3.2 a drawing of the transducers is shown and in figure 3.3 a photograph is given of an assembled transducer beside a transducer body with the piezoelectric crystals on the right hand side of the photograph.

The transducer housings are constructed of aluminum. Aluminum was chosen because it has a similar acoustic impedance, defined as the product of velocity and density, to that of the granitic rock. The crystals used to generate and receive the acoustic signals were made from PZT-5 (Lead-Zirconate-Titanate) piezo-electric material.

A high-voltage pulse generator supplied electrical pulses to excite the transmitting transducers. It also generated a synchronizing pulse which coincided with the rise of the high voltage pulse. The synchronizing pulse was then used as a trigger for the transmission time measurements, on the oscilloscope and on the tape recordings. The high voltage pulse was generated by discharging a capacitor through the primary of a step-up transformer. A silicon-controlled rectifier (SCR) acted as a switch to initiate current flow. The SCR was triggered by an internal oscillator, the frequency of which controlled the pulse repetition rate. The pulse repetition rate was set low enough frequency to allow time for the ultrasonic signal to dissipate between pulses. The period of the repetition rate was 30 milliseconds. A block diagram of the equipment is shown in Figure 3.2. Separate compressional (P) and shear (S) wave transducers of nominal 220 kHz resonant frequency were used as transmitters and receivers of pulses of acoustic energy in the boreholes.

Figure 3.5 shows the field equipment. Note the transducers in the hands, both similar looking and made up of two semicylinders. The thin metal pieces protruding from the aluminum housings are the rods that operate the worm screw forcing the two semi-cylinders apart. The equipment from left to right consists of the switchbox for the P or S wave receiver; next follows the Hewlett Pacard 1743 A time-interval oscilloscope, the Hewlett-Packard 3964A AM-tape recorder, the back-up oscilloscope and finally the pulse generator.

The transmitter and receivers were placed at the appropriate depths by lowering them down in the boreholes attached to 1/2 inch-diameter pipe. The pipes were in 1.5 m sections to make them easy to handle.

3.3 Data

The total instrument delay was obtained simply by clamping the transmitter and receiver together, and recording the arrival time for the P and the S wave respectively. The instrument delay was found to be 6.2 μs for the P-wave pulses and 11.3 μs for the S-wave pulses.

A test of the transmission pattern and signal delays for different directions of transmission and receiving was made. It was found that the P-wave transmitter generated strong S-wave pulses 45 degrees from the transmission direction, but the arrival of the P-wave was not delayed in that direction.

A line between boreholes M6 and M9 at a depth of 1 m from the surface of the drift, which is 3.2 m above the heater midplane, was chosen as a reference line. This line is shown in Figure 3.1. Although small perturbations of the travel times and the wave characteristics were expected when the H9 heater was turned on, the disturbance was expected to be small. Indeed, the velocity change in the reference line turned out to be very small. The velocity changed about 20 m/s (0.3 %) over the 750 day long experiment. The amplitude spectra changed considerably more. In the reference line the Q-values for the P-waves changed from 14 to 25 (80 %). This was of the same order as the change in other lines which are in the heater midplane. The reference line proved to be very helpful for detecting bad transducers or other problems. The equipment used was a prototype with some flaws. The aluminum transducer housings were not rigid enough; they flexed slightly during each jacking process. This meant that the piezoelectric crystals, which were cemented to the aluminum loosened after a number of measurements. To make sure that the data were collected with good

transducers, the instrument system was checked using the reference line before and after work each day. P and S arrival times and waveforms were recorded. If the transducers were found faulty they were repaired and the experiment was repeated.

The possible effect of heat on the characteristics of the transducers was investigated by placing cool transducers at the midplane in bore holes M7 and M6 for 6 hours, and monitoring the travel times. It was concluded that in the temperature range experienced in the Stripa experiment, from $10 - 110°$ C, temperature changes did not alter the transducer performance significantly.

A reverse profile was also run, and it was found that reversing the transmission direction did not alter the results.

The P- and S- wave received signals were displayed on an oscilloscope screen and recorded in analog form on an instrumentation AM tape recorder for later analysis in the laboratory. The arrival time was obtained by delaying the signal to the zero time line and recording the digital display of the delayed time. Typical oscilloscope traces for boreholes 2.8 m apart are illustrated in Figure 3.6. It will be observed that both P- and S-wave arrivals are sharp and may be picked precisely. The resolution of the arrival time is estimated to be ± 0.1 μs, based on picking the arrival time for the same wave several times. This corresponds to a precision of 1 part in 7000 or 0.014 %. Together with the uncertainty in the coordinates for each data point one obtains a total accuracy of better than 0.1 % of the travel times calculated. In the case of M8-M6 were the P-wave velocity was approximately 6000 m/s, resulting in a velocity resolution of ± 3 m/s.

The field data are divided into several different modes according to sampling technique and density. The monitoring mode consisted of sampling the arrival-times for four lines in the heater midplane. Because there were only a few lines this could be done often and one obtained good control over transient events. The survey mode consisted of sampling the six cross-sections a few times to obtain data on velocity versus geology and thermal stresses outside the midplane. The third mode is the tomography mode. This involved so much data collection that it could only be performed twice. This part of the cross hole experiment will not be further discussed in this report because there were insufficient funds to analyze data. The fourth mode is the down-hole survey. This was performed only a few times because limited availability of personnel to make the measurements.

The lines utilized for the monitoring mode are shown in Figure 3.1. The first transmitter was placed in borehole M8 and directed towards borehole M6. The second transmitter was placed in borehole M7 and directed towards borehole M9. While the two lines M8-M6 and M7-M9 are considered to be the main monitoring lines, data were also collected by utilizing the line M7-M6 and M8-M9. However, the transducers were not turned to face each other for the latter two lines, so in effect both the transmitter and the receiver were directed approximately 45 degrees from the line connecting the boreholes, as shown in Figure 3.1. This did not affect the transmission time, but the waveforms were considerably altered. There are approximately 100 recordings of both P- and S- waves from each of the four monitoring lines. Because of time constraints before the turn-on of the H9 heater it was not possible to collect as much data before heating of the rock started as one would have desired.

When the heater experiment was turned on, there were some operational problems with the ultrasonic instruments. Because of these problems very little data was collected during the initial phases of the heater experiment. During the "steady state" part of the heater experiment, seismic data were collected on a biweekly schedule. Finally, when the H9 heater was turned off, data were collected twice a day in the heater mid-plane for a period of two weeks.

The second method by which data were acquired was in the survey mode. The principle of this mode is shown in Figure 3.5. Only the transmission lines of the surveys of the profiles M8-M6 and M7-M9 are shown. Surveys were made over all six profiles. Emphasis was placed on the two main profiles, over which survey data were collected most frequently both in space and in time. Ten surveys were made over these two profiles during the course of the experiment. For the remaining four profiles, five surveys with less dense sampling vertically were performed. It will be clear from the plotted curves how frequently in the vertical direction the data were collected.

From the cross-hole surveys one can, first, correlate the low velocity zones with geological features and second, see the different response of the rock as a function of vertical and horizontal distance from the heater during the course of the experiment.

The down-hole experiment was performed with an instrument lend by the University of Saskatchewan. King (1972) has described the equipment shown in Figures 3.8 and Figure 3.9. Two surveys were performed with the down-hole instrument. The first was performed in May, 1978, before the heaters had been turned on. This was also before de-watering of the rock mass had been started. The second survey was performed in

July, 1980, immediately after de-watering the rock around H9 had stopped. The main reason for the sparsity of down-hole data was again the time constraint.

The first step in the processing was to transfer the data, over 20000 entries and 4000 waveforms to a minicomputer memory. This made it possible to handle the data in a rational fashion. For harmonic analysis of the waveforms, it was simply necessary. In Figure 3.4 block diagram of the laboratory data analysis system is shown. The AM tape recorder is the same tape recorder used in field, thus providing the connecting link between the field work and the analysis of the data. All the waveforms and amplitude spectra were generated on the minicomputer and transferred to paper via the hard copy unit.

To obtain the velocity data, the length of each of the 240 cross-hole lines were computed from the X,Y and Z coordinates by,

$$l_i = \sqrt{(x_1 - x_2)^2 + (y_1 - y_2)^2 + (z_1 - z_2)^2}$$

The travel-times minus the instrument delay were then used with the path distances to obtain the apparent mean P- and S-wave velocities between the two boreholes. At all times it has been assumed that the waves travel along straight paths between the boreholes. This is only true if the velocity distribution is uniform between the two boreholes; this is of course not necessarily the case. The velocity anisotropy is not considered sufficient to cause any noticeable difference in travel path. Assuming the rock mass between the transmitter and the receiver to be elastic, homogeneous and isotropic, the Poisson's ratio, Young's Modulus, bulk modulus and the shear modulus have been calculated using the P and the S-wave velocities and the mean rock density

reported by Swan (1978). In the laboratory experiment described in this report it is shown that there is a good correlation between dynamic and static moduli calculated for dry specimens of the Stripa quartz monzonite.

The analog signals recorded on a tape recorder in the field were played back in the laboratory and digitized. The procedures to calculate the Q-values is a rather involved and requires several steps. The initial step is of course to record the signals in a fashion such that the Fourier amplitude spectra can be calculated. The ultrasonic signals were recorded on the instrumentation tape recorder at a speed of 15 ips in order for the tape recorder to have the necessary bandwidth. Each signal was recorded for at least 15 seconds to make it possible to digitize a signal several time without replay the tape. The tapes were then replayed in the laboratory and digitized utilizing a Tektronix Digital Processing Oscilloscope (DPO). The DPO is connected to a DEC 11-34 computer and the software and data is stored on floppy discs via two floppy disc drives. The system is marketed with a software package for waveform processing. Using this processing package the signals were replayed and digitized. The signals were averaged at least 4 times to improve the signal/noise ratio. In Figure 3.10 is shown the difference between a signal only digitized once and the same repetitive signal digitized and averaged 4 times. This was the maximum number of times one could digitize a 15-second record. The noise appears to be random, and consequently the signal/noise ratio should improve as $\sqrt{N}$. By taking the ratio of the amplitude at 50 kHz and 150 kHz one gets a ratio of 6 for the first waveform. For the waveform which was averaged one obtains an approximate ratio of 30. This is much better than $\sqrt{N}$ but by

integrating the signal/noise ratio from 125 kHz to 1.25 MHz one would probably get a value close to $\sqrt{N}$. During digitization the delay function of the Digital Processing Oscilloscope (DPO) was used to be able to digitize only the arrived wavelet. The digitization window is 200 microseconds wide and the signals were digitized with 512 points. The DPO digitizes a waveform by sampling one of the 512 "buckets" in a pseudo-random fashion every 6.5 μs. That means that the minimum time to sample one waveform is 3.3×10^{-3} seconds. In reality it takes 1 - 3 seconds or 10^3 times as long. The bulk of this is composed of the transfer time from the DPO to computer.

Following digitization, the signal was windowed with a 70 μs wide half-cosine window (Figure 3.11). The signal was then normalized so the peak amplitude is unity. The resulting wavelet was then Fourier transformed. The reason for normalization is that there is no control over absolute amplitude of the signal. The amplification of the incoming signal to the tape recorder was adjusted for each record to minimize distortion. The amplitude of the signal proved to be a function of the age of the bond between the crystal and the aluminum housing. The amplitude also varied as a function of the smoothness of the borehole wall. So the field system used in this case did not lend itself to absolute amplitude control of the signals. The lack of absolute amplitude does not alter the slope of the natural logarithm of the spectral ratio versus the frequency, which is used in the calculation of the Q-values. This standard spectral ratio technique has been described by McDonal *et al.* (1958), Tullos and Reid (1969) and Toksoz *et al.* (1979).

Monitoring Configuration
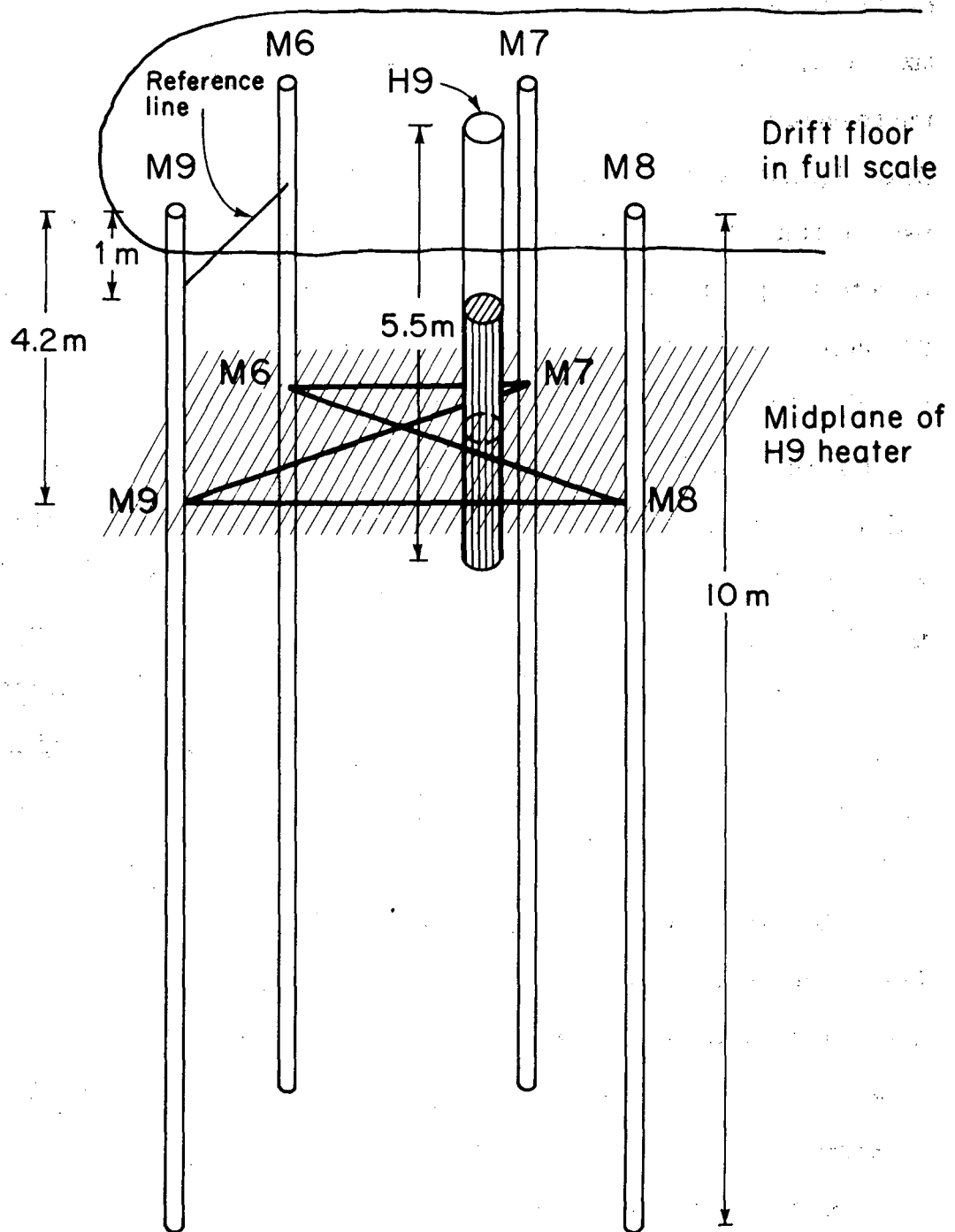
XBL 7910-13054A

Fig. 3.1 Between-hole monitoring site showing heater borehole, monitor boreholes, the reference line and the monitor lines.

BOREHOLE

56 mm

¾ in. PIPE

STEEL GUIDE

P–WAVE
PZT-CRYSTAL

182 mm

WORM SCREW

S–WAVE
PZT-CRYSTAL
(Horizontally
polarized)

40 mm

SIDE VIEW

BOREHOLE

CRANK

CABLE FOR
P–WAVE CRYSTAL

CABLE FOR
S–WAVE CRYSTAL

42 mm

40 mm

FRONT VIEW (OPEN)

0 10 20 30 40 50 mm

XBL 8212 - 4394
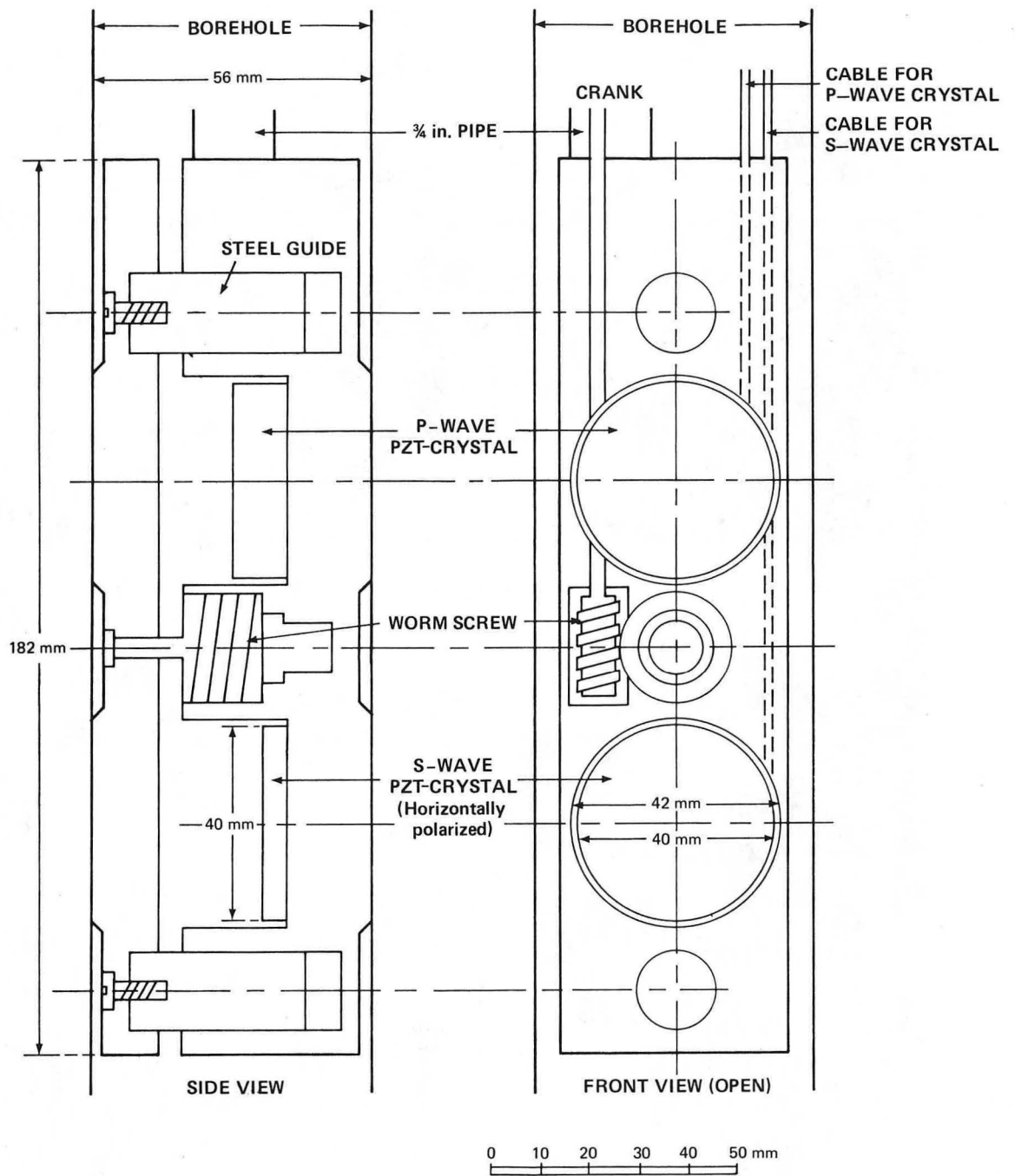
Fig. 3.2 Detailed diagram of a cross hole transducer. The only difference between the transmitter and the receiver are the cables and that the receiver is equipped with a line matching transformer.
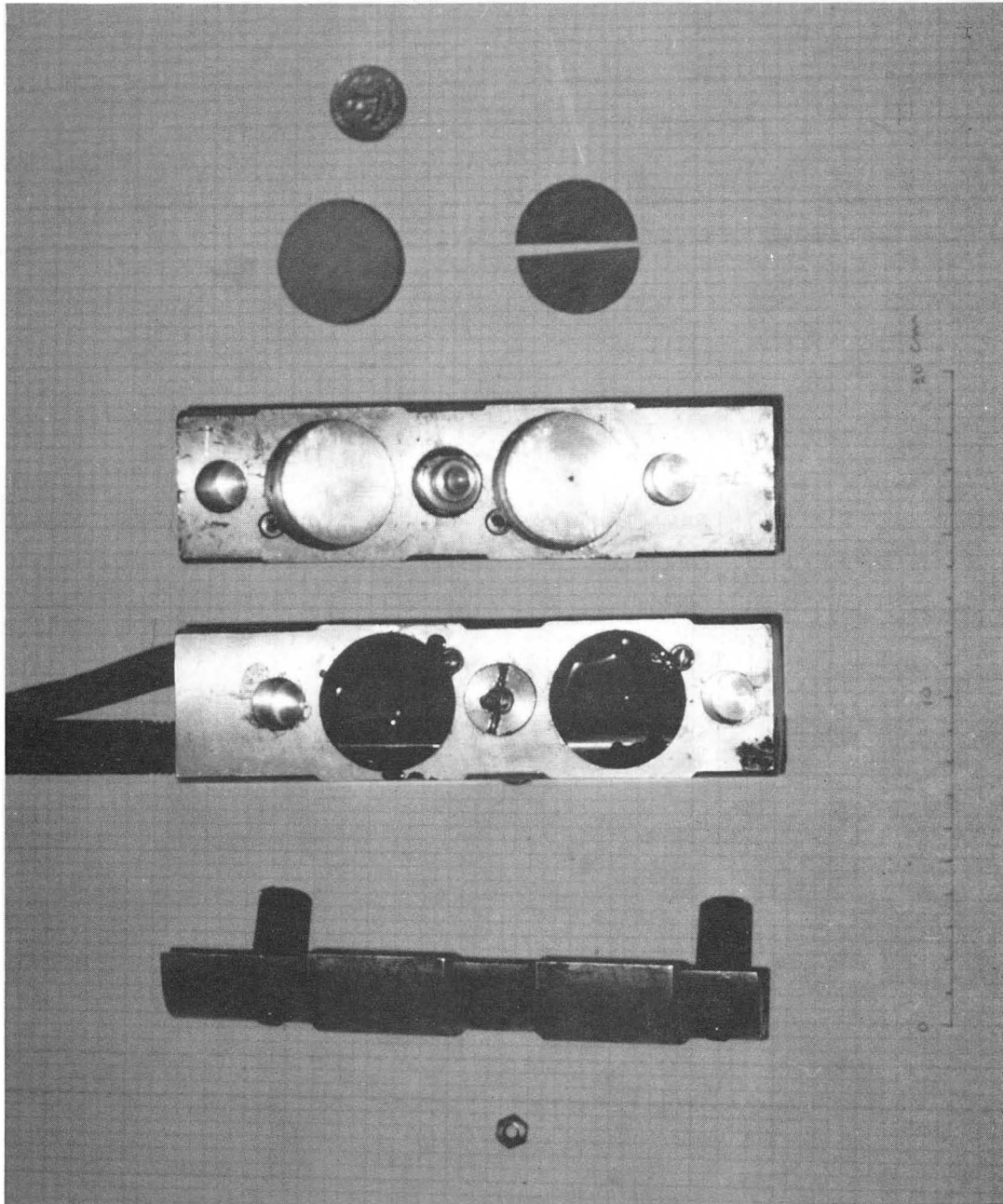
Fig. 3.3 Photo of transducers. The left transducer is assembled, except for the top, which appears to the left of the aluminum housing. In the middle a aluminum housing is shown. To the right the PZT-crystals are shown with the P-wave crystal on top and below the two halves of the S-wave crystal.

XBB 820-10695
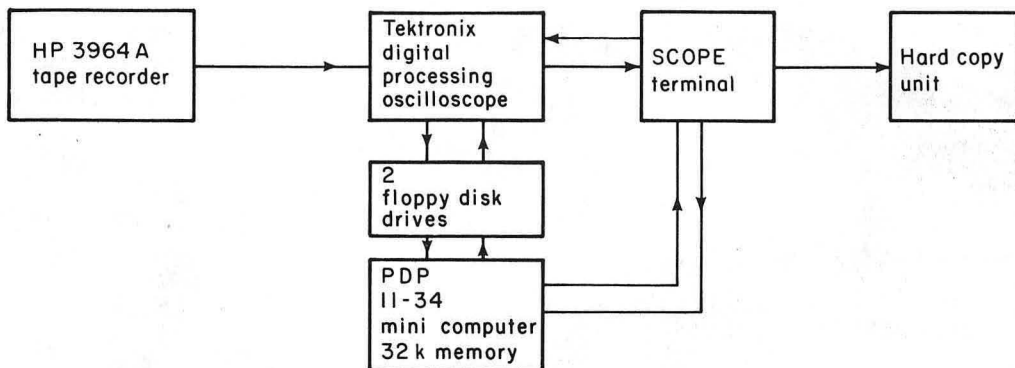
Block diagram of the signal-analysis system
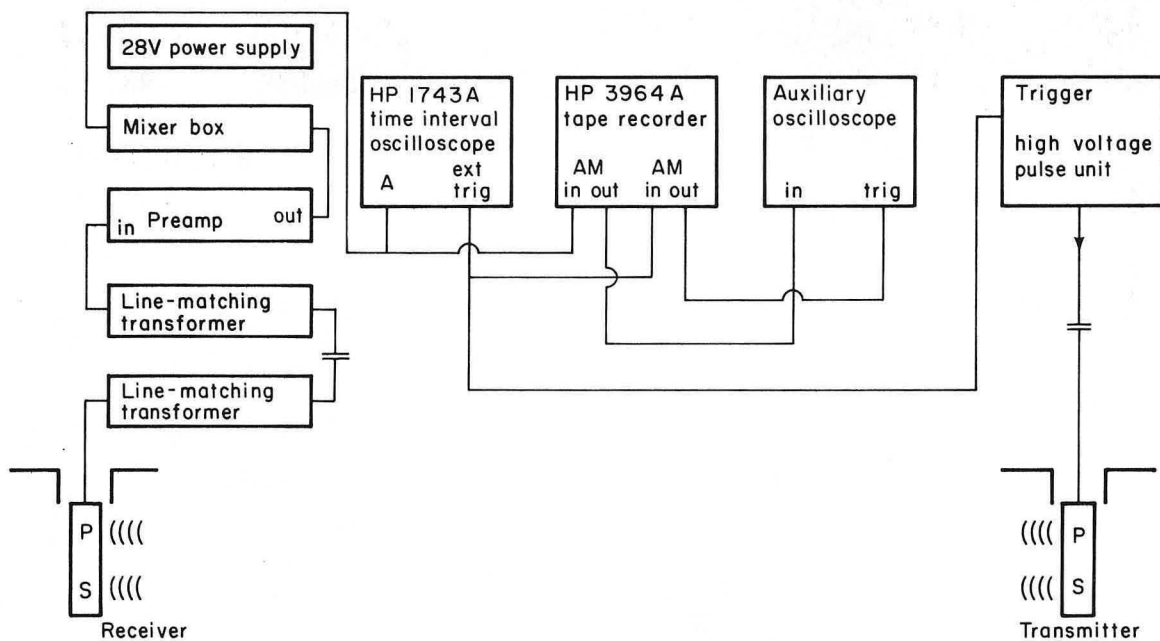
Block diagram of cross-hole seismic equipment

XBL 795-855

Fig. 3.4 Block diagram of cross-hole ultrasonic velocity and attenuation equipment

CBB 790-14258

Fig. 3.5 Field equipment and operator
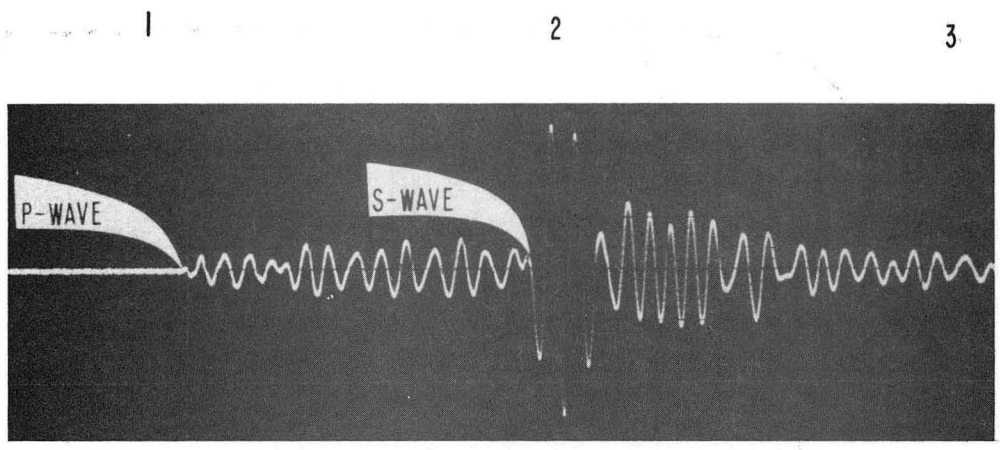
Arrival time P: 0.4755 m sec 0.2V/div 50μsec/div M9-M6
S: 0.8125 m sec
Arrival time: 0.4755 m sec 1V/div   50μsec/div M9-M6
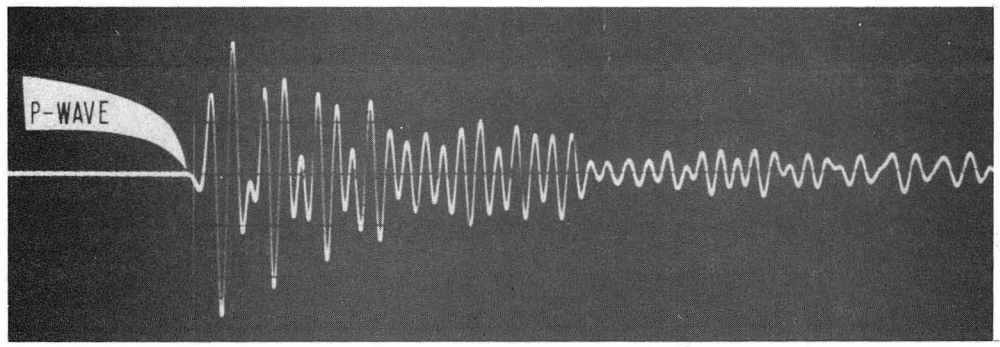
XBB 790-14040A

Fig. 3.6 Oscilloscope traces of received ultrasonic signals in the reference line (M9-M6)

Surveying Configuration
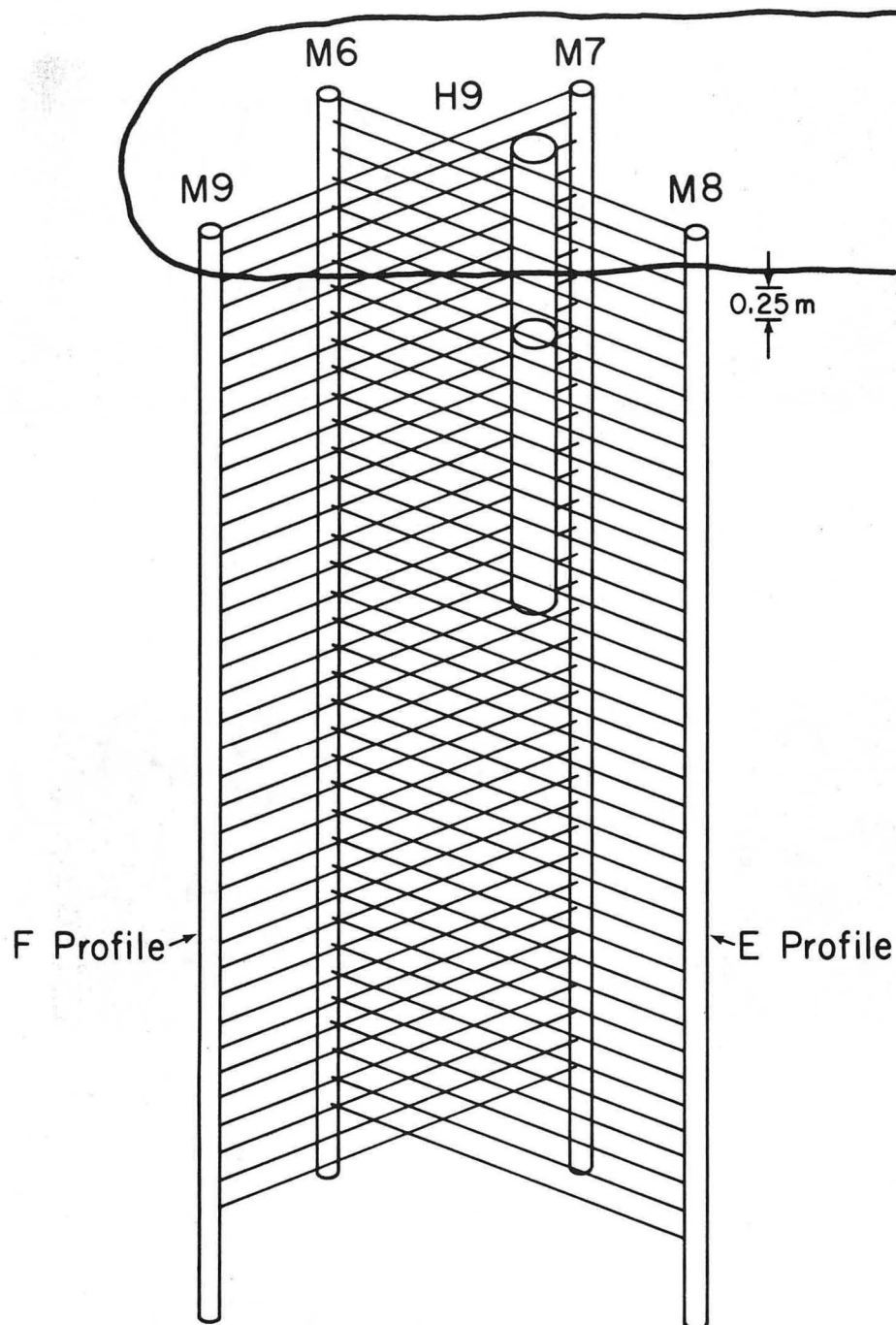
Fig. 3.7 Isometric drawing of experiment site with the surveying lines for section E and F shown, distance between each line is 0.25 m

Fig. 3.8 Ultrasonic down-hole equipment

HYDRAULIC SYSTEM

12V. BATTERY

OSCILLOSCOPE

PULSING UNIT

CABLE

CAMERA

LOGGING SONDE

TRANSMITTING SHOE

RECEIVING SHOE

EXTENSION PIECE

PIVOT

TRANSMITTER
SECTION

PULSE
TRANSFORMER

PIEZOELECTRIC
TRANSDUCER
STACK

TRANSMITTING
SHOE

BAFFLES

DOUBLE ACTING
PISTON

RECEIVING
SHOE

ACCELEROMETER

RECEIVER
SECTION

PREAMPLIFIER

PIVOT

EXTENSION PIECE
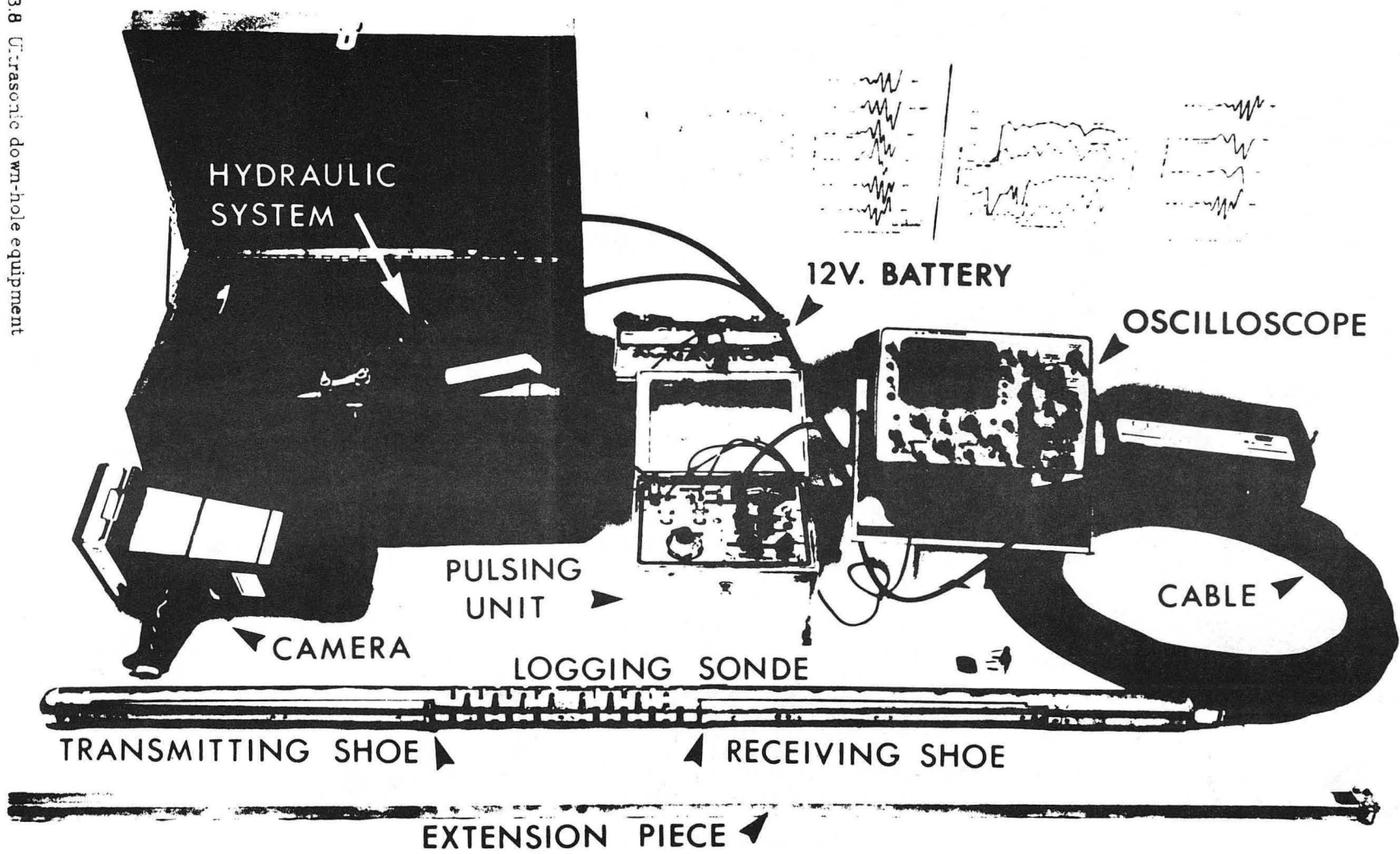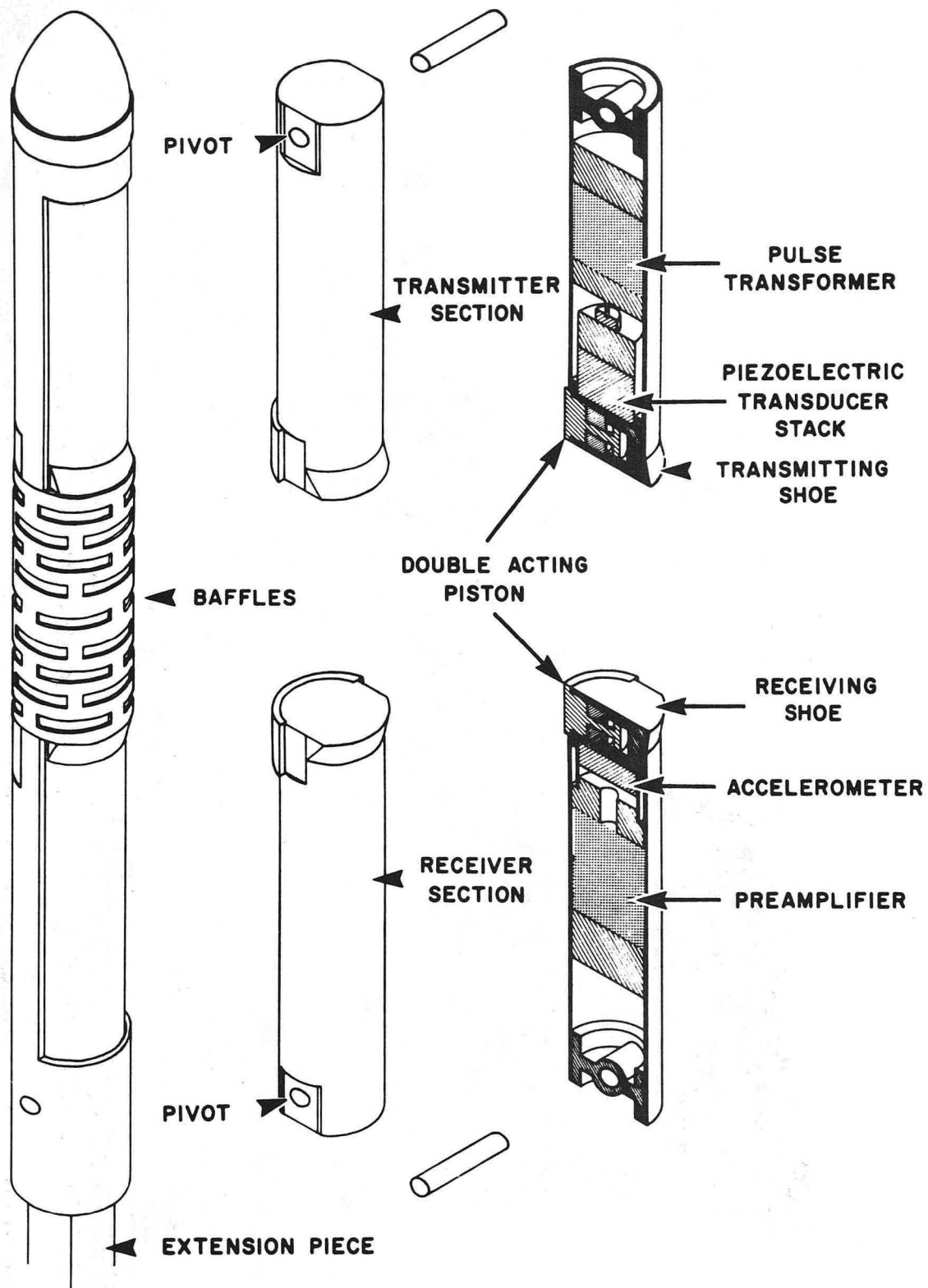
Fig. 3.9 Detail of ultrasonic down-hole equipment

S86PO.15 - P waves   No stack

S86PO.15   4 Fold stack   P-waves

Truncated P-waves   No stack

0   [µs]   200

Truncated P-waves   4. Fold STACK

0   [µs]   200

Amplitude spectra   No stack

Amplitude spectra   4 Fold STack

0   f [MHz]   1.3

0   f [MHz]   1.3
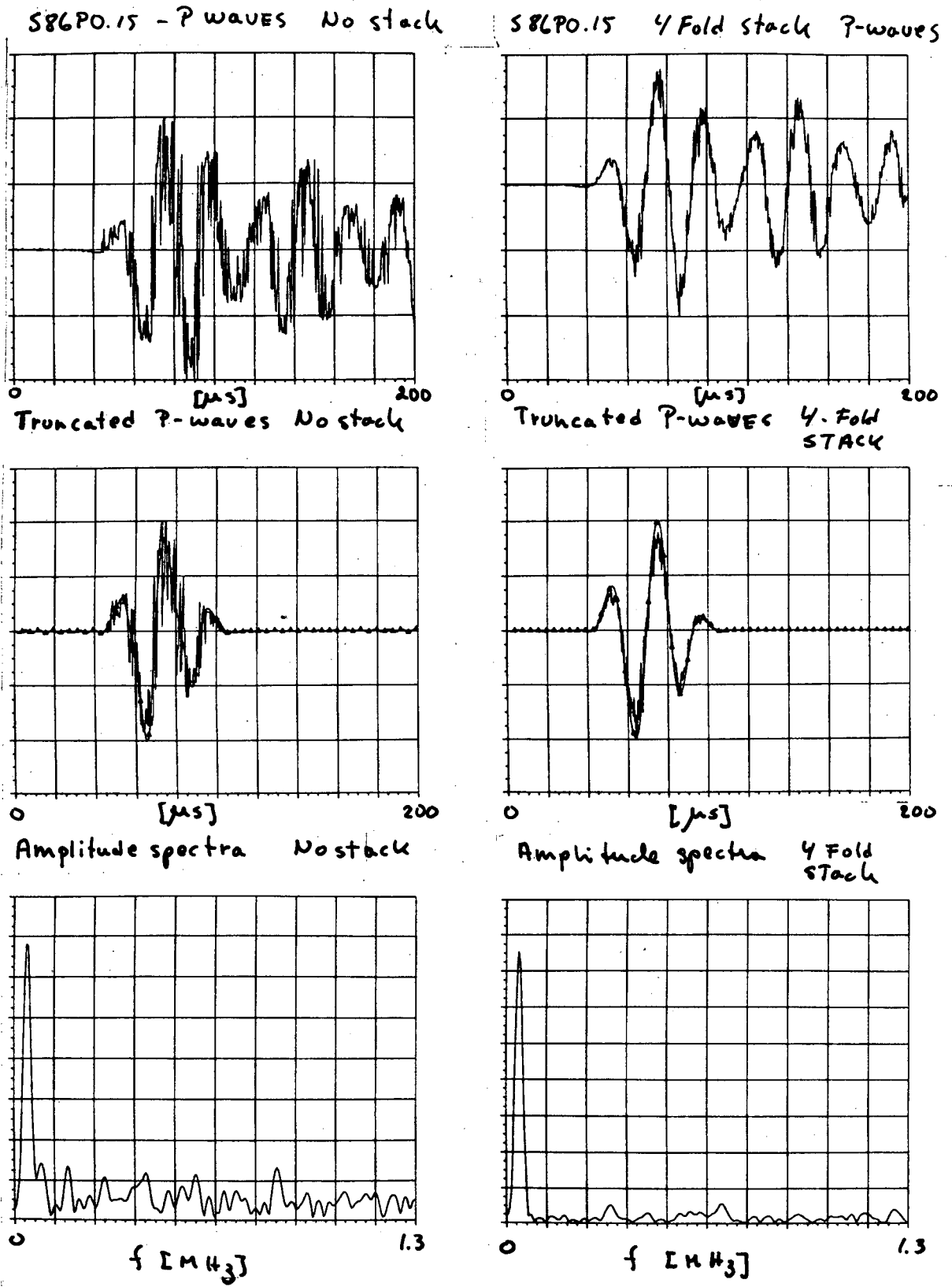
Fig. 3.10 Cross hole signals digitized on DPO; first column : no averaging, second column : four fold average
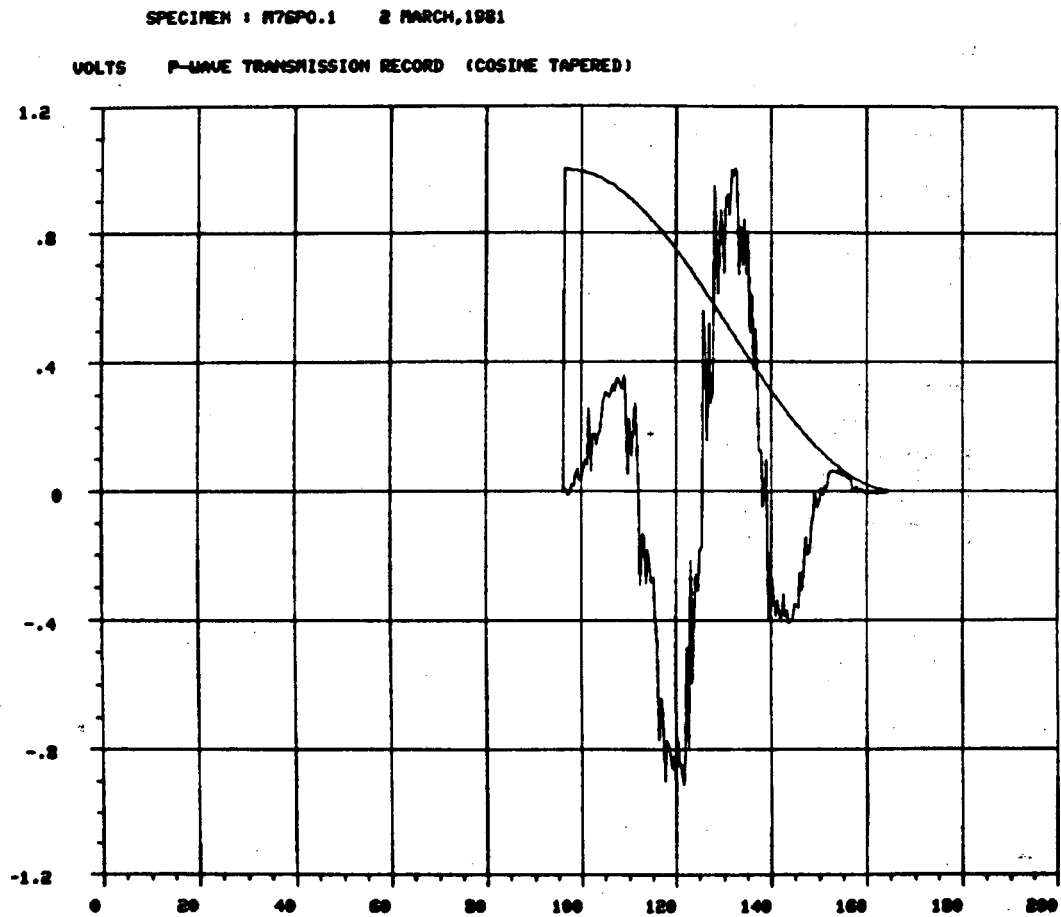
Fig. 3.10 70 μS truncation window before the Fourier transform

4 THERMAL AND THERMOMECHANICAL HISTORY

The Stripa heater experiment was closely monitored by thermocouples, stress gauges and extensometers. The water inflow to the instrument holes was recorded when the water was removed on a daily basis during the course of the experiment. The 3.6 kW H9 heater was turned on 28 August, 1978, at 1400 hours for a period of 398 days, until 26 September, 1979, at 1400 hours. Approximately 50 million measurements were made with all these instruments, Chan et al. (1980). The result is a detailed knowledge in space and time of the variation of the temperature, stress and water inflow. In the present chapter, a presentation of these measured parameters will be made. The data is compiled from the Stripa data base and from reports published in the SAC-report series published by Lawrence Berkeley Laboratory.

De-watering of the rock mass which has been described in detail by Schrauf *et al.* (1979) and Nelson *et al.* (1981) commenced 41 days prior to the the turn-on of heater H9. The dewatering of the rock mass was performed on a daily basis for a total of 586 days: 545 days after the turn-on of the heater, and 147 days more after the turn-off of the heater.

There were thus two active processes occurring in the rock mass: heating and dewatering, which changed the properties of the rock surrounding the heater hole and the dewatering holes. The change of the rock mass property due to heating was fairly well understood, and theoretical calculations of the temperatures were very close to the those actually measured. The stresses and displacements calculated prior to the experiment were less than the observed stresses and the

displacements, but their general behavior was in accordance with the theoretical model. A likely reason for the measured displacements being smaller than estimated is that the bulk of the thermal expansion was probably absorbed by the abundant fracturing of the Stripa quartz monzonite. There were however no predictions of the effect of the dewatering, and it will be shown in Chapter 6 that the effect of withdrawing the pore fluid as was done in the Stripa experiment has a profound long-term effect on the properties, both around the heater and deeper in the rock mass.

4.1 Temperatures

The theoretical temperature fields have been described by Chan *et al.* (1978). The measured temperatures followed the theoretical predictions closely in most cases. In Figure 4.1 the measured temperatures in the heater midplane at four different radial distances from the heater are shown. The heater had a radius of 0.2 m which should be deducted to obtain the distance from the heater wall to the thermocouple. The four thermocouples are 0.20, 0.69, 1.30 and 2.79 m from the wall of the heater, respectively.

The travel times recorded in the heater midplane during the course of the experiment depend on the average property of the material between the transmitter and the receiver. The temperature distribution has a steep spatial gradient. There are however, 15 thermocouples in the heater midplane within a radius of five m from the heater. Seven of the thermocouples are within one m from the H9 heater where the thermal gradient is steepest. The thermal data are used in Chapters 5 and 6 to establish the temperature - compressional velocity relationship. The

boreholes, and their position is given in table 4.1.

Temperature gauges in the heater midplane							
bore-hole	sensor number	sensor label	cylindrical coordinates			depth [m]	hole length [m]
			rho	ϑ	z		
T13	86	T13C	.40	357.6	-.01	4.27	7.64
T14	91	T14C	.89	000.0	.00	4.30	7.70
T15	96	T15C	.68	44.1	-.01	4.25	7.64
T16	101	T16C	.50	186.0	.00	4.15	7.57
T17	106	T17C	.81	226.2	.00	4.23	7.64
T18	111	T18C	.62	314.7	.00	4.32	7.72
E6	122	TE6F	1.00	180.9	.18	4.03	12.95
E7	125	TE7G	2.00	180.4	.01	4.33	12.69
E8	26	TE8B	2.99	180.3	.02	4.30	12.67
E9	30	TE9B	1.50	225.2	.14	4.10	12.58
E10	34	TE10B	2.51	225.0	.01	4.25	12.63
E19	48	TE19A	1.23	89.5	.05	8.69	8.90
E19	47	TE19B	2.48	89.8	-.01	7.44	8.90
E19	46	TE19C	3.47	89.9	-.06	6.44	8.90
E19	45	TE19D	4.97	89.9	-.14	4.94	8.90

Table 4.1

For each of the days on which the transit times for the seismic waves were recorded, the radial distribution of the temperature from the H9 heater was projected onto the 4 lines which constitute the heater midplane monitor lines. Using the recorded temperature from the 15 thermocouples, a standard cubic spline routine was used to interpolate the temperatures for points at a radial distance between thermocouples. One hundred equally spaced points between the boreholes in the four lines, M7-M6, M8-M9, M8-M6 and M7-M9 were calculated and the radial distance for each of the points was used to find the corresponding temperature from the cubic spline routine. Having obtained the temperature distribution for this particular day a simple average was formed:

$$T_d = \frac{1}{100} \sum_{n=1}^{100} T_{r,d} \qquad\qquad [4.1]$$

This was performed 103 times corresponding to the days when seismic monitoring data were collected. In Figure 4.2 the average temperature in the four lines is shown. Note especially the rapid increase of the mean temperature when the heater was turned on, and the equally rapid decrease of the mean temperature when the heater was turned off.

There are approximately 75 thermocouples in the rock mass around the H9 heater hole within a radius of 4.0 m. These data were used to plot the temperature distribution in all the six cross sections A-F. In Figures 4.3 - 4.8 these temperature distributions for the the last day of operation of the 3.6 Kw heater are shown. Also shown on top of each figure is the particular cross-section's position relative to the heater hole. The sharp temperature gradient is apparent, especially in Figures 4.7 and 4.8. The temperature distributions over these cross-sections are important in interpreting the surveying data given in chapter 5.

The direction of the cross-sections with the highest average velocities, M8-M7 and M8-M6, do correspond with the general direction of the maximum principal stress determined from the over-coring and hydro-fracture experiments, as reported by Carlsson (1978) and Doe (1980).

4.2 Thermal stresses

Using the thermally-dependent properties of the Stripa quartz monzonite, shown in Figure 4.9, Chan *et al.* (1981) calculated the thermal stresses around heater H9. The radial, tangential and vertical stresses have been calculated for heater day 398 in Figure 4.10 for a finite-length line-source utilizing a finite element technique with thermally-dependent thermal expansion, Young's modulus, Poisson's ratio and thermal conductivity. The stresses along the lines M8-M6 and M7-M9 in the heater midplane have been calculated using a transformation of axis with different angle and different distance from the source for each point calculated, (Jaeger and Cook, 1976). The distances and the angle between the radial projection and the lines are shown in Figure 4.11 and 4.12. The thermal stresses in cylindrical coordinates for the H9 heater along the lines M8-M6 and M7-M9 are shown in Figure 4.13 and 4.14.

To change the axes so the stresses are expressed in directional and transversal stresses with respect to the transmission lines, the following formulas are used (Jaeger and Cook, 1979), using σ_ϑ and σ_r as σ_x and σ_y to conform with a two dimensional rectangular system. In Figure 4.15 the geometry changing the axes is shown.

$$\sigma_{x'} = \sigma_x \cos^2\vartheta + 2\tau_{xy}\sin\vartheta\cos\vartheta + \sigma_y \sin^2\vartheta \qquad [4.2]$$

Thermal stresses from thermally dependent coefficients							
as function of distance from center of H9							
Distance [m]	σ_r [MPa]	σ_ϑ [MPa]	σ_z [MPa]	Distance [m]	σ_r [MPa]	σ_ϑ [MPa]	σ_z [MPa]
0.20	0	-	-	2.10	14.2	5.5	5.5
0.30	23.5	-	-	2.20	13.0	5.0	5.0
0.40	35.0	49.0	54.0	2.30	12.5	4.7	4.8
0.50	37.0	39.0	43.0	2.40	12.0	4.4	4.5
0.60	35.5	30.0	35.0	2.50	11.2	4.1	4.0
0.70	33.2	23.5	29.5	2.60	10.9	3.9	3.9
0.80	31.0	20.5	25.0	2.70	10.2	3.6	3.6
0.90	29.2	17.5	21.5	2.80	9.6	3.4	3.4
1.00	27.2	15.3	18.0	2.90	9.4	3.2	3.2
1.10	25.5	13.5	16.5	3.00	9.0	3.0	3.0
1.20	24.2	12.5	14.5	3.10	8.4	2.9	2.9
1.30	22.0	10.5	12.3	3.20	8.3	2.8	2.8
1.40	20.7	9.5	11.0	3.30	7.9	2.7	2.7
1.50	19.5	8.5	9.5	3.40	7.5	2.6	2.6
1.60	18.5	8.0	9.0	3.50	7.20	2.5	2.5
1.70	17.5	7.5	8.0				
1.80	16.5	7.0	7.5				
1.90	15.5	6.5	6.5				
2.00	15.0	6.0	6.0				

Table 4.3

$$\sigma_{y'} = \sigma_x \sin^2\vartheta - 2\tau_{xy}\sin\vartheta\cos\vartheta + \sigma_y\cos^2\vartheta \qquad [4.3]$$

and

$$\tau_{x'y'} = \frac{1}{2}(\sigma_y - \sigma_x)\sin2\vartheta + \tau_{xy}\cos2\vartheta \qquad [4.4]$$

by adding the first two equations one finds:

$$\sigma_{x'} + \sigma_{y'} = \sigma_r + \sigma_\vartheta \qquad [4.5]$$

and from that follows that

$$\tau_{x'y'} \neq 0 \qquad [4.6]$$

because

$$\tan2\vartheta \neq \frac{2\tau_{xy}}{\sigma_r - \sigma_\vartheta} \qquad [4.7]$$

In Table 4.4 the thermal stresses for the line M8-M6 are given. The stress σ_p is the stress which is parallel to the lime M8-M6, and σ_t is the stress which is transverse to the line. In Table 4.5 the stresses for the line M7-M9 are given. In Figure 4.16 and 4.17 these stresses are plotted.

The analytic solution for the thermal stresses for an infinite hollow cylinder should provide a reasonable approximation in the heater mid-plane. Formulae for the radial displacement u_r and the radial, tangential, and axial stresses, σ_r, σ_ϑ, and σ_z are derived from the equations given by Timoshenko and Goodier (1951) for an infinitely long hollow cylinder with an internal radius, a, and an external radius, b, subjected to a radial temperature distribution T(r):

$$u_r = \frac{1+v}{1-v}\left[\frac{\alpha}{r}\frac{(1-2v)r^2+a^2}{b^2-a^2}\int_a^b T(r)r\,dr + \int_a^r T(r)r\,dr\right] \qquad [4.8]$$

			M8-M6			
			Thermal Stresses			
Distance [m]	Θ [deg]	σ_r [MPa]	σ_ϑ [MPa]	σ_p [MPa]	σ_t [MPa]	τ [MPa]
2.07	14.0	14.0	6.0	13.5	6.5	-1.88
1.88	15.0	15.5	6.5	14.9	7.1	-2.25
1.70	17.5	17.5	7.5	16.6	8.40	-2.87
1.50	19.5	19.5	8.5	18.3	9.7	-3.46
1.31	22.0	22.0	10.5	20.4	12.1	-4.0
1.13	26.0	25.5	13.5	23.2	15.8	-4.7
0.95	31.5	28.5	16.0	25.1	19.4	-5.6
0.78	39.0	31.0	20.5	26.8	24.7	-5.1
0.64	50.5	34.0	25.0	28.6	30.4	-4.4
0.53	67.0	35.5	32.0	32.5	35.0	-1.3
0.49	88.5	37.0	39.0	39.0	37.0	0.1
0.53	69.0	35.5	32.0	32.4	35.1	-1.2
0.63	51.0	34.0	25.0	28.6	30.4	-4.4
0.77	39.8	31.0	20.5	26.7	24.8	-5.2
0.94	31.5	28.5	16.0	25.1	19.4	-5.6
1.11	26.3	25.5	13.5	23.1	15.9	-4.8
1.29	22.5	22.0	10.5	20.3	12.2	-4.1
1.48	19.5	19.5	8.5	18.3	9.7	-3.5
1.66	17.5	17.5	7.5	16.6	8.4	-2.9
1.86	15.5	15.5	6.5	14.9	7.1	-2.3
2.05	14.0	14.0	6.0	13.5	6.5	-1.9
2.22	13.0	13.0	5.5	12.6	5.9	-1.6

Table 4.4

The displacements from the axis of the heater are positive.

$$\sigma_r = \frac{\alpha E}{1-v} \frac{1}{r^2} \left[\int_a^r T(r)r\,dr - \frac{r^2-a^2}{b^2-a^2} \int_a^b T(r)r\,dr \right]$$ [4.9]

M7-M9						
Thermal stresses						
Distance [m]	Θ [deg]	σ_r [MPa]	σ_ϑ [MPa]	σ_p [MPa]	σ_t [MPa]	τ [MPa]
3.46	6.8	7.1	2.5	7.0	2.6	-0.5
3.28	7.4	7.9	2.7	7.8	2.8	-0.7
3.07	8.0	8.6	2.9	8.5	3.0	-0.8
2.88	8.4	9.4	3.2	9.3	3.3	-0.9
2.67	8.9	10.3	3.7	10.1	3.9	-1.0
2.47	9.8	11.5	4.2	11.3	4.4	-1.2
2.28	10.5	12.5	4.8	12.2	5.1	-1.4
2.08	11.3	14.2	5.5	13.9	5.8	-1.7
1.89	12.5	15.5	6.5	15.1	6.9	-1.9
1.70	14.0	17.5	7.5	16.9	8.1	-2.3
1.50	15.5	19.5	8.5	18.7	9.3	-2.8
1.31	18.0	22.0	10.4	20.9	11.5	-3.4
1.12	21.3	25.5	13.4	23.9	15.0	-4.1
0.94	25.0	28.5	16.0	26.3	18.2	-4.8
0.76	31.5	32.0	21.5	29.1	24.4	-4.7
0.60	42.3	35.5	30.0	33.0	32.5	-2.7
0.47	59.0	37.0	42.5	41.0	38.5	+2.4
0.41	83.5	35.0	49.0	48.8	35.2	+1.6
0.43	68.5	36.0	45.0	43.8	37.2	+3.1
0.54	48.0	37.0	32.0	34.2	34.8	-2.5
0.69	35.5	33.2	23.5	29.9	26.8	-4.6
0.86	28.0	30.2	16.0	27.1	19.1	-5.9

Table 4.5

$$\sigma_\vartheta = \frac{\alpha E}{1-v} \frac{1}{r^2} \left[T(r)r^2 - \int_a^r T(r)rdr - \frac{r^2+a^2}{b^2-a^2} \int_a^b T(r)rdr \right] \qquad [4.10]$$

and

$$\sigma_z = \frac{\alpha E}{1-v} \left[T(r) - \frac{2v}{b^2-a^2} \int_a^b T(r)rdr \right] \qquad [4.11]$$

Compressive stresses are positive. α = linear coefficient of thermal expansion, v = Poissons ratio, E = Young's modulus.

In the case of an infinite medium, $b \to \infty$, and the temperature decrease monotonically as function of r,

$$\lim_{b \to \infty} \frac{1}{b^2 - a^2} \int_a^b T(r)r\,dr = 0 \qquad [4.12]$$

and the equations reduce to :

$$u_r = \frac{1+v}{1-v} \alpha \bar{T} r \qquad [4.13]$$

$$\sigma_r = \frac{\alpha E}{1-v} \bar{T} \qquad [4.14]$$

$$\sigma_\vartheta = \frac{\alpha E}{1-v} (\bar{T} - T) \qquad [4.15]$$

and

$$\sigma_z = \frac{\alpha E T}{1-v} \qquad [4.16]$$

where

$$T(r) = \frac{1}{r^2} \int_a^r T(r)r\,dr \qquad [4.17]$$

These equations have been utilized by several people in their studies of nuclear waste storage, e.g. Cook (1978) and Leijon (1978).

The equations quoted above are only strictly true if the elastic and the thermal coefficients can be regarded as independent of temperature. It has been shown by Chan *et al.* (1980 b), however, that there is a considerable temperature dependence of all the pertinent parameters.

Wollenberg *et al.* (1981) found from an investigation of thin sections of the Stripa granite that microfractures were abundant throughout the rock, and found between each crystal. As the rock mass is heated, thermal expansion increases the normal stress on fractures, and depending on the orientation and size of the aperture and the asperities, tends to close them. The most pronounced effect of this phenomenon is of course found in the highest stress zone adjacent to the heater. This results in a less homogeneous rock mass upon heating, with more closed fractures near the heater. In Figure 4.18 a visual example of a fracture under three different stress conditions is shown. Under a small normal stress the fractures are long and only a few asperities are in contact. The aspect ratio is small and the fracture close easily. When the normal stress increase the aspect ratio of the fractures is increasing and the fractures become more and more difficult to close. The effect of stress on a fracture is one of the fundamental questions in rock mechanics and geophysics. The fractures, microscopic and macroscopic, are of primary importance in determining to rock properties under *in situ* conditions. Elastic moduli are increased in this region by the thermal stress.

Timur (1977), has discussed the temperature dependence of P and S-wave velocities: the values he reports for saturated Berea sandstone, subjected to 34.5 MPa confining pressure, are a P-wave velocity decrease by 1.59 % per $100^{\circ}C$, and a S-wave velocity decrease by 1.18 % per $100^{\circ}C$. The reported porosity for the Berea sandstone is 17 %, but

similar results were reported for a carbonate with a porosity of 1.3 %. The expected reduction of elastic moduli of the intact rock due to an increase in temperature appears to be over-ridden by the concomitant increase in moduli due to closure of fractures present in the rock mass.

4.3 Field Stresses

Field stresses play a very important role in all geophysical surveys *in situ*. The major problem is that it is difficult to obtain a reliable estimate of the direction and the magnitude of stresses in a rock mass. This is partly due to the fact that most techniques used measure the stress over a very small volume. There are however geological indications of stresses as well. So there are two methods for determining field stresses which are applicable to the work in the Stripa full-scale drift. The first is the search for geological phenomena which can provide an indication of the stress directions. The indications provided in the H9 heater area are the fault directions and the pegmatite dikes. In Figure 4.19 the faults mapped on the wall in the extensometer drift are shown. Also shown in this pole plot are the major pegmatite dikes found on the north western wall in that drift. In Figure 4.20, the principal stress directions obtained from surface boreholes as well as boreholes drilled in the mine are shown. Also shown are the direction of the faults in the H9 and the H10 areas. The polar representation of pegmatite dikes A and B from core and map data from the full-scale drift are also shown. In Figure 1.6 it is clear that the faults H9-1 and H9-2 are reverse faults. In Jaeger and Cook (1979) it is shown that these kinds of faults indicate a principal compressive stress σ_1 which is horizontal and perpendicular to the strike of the fault. The minimum principal stress σ_3 is vertical. In Figure

4.20 the polar representations of the faults fall closely to the line M8-M6. In Figure 2.12 in Chapter 2 it is clear that there is also a strike-slip component in the faulting. That also points to a principal compressive stress σ_1 being horizontal. In strike-slip faulting the intermediate stress is vertical and the minor principal stress being horizontal. From the steeply dipping pegmatite dike the direction of the minor principal stress at the time of intrusion of the dike can be inferred as being normal to the plane of the dike. The maximum principal stress was close to the direction of the line M8-M6. The stresses might have changed from the time of the faulting and intrusion of the pegmatite, but the ancient state of stress which caused the faults and determined in which direction the dikes went, certainly disrupted the rock mechanically; that disruption remains. Doe *et al.* (1981) and Doe (1982), measured the field stresses with both overcoring and hydro-fracturing techniques. There is a considerable scatter in the data, but their findings are at least fairly close to the stresses discussed above. In Figure 4.20 results from Carlsson (1978) and Doe *et al* (1981) are shown together with the fault and dike data. Also shown on this figure is the direction of the six ultrasonic cross-hole lines A - E. Doe (1982) reported a maximum stress which is close to horizontal, but directed in a north-eastern direction, as seen in Figure 4.21. The boreholes for the stress measurements in Figure 4.21 were drilled between the H9 and H10 heater experiments. BSP-1 is vertical and was drilled from the full-scale drift. BSP-2,3 are horizontal are were drilled from the extensometer towards the fullscale drift. The stresses shown in Figure 4.21 are the average stresses from the overcoring and the planes of the hydro-fractures in BSP-2. The direction of the field stresses are influenced by the presence of the drifts, but the degree

of their influence is not clear. In Figure 4.22 the principal stress distribution around the full-scale and extensometer drifts is shown, as calculated from far field measurements, Chan (1981). The field stresses influence the seismic velocities and attenuation, so these results will be used in later chapters.

4.4 Dewatering of the rock mass

The dewatering of the rock mass has been described in detail by Nelson *et al.* (1981). The purpose of the dewatering system was to remove excess water after it was discovered that rather large quantities were flowing into the boreholes. The original purpose was mainly to preserve the heaters and the instruments. The amount of water was recorded after removal each day; this water flow into the boreholes turned out to be an important part of the data base collected in Stripa. In Figures 4.23 -4.25 from Nelson *et al.* (1981), the inflow in all the dewatered boreholes in the H9 area is shown. In Table 4.6 the inflow to the four M-holes is presented. The M-holes in the H9 area were blown dry with high-pressure air. Prior to 23 July, 1979, the holes were covered with a barrel before the water was blown out, to confine the water to the area around the borehole. The water was then collected carefully and put into a measuring bucket. From that date the volume was measured by measuring the depth to the top of the water surface in each borehole, and then converting to volume at 2.46 liters per m of borehole.

Nelson *et al.* (1981) noted that upon the turn-on of all four heater experiments there was an increase of the water inflow in the boreholes. A likely explanation for this is the closure of the fractures due to the thermal expansion of the rock when the heaters are turned on. Upon

Dewatering of M-boreholes					
Day	Date	Boreholes			
		M6 [l (ml/day)]	M7 [l (ml/day)]	M8 [l (ml/day)]	M9 [l (ml/day)]
0	24 Aug.1978	0	2.0	0.3	2.0
20	13 Sep.1978	0.25(13)	3.0(150)	1.0(50)	4.0(200)
110	12 Dec.1978	2.8(31)	4.0(44)	2.5(28)	1.5(17)
252	3 May 1979	Amount not recorded			
333	23 Jul.1979	1.0(12)	4.25(52)	0.5(6)	11.0(136)
398	26 Sep.1979	2.2(34)	0.55(8)	2.1(32)	7.0(108)
626	11 May 1980	3.78(17)	10.42(46)	5.38(24)	15.4(68)
677	1 Jul.1980	4.24(83)	8.62(169)	4.36(85)	22.35(438)
699	23 Jul.1980	1.33(60)	0.39(18)	0.91(41)	5.0(227)
706	30 Jul.1980	0.12(17)	0.05(7)	0.25(36)	1.33(190)
Σ^*		20.1	39.5	21.4	89

* assuming an inflow of 31,44,28 and 136 ml/day respectively at day 252

Table 4.6

closure of the fractures the permeability decreases drastically. In fractures however, which are intersected by boreholes the pore fluids can escape into the boreholes. Morrow *et al.* (1981) showed that the permeability of a granite was reduced between 1 and 2 orders of magnitude when it was heated and the magnitude of permeability decrease depended on the temperature. In Stripa the H9 heater borehole wall

temperature reached a maximum of approximately 300° C. Morrow *et al.* (1981) showed that in the case of a temperature of 200° C the permeability decreased one order of magnitude in a specimen of Westerly granite over one month. Around the H9 heater a very sharp temperature gradient existed, so, over a large volume around the heater the temperatures were much lower than the values Morrow *et al.* used in their experiment. Flows in boreholes T17 and T18 in Figure 4.23 were observed to decrease and become zero after 100 days. For borehole C1 in Figure 4.24, the water inflow follows a more complicated pattern. The inflow was zero when the heater was switched on. Then there appeared to be a period during which water was squeezed out, and after 280 days the water inflow was observed to stop almost completely. Nelson *et al.* (1981) observed that the boreholes in the end of the drift had a much higher inflow during the course of the experiment. There are two possible reasons for this higher water inflow. The first is that these boreholes are close to the end wall of the drift, where the state of stress is quite different from that existing along the side walls. These boreholes are also the farthest from the H9 heater and thus are not subjected to the high temperatures close the heater. In Figure 4.25 the water inflow to the boreholes situated close to the end of the drift are shown.

It is concluded that the rock is fully saturated at all times for the following reason. The attenuation of the compressional waves is very sensitive to a small reduction (a few percent) in saturation from 100 %, as indicated in Chapter 7 of this report. No sharp increase in P-wave attenuation was observed anywhere in the field data, as shown in Chapter 6 of this report.

Nelson *et al.* (1981) considered the effect of a porosity change of 0.1% and with an average fracture spacing of 0.10 m, (from Paulsson *et al.* 1981), and find it satisfactory explains the 5000 ml of water which flowed into the holes after the H9 heater was turned on. The fracture width considered was 0.1 mm, which is a reasonable assumption. The porosity found in this report, (as indicated in Chapter 7), is close to 1.0 % instead of 0.1 % assumed by Nelson *et al.* There could be two reasons for this: the first is that only a small fraction of the water is squeezed out of the rock. This argument becomes important for the discussion later in Chapter 8. The other reason is that there must be many more fractures than the number reported in Paulsson *et al.* (1981). This point will also be further discussed in chapter 8. The problem with the water inflow data is that there was no knowledge of at what depth the water entered the boreholes. It is well-known that the bulk permeability in crystalline rock is determined by the presence of fractures and their apertures, as indicated by Gale (1975). If the water inflow to a borehole is mainly through a fracture which occurs at the same depth as the mid-plane of the heater, the flow would probably decrease rapidly after turn-on of the heater. At the bottom of the ultrasonic profile the temperature only increases, by 10° C, to approximately 20°C, which, with a linear thermal expansion coefficient of $10^{-5 \, \circ} \, C^{-1}$, results in a thermal expansion of 0.2 mm for a 2 meter line. This is not sufficient This expansion is insufficient to close all the open fractures. In Chapter 8 the effect of the thermal expansion of water will be discussed. The specific volume and the viscosity of water as function of temperature is shown in Figure 4.26. In Table 4.7 the total inflow of water in the C, U and T holes is shown, (after Nelson *et al.* 1981).

Total inflow of water in U, C and T holes in the H9 area	
Borehole	Total inflow
	[l]
C1	2.9
C2	51.6
T13	0.1
T14	0.9
T15	1.0
T16	2.7
T17	1.6
T18	0.4
U1	0.3
U2	14.2
U3	54.3
U4	0.4
U5	0.4
U6	0.5
U7	7.0
U8	34.8
U9	21.7
U10	8.6
$\sum$	203.4
H9	19.1
M-holes	170.0
Total $\sum$	392.5

Table 4.7

It is interesting that the 18 borehole in Table 4.7 collected approximately the same amount of water as the four M-holes. The boreholes in Table 4.7 are 7 meter deep while the M-holes are 10 m. This indicates that the permeability is ra larger below 7 m under the drift floor during the course of the H9 heater experiment. Nelson *et al.* (1981) also finds

the permeability in the H10 area being a function of the radial distance from the H10 heater,with the permeability being lowest in the vicinity of the heater. This will be further discussed in Chapter 5.

4.5 Porosimeter experiment

Using a 60 kpsi mercury injection porosimeter, which normally is used to determine the porosity of ceramics and metals, the porosity and distribution of fracture apertures has been obtained for an intact specimen of the Stripa quartz monzonite. The mercury porosimeter measures the intrusion of mercury into the pores and, assuming a Hg-rock mineral contact angle of 130°, (Good and Mikhail, 1981) the width of the opening can be calculated from the total pressure in the vessel where the specimen is submerged in mercury. A review of the principels and apparatus involved in a mercury intrusion test is given by Orr (1969). Using the volume expelled from the pores as function of decreasing pressure, information can also be obtained about the shape and the structure of the pores. The technique is further discussed by Kloubek (1981) and Spitzer (1981). In Table 4.8 are shown the results of a test on a specimen from borehole E21 drilled from the Extensometer drift 11.85 m from the collar. That is very close to the H9 heater.

The total porosity found from the mercury intrusion experiment, 0.72 %, is very close to the porosity found by other investigators, as reported in Nelson *et al.* (1979). In Chapter 7 a porosity of 0.9 % is reported, which was obtained by vacuum drying a saturated specimen. The result of the porosimeter test is shown in Figure 4.25. The results up to 10 kpsi pressure are as expected. However the result from 10 kpsi to 57 kpsi indicates a dilatancy effect. 3 specimens were tested and all

MERCURY INTRUSION AND PRESSURE DATA

Stripa Quartz monzonite, borehole E21

Sample weight : 5.1635 gram

Date : Sept. 16 1982

(1) Hg head Pressure Correction (psia)	(2) Gauge Reading 0-15 (psia)	(3) Gauge Reading (psia)	(4) Absol. Pressure (psia)	(5) Meas. Intrusion Uncorrected (cc)	(6) Blank Correction (cc)	(7) Corr. Intrusion (cc/g)
-4.84	6.0	-	1.16	0.0	0.0	0.0
-4.79	8.0	-	3.21	0.004	0.0	0.000775
-4.79	9.0	-	4.21	0.004	0.0	0.000775
-4.79	10.0	-	5.21	0.0045	0.0	0.000872
-4.78	11.0	-	6.22	0.005	0.0	0.000968
-4.78	12.0	-	7.22	0.005	0.0	0.000968
-4.78	13.0	-	8.22	0.005	0.0	0.000968
-4.78	14.7	-	9.92	0.005	0.0	0.000968
-4.76	-	25	34.94	0.006	0.0	0.001162
-4.76	-	75	84.94	0.006	0.0	0.001162
-4.75	-	150	159.95	0.007	0.0	0.001356
-4.74	-	250	259.96	0.008	0.0	0.001549
-4.74	-	500	509.96	0.008	0.0	0.001549
-	-	1000	1015.0	0.009	0.0	0.001743
-	-	-	1500	0.013	0.0	0.002518
-	-	-	2000	0.012	0.0	0.002324
-	-	-	3000	0.013	0.0	0.002518
-	-	-	4000	0.015	0.0	0.002905
-	-	-	7500	0.015	0.0	0.002905
-	-	-	10000	0.015	0.0	0.002905
-	-	-	15000	0.013	0.001	0.002324
-	-	-	20000	0.012	0.002	0.001937
-	-	-	30000	0.011	0.003	0.001549
-	-	-	40000	0.009	0.004	0.000968
-	-	-	57500	0.008	0.004	0.000775

Table 4.8

1) Below atmospheric pressure, Absolute pressure (4) equals (2) minus (1). Above atmospheric pressure, Absolute Pressure (4) equals (3) plus atmospheric pressure minus (1)

2) Corrected Intrusion (7) equals (5) minus (6) divided by sample weight. three showed the same effect, so it is apparently a real phenomenon. The effect appears at approximately 70 MPa (10 kpsi).

POROSITY DETERMINATION

1. Wt. of penetrometer, empty g.   63.87

2. Wt. of penetrometer, filled with mercury, g.   157.91

3. Wt. of sample, g.   5.1635

4. Wt. of penetrometer with sample and mercury, g.   135.88

5. Displacement volume of sample $(2 + 3 - 4)/13.55$, cc.   2.008

6. Apparent Density, g./cc.   2.571

7. Real density g./cc.   2.590

8. Apparent volume of sample, $(3/6)$, cc   2.008

9. Real volume of sample, $(3/7)$, cc.   1.994

10. Total pore volume of sample, $(8 - 9)$, cc   0.014

11. Total porosity of sample, $100*10/8$, %   0.72

Table 4.9

THEORETICAL AND MEASURED TEMPERATURES
IN MIDPLANE OF H9 HEATER
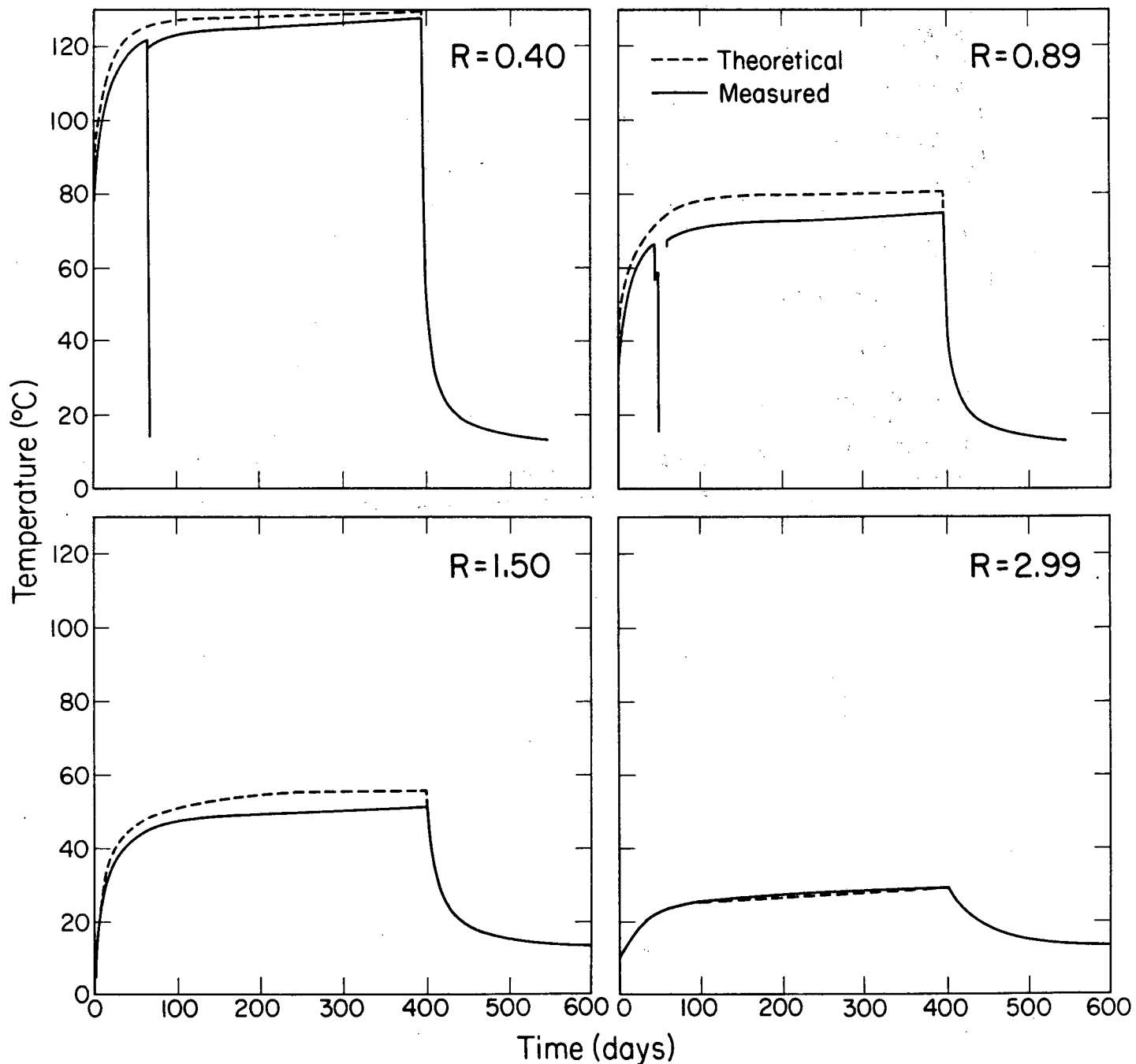
Fig. 4.1 Temperature record from four thermocouples in the H9 heater midplane
at 0.40, 0.89, 1.50 and 2.99 m from the center of the heater, respectively.
The temperatures are shown for the period from the turn-on of the
H9 heater until the day 600. The heater was turned off at day 398.

XBL 837-2153
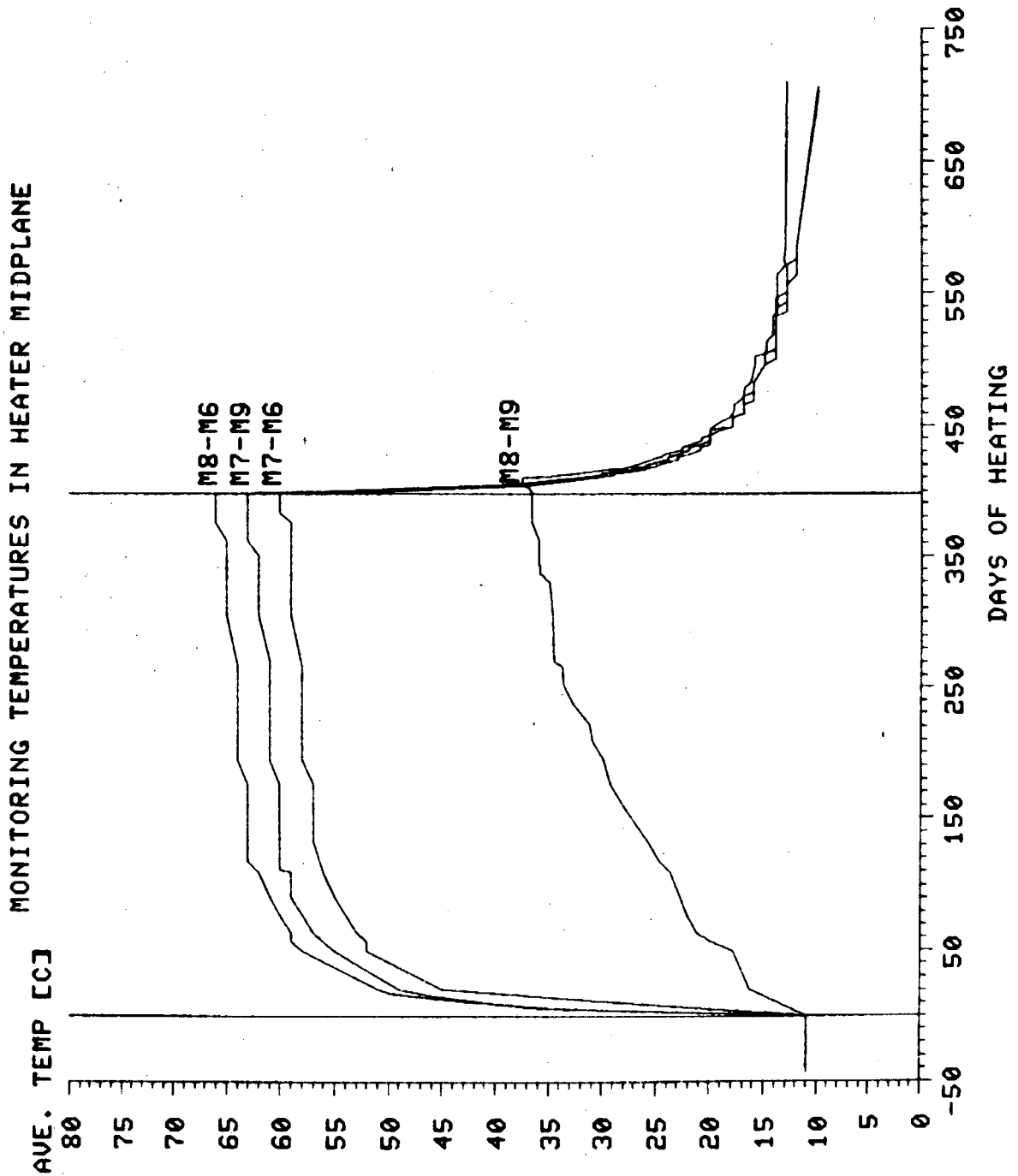
Fig. 4.2 Average temperatures over the four monitor lines from day -40 to day 670 These mean temperatures were obtained by project the radial temperature function from the heater onto 100 equally spaced points along lines connecting the M-boreholes. This was done for the 103 days data was collected in the heater midplane.
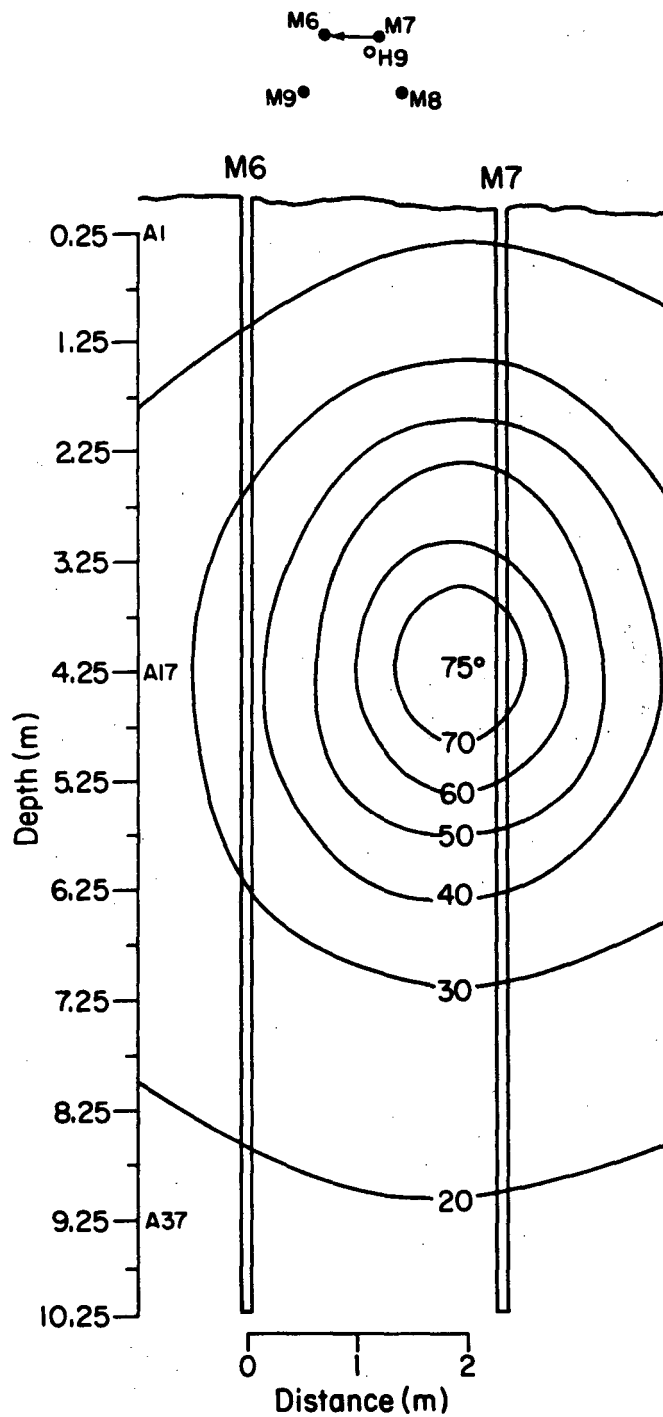
Fig. 4.3 Temperature distribution in cross section M7-M6 at day 398 after H9 heater turn-on. This spatial temperature distribution was obtained by projecting the observed temperatures for 70 thermocouples onto the plane between the M-boreholes.
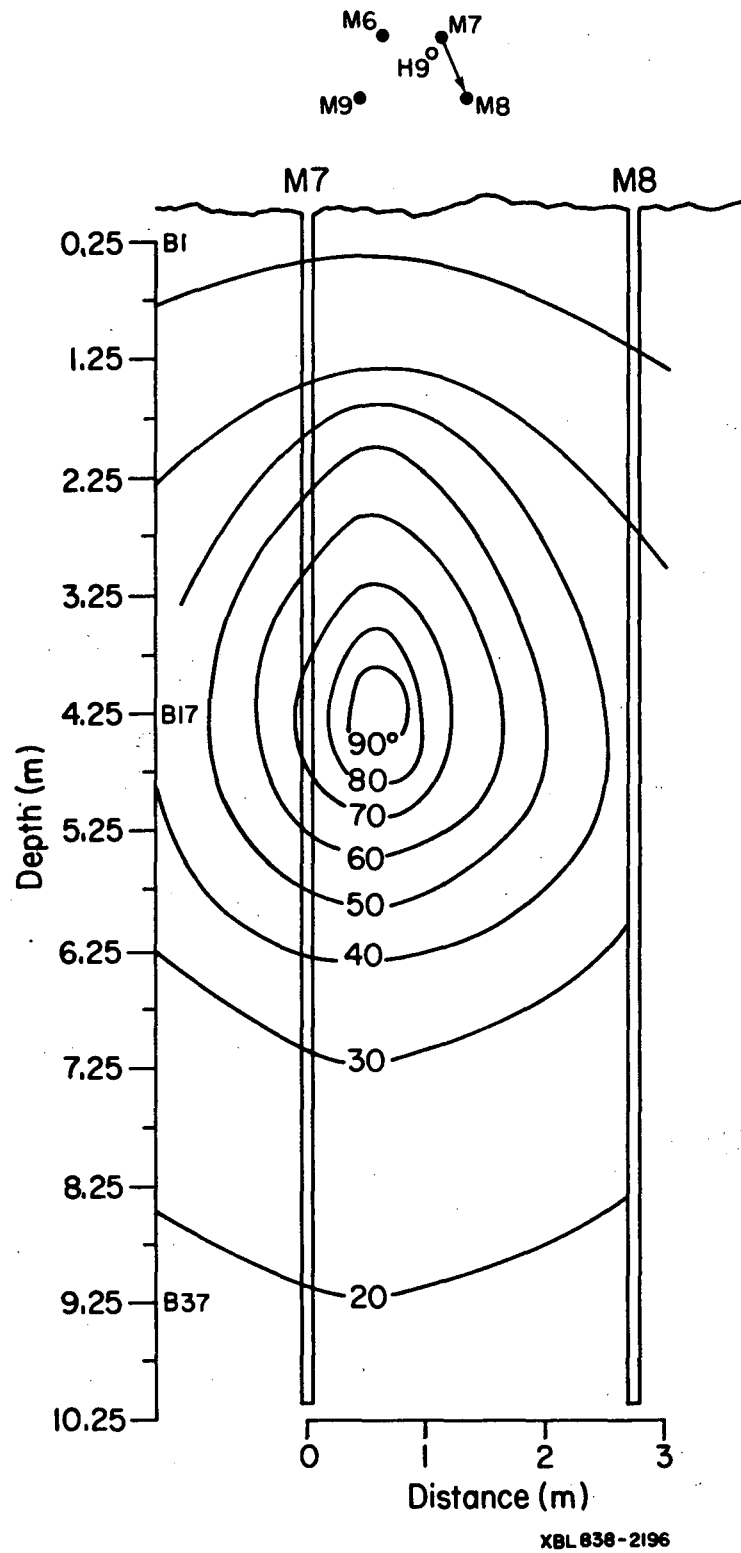
Fig. 4.4 Temperature distribution in cross-section M7-M8 at day 398 after H9 heater turn-on.
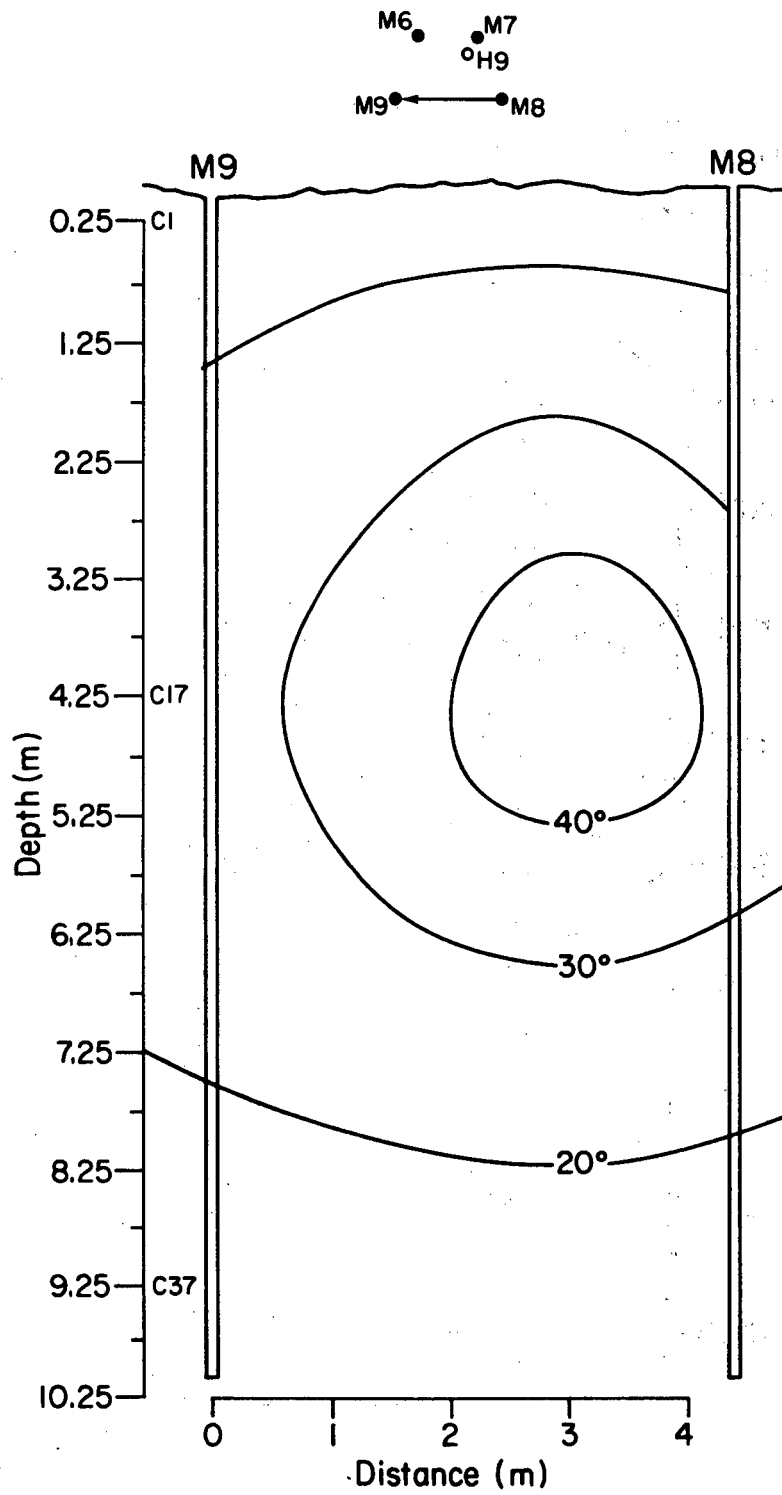
Fig. 4.5 Temperature distribution in cross-section M8-M9 at day 398 after H9 heater turn-on.
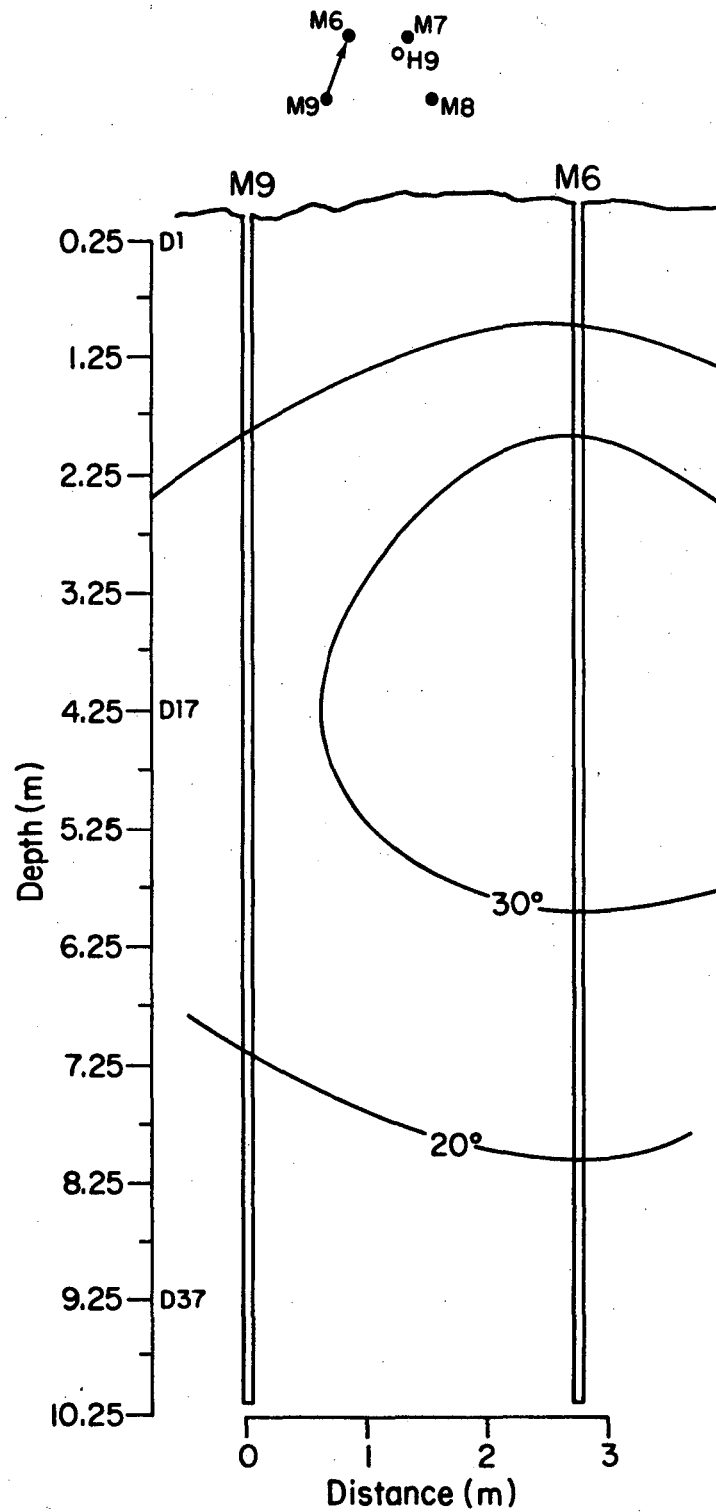
XBL 838-2194

Fig. 4.6 Temperature distribution in cross-section M9-M6 at day 398 after H9 heater turn-on.
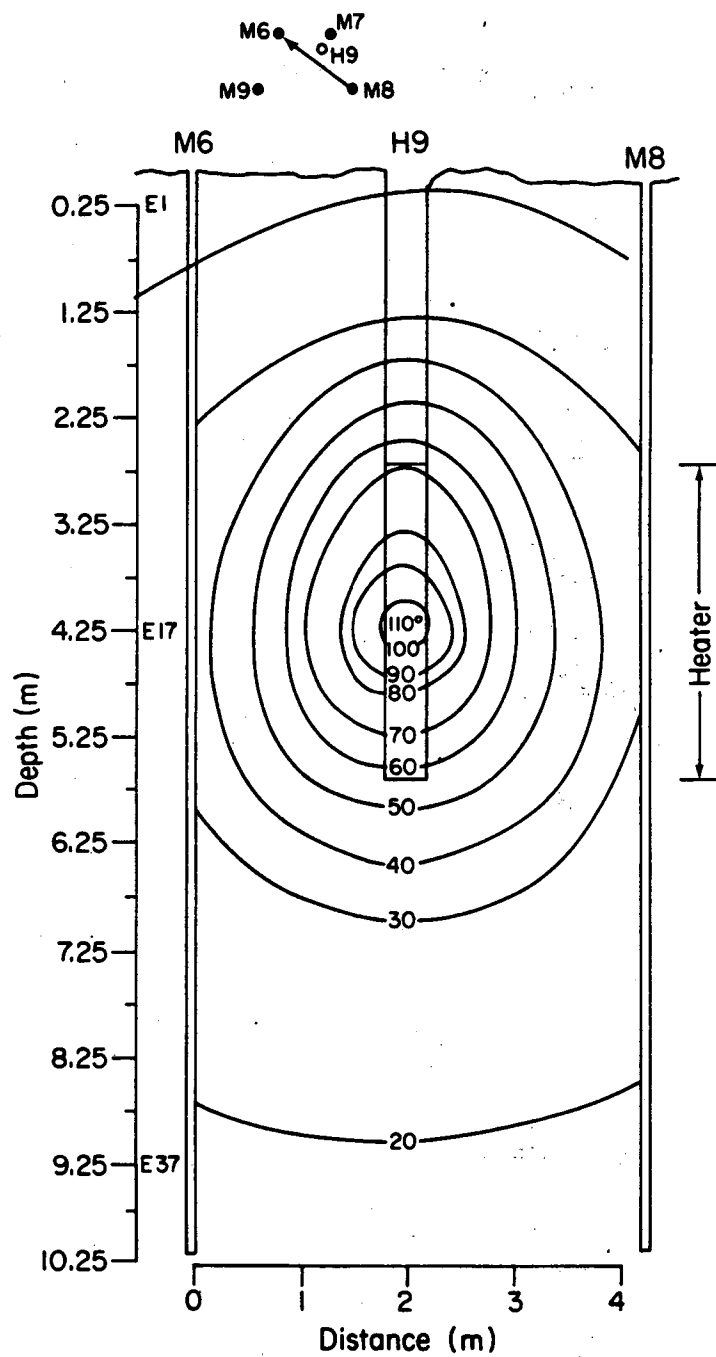
XBL 838-2193

Fig. 4.7 Temperature distribution in cross-section M8-M6 at day 398 after H9 heater turn-on.

XBL 838-2168
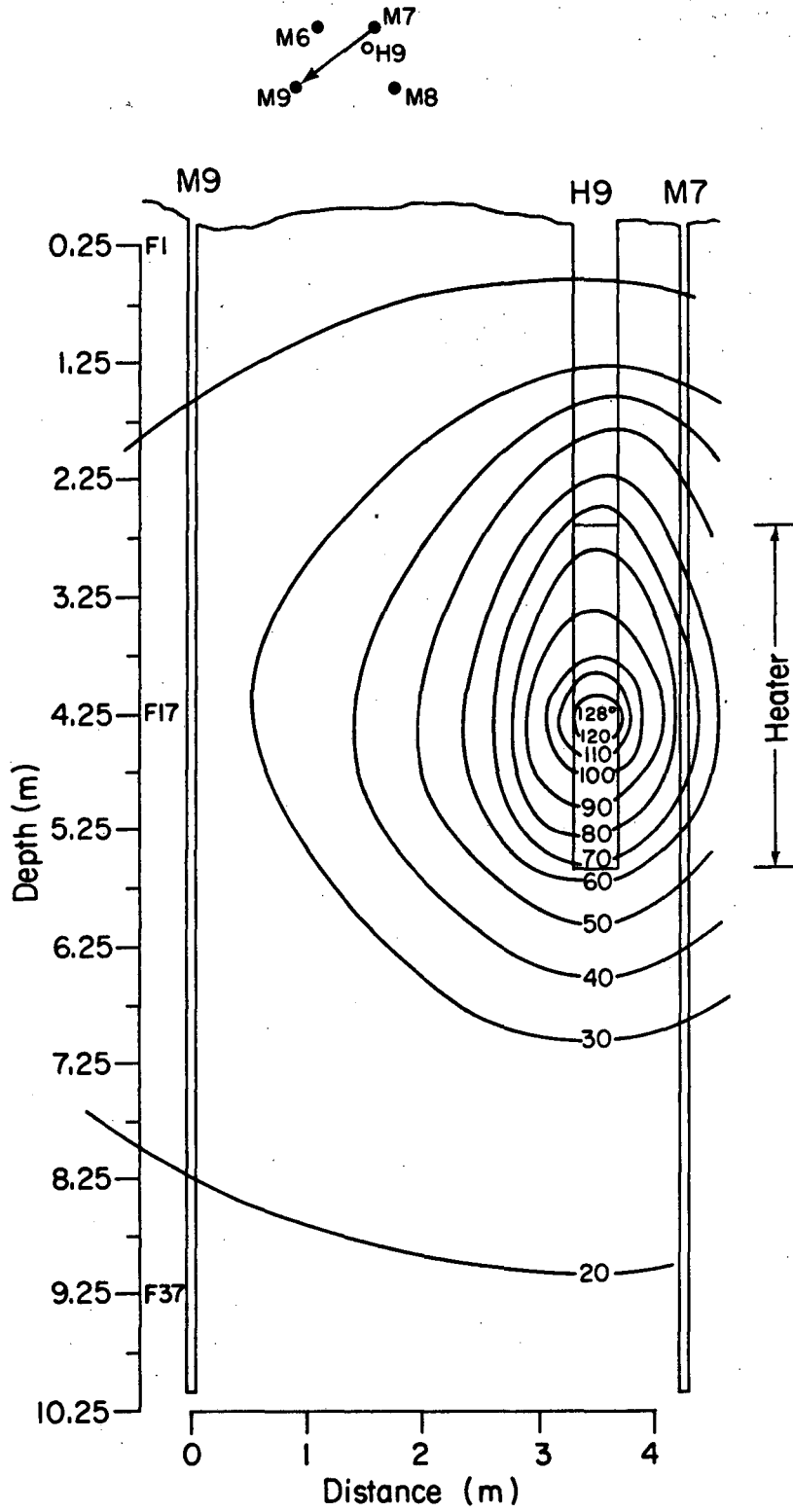
Fig. 4.8 Temperature distribution in cross-section M7-M9 at day 398 after H9 heater turn-on.

XBL 837-2133

XBL 801-4613
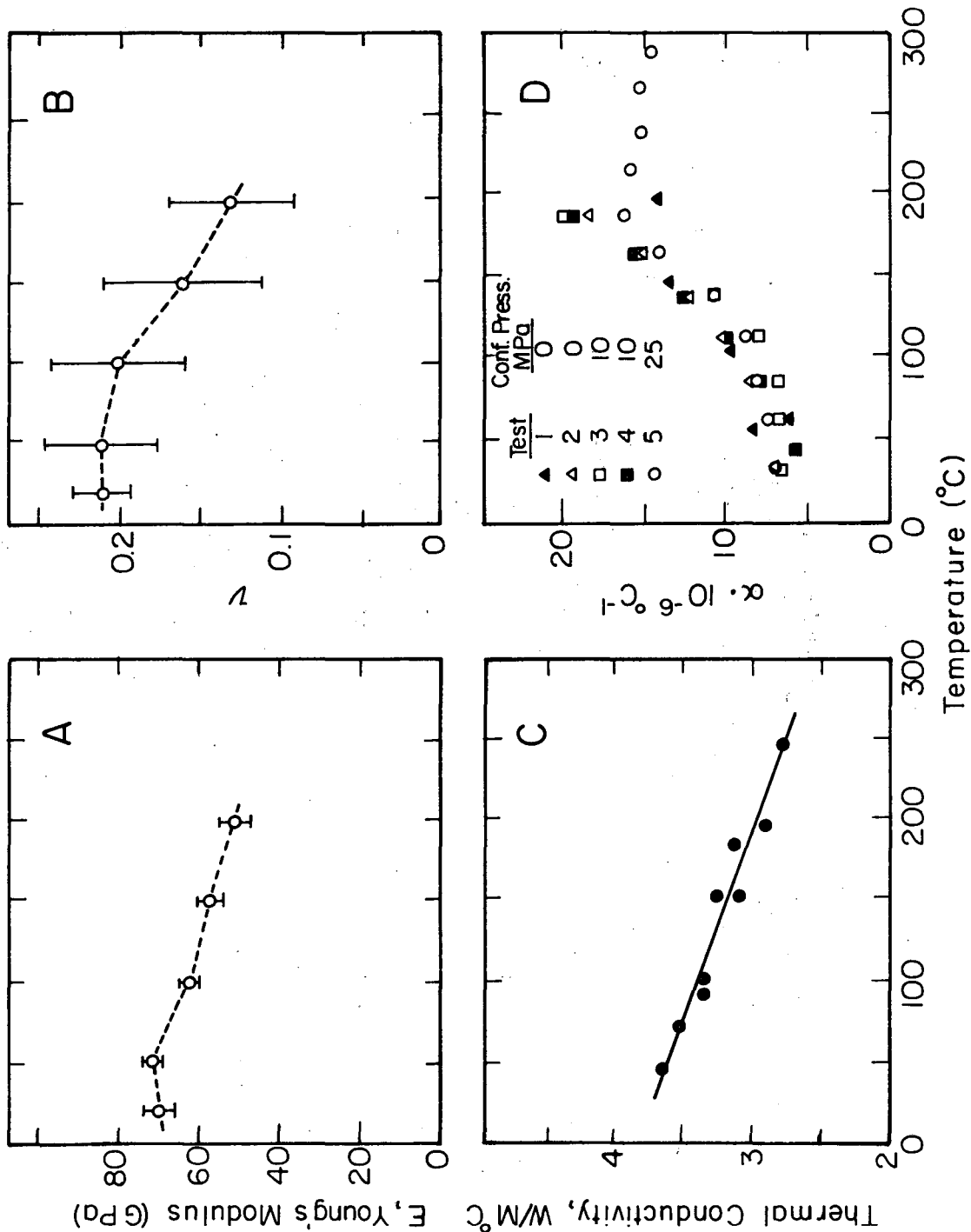
Fig. 4.9 Young's Modulus, Poisson's ratio, thermal conductivity and the coefficient for linear thermal expansion as functions of temperature for the Stripa quartz monzonite.
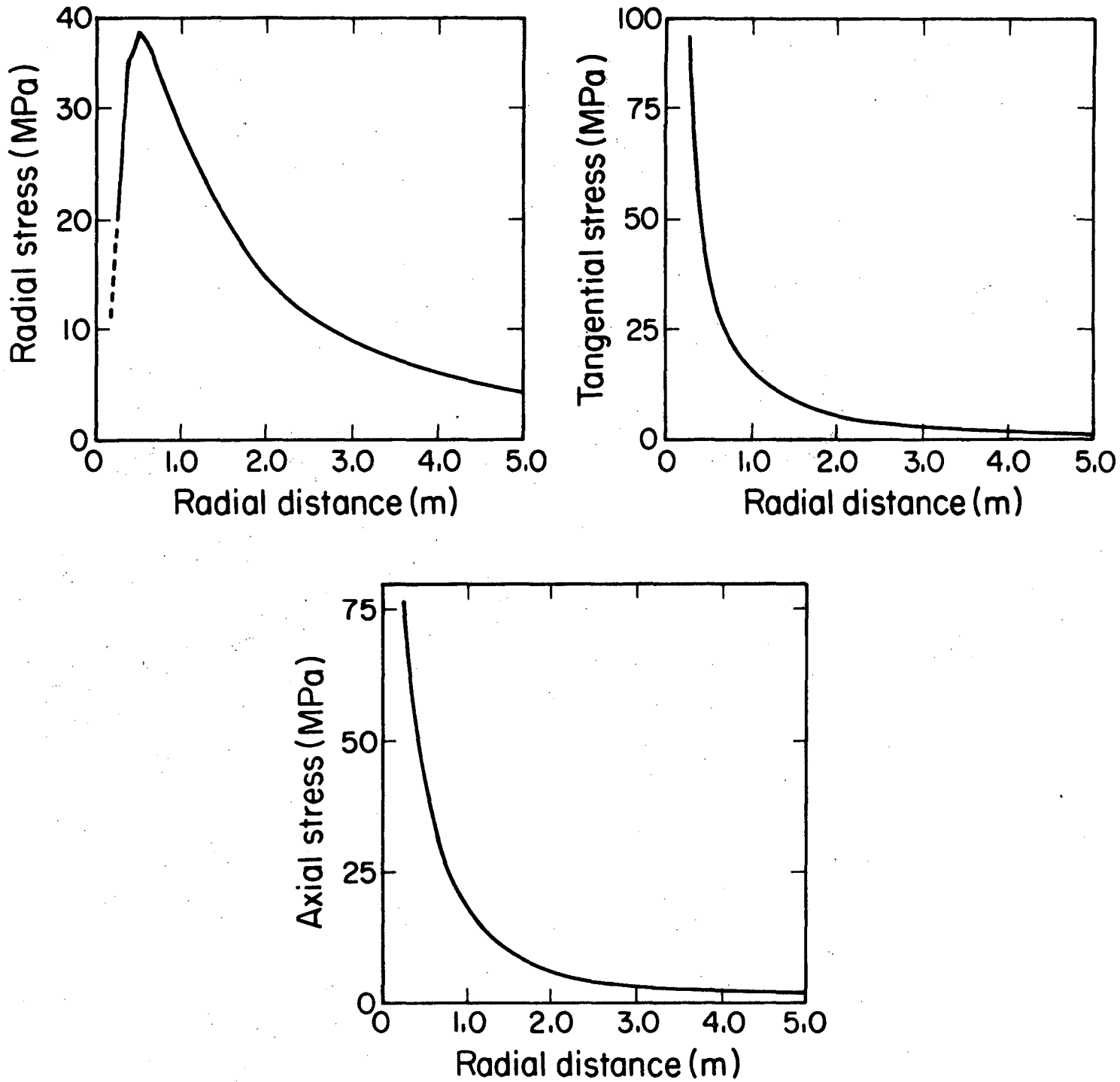
Fig. 4.10 Radial, tangential and axial thermal stresses for H9 heater at day 398 calculated from thermally-dependent material properties (see Fig. 4.3)

XBL 838-2170
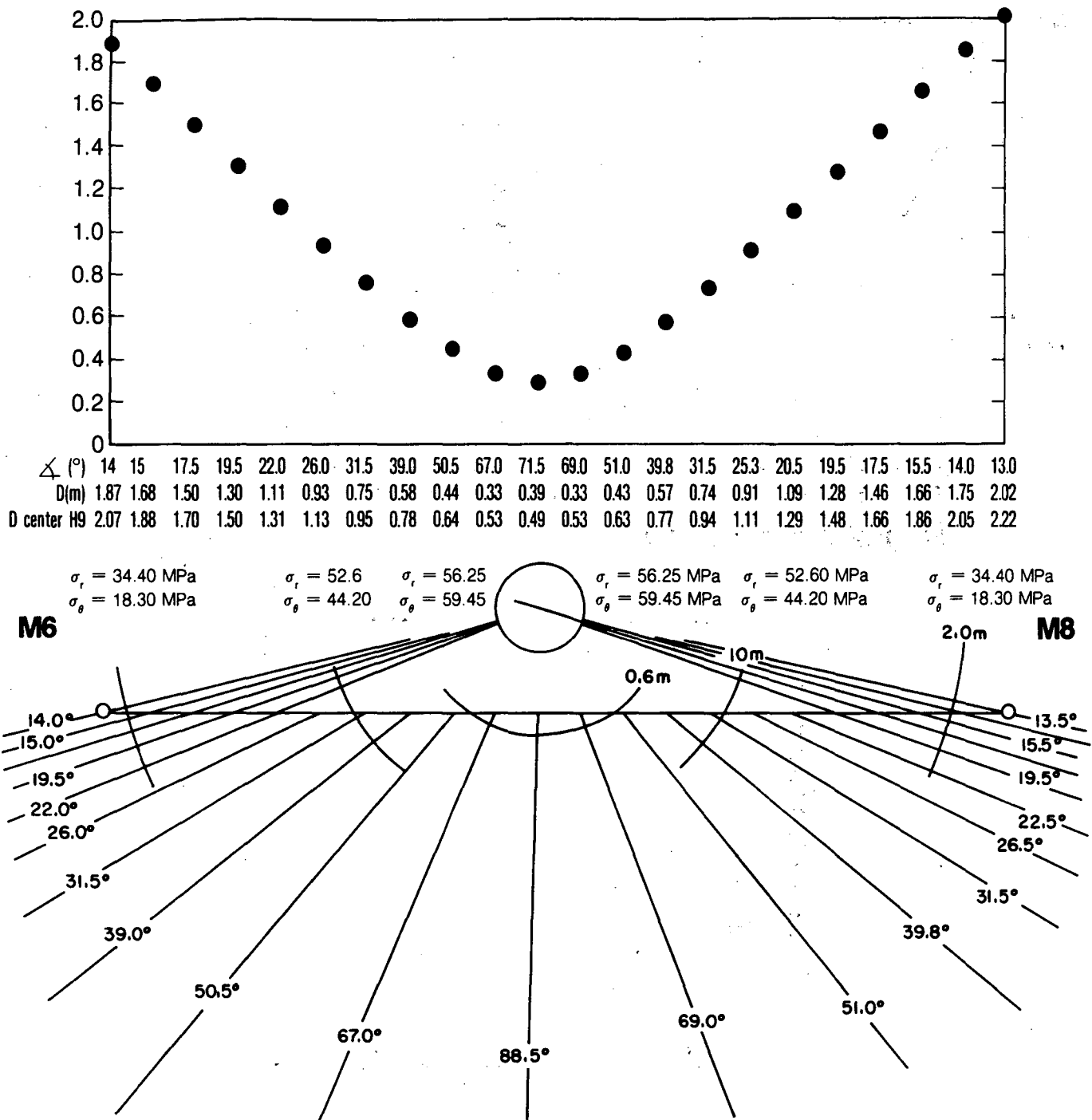
Fig. 4.11.   Distance and angle between a radial projection from
             H9 and the line connecting M8-M6

∡ (°)	6.8	7.4	8.0	8.4	8.9	9.5	10.5	11.3	12.5	14.0	15.5	18.0	21.3	25.0	36.5	42.3	59.0	53.5	68.5	46.0	35.5	28.0
D(m)	3.26	3.08	2.87	2.68	2.47	2.27	2.08	1.88	1.69	1.50	1.30	1.11	0.92	0.74	0.56	0.40	0.27	0.24	0.23	0.34	0.49	0.66
D center H9	3.46	3.28	3.07	2.85	2.67	2.47	2.28	2.05	1.89	1.70	1.50	1.31	1.12	0.94	0.76	0.60	0.47	0.41	0.43	0.54	0.69	0.86
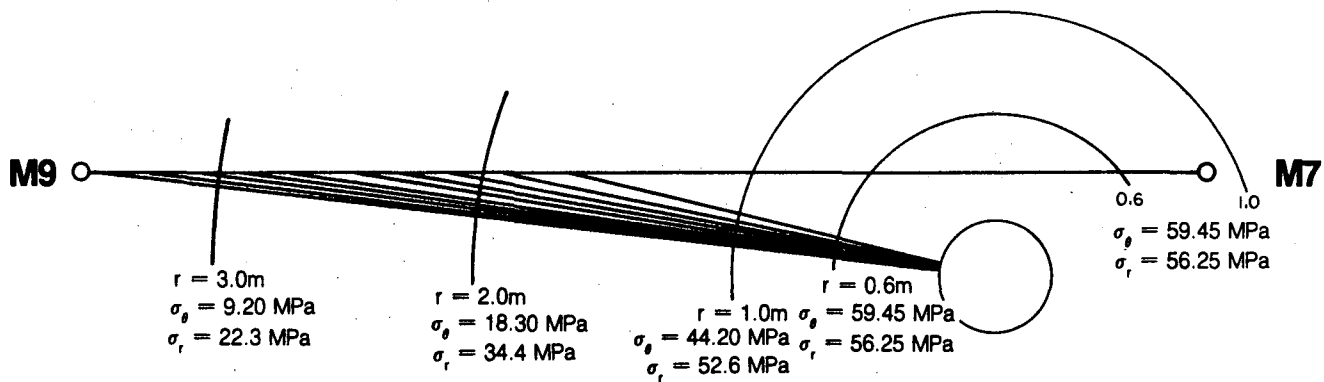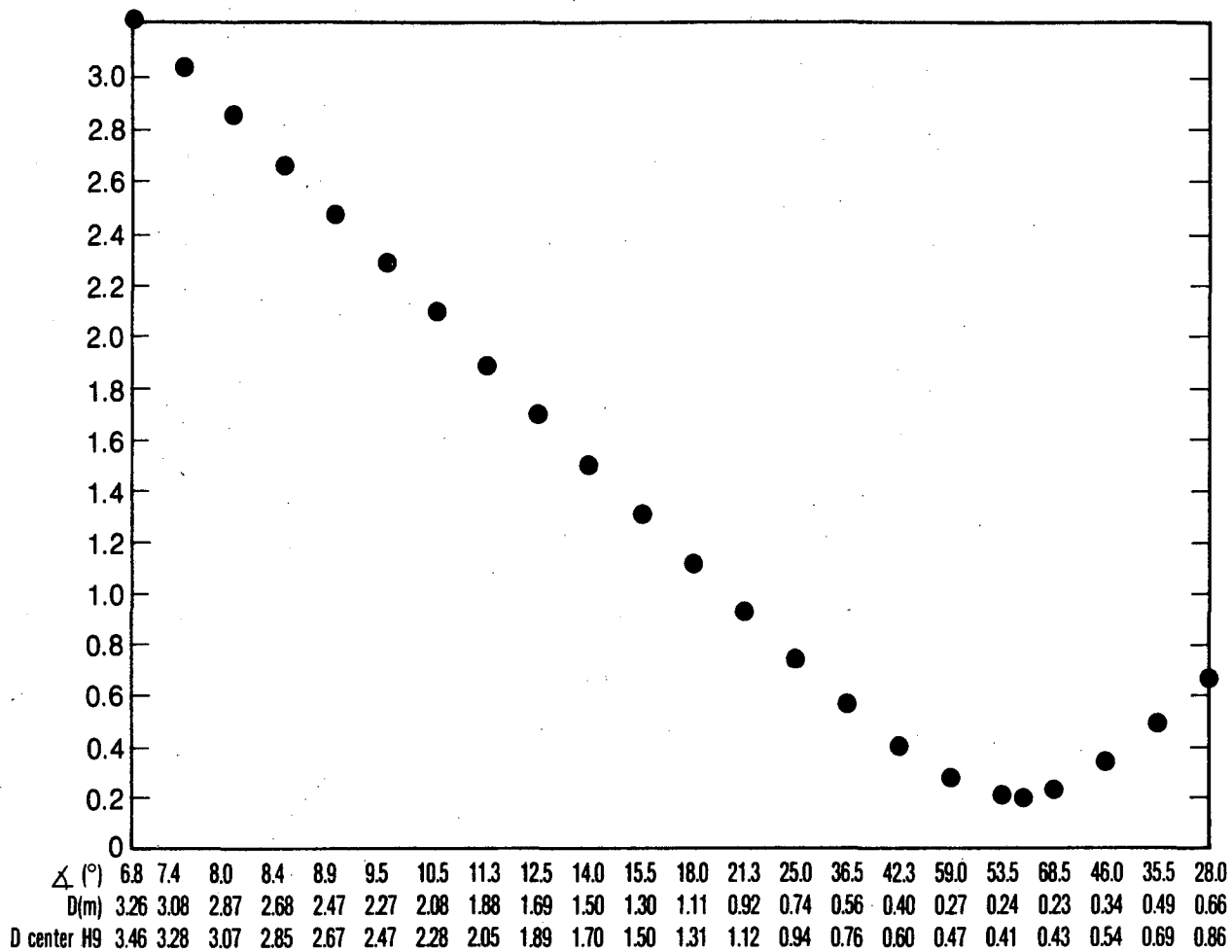
Fig. 4.12 Distance and angle between a radial projection from H9 and the line connecting M7-M9
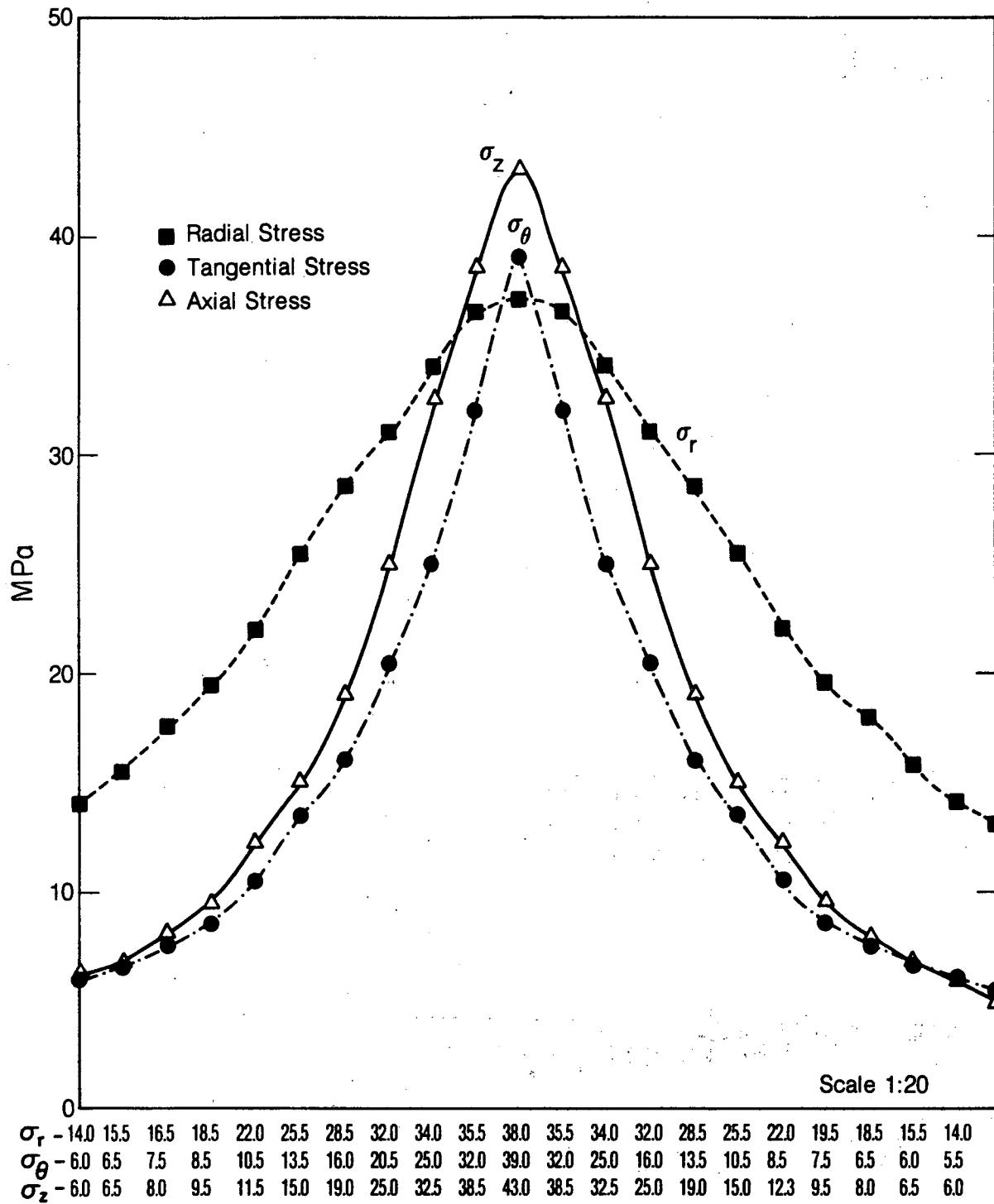
XBL839-2223

Fig. 4.13 Radial, azimuthal and vertical thermal stresses along line M8-M8 before the heater turn-off at day 398
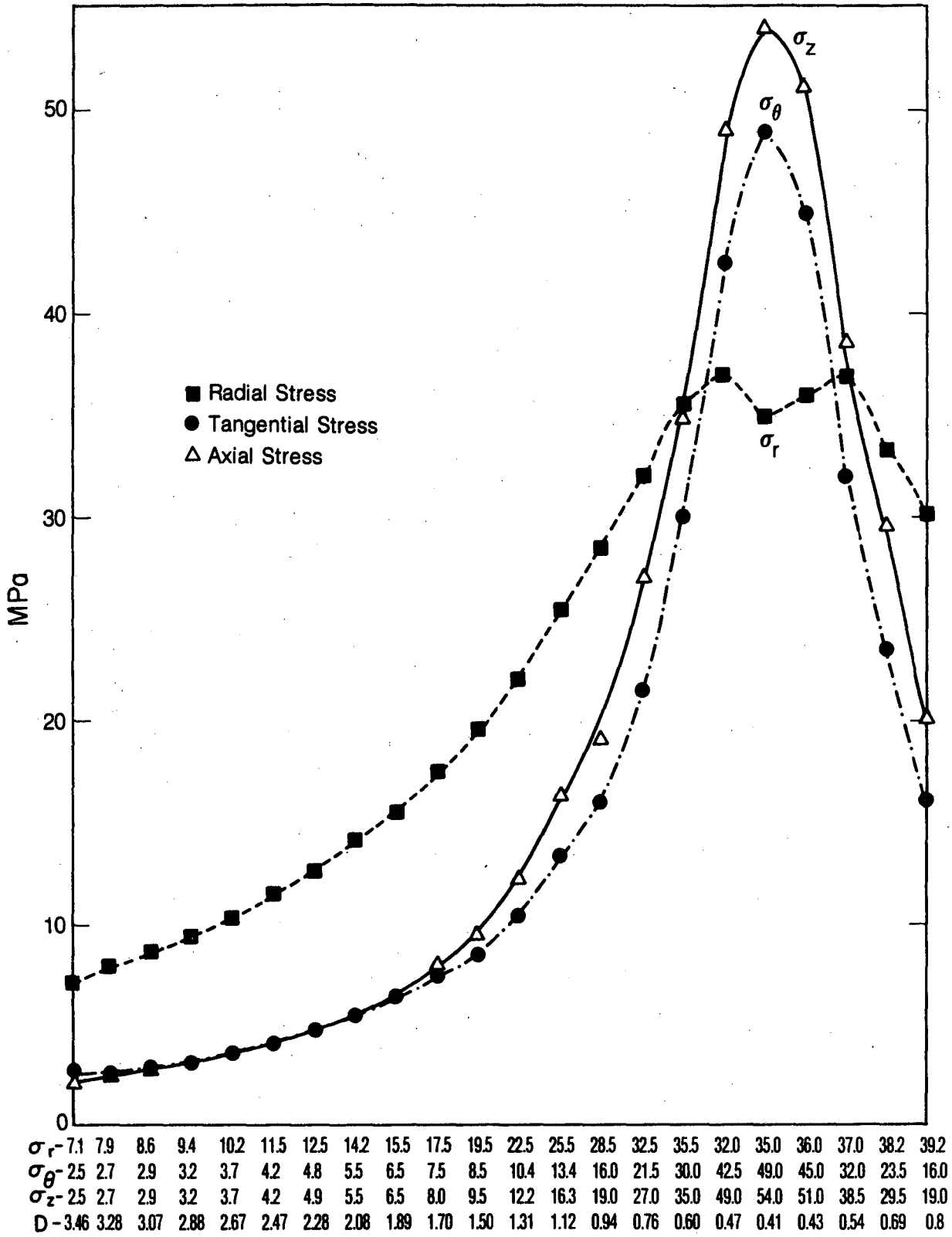
XBL 839-2220

Fig. 4.14 Radial, azimuthal and vertical thermal stresses along line M7-M9 before the heater turn-off at day 398

XBL 839-2221
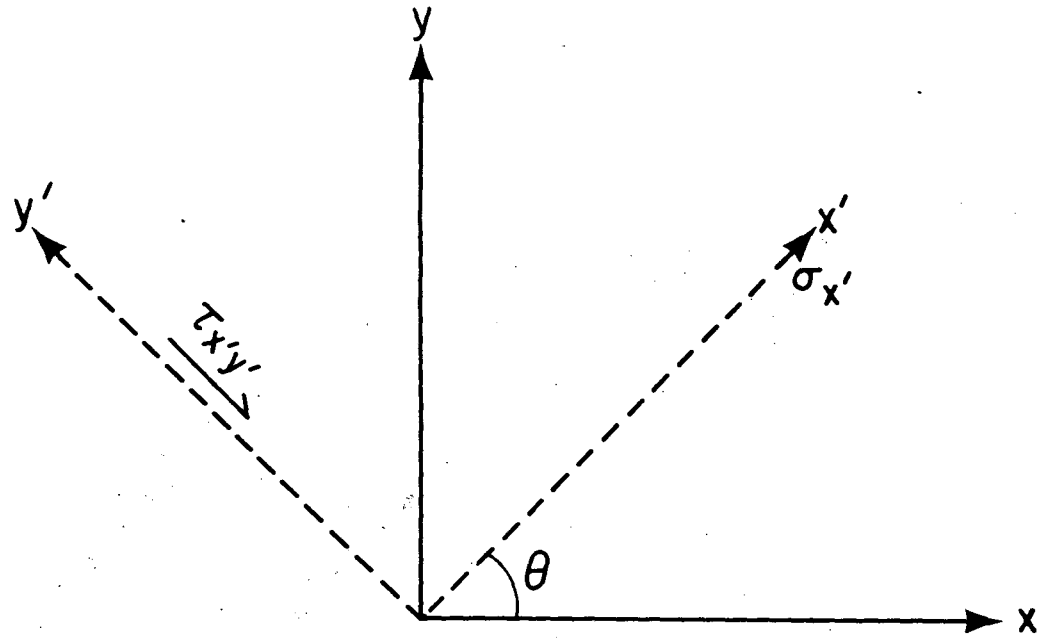
θ : ∢ between a radial projection and the monitor line.

XBL 838-2171

Fig. 4.15 Change of axes
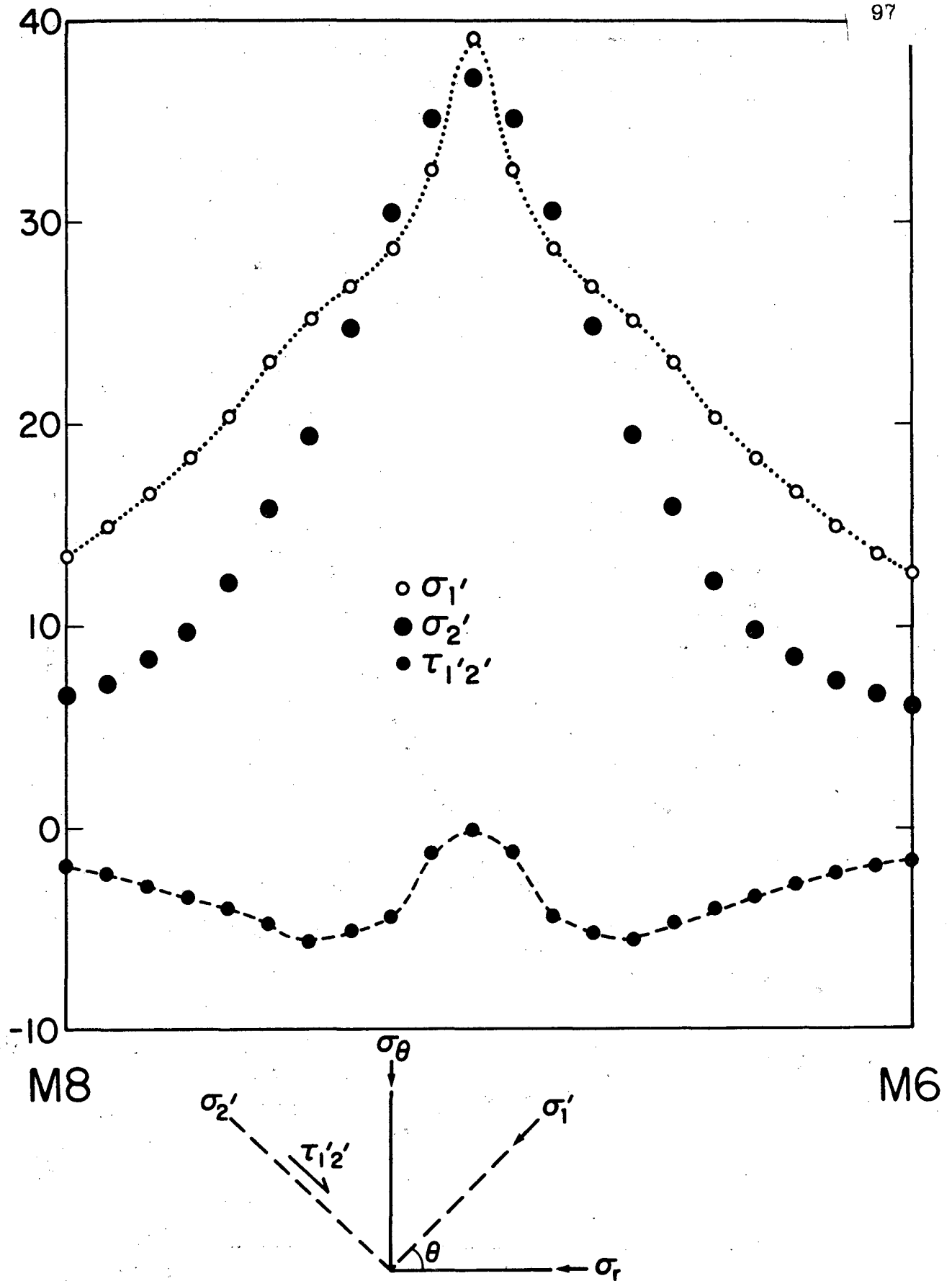
Fig. 4.16 Thermal stresses in direction of, and transverse to, the line M8-M6 at day 398

XBL 838-2181

XBL 838-2182
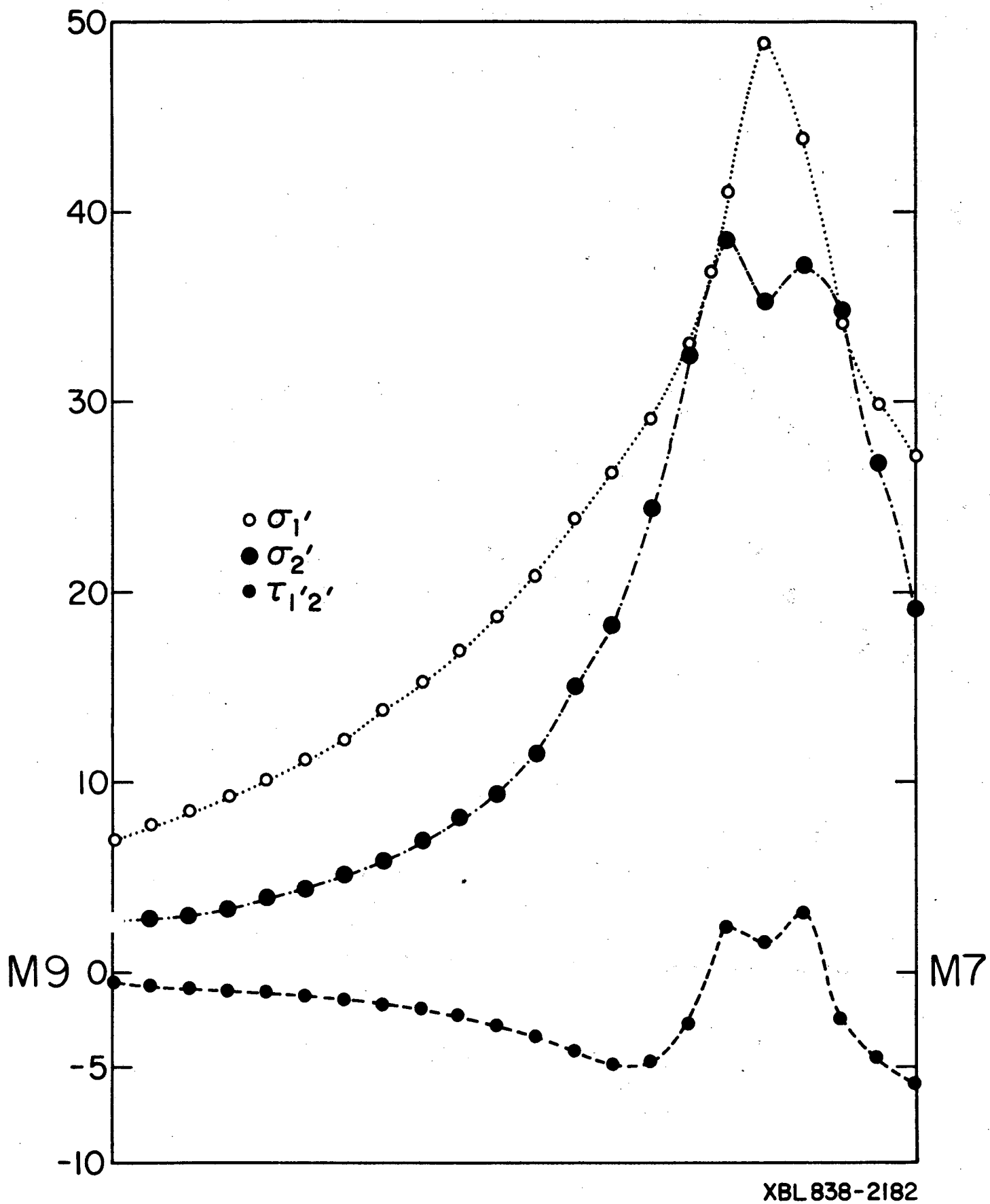
Fig. 4.17 Thermal stresses in direction of and transverse to, the line M7-M9 at day 398

(a) at normal stress σ_1

$$\longleftarrow \text{---} 2d \text{---} \longrightarrow$$
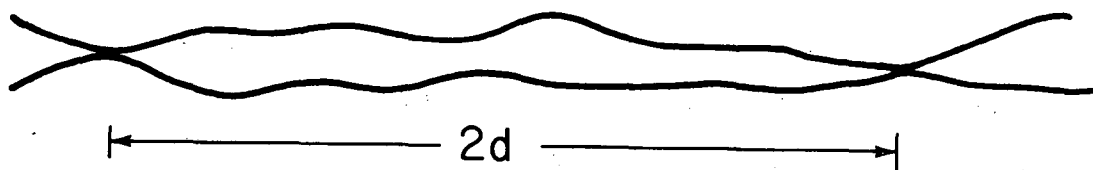
(b) at normal stress $\sigma_2 > \sigma_1$

$$\longleftarrow \text{---} 2d_1 \text{---} \longrightarrow \longleftarrow \text{---} 2d_2 \text{---} \longrightarrow$$
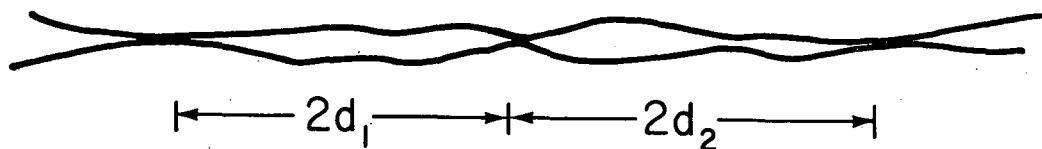
(c) at normal stress $\sigma_3 > \sigma_2$

$$\longleftarrow \text{---} 2d_1 \text{---} \longrightarrow \longleftarrow 2d_2 \longrightarrow \longleftarrow \text{---} 2d_3 \text{---} \longrightarrow \longleftarrow 2d_4 \longrightarrow$$
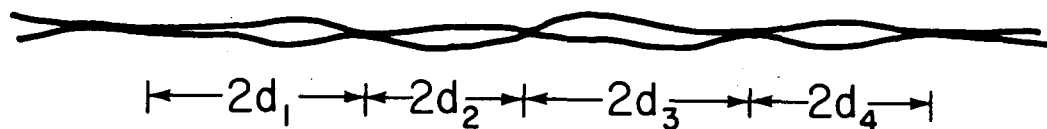
XBL 8011-2975

Fig. 4.18 Fracture closure with increasing stress This figure shows the effect of increasing normal stress. The fracture has a low aspect ratio initially and is easy to close. The higher the aspect ratio the fractures have the more asperities are touching per surface unit so they become increasingly more difficult to close.

Schmidt equal-area pole plot for fractures on wall in Extensometer drift

Lower hemisphere   H9   mineralizations

Magnetic North

100% =29 points

C Fullscale
Drift
N51°E

W ——— E

Fault

Fault ×× Fault

A

B

S

× Chlorite,Epidote,Calcite
■ Pegmatite
● Crush zone
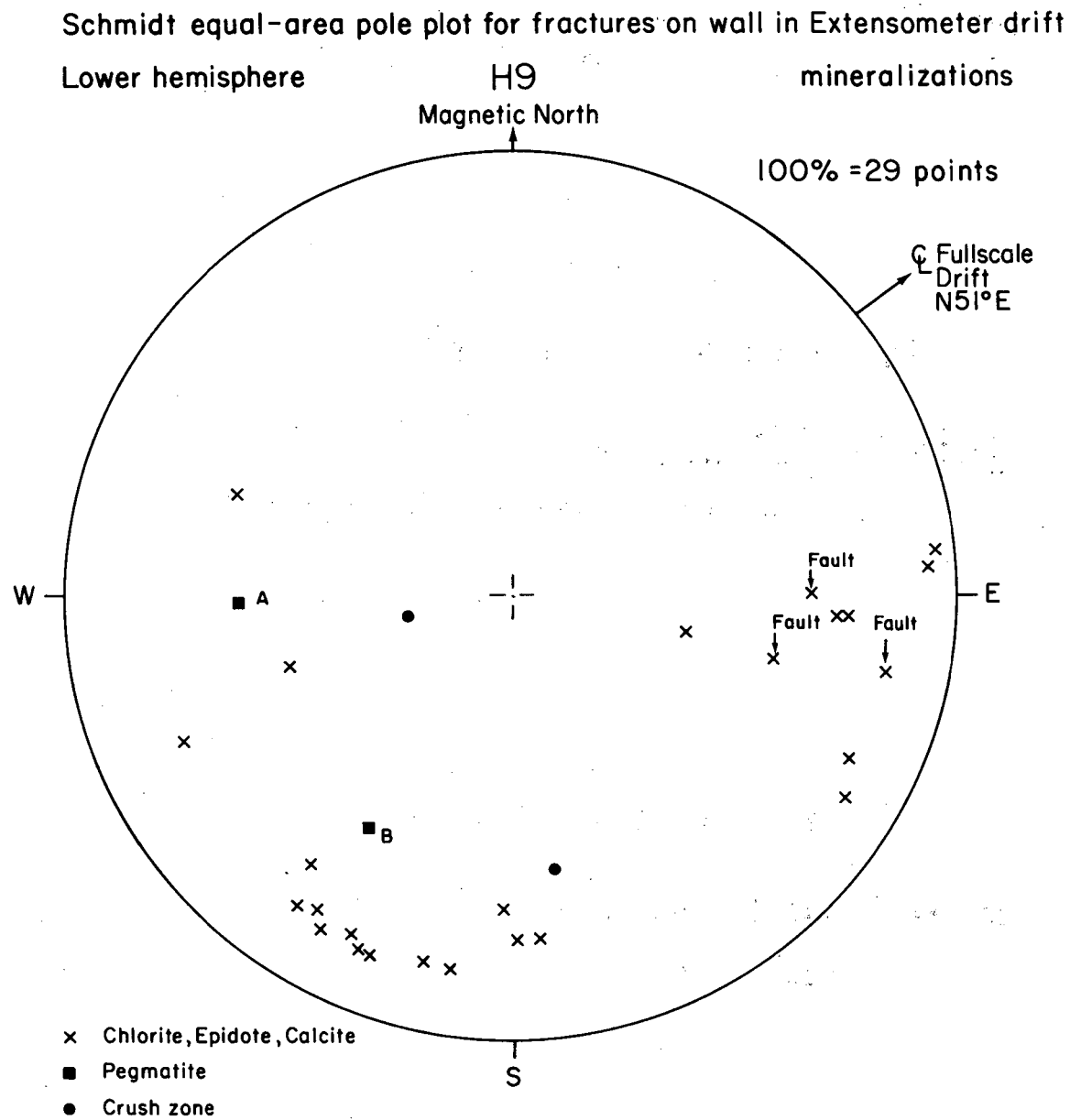
XBL 8010-2941

Fig. 4.19 Direction of faults and dikes mapped on the north-western wall in the extensometer drift

Schmidt equal-area pole plot for principal stress directions, pegmatite dikes and faults in the fullscale and extensometer drifts
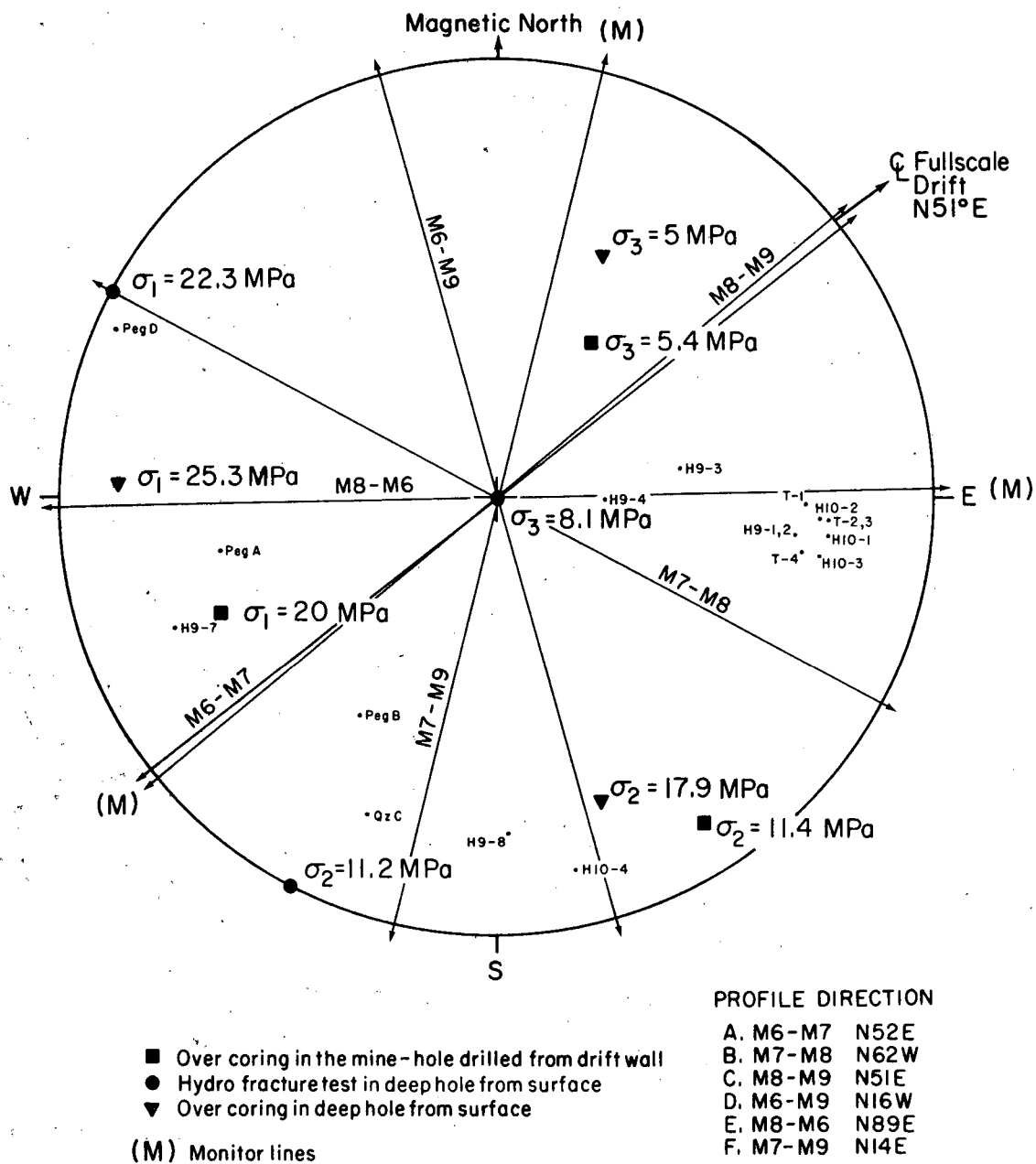
Fig. 4.20 Schmidt equal-area pole plot for principal stress directions, pegmatite dikes and faults in H9 heater area are shown. Also the direction of the 6 ultra sonic cross-sections.
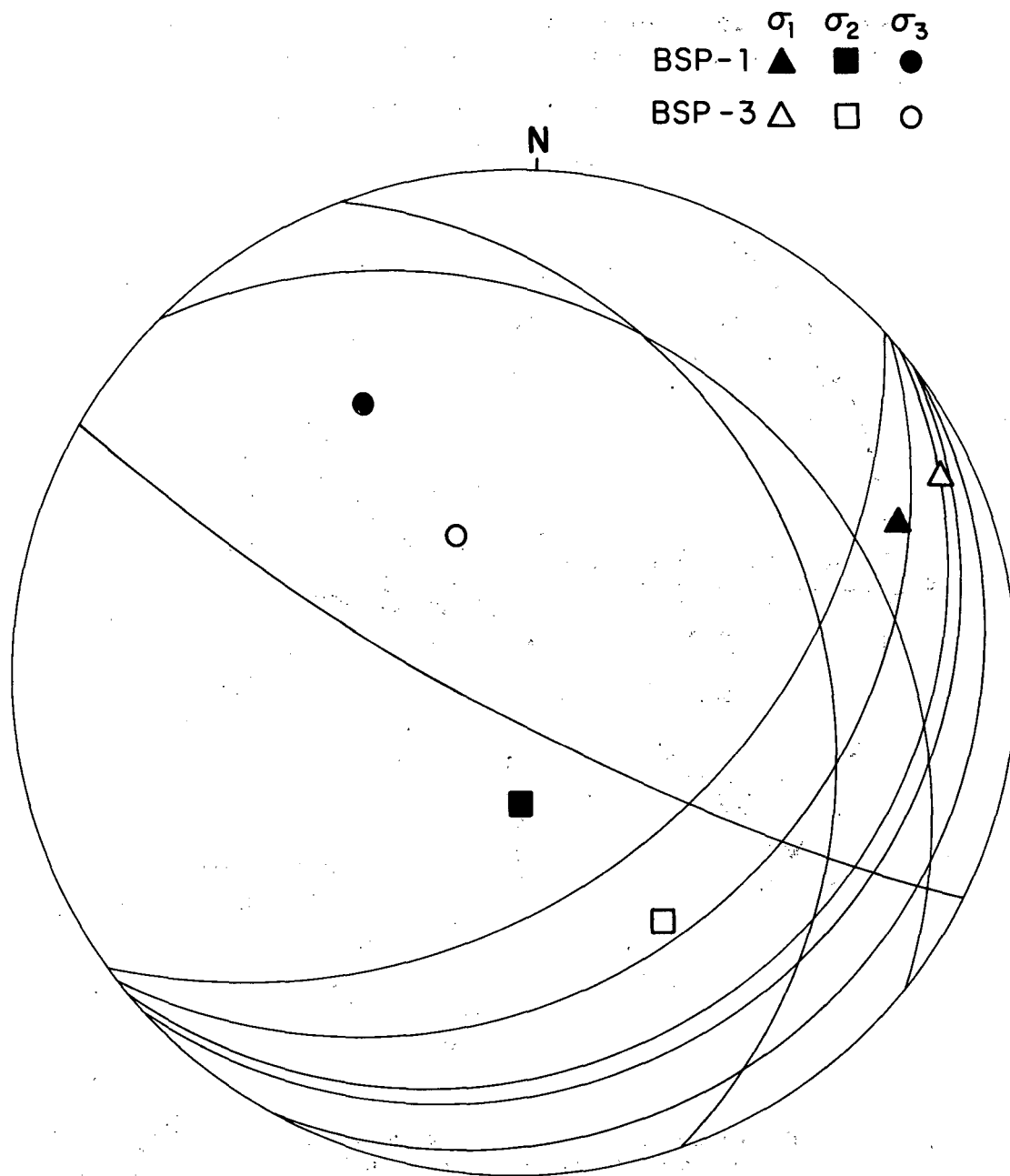
Fig. 4.21 Principal stresses measured in the full-scale and extensometer drifts. The filled symbols indicate results from overcoring from a vertical hole, BSP-1, drilled between the H9 and H10 heaters. The open symbols indicate results from overcoring in a horizontal hole, BSP-3. The lines represent stereographic projection of planes of hydro-fractures in a horizontal borehole BSP-2, also drilled from the extensometer drift between the H9 and H10 experiments. After Doe (1982).
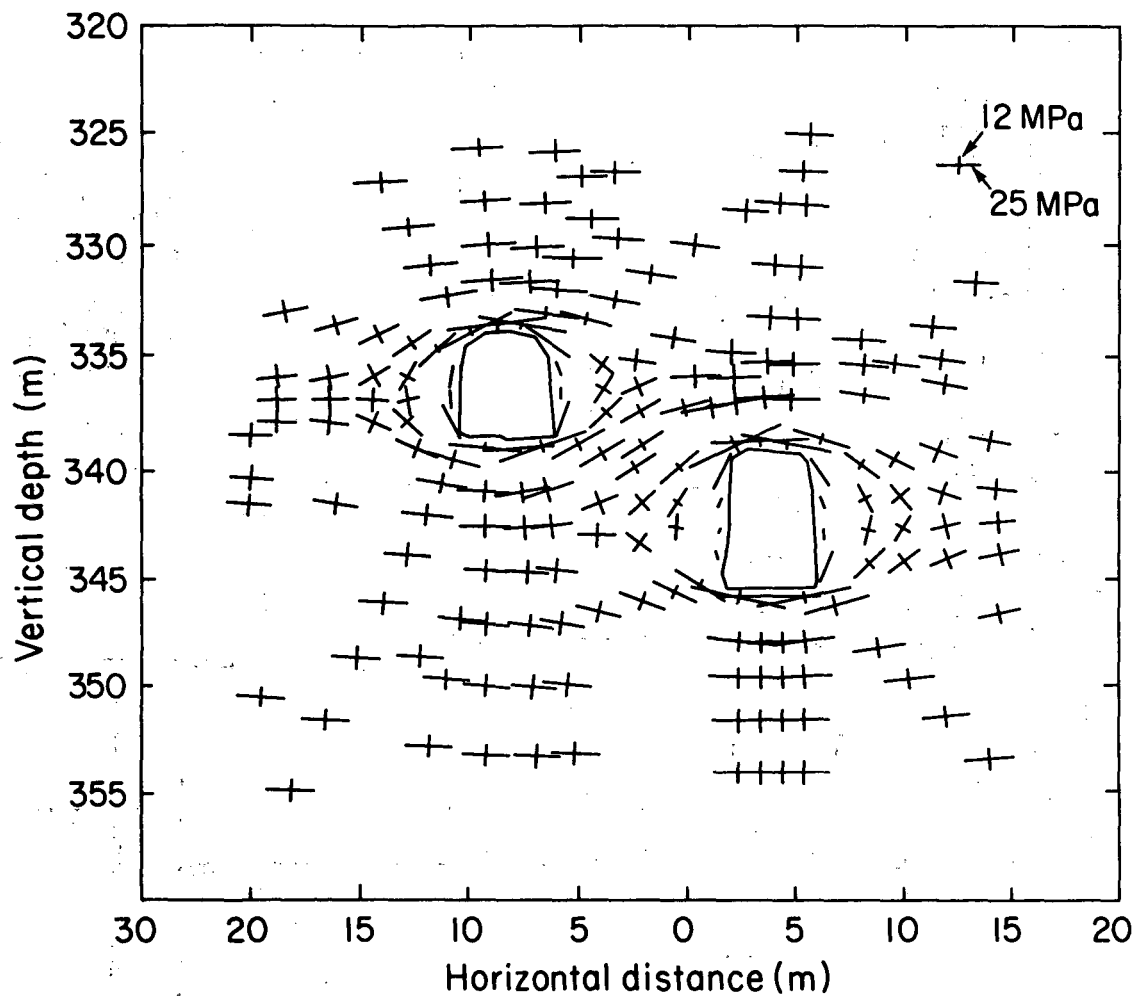
XBL 821-1612

Fig. 4.22 Principal stress distribution around full-scale and extensometer drifts as calculated from far field stress measurements, after Chan (personal communication).
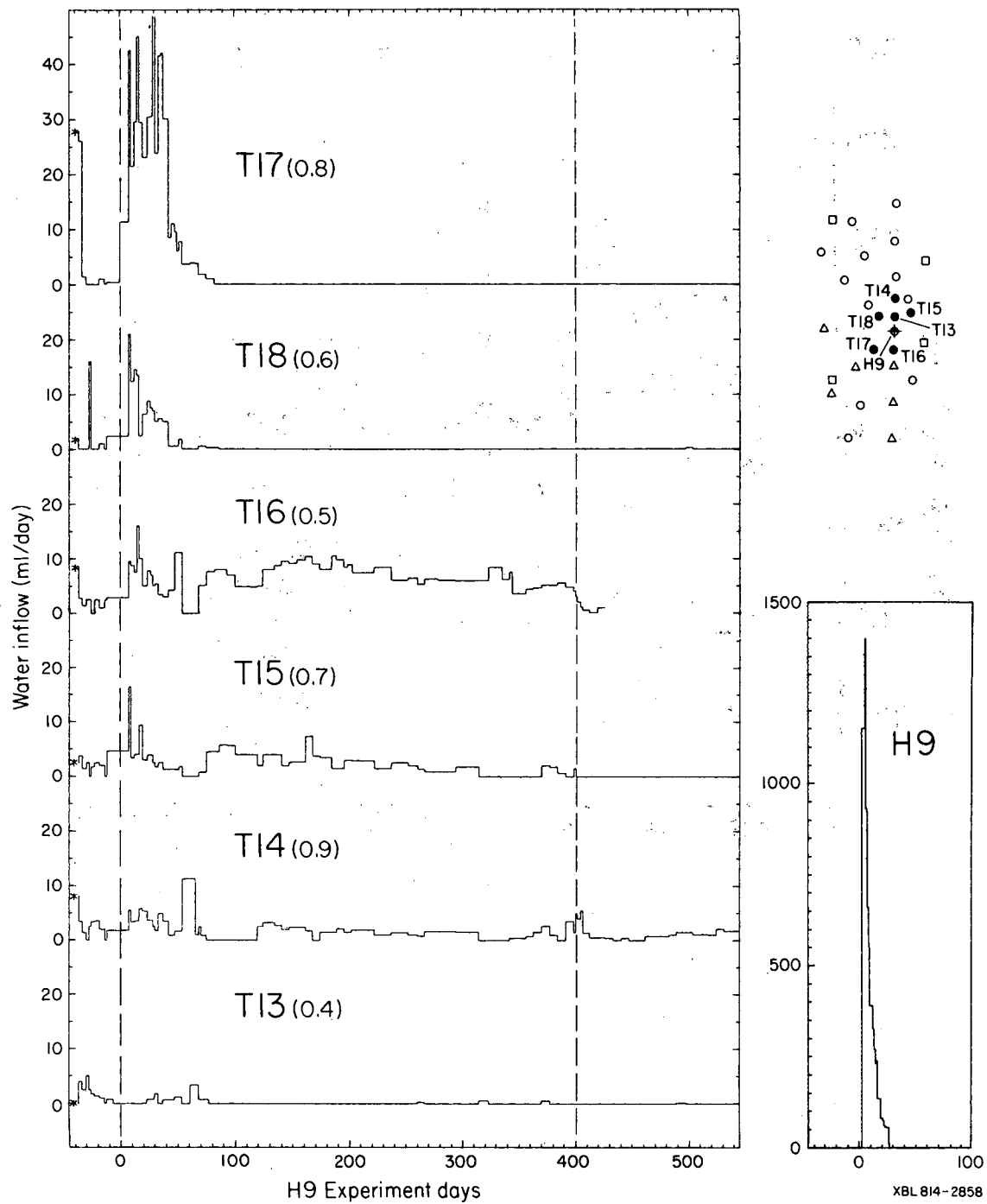
Fig. 4.23 Water inflow record for H9 and associated T-holes. The increase in the inflow of water is seen in most of the boreholes. The inflow of water in the H9 heater borehole indicate fracture closure after the turn-on of the heater. Also shown is a map with the position of the boreholes in this figure. (after Nelson et al. 1981)
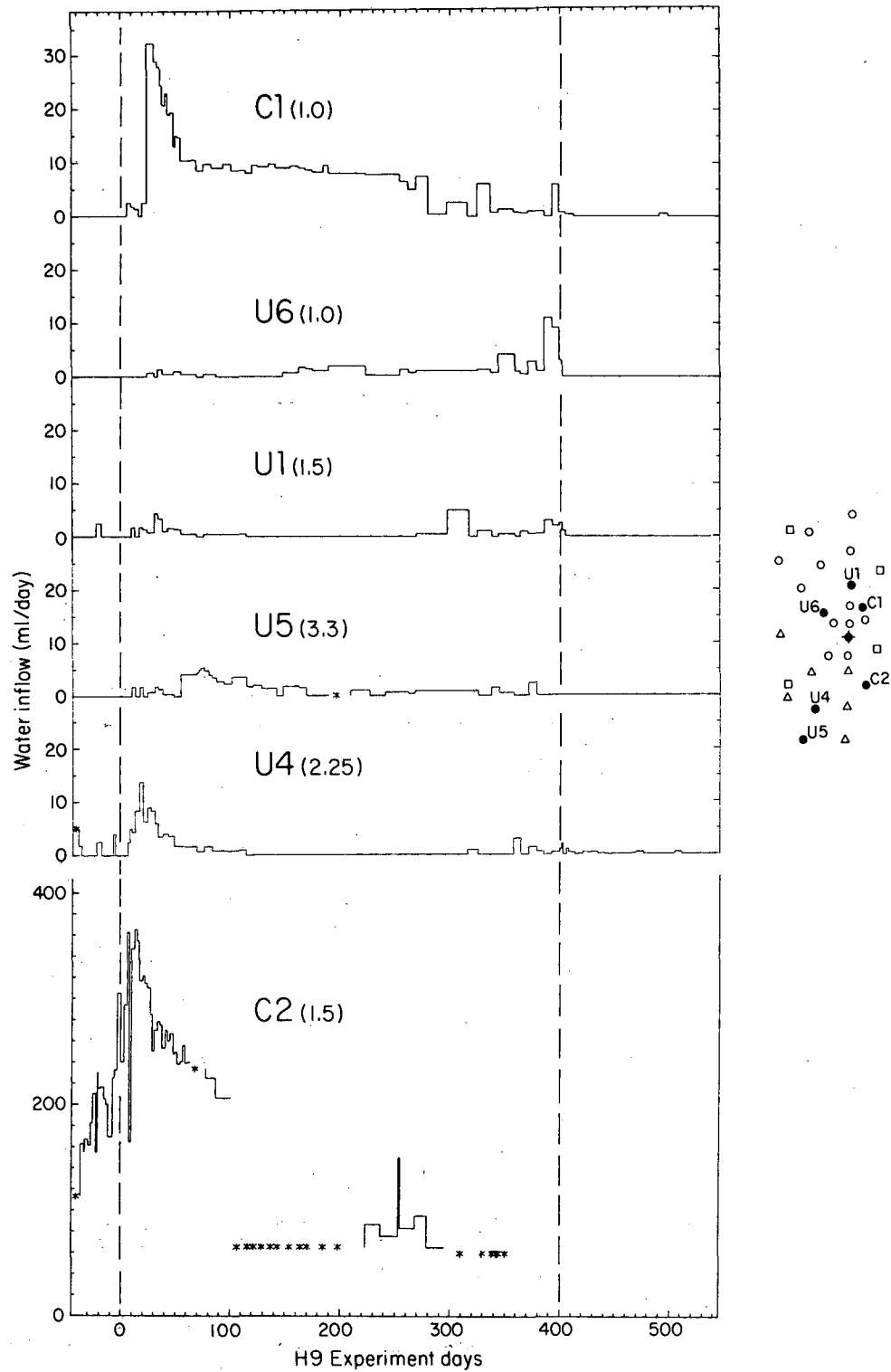
Fig. 4.24 Water inflow record for H9 area U- and C-holes. The water flow increase after the turn-on of the H9 heater at day 0, is seen in most of the boreholes in this figure. Also seen is the gradual decrease of inflow of water in the C1 and C2 boreholes. The map on the right hand side of the figure shows the position of the boreholes in the figure. (after Nelson et al. 1981)
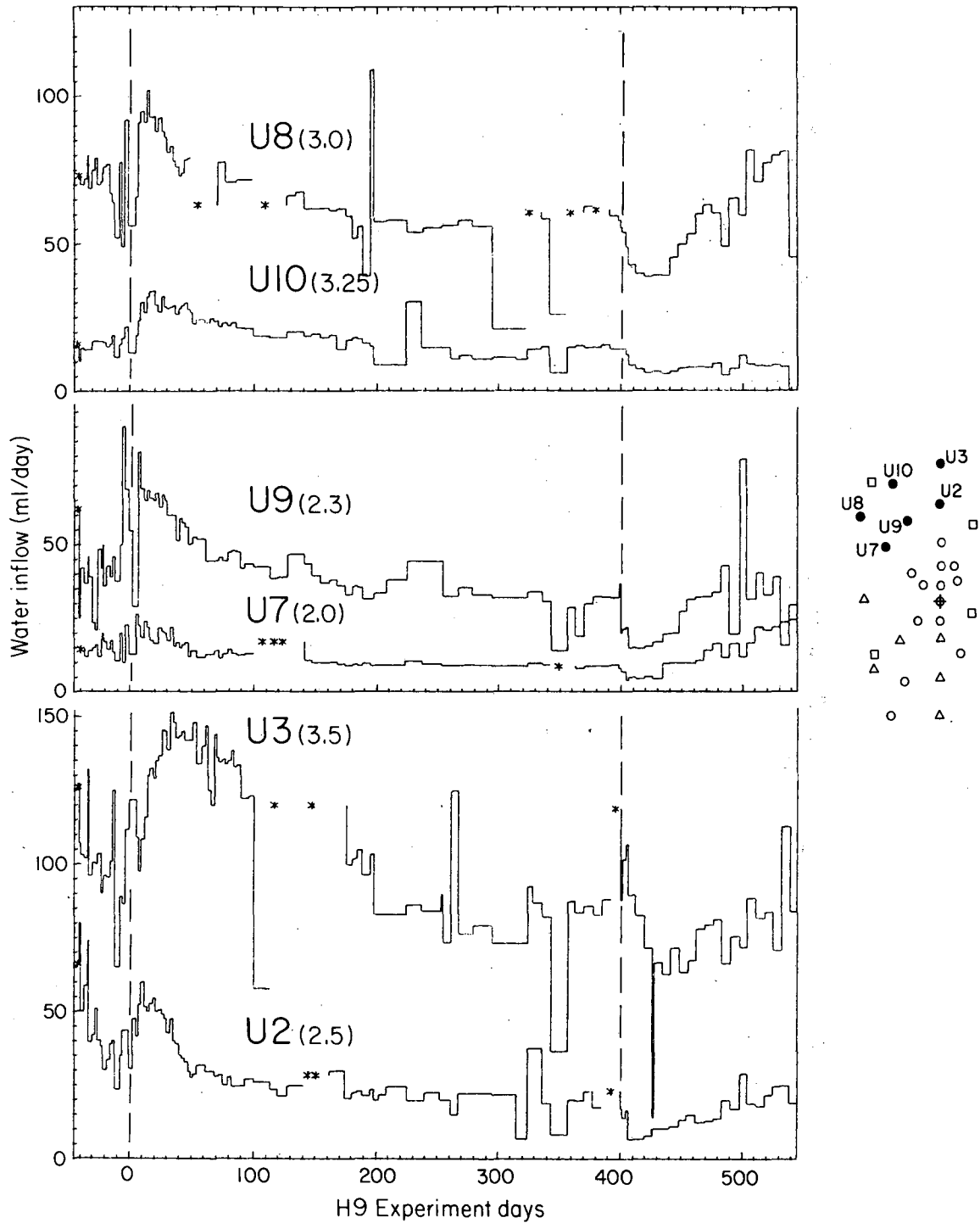
XBL 814-2860

Fig. 4.25 Water inflow record for H9 area U-holes This shows the high water inflow into boreholes situated in the back of the full-scale drift. A general trend in most of the boreholes is a gradual decrease of the water inflow with time. The initial increase of the water into the boreholes after the H9 heater was turned on is not so obvious in these boreholes. The stars indicate no data. The dotted line indicate the turn-on and turn-off dates for the H9 heater. On the right hand side is the map of the boreholes discussed in this figure. (after Nelson et al. 1981)
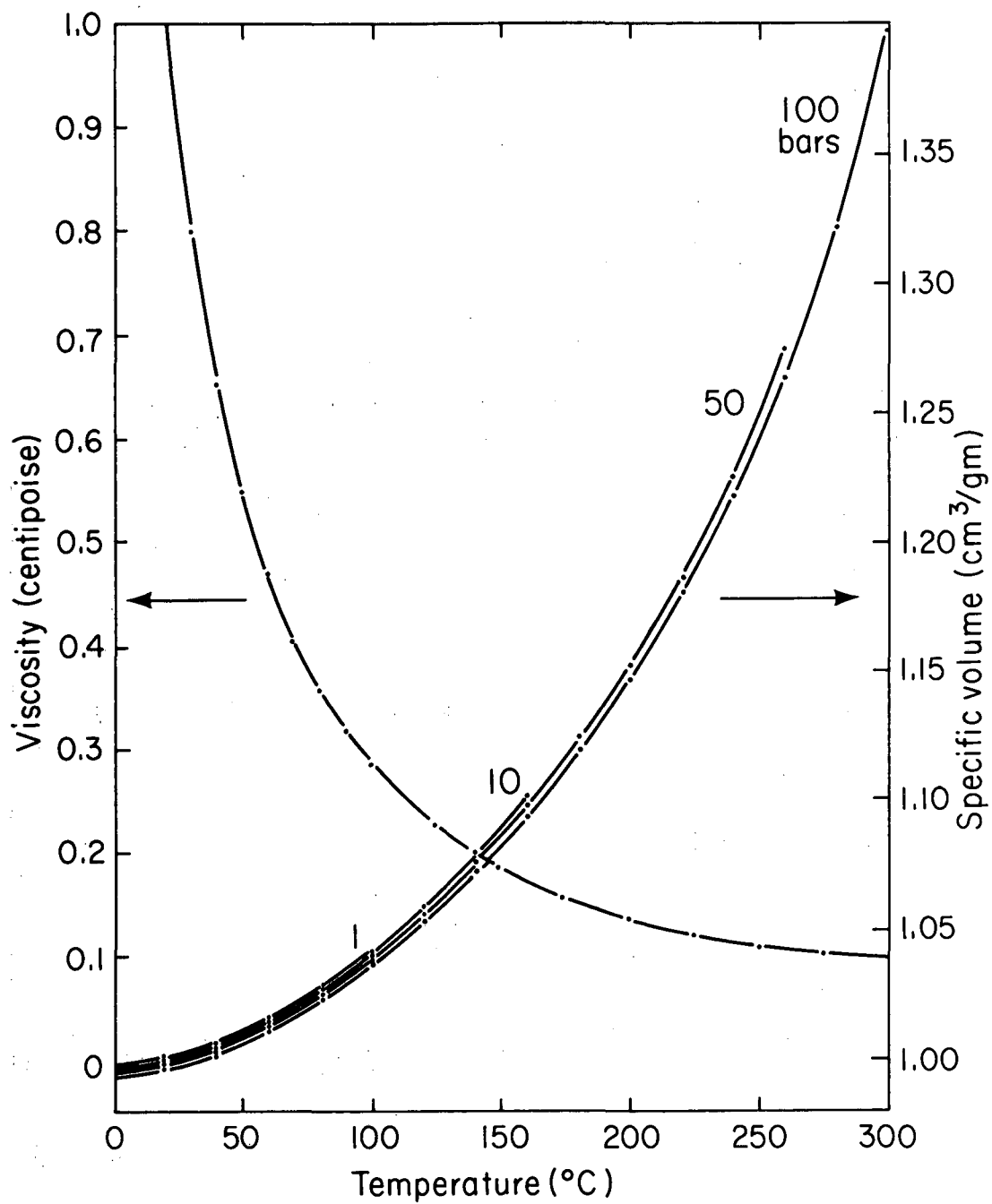
Fig. 4.26 Viscosity and specific volume of water as a function of temperature. Viscosity data from Dorsey (1940). Specific volume data from Kennedy and Holster (1966), for four values of pressure (10 bars = 1 MPa).

XBL 814-2881
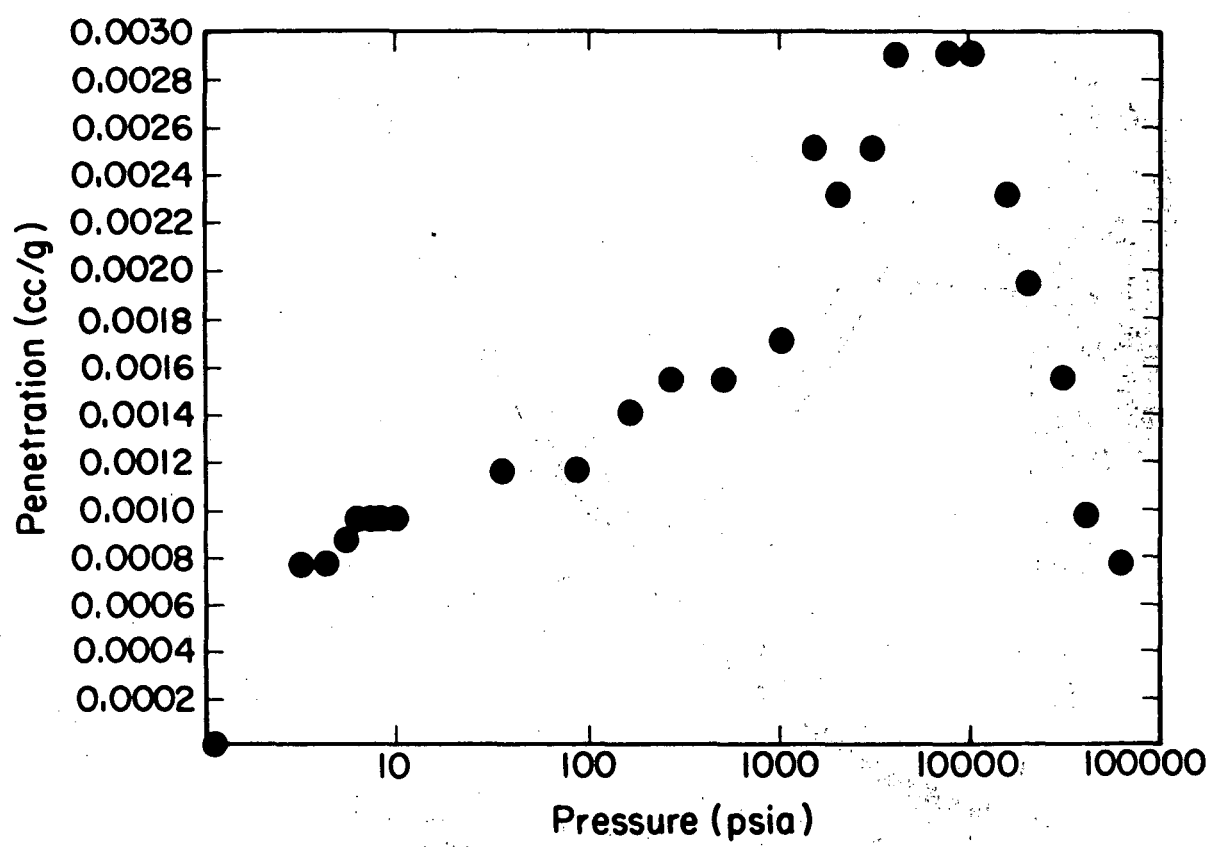
Fig. 4.27 Porosity and fracture aperture determination with a 60 kpsi mercury porosimeter

5. TRAVELTIME VARIATION

Introduction

Elastic wave velocities have been viewed as a potential means to monitor physical changes in a rock mass. In this section results from a cross-hole field study will be presented. The work is divided into three sections; In the monitor mode, data are collected frequently at the level of the heater midplane to monitor changes with increasing time. In the survey mode the six cross-sections between the four boreholes are scanned starting at the top of the boreholes moving the transducers in equal incremental steps down to the bottom of the section. This is done several times over the course of the heater experiment to get information about the response of the rock at different depths. Finally, in the down-hole survey, both transmitter and receiver are in the same borehole 0.3 m apart. The result from the down-hole work will serve as a comparison with the cross-hole work.

One objective of this study was to investigate the potential of cross-hole velocity measurements as a means to extract information about the medium heterogeneity including fracture zones. A second objective was to investigate the sensitivity of velocities and attenuation of elastic waves to saturation, pore pressure and field stresses, as they change over the course of the experiment.

Discontinuities, both macroscopic and microscopic, are affected by the state of stress, insofar as fractures tend to close under increased normal stress. This leads not only to increases in wave velocities but also to decreases in the attenuation of seismic waves due to linear loss

mechanisms as discussed by Toksoz *et al.* (1979). The changes in attenuation will be discussed further in chapter 6.

The velocities are calculated from the travel-times corrected for the instrument delay and the calculated distances between the transducers. There are six cross-sections between the four M-boreholes. To facilitate treatment of the data from the different cross-sections, the latter have been labeled from A through F.

Cross-sections				
Label	Cross-section	Distance between boreholes	Profile Direction	Delay of waveforms
		[m]		[μs]
A	M7-M6	2.248	N52E	330
B	M7-M8	2.679	N62W	400
C	M8-M9	4.395	N51E	690
D	M6-M9	2.775	N16W	400
E	M8-M6	4.181	N89E	650
F	M7-M9	4.202	N14E	650

Table 5.1

The first "M-number" indicates the transmitter borehole and the second the receiver borehole. Delay of waveforms in Table 5.1 refer to the part of the signal from the trigger which is not digitized. This makes it possible to expand the part of the signal containing the P and S-waves.

5.1 Monitor Data

The monitoring was performed in the heater midplane depth. The transducers were left in place in pairs of boreholes for as long periods as possible. The monitor mode emphasised frequent sampling of data in time. Thus only a few lines (i.e A17, C17, E17 and F17) could be sampled. The four lines sampled are shown in Figure 3.1. The transmitters were placed in boreholes M7 and M8 and the receivers in boreholes M9 and M6.

5.1.1 P-wave velocities

Thermal effects

The results of monitoring the P-wave velocities in the heater midplane are shown in Figure 5.1. The S-wave velocities are shown in Figure 5.2. Immediately following the turn-on of the H9 heater, sharp increases of the P wave velocities were recorded. The velocities then increased more slowly until about day 150 after the heater turn-on, after which they remained fairly constant until the heater was turned off on day 398. The velocity increase in the heater midplane varies between 60 and 200 m/s for the four monitor lines.

When the H9 heater was turned off travel-times were closely monitored. The velocities decreased sharply to values below those that had been recorded before the heater was turned on. Over line M7-M9 the effect is particularly noticeable. It should be noted that this is the path which passes closest to the heater: the shortest distance between the heater borehole wall and the M7-M9 cross-section is 0.2 m. Over all four lines the velocity passes through a minimum between 50 to 200 days after the heater turn-off, and from then on the velocity increases

slightly.

During the initial stages, at approximately day 30, the P-wave velocity stopped increasing or reversed for a period of about 50 days on path M7-M6. A possible explanation for this behavior rests on the thermal expansion of the trapped water causing pore pressure to increase and thereby decreased the effective stress. This point will be further discussed in Chapter 8.

Upon turning off the heater on day 398 the travel-times for the compressional waves increased sharply. Along three of the four lines the travel-times of the compressional and transversal waves were longer after the heater experiment than values measured prior to heating. Figures 5.3 and 5.4 show the waveforms of the P-wave arrivals for the monitoring lines. For these figures the traces have been delayed by a fixed time which is given in Table 5.1. This was done to obtain a clear picture of the wavelet, given a fixed data window. The waves were digitized from the tape recorder, normalized to the peak amplitude, and plotted. In Figure 5.5 a) the P-waves from the reference line, Figure 3.1, are shown. In contrast to the monitor lines, each of the signals in the reference line are collected with transducers which were reset between each recording. The velocity change of the compressional waves for the reference line, Figure 5.1, can be seen in the shorter arrival times in Figure 5.5 a).

Dewatering effects

Dewatering of the rock mass was done on a daily basis by pumping the 18 38 mm boreholes around the H9 heater hole. The dewatering started 41 days prior to heater turn-on and continued through day 545. The amounts for the 38 mm holes are given in Figures 4.21 to 4.23 and in

Table 4.7. At the beginning of monitoring the four lines there are insufficient data to draw any conclusions about the effect of dewatering in the heater midplane. When the dewatering of the rock mass stops at day 545 the effect is monitored by the cross-hole signals. It was found that the P-wave velocities increased between 20-50 m/s in the different monitor lines after 150 days after the dewatering was terminated. Except for the line M7-M9 this effect is seen for all lines. The same effect is evident also for the S-wave velocities over the monitor lines. An explanation for the minimum velocity occurring 50 - 100 days after heater turn-off is as follows: when the heater was turned off thermal contraction caused fractures to open; because of the low permeability of the rock away from the heater, water did not re-enter until several months after the dewatering of the rock mass was terminated at day 545. In this model some of the rock around the H9 heater became partially saturated for a period lasting from a couple of months up to one year.

5.1.2 S-wave velocities

Thermal effects

The S-wave velocities in the four monitor lines and the reference line are shown in Figure 3.1 and the results are given in Figure 5.2. S-wave velocities also increased when the heater was turned on.

When the heater is turned off the S-wave velocities decreased in all four lines. In two of the lines, M8-M6 and M8-M9 the change was small and the S-wave velocities remained higher in these two lines after the heater experiment than prior. In Figure 5.5b the S-waveforms from the reference line are shown. The signal/noise ratio is not as good as for

the P-waves, but there are no problems recognizing the arrival of the S-waves.

Dewatering effects

The dewatering effect seen in the V_s from the monitor lines is a gradual increase of the velocities in three of the four lines after the dewatering was turned off. This indicates that also the S-wave velocities are sensitive to the water content in the rock mass.

5.2 Survey Data

The first surveys were performed 44 days before the heater was turned on. Dewatering of the rock mass commenced 41 days prior to heater turn-on, so the first surveys measured the rock mass before any appreciable volume of water had been drawn from it. Preheating data were collected over all six sections. The physical parameters affecting the velocities in this set of data were the degree of fracturing and the orientation of the profile under consideration. The degree of fracturing affects the stiffness of the rock and the direction of the cross-section determines the direction relative to the principal axes of stress. A key to the surveys and the survey numbering in the six cross-sections is given in Table 5.2. In Figure 5.6 the direction of the six cross-sections are indicated on a polar chart along with the major faults, dikes, and principal stresses. Figure 5.7-5.12 show the surveys in the six hole pairs.

5.2.1 P-wave velocities

Fracture effects

The six preheating surveys indicate that there are vertical velocity variations in all cross-sections. There seems to be a correlation between the size of the velocity anomaly and how close the cross-section passes the H9 heater, even though the power had had not yet been applied in H9. The two cross-sections which are most removed from the heater, M8-M9 and M6-M9, appear to have the smallest anomalies. The most likely reason for these anomalies , which are most visible at heater depth is a combination of drilling vibrations and weak fractures. During the drilling of the H9 heater a XF 60/90 drill-rig was used for the first three meters as reported by Paulsson *et al.* (1981). The XF 60/90 drill-rig did not provide the capacity to diamond drill a 406 mm borehole in a satisfactory manner. Drilling stopped and a high torque Toram drill-rig was used for the remaining depth of the borehole. Drilling with the XF 60/90 drill-rig was accompanied by severe vibrations between 1 and 3 m depth below the drift floor. These vibrations probably effected the calcite fractures in the vicinity of the boreholes. Figures 2.5 to 2.10 in Chapter 2 indicate the calcite fractures found in the boreholes. The calcite fractures at depths between 1 and 5 m correlate well with low velocity zones. From Paulsson *et al.* (1981) it is clear that the calcite fractures display a much lower strength than fractures with other infilling materials. At other depths there is a less marked but still apparent correlation between the presence of calcite fractures and low velocities.

In cross-section M7-M6, shown in Figure 2.5, the calcite fractures between the boreholes extend from a depth below the drift floor of 2.25

	Survey # and dates for surveys in the six cross-sections			
Label	Cross-section	#	Day #	Date
A	M7-M6	1	-44	11 July, 1978
		2	344	3 August, 1979
		3	424	22 October, 1979
		4	701	25 August, 1980
B	M7-M8	1	-44	13 July, 1978
		2	112	14-15 December, 1978
		3	348	7 August, 1979
		4	456	23 October, 1979
		5	708	1 August, 1980
C	M8-M9	1	-42	13 July, 1978
		2	118	20 December, 1978
		3	343	2 August, 1979
		4	425	23 October, 1979
		5	711	4-5 August, 1980
D	M6-M9	1	-24	13 July, 1978
		2	119	21 December, 1978
		3	343	2 August, 1979
		4	426	24 October, 1979
		5	710	3-4 August, 1980
E	M8-M6	1	-44	11 July, 1978
		2	-7	17 August, 1978
		3	6	30 August, 1978
		4	15	8 September, 1978
		5	20	13-14 September, 1978
		6	111	13 December, 1978
		7	118	20 December, 1978
		8	341	31 July, 1979
		9	420	18 October, 1979
		10	704	28 July, 1980
F	M7-M9	1	-43	12 July, 1978
		2	0	23-24 August, 1978
		3	6	30 August, 1978
		4	13	7 September, 1978
		5	20	14 September, 1978
		6	111	13 December, 1978
		7	132	3 January, 1979
		8	133	4 January, 1979
		9	349	8 August, 1979
		10	419	17 October, 1979
		11	707	30 July, 1980

Table 5.2

m to approximately 6.25 m. Between these depths also is found the low velocity zone shown in Figure 5.7. In the same figure there is a low velocity zone at depth of 9.25 m. In Figure 2.5 it is shown that there are some calcite fractures in that particular zone. In Figure 5.8 the low velocity zone in cross-section M7-M8 is apparent between depths of 2.25 m and 5.75 m. In Figure 2.6 it is apparent that there are many calcite fractures in this zone. The largest cluster is found at 3.25 m below the floor of the drift, where also the lowest P-wave velocities are found. Also in this cross-section there is a small but noticeable low velocity zone in a zone around a depth of 9.25 m.

In Figure 5.9 line M8-M9 has the lowest velocities occurring from a depth of 8.25 m to the maximum depth of the cross-section. There are some calcite fractures over this depth interval but what is interesting is that the calcite fractures occurring at 3.25 m do not result in any low P-wave velocities.

Over line M6-M9 the lowest velocities occur at 5.25 below the drift floor as shown in Figure 5.10. Again there are some calcite fractures present but no clear correlation. Line M6-M9 is more than 2 m from the center of the heater. Line M8-M9 is 1.7 m from the center of the H9 heater-hole.

In Figure 5.11 the P-wave velocities over one of the main cross-sections are shown. The M8-M6 cross-section is the one for which most of the data have been collected. The low velocity zone between 1.25 m and 4.25 m below the drift floor is well-correlated with an abundance of calcite fractures. There are some calcite fractures outside this zone, but they have no corresponding low-velocity zone associated with them. This tends to confirm the theory that the weak calcite fractures were

disturbed by drilling using the first drill rig.

Finally cross-section M7-M9 shows a broad low velocity zone between depth of 1.25 m and 6.25 m. This again is associated with calcite fractures. Other zones with calcite fractures do occur, but except at z = 9.25 m there is no low velocity zone associated with them.

Thermal effects

When then H9 heater was turned on, the velocities increased over all 6 cross-sections above and below as well as at the same depth as the heater. In Figures 5.7 to 5.12 this is clearly shown.

M7-M6

In Figure 5.7 for line M7-M6 only one survey was performed during the time the heater was turned on, i.e. the 344 day curve. The two curves for day 424 and 701 indicate a zone around level A13 which has lower velocities after the experiment than prior to it. In Figure 4.3 it can be seen that the highest temperature occurring over this line was $60°C$. It appear that this temperature was sufficiently high to further disturb the fractures over this cross-section, beyond the apparent effect of drilling. However the effect is reversed below line A17.

M7-M8

In Figure 5.8 for line M7-M8 two surveys were performed during the time the heater was turned on, i.e. on days 112 and 348. The curve for day 348 indicates a slight increase in velocity across the heater beyond that seen for day 112. This is expected as the thermal stresses are highest at these levels. Also over this cross-section lower velocities were

observed at level B13 after the heater experiment than before. Again, the effect is reversed below B17. In Figure 2.6 one can see that at this level there are a cluster of calcite fractures.

Cross-section M8-M9, shown in Figure 5.9, with the closest point to the center of the H9 heater at 1.7 m, indicates very little change is caused by heating. The maximum P-wave velocity change is 80 m/s in line C13. Over cross-section M8-M9 the maximum temperature change is $35^{\circ}C$, as seen in Figure 4.5. The change in velocity is only slightly larger at the depth of the heater than at other depths.

M6-M9

Cross section M6-M9 shown in Figure 5.10 is never closer to the center of the H9 heater than 2.1 m. The change in temperature over section M6-M9 is a maximum of $25^{\circ}C$, as seen in Figure 4.6. The largest P-wave velocity change is 160 m/s in line D13. Except for this line the largest changes are found in the heater midplane. The large change seen in line D13 is only seen in one reading and the reason is not clear.

M8-M6

Cross-section M8-M6, seen in Figure 5.11, offers an interesting study of P-wave velocities as a function of changes in temperature. Over this cross-section four surveys were performed while the H9 heater was turned on. Surveys were performed at days 20, 111, 118 and 341 after heater turn-on. The velocities were observed to increase over the whole time span. The difference between day 118 and 341 is small but noticeable. Especially evident is the high P-wave velocity caused by the high temperature between depth E13 and E25. The first post heater turn-off

survey at day 420, 22 days after the turn off of the H9 heater, shows how sharply the velocities decrease. This behavior in fact mirrors the very rapid decrease in temperature observed around the H9 heater, shown in Figures 4.1 and 4.2. The last survey, which was performed at day 704, shows the low velocity zone between depths E9 and E17, with the largest P-wave velocity change at line 13. The maximum temperature adjacent to the heaters was naturally at the midplane, but it is significant that the largest velocity change of 260 m/s occurred in a zone with calcite fractures. This indicates that comparatively low temperatures, in this case 60° C, at depth E13, are required to cause permanent damage where clusters of calcite fractures occur.

M7-M9

The last cross-section is the M7-M9 section, shown in Figure 5.12. This is the section which comes closest to the H9 heater. At the closest point the cross-section is only 0.2 meter from the H9 borehole wall. This fact is also reflected in the high temperature occurring at the closest point, shown in Figure 4.8. In this figure it is seen that the temperature reached almost $130^o C$. Four surveys were performed over this cross-section during the period the H9 heater was turned on. The surveys were performed at days 13, 20, 111 and 349. The same pattern as for the section M8-M6 is observed. The velocities increase in this section over the entire heating period with the highest velocities being found in the survey at day 349. The largest velocity change due to heating was 290 m/s in this section. When the heater was turned off at day 398, a rapid decrease was found in this section. The velocity decreased faster in this section than for the other sections discussed. At depth F16 a very low

velocity is observed. A likely reason is that the fractures in this line open and become partially saturated when the heater is turned off. The last survey at day 707 shows that between F6 and F19 the post-heating velocities are found to be lower compared with the pre-heating survey. Again, the effect is reversed below F19.

In Figure 5.13 the waveforms from surveys # 8 and # 10 (see Table 5.2) from cross-section M8-M6 are shown. These figures are included to illustrate the effect of turning off the heater on arrival times for P-waves. In Figure 5.14 the waveforms from surveys # 9 and # 11 are shown for cross-section M7-M9. In Appendix C:4 the waveforms for the other surveys in these two as well as the other four cross-sections are shown.

There is still some uncertainty about the magnitude of the stresses around the H9 heater, due to the temperature dependence on moduli and thermal expansion coefficient, as shown in Figure 4.9. The temperatures are easier to predict and it is temperature changes which are causing the expansion of the rock and subsequent narrowing of cracks and increase in stresses. It was therefore considered to be less ambiguous to plot the change of velocity as a function of the change in temperature. This was done for the velocity data collected around day 340, which was the last survey performed before the H9 heater was turned off. Data collected 7 days before H9 heater turn-on in section M8-M6 were used as reference data and the data collected 43 days before heater turn-on in section M7-M9 were used as reference data for that cross-section. For the other cross-sections the data obtained around day -40 was utilized as reference data for the analysis. The change of velocity was plotted as a function of the change in mean temperature

for every second depth, starting with depth 3 for all the cross-sections. The first point plotted is a low temperature - low velocity point. The largest change is found for depths near the heater midplane. Below the midplane the temperatures changes and velocity changes become gradually smaller again. The change in velocity with temperature varies significantly with direction of the particular cross-section. The higher the field stress in the direction of the particular cross-section the smaller is the change of velocity with temperature.

It should be noted that cross-sections M8-M9 and M6-M9 have small temperature changes and a small number of data points; for these two cross-sections only every fourth depth was used. A statistical analysis was run on the resulting plots to see if the differences for the six cross-sections was statistically significant. The results are given in Table 5.3

Temperature - Velocity function							
Line	Corr-elation	Inter-cept	Standard error of Intercept	Regress. Coeff. (slope) $[\frac{m}{s}/^{\circ}C]$	Standard error	$\overline{V_p}$ at non-of reg. coeff.	$V_{p\,(max)}$ anomaly zones
M7-M6(A)	0.77	17.9	38.8	3.05	0.63	5872	5938
M7-M8(B)	0.81	5.6	46.3	4.00	0.71	5951	5979
M8-M9(C)	0.69	41.9	10.4	1.22	0.48	5855	5888
M6-M9(D)	0.77	39.7	14.6	2.86	0.89	5847	5901
M8-M6(E)	0.80	22.2	24.1	1.95	0.37	5955	5970
M7-M9(F)	0.93	7.7	19.7	3.26	0.31	5907	5932

Table 5.3

The data and the results from the linear regression are shown in Figure 5.15 for cross-sections M7-M6 and M7-M8. In Figure 5.16 the result are given for cross-sections M8-M9 and M6-M9, and finally the results from cross-sections M8-M6 and M7-M9 are given in Figure 5.17. An interpretation of the data in the Table 5.3 is shown in Figure 5.18. In this figure the inverse slope $(^{o}C/m/s)$ ot te line form the linear regression and the average velocity of zones outside the anomaly zones are shown. For both these quantities there is a maximum occurring in the direction of the cross-section M8-M6(E). The result of the cross section M8-M9 was not considered because of the small temperature increase. The effect from the temperature was masked by the effect of closing fractures caused by the dewatering (more about this later).

Fehler (1981) reported a decrease in the P-wave velocity of 1.07 km/s for a decrease in temperature of 100° C (11 m/s $/^{o}C$). This may to be compared with the results in Table 5.3, where the results for cross-sections A, B, E and F in the full scale drift ranges from 1 to 4 $m/s/^{o}C$ for a maximum change in temperature of about 60° C. Fehler concludes that the compressional velocity changes linearly with temperature. This agrees well with the result in this study. The difference in fracturing, both macroscopic and microscopic, is the most likely reason for the factor of difference in the slope values obtained in the two granitic rocks. In addition, the higher the field stresses, the smaller effect one gets from an increase in the temperature.

The linear coefficient of thermal expansion is approximately $10^{-5}/C^{o}$. Using the average temperature increase in the line M8-M6 at day 398, which is 56°, a total thermal expansion of 2.34 mm over the 4.2 m path is obtained. The closure of water filled fractures caused by the

dewatering over the 4.2 m path between the M8 and M6 boreholes amounts to 9.9 mm . This is interesting insofar that a decreased pore pressure should have a larger impact on fracture closure than thermal expansion.

Thermal effect on the pore fluid

The total fracture porosity in cross-section M8-M6 is given in Table 5.4 as 1.45 %. The part of the path of 4.18 m which is occupied by water is thus 60.8 mm. Using the linear thermal coefficient of expansion of $1.7\times10^{-4}C^{-1}$ and the average temperature increase of $56^{\circ}C$ a thermal expansion of the water in this line is found to be 0.6 mm. This should be compared with the thermal expansion of the rock which was found to be 2.34 mm. A cylinder 1 m thick and with a radius of 2.3 m, which is the distance from the heater borehole to the M8 borehole, has a total pore-volume of 0.25 m^3. With a cubic thermal expansion coefficient of the fluid of $5\times10^{-4}C^{-1}$ obtained from Table 8.2, an increase in the volume of the pore fluid of 7×10^{-3} $msu3$ is found. This volume increase in the pore fluid would tend to increase the saturation in fractures which are not fully saturated.

Dewatering effects

Over two of the cross-sections, M8-M6(E) and M7-M(F) two surveys were performed before the heater was turned on. For cross-section M8-M6 they were performed 44 and 7 days before heater turn-on; for cross-section M7-M9, 43 days before and on the day the heater was turned on. In Figures 5.11 and 5.12 only one of the preheating surveys is plotted, but the data are provided in Appendix C:3 and the waveforms are shown

in Appendix C:4. The zone which is outside the low velocity area is found below 5.25 m under the surface of the drift. Taking the difference of the P-wave velocities obtained during the two preheating surveys below the depth of 5.25 m it should prove possible to extract the influence of dewatering on the rock mass. When the rock mass is dewatered, the pore pressure due to the constant seepage of water into the boreholes is decreasing to some lower value. In effect a low pore pressure zone around the boreholes is being created. The pore pressure in the rock mass can be as high as 1.75 MPa, as indicated by Forster and Gale (1981). Continually removing water from the boreholes causes the pore pressure to decrease slowly; the result is that the fractures close which had previously been held open by the pore pressure. The closure of these fractures can be calculated. The intrinsic velocity of the Stripa quartz monzonite is given in Table 8.1, in which the P-wave velocity is a volume average of the calculated averages for aggregates based on Voight and Reuss limits. The value shown is a room temperature value. The intrinsic velocity V_i = 6194 m/s. The averages have been calculated using velocities at a depth of 5.25 m and below. This zone in the cross-section is the one least influenced by heating. The measured velocity V_m is given by:

$$V_m = \frac{d_t}{(t_r + t_w)}$$ [5.1]

where t_r is the travel-time in the rock and t_w is the traveltime in water, and d_t is the total distance between the boreholes. The travel-times in the rock and water respectively are given by:

$$t_r = \frac{(d_t - d_w)}{V_i}$$ [5.2]

and

$$t_w = \frac{d_w}{V_w} \tag{5.3}$$

so the following gives the travel-path in water d_w of the total travel-path d_t:

$$d_w = \frac{1}{V_i - V_w} \left[\frac{V_i d_t V_w}{V_m} - V_w d_t \right] \tag{5.4}$$

Using the parameters shown in column 3 - 5 in Table 5.4 the result is given in column 6 and 7. In column 8 the total fracture porosity is given and in column 9 the effective fracture porosity is shown.

Cross-section	Day	V_m	d_t	V_w	d_w	∇d_w	$\frac{d_w}{d_t} * 100$	$\nabla \frac{d_w}{d_t} * 100$
		[m/s]	[m]	[m/s]	[mm]	[mm]	[%]	[%]
[1]	[2]	[3]	[4]	[5]	[6]	[7]	[8]	[9]
M8-M6	-44	5920	4.181	1480	60.8	-	1.45	-
M8-M6	-7	5936	4.181	1480	57.1	3.7	1.37	0.08
M8-M6	420	5963	4.181	1480	50.9	9.9	1.22	0.23
M7-M9	-43	5889	4.202	1480	68.3	-	1.63	-
M7-M9	0	5906	4.202	1480	64.3	4.0	1.53	0.10
M7-M9	419	5917	4.202	1480	61.8	6.5	1.47	0.16

V_p and fracture porosity for H9 area

Table 5.4

Gale *et al.* (1982) describes a new procedure developed to determine the fracture porosity at the Stripa site. Gale *et al.* suggested the value 0.1 % as a mean total effective fracture porosity. The effective porosity over the two lines M8-M6 and M7-M9 is given in Table 5.4 as 0.23

and 0.16 % respectively. It is also suggested in their paper that a 2.5 m thick layer of lower permeability exists around the mine openings. This finding agrees with the result obtained by Lytle *et al.* (1979) using an electromagnetic tomography technique. Forster and Gale (1981) conclude that the presence of adjacent boreholes has a large influence on the pore pressure existing around a borehole. If the borehole affects the pore pressure measured from an adjacent borehole, it is reasonable to assume it would affect the pore pressure without the second borehole.

An interesting phenomenon observed over the cross-sections M8-M9 and M6-M9 is that the velocities were observed to increase uniformly over the entire depth range. It has been seen in cross-sections which pass close to the heater that the velocity increase is confined to levels between 1 m above the top and 1 m below the bottom of the heater. That would indicate that this velocity increase is related to the dewatering of the rock mass. This indicates that the dewatering process influences the velocity more than the thermal process at a distance of approximately 2 m from the heater centerline. The change in the fracture porosity in the M8-M6 and M7-M9 lines are both found to be approximately 0.2 %, Table 5.4. The volume around the H9 area which is affected by dewatering is approximately 5×5×10 m. With a volume of $250m^3$ and a change of the fracture porosity of 0.2 % one obtain a change in fracture volume of 0.5 m^3. The water volume recovered in the M-holes is shown in Table 4.6 and and the water inflow in the U, C and T holes in the H9 area are given in Table 4.7. The total amount of water recovered is 0.4 m^3 which is close to the change in the calculated change in the fracture volume. The inflow of water in the boreholes can therefore be explained by the change in porosity without any

contribution of water outside this volume. The water inflow in the boreholes, Figures 4.21 - 4.23 indicate that in most cases the flow decrease with time. This tends to confirm the conclusion that the fractures in the area are closing.

Over cross-section M8-M9 the maximum temperature change is $35°C$ (Figure 4.5). The change in velocity is slightly larger at the depth of the heater than at other depths. Employing similar calculations as those used for cross-sections M8-M6 and M7-M9 previously, the total thickness of the water filled fractures is found to be 79.9 mm for survey # 1 and 65.8 mm for survey # 2. This represents a directional porosity of 1.82 % and 1.50 % respectively. The closure of the fractures is found to be 14.1 mm, or a change in porosity of 0.32 %.

The change in temperature over section M6-M9 is a maximum of $25°C$. The change in the heater midplane is slightly larger than in other parts of the cross-section, but the changes ae of the same magnitude. There must be another process than the thermal which influences the velocities in this section. Using the same reasoning as before it is found that for survey # 1 for all velocities there is an average of 52 mm water filled fractures. For the survey # 2 at day 119, Table 5.2, there is and average of 40 mm water filled fractures. This means that over this cross-section the fractures have closed on the average 12 mm. The directional porosity has changed from 1.86 % to 1.43 %, a not unreasonable value considering that a homogeneous core specimen without macroscopic fractures was found to have 0.9 % porosity. Furthermore, the two cross-sections M8-M9 and M6-M9 have path lengths of 4.4 and 2.8 m respectively; it is significant that despite a difference of a factor of two in the distance between the two boreholes over the cross-sections,

the porosities calculated are of the same magnitude.

In section M7-M9 there is a section where the velocities do not get back to the values recorded prior to the heater experiment. It is possible that some locking mechanism prevented the opening of these fractures. A possible mechanism might be an unfavorable fracture orientation, or that the fractures which expanded above the heater midplane did this at the expense of some fractures below the heater midplane.

5.3   Down-hole data

The limited down-hole work performed is important insofar that it provides the velocities in the immediate vicinity of the monitor boreholes. In Figure 5.19 an example of a recorded waveform is shown. Also indicated in the figure are the P and S-wave arrivals. In Figures 5.20 and 5.21 the compressional wave velocities are plotted for the four M-boreholes. Note the low velocities found in the boreholes M7 and M6 which are the closest to the H9 heater. In boreholes M8 and M9 there are a couple of interesting features. In both boreholes the velocities decrease near the drift. In borehole M9 there is a low velocity zone at a depth of between 4 and 5 m. There is a cluster of calcite fractures at this level, which is the most likely reason for these low velocities at this level. In Figures 5.22 and 5.23 the S-wave velocities are shown, but these do not show the same character as the P-waves. Lockner *et al.* (1977) showed that the effect of fractures on S-waves depended strongly on the orientation between the fractures and the polarization of the S-wave. In Figures 5.24 and 5.25 the Ratio $\left[\dfrac{V_p}{V_s}\right]$ as function of depth is shown. Considerable interest has been shown for the diagnostic ability of this ratio,

as indicated by Hadley (1976). Bonner (1975) and Anderson *et al.* (1974) showed that P-wave velocities are much more affected by a high aspect ratio fracture than S-waves when the seismic waves are propagated parallel to the normal of the fracture. The down-hole instrument propagates P and S-waves parallel to the borehole which is vertical. This would indicate that the fracture system which causes the low $\left[\frac{V_p}{V_s}\right]$ zone between 2 and 4 meters below the drift of the floor is horizontal. Hadley (1975) concludes that opening of dry cracks produces large changes in $\left[\frac{V_p}{V_s}\right]$, in fact larger than any other mechanism and this point to that the fractures in this zone would be less than fully saturated.

Summary

It has been shown in this chapter how ultrasonic P and S wave velocities can be used to monitor the effect of thermal and dewatering processes. The P-wave velocity was found to be a linear function of spatially distributed temperatures. A statistically significant difference of the function between temperature increases and P-wave velocity increases for different transmission directions was found. It was shown that the P-wave velocity in part can be explained by the thermal expansion of the rock combined with the thermal expansion of the pore fluids as well as a narrowing of fractures due to an elastic response when the pore pressure is changed. The survey data show how well a low velocity zone removed from both instrument holes can be found with a cross-hole technique. The surveys also provided data for an estimate of the total and connected porosities in different directions. The down-hole data provided information about the rock in the vicinity of the M-holes.

The inferred damage of the rock around the H9 heater hole was confirmed by the down-hole results from the M7 borehole.
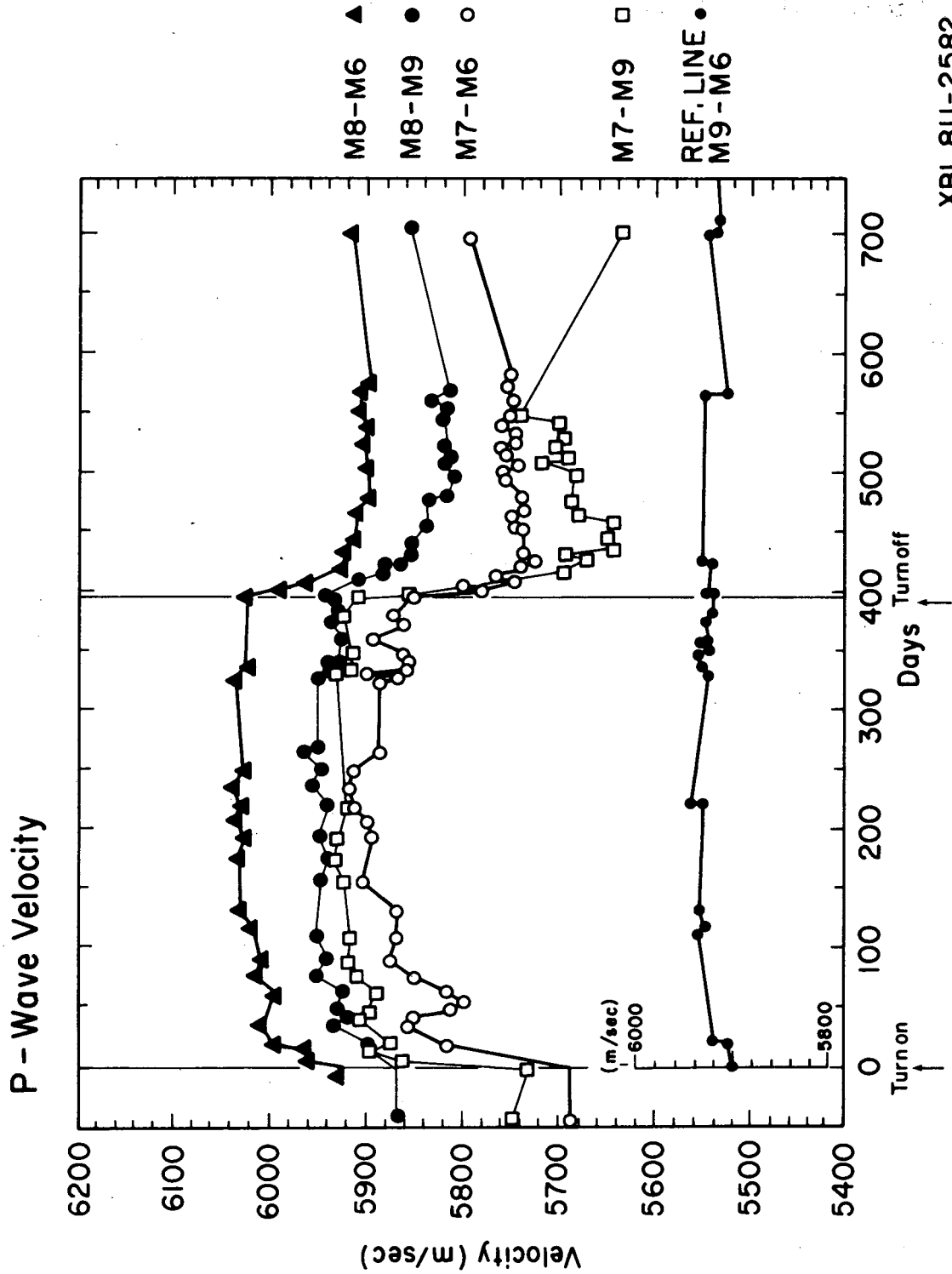
Fig. 5.1 P-wave velocities in the four monitoring lines and the reference line. Note that only every second data point is plotted.
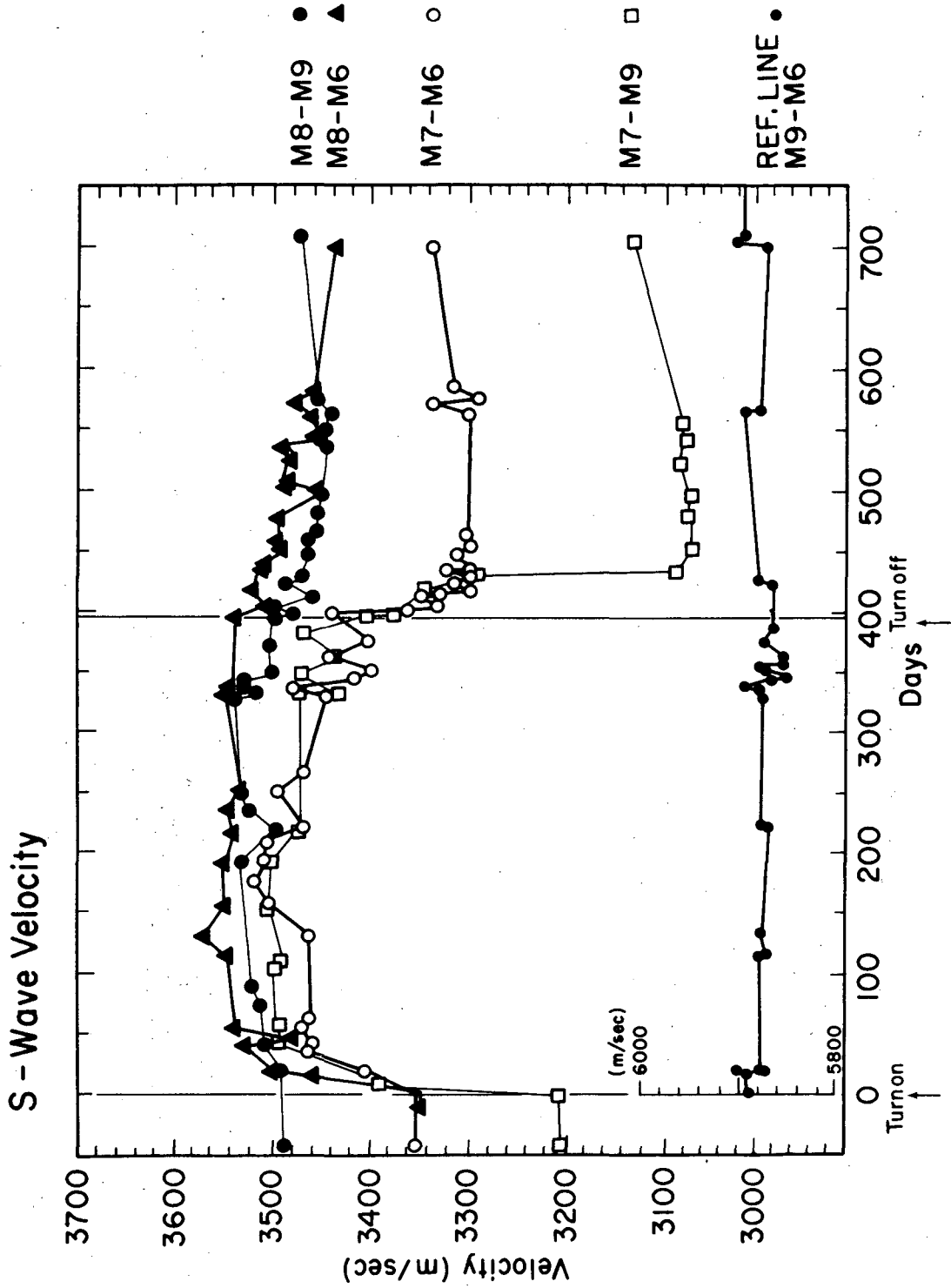
133

Fig. 5.2 S-wave velocities in the four monitoring lines and the reference line. Note that only every second data point is plotted.

PROFILE AND FILE NAME : M7-M6, M76PO., P-WAVES
FIELD WORK :1978-80 HEATER DAYS : -44-701 PLOTDATE : 830112
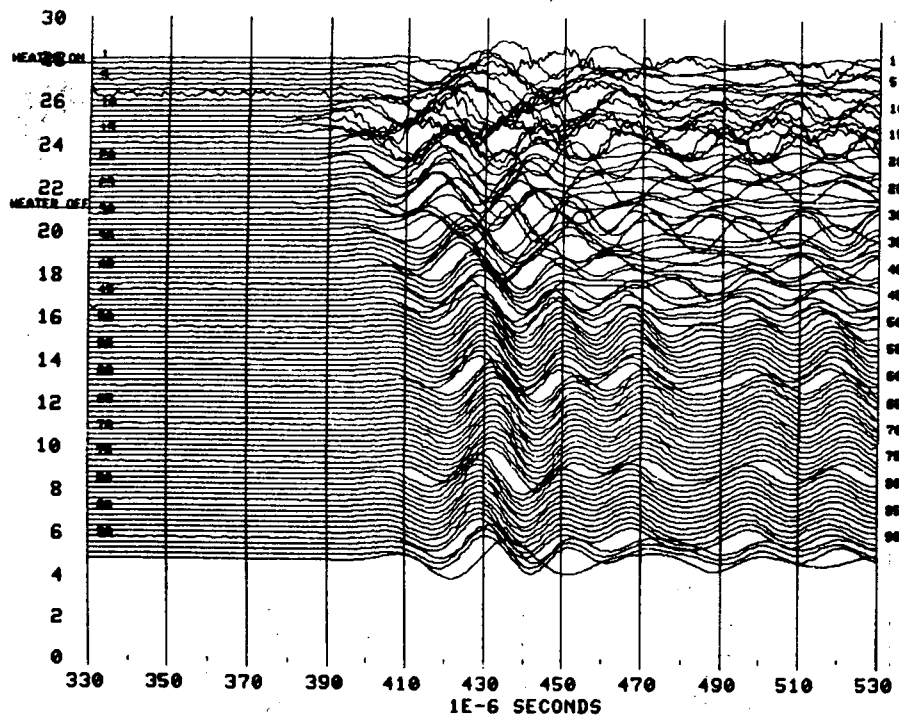
PROFILE AND FILE NAME : M8-M9, M89PO., P-WAVES
FIELD WORK :1978-80 HEATER DAYS : -42-711 PLOTDATE : 830112
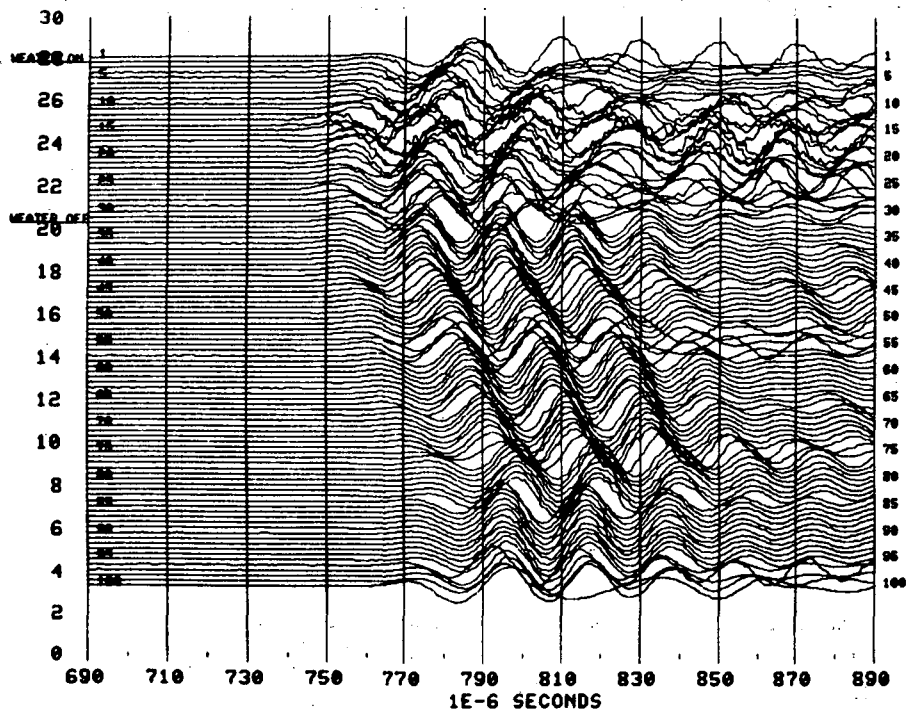
Fig. 5.3 P-waveforms for monitor lines M7-M6 and M8-M9. The time sequency is from top to bottom. The spacing between each waveform does not represent equal time.

PROFILE AND FILE NAME : M7-M9, M79PO., P-WAVES
FIELD WORK :1978-80 HEATER DAYS : -43-706 PLOTDATE : 830112

1E-6 SECONDS
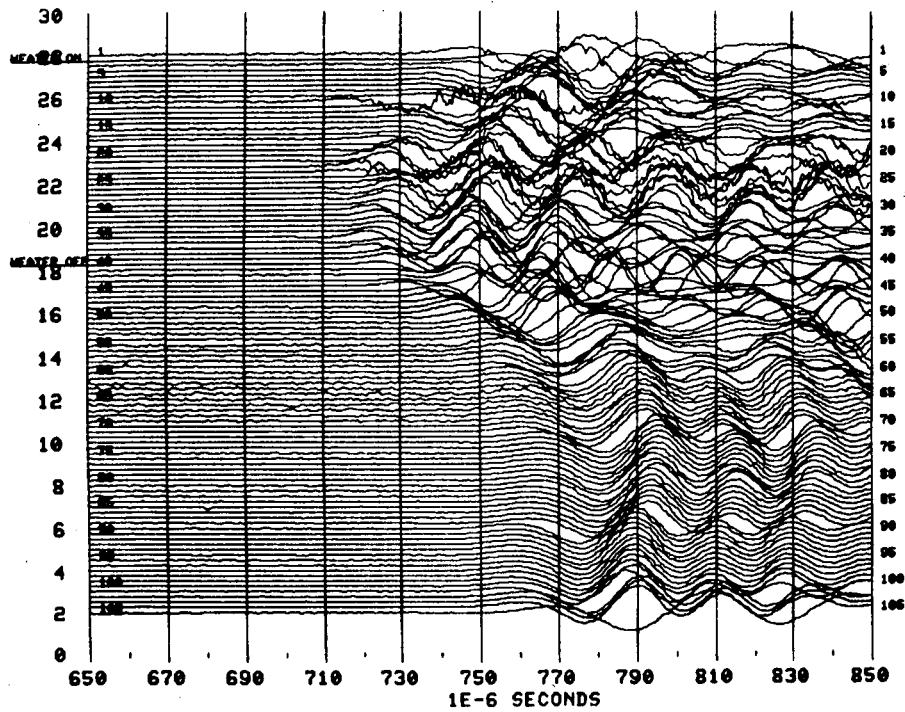
PROFILE AND FILE NAME : M8-M6, M86PO., P-WAVES
FIELD WORK :78-80 HEATER DAYS : -43-704 PLOTDATE : 830112

1E-6 SECONDS
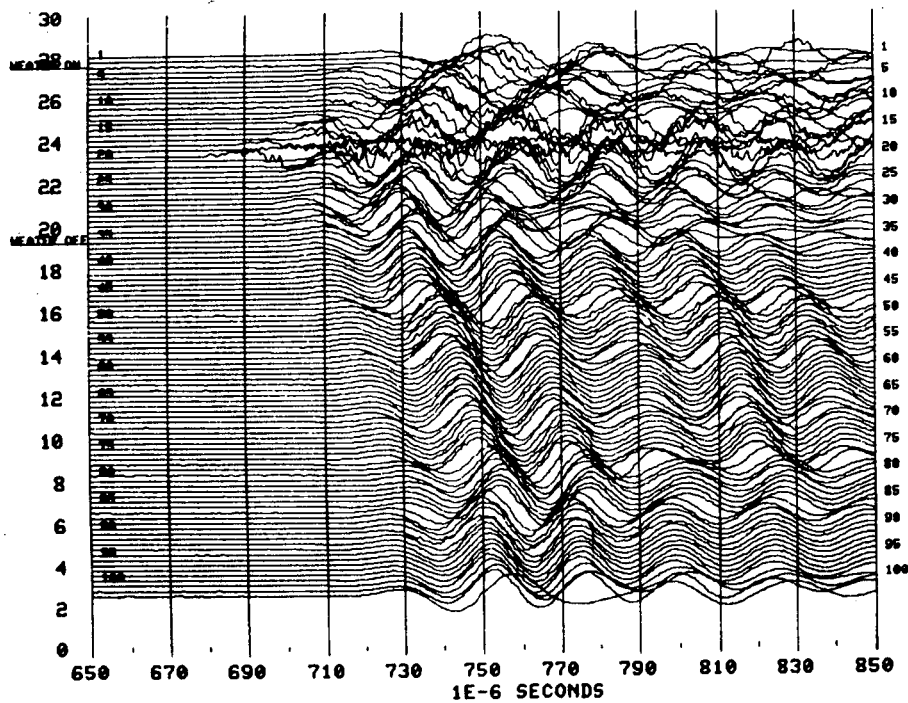
Fig. 5.4 P-waveforms for monitor lines M8-M6 and M7-M9. The time sequence is from top to bottom. The spacing between each waveform does not represent equal time.

PROFILE AND FILE NAME : M9-M6, R96PO., P-WAVES
FIELD WORK :78-80 HEATER DAYS : -1-756 PLOTDATE : 830112

PROFILE AND FILE NAME : M9-M6, R96SO., S-WAVES
FIELD WORK :78-80 HEATER DAYS : -1-756 PLOTDATE : 830112
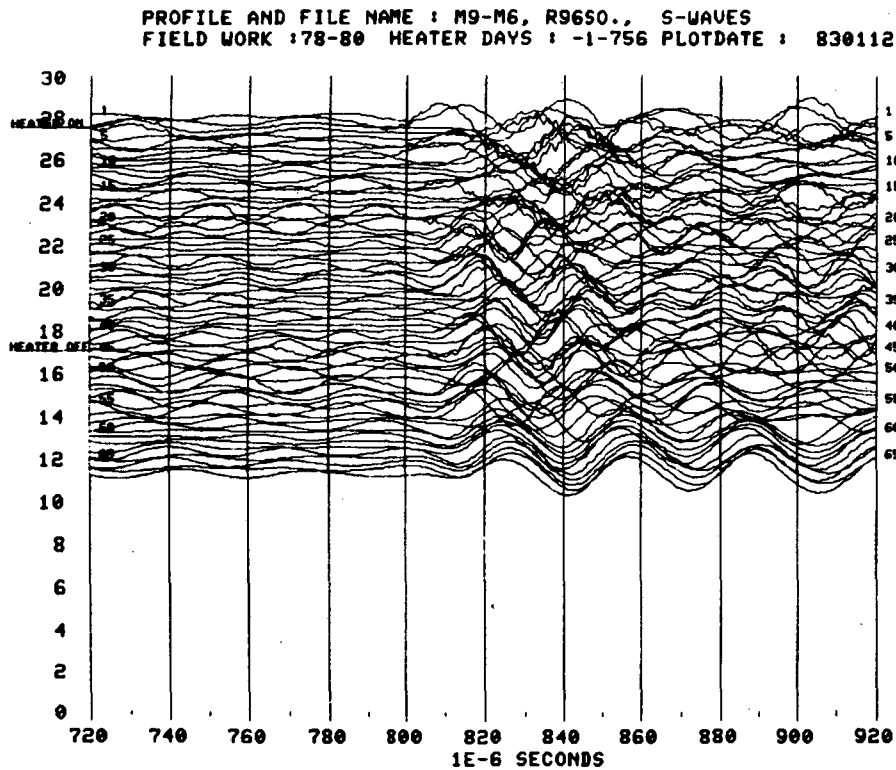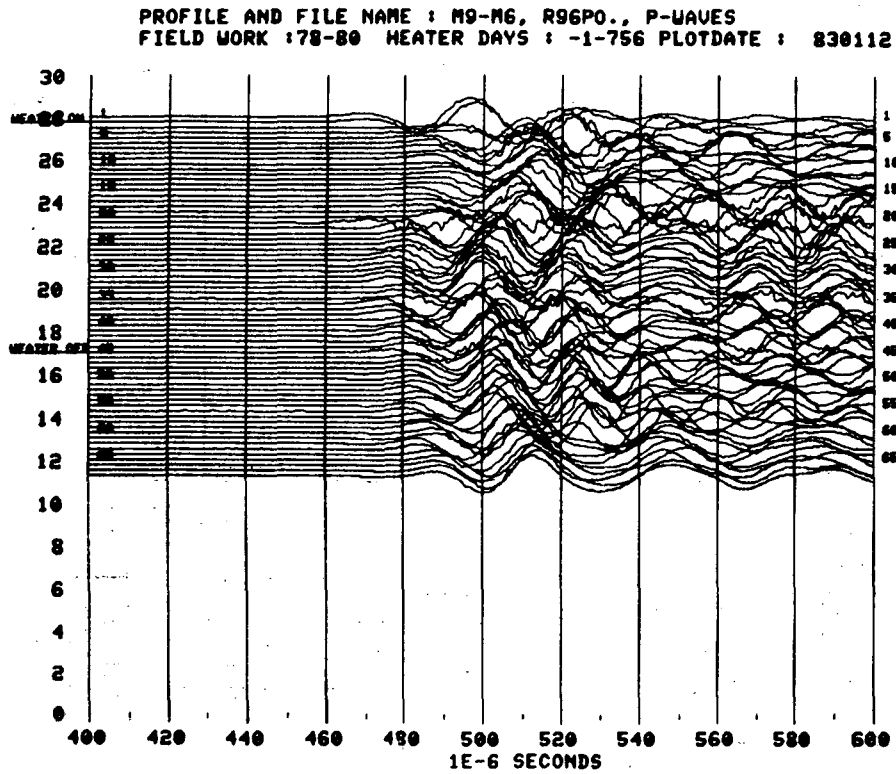
Fig. 5.5 a) P-waveforms for the reference line, boreholes M6-M9. Note the delay error amounting to 20 μs for the first two signals.. b) S-waveforms for the reference line, boreholes M6-M9.

Schmidt equal-area pole plot for principal stress directions,
pegmatite dikes and faults in the fullscale and extensometer drifts

PROFILE DIRECTION

A.	M6-M7	N52E
B.	M7-M8	N62W
C.	M8-M9	N51E
D.	M6-M9	N16W
E.	M8-M6	N89E
F.	M7-M9	N14E

XBL 811-2558
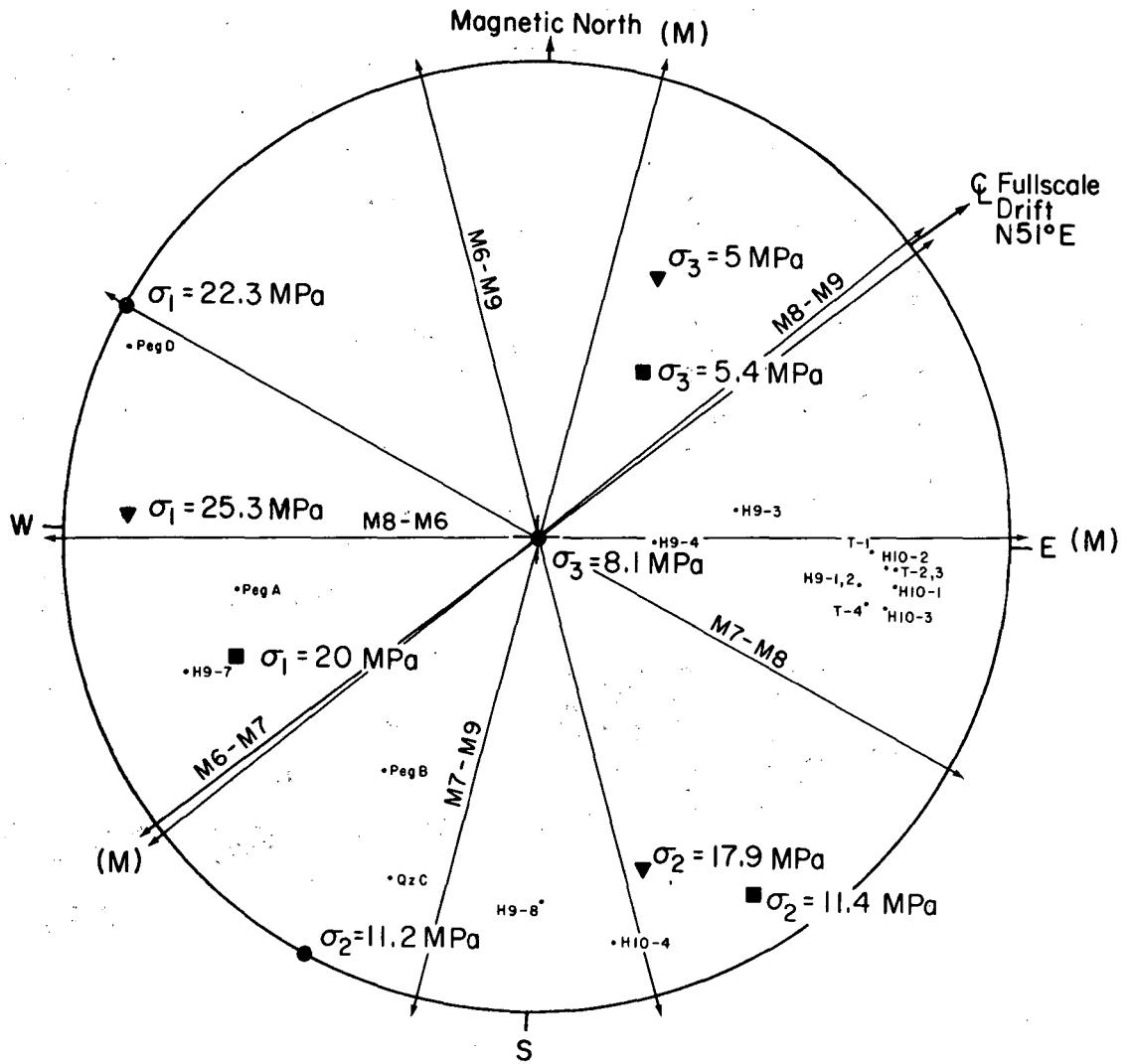
■ Over coring in the mine-hole drilled from drift wall
● Hydro fracture test in deep hole from surface
▼ Over coring in deep hole from surface

(M) Monitor lines

Fig. 5.6 Strike of the six cross-sections and the principal stresses obtained from overcoring and hydro fracture experiments.
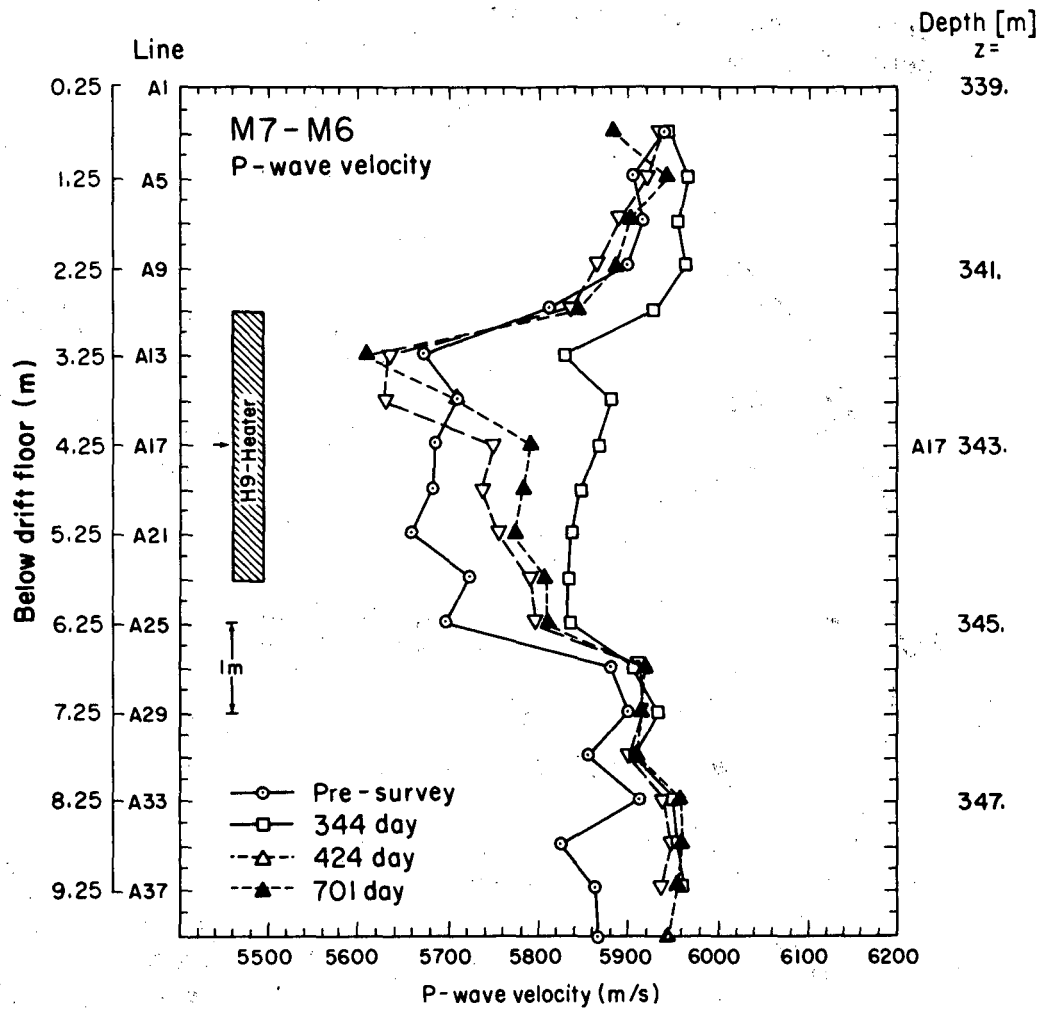
Fig. 5.7 P-wave velocities in cross-section M7-M6 for four surveys.
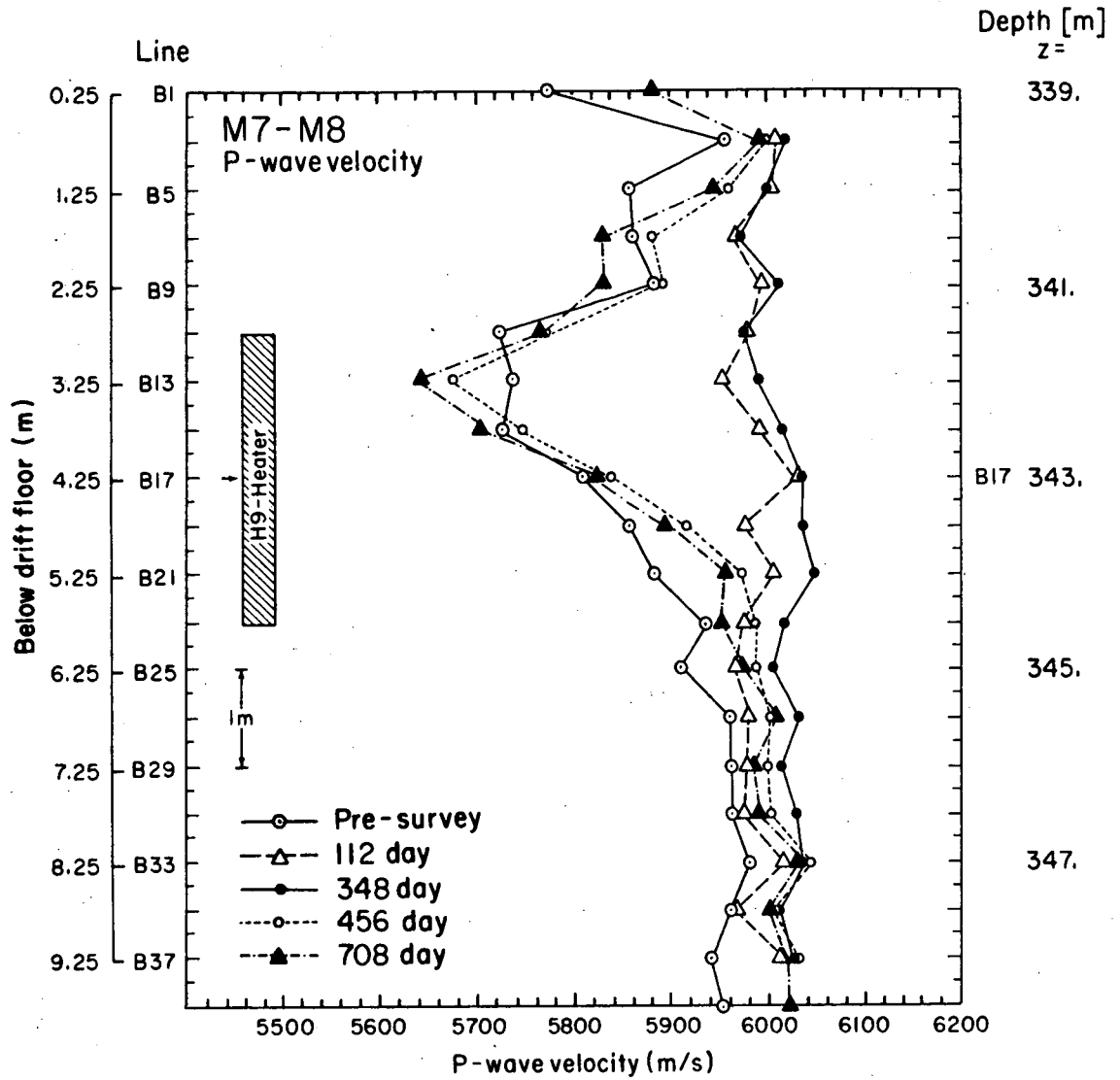
Fig. 5.8 P-wave velocities in cross-section M7-M8 for five surveys.
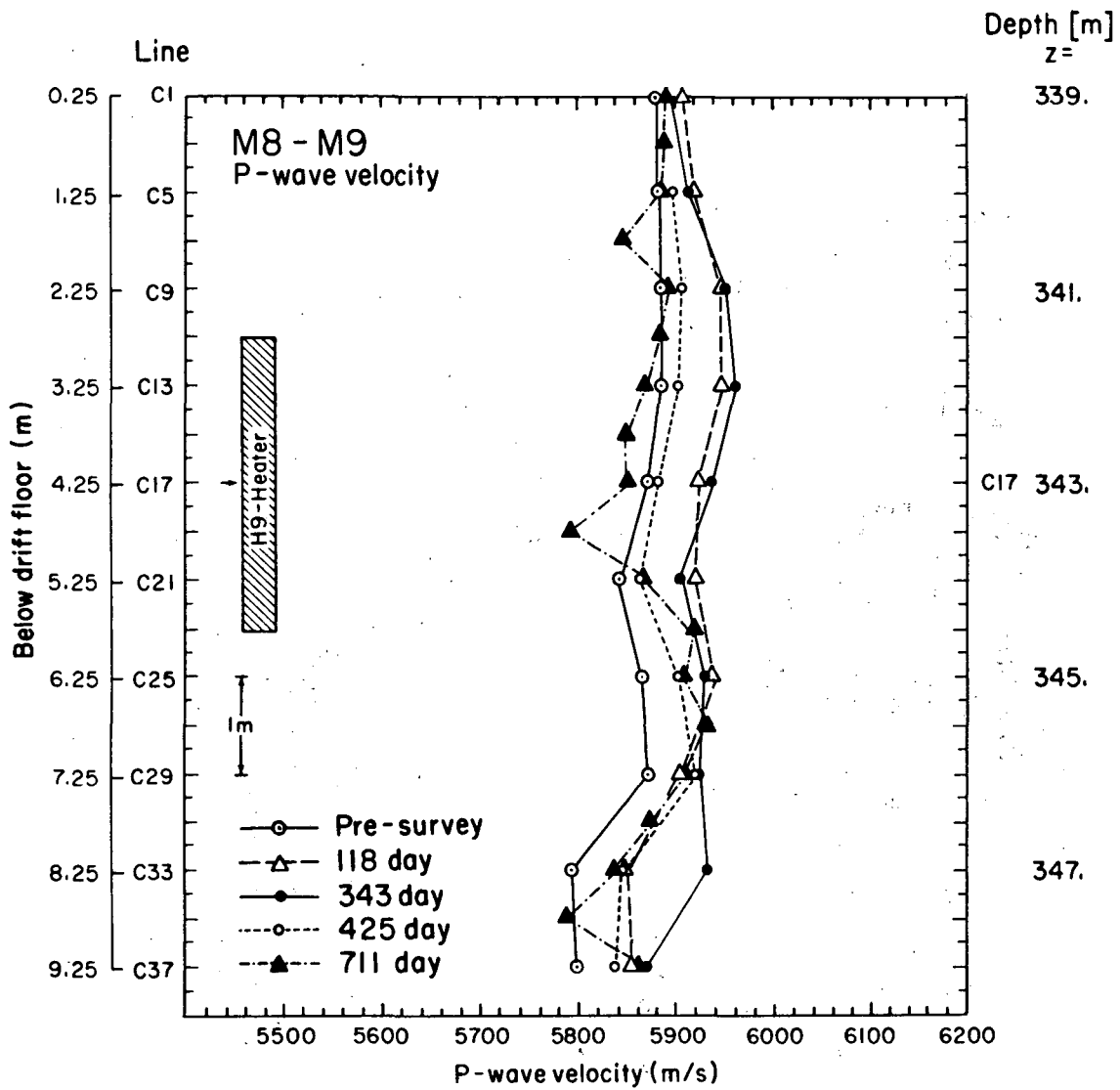
XBL 815-3079

Fig. 5.9 P-wave velocities in cross-section M8-M9 for five surveys.

141
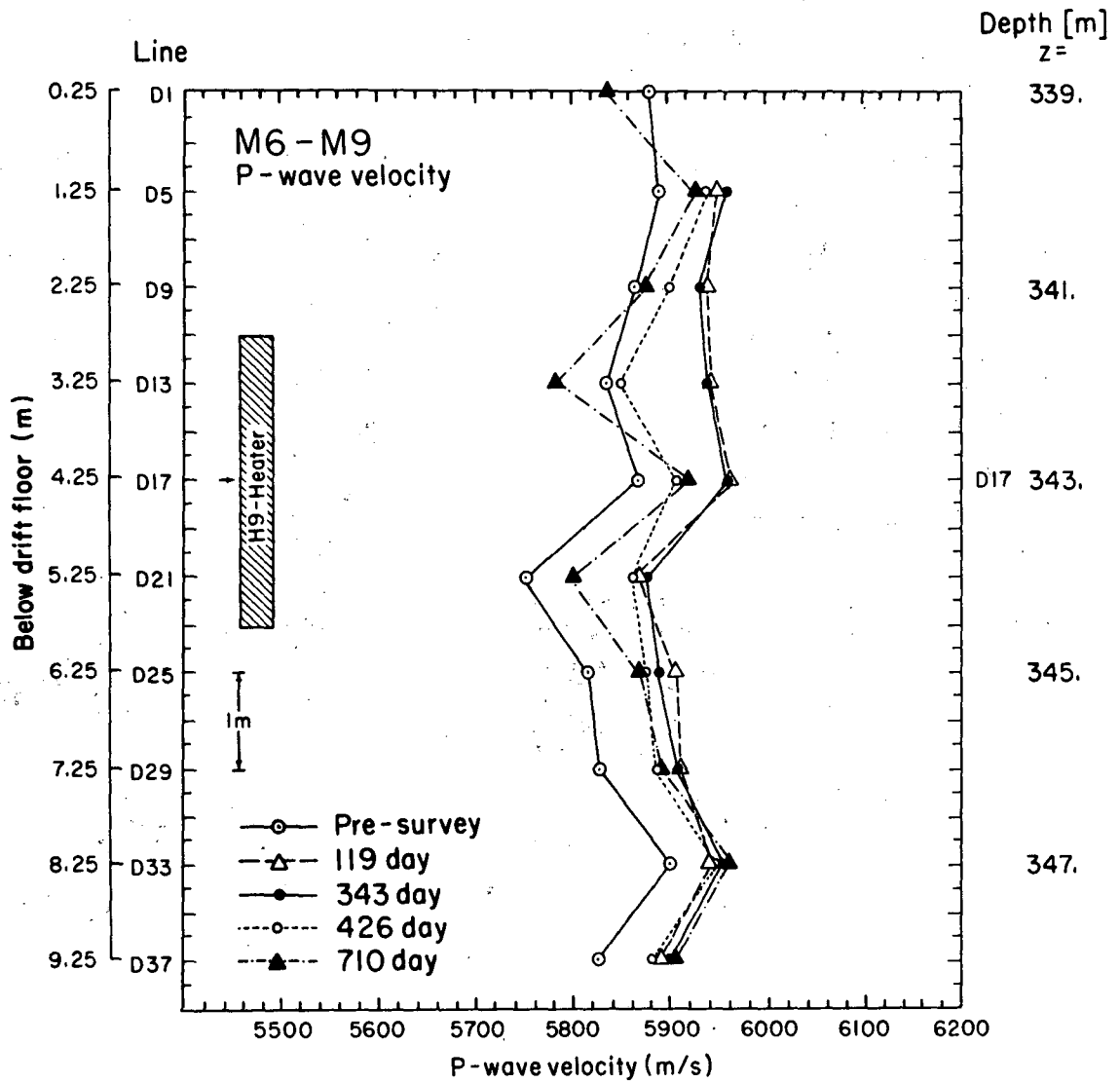
Fig. 5.10 P-wave velocities in cross-section M6-M9 for five surveys.
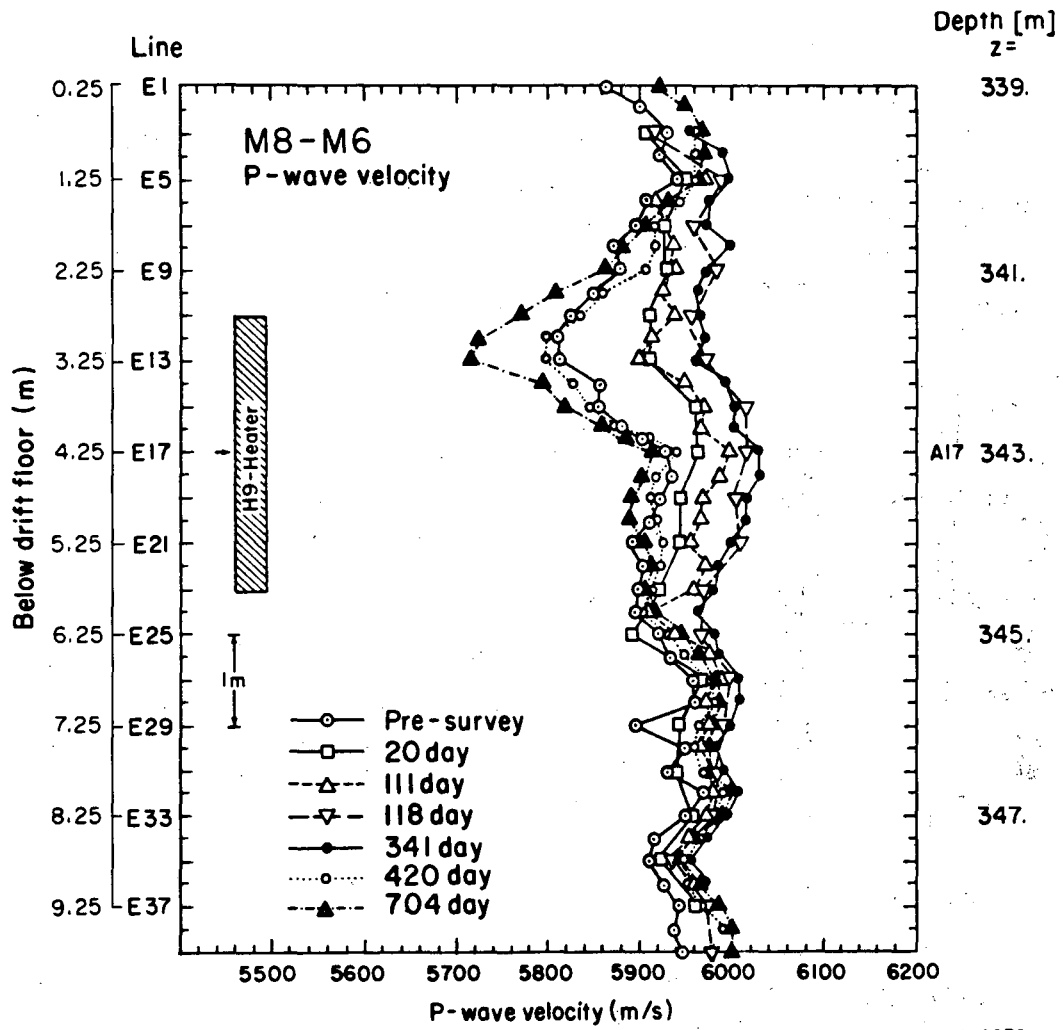
Fig. 5.11 P-wave velocities in cross-section M8-M6 for seven surveys.
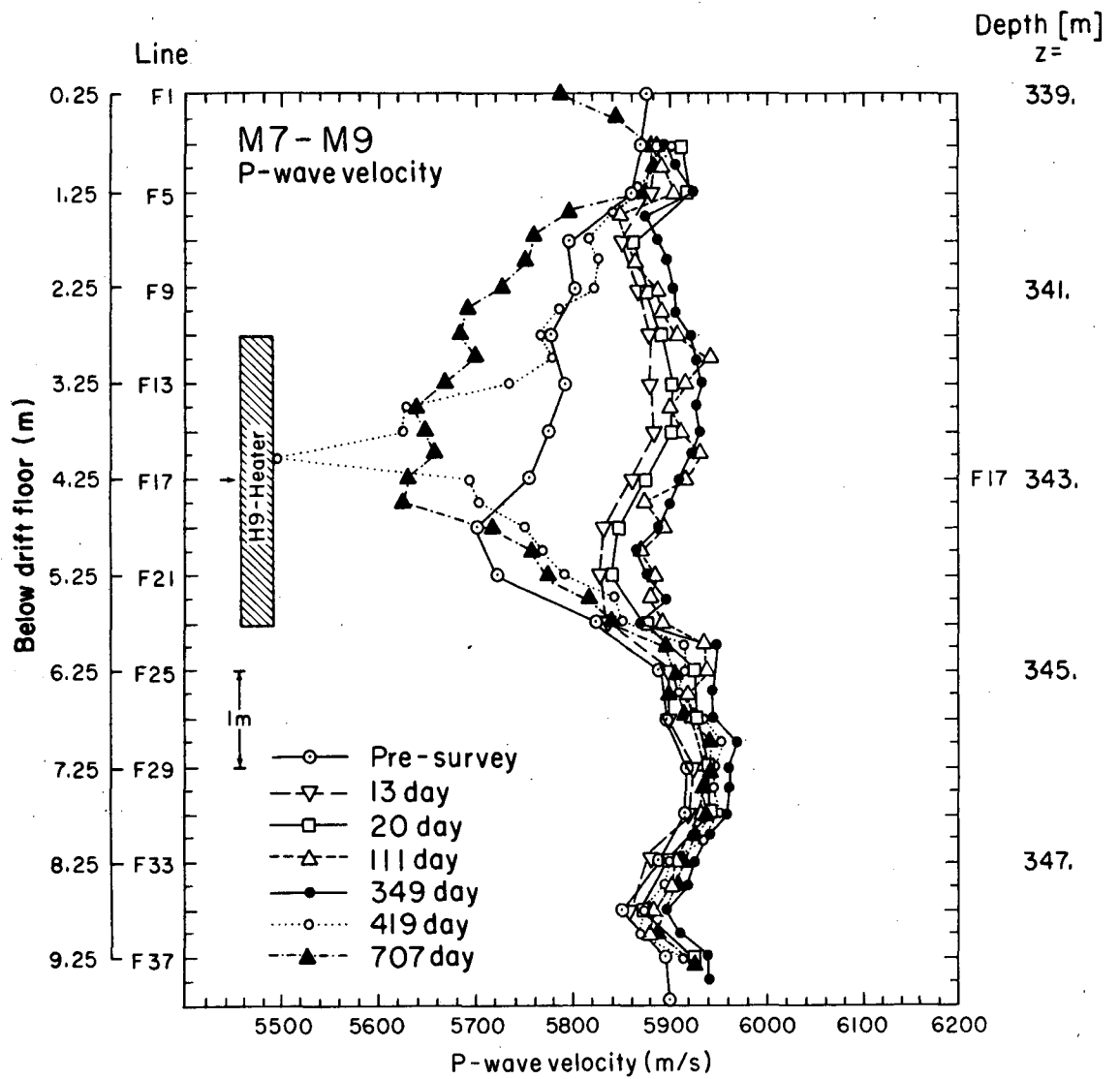
Fig. 5.12 P-wave velocities in cross-section M7-M9 for seven surveys.

PROFILE AND FILE NAME : M8-M6, SURVE.8
DATE FOR FIELD WORK : 790712 HEATER DAYS : 341 PLOTDATE : 821115
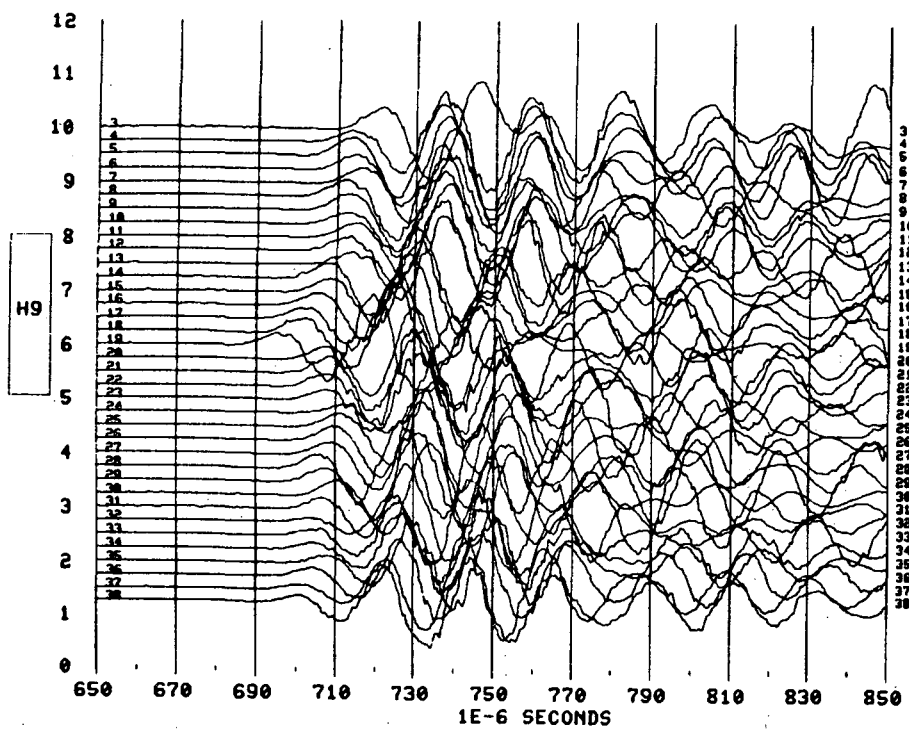
PROFILE AND FILE NAME : M8-M6, SURVE.10
DATE FOR FIELD WORK : 800728 HEATER DAYS : 704 PLOTDATE : 821115
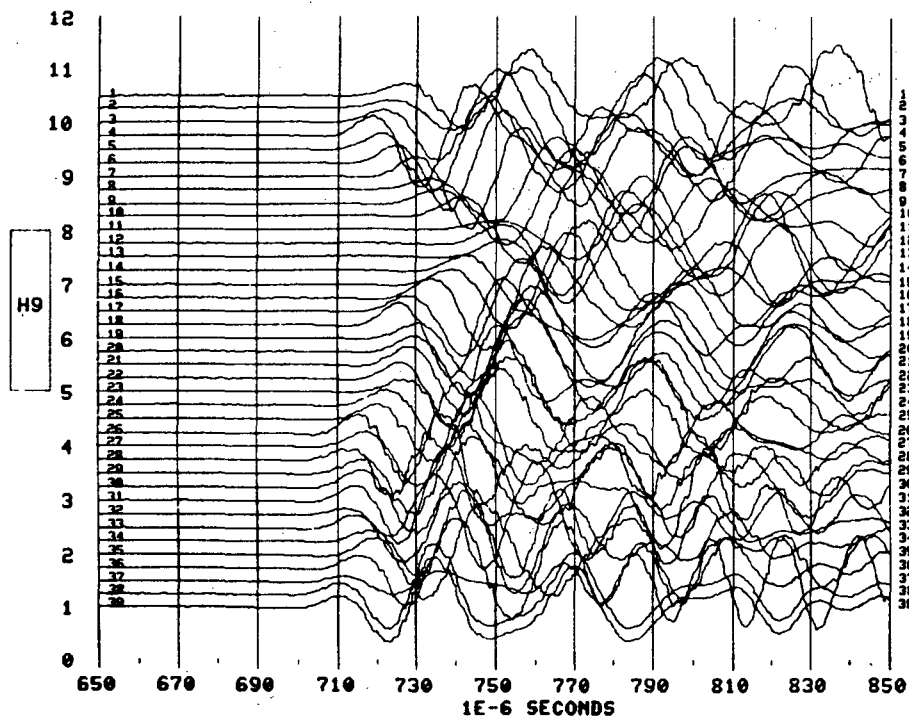
Fig. 5.13 Waveforms from cross-section M8-M6, for survey # 8 at day 341 and survey no 10 at day 704.

145

PROFILE AND FILE NAME : M7-M9, SURVF.9
DATE FOR FIELD WORK : 790808   HEATER DAYS :   349 PLOTDATE :   821115

1E-6 SECONDS
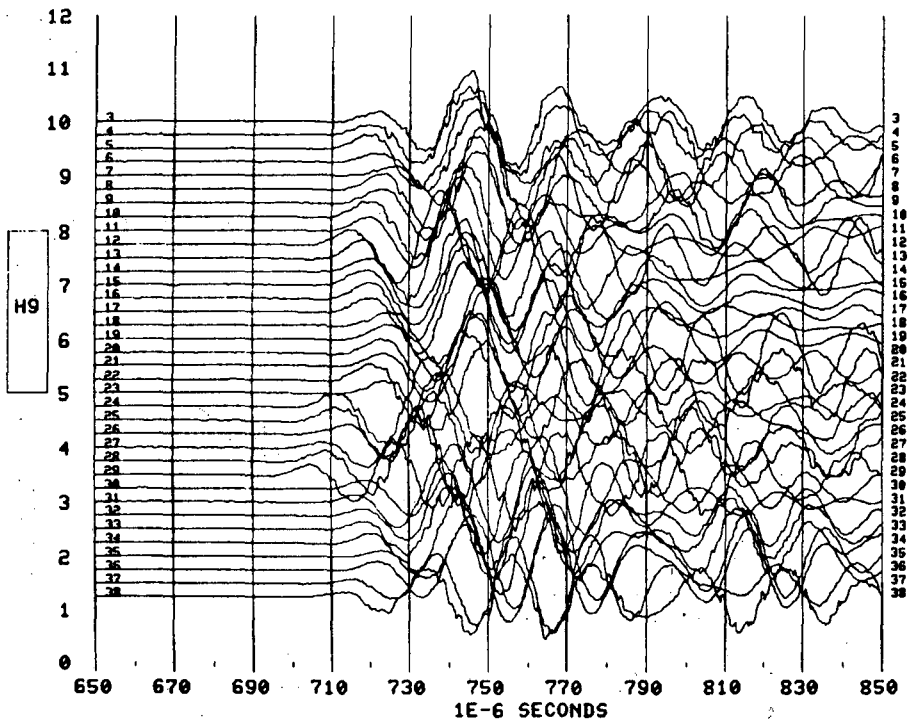
PROFILE AND FILE NAME : M7-M9, SURVF.11
DATE FOR FIELD WORK : 800730   HEATER DAYS :   707 PLOTDATE :   821115

1E-6 SECONDS
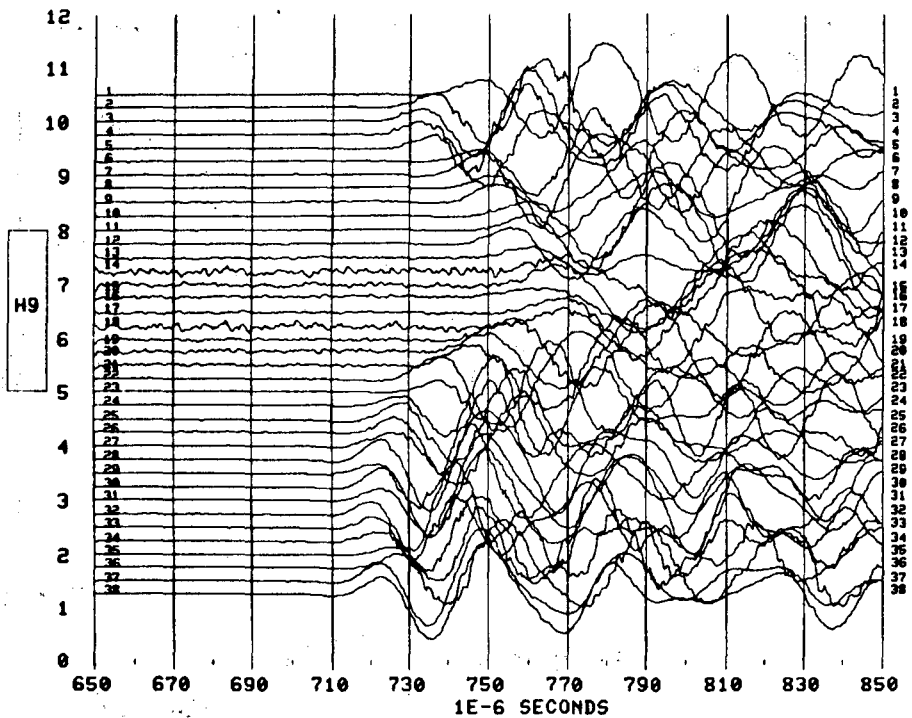
Fig. 5.14 Waveforms from cross-section M7-M9, for survey # 9 at day 349 ant survey # 11 at day # 707.
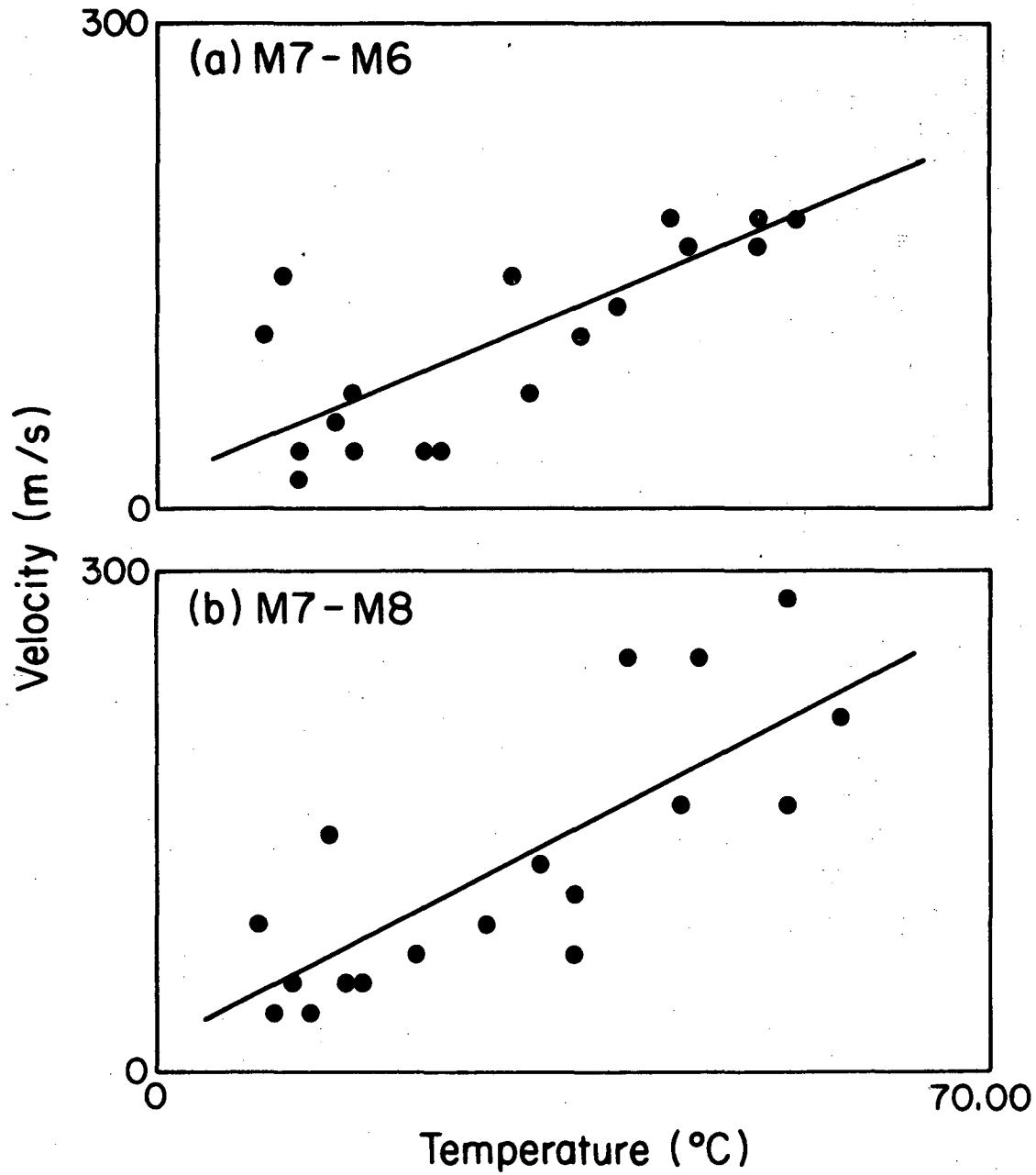
Fig. 5.15 Change of P-wave velocity as function of temperature change spatially from line 1 to line 39 at day 398 for cross-section M7-M6 and M7-M8.
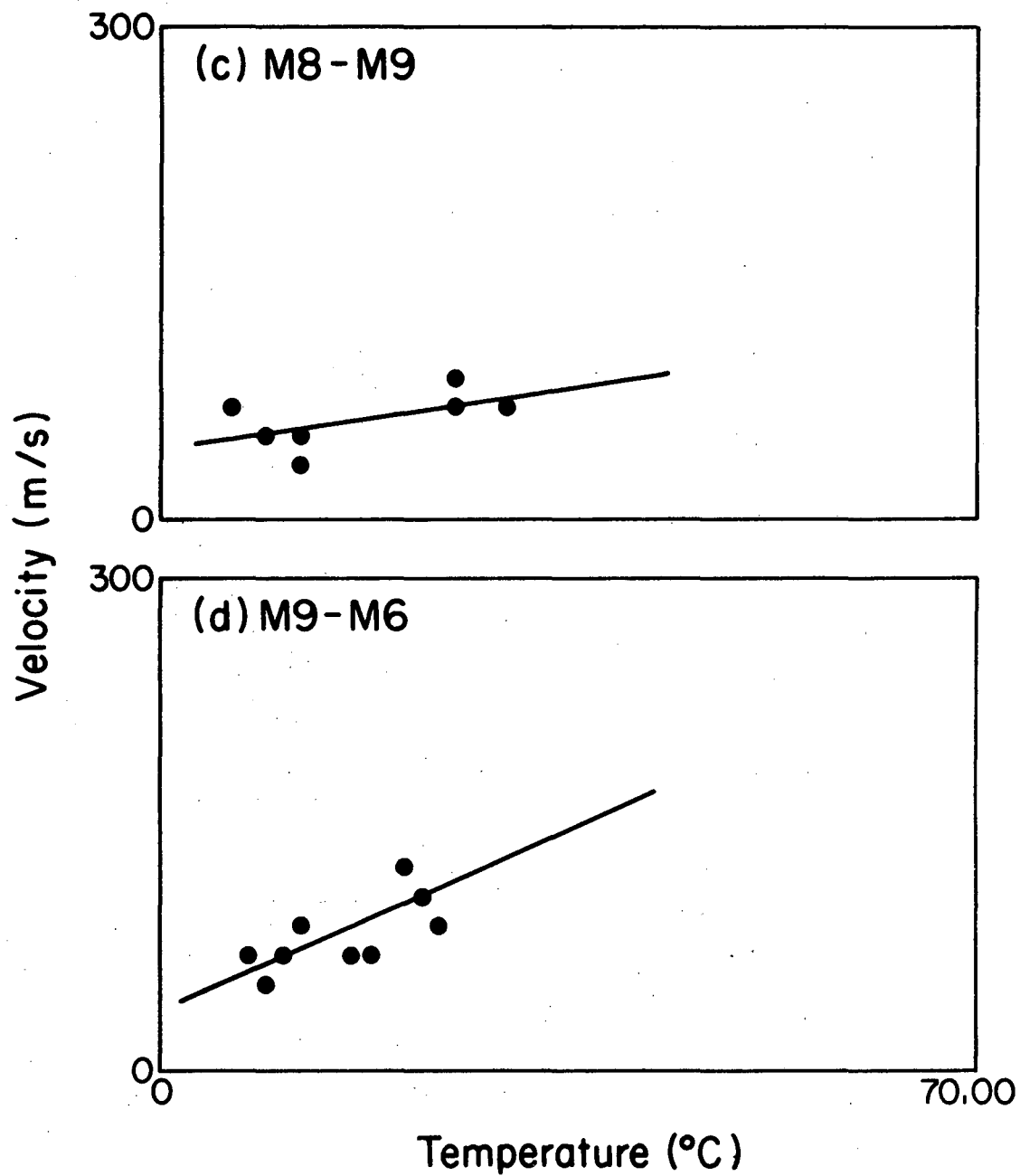
Fig. 5.16 Change of P-wave velocity as function of temperature change spatially from line 1 to line 39 at day 398 for cross-sections M8-M9 and M9-M6.
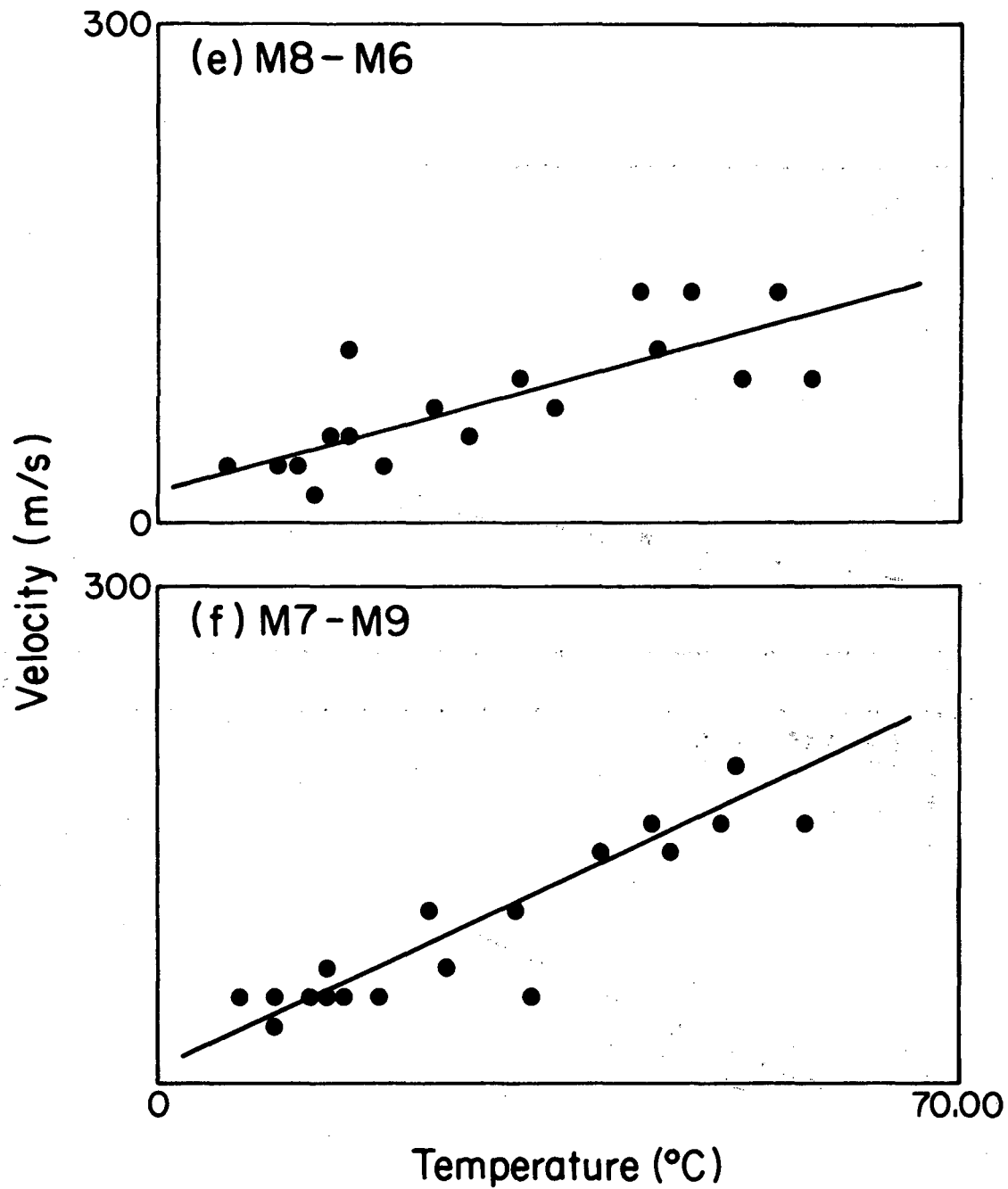
XBL 838-2185

Fig. 5.17 Change of P-wave velocity as function of temperature change spatially from line 1 to line 39 at day 398 for cross-sections M8-M6 and M7-M9.

149
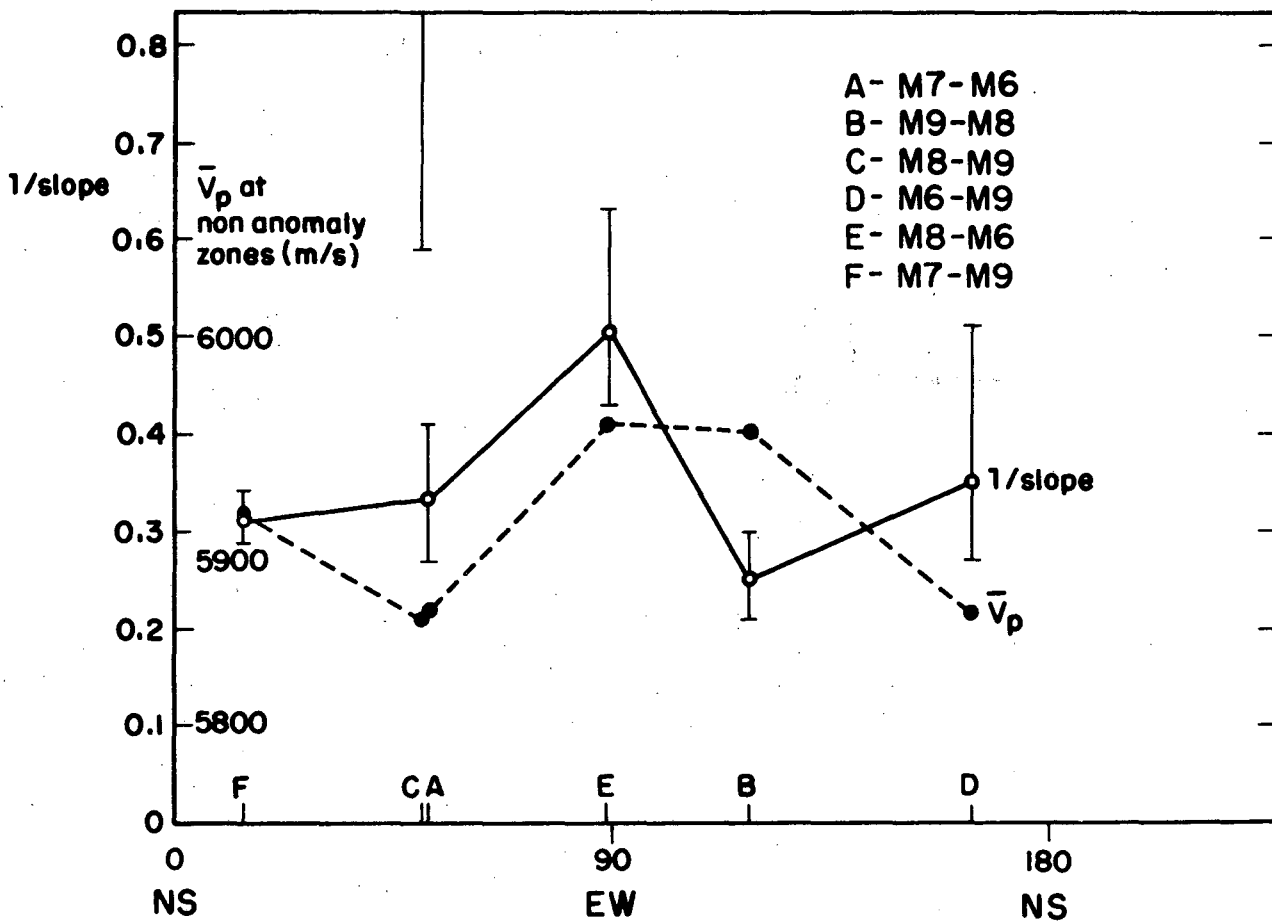
Fig. 5.18 $\overline{V_p}$ and 1/slope of regression line from the spatial temperature-velocity function in six cross-sections.
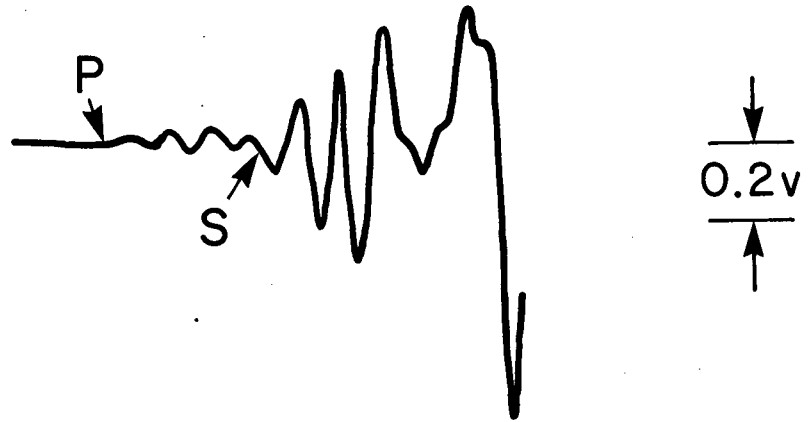
VERTICAL SCALE EXPANDED X 10
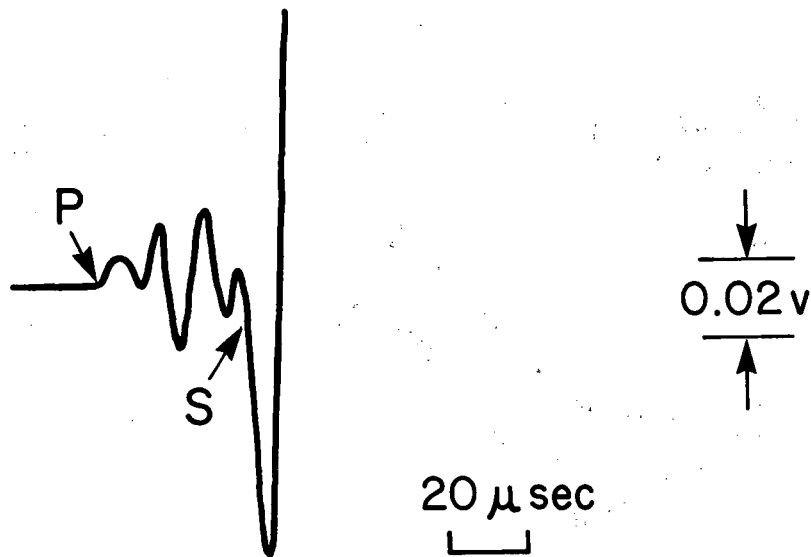
XBL 824-9031

Fig. 5.19 Waveform from the down-hole ultrasonic experiment showing the P and S-waves.
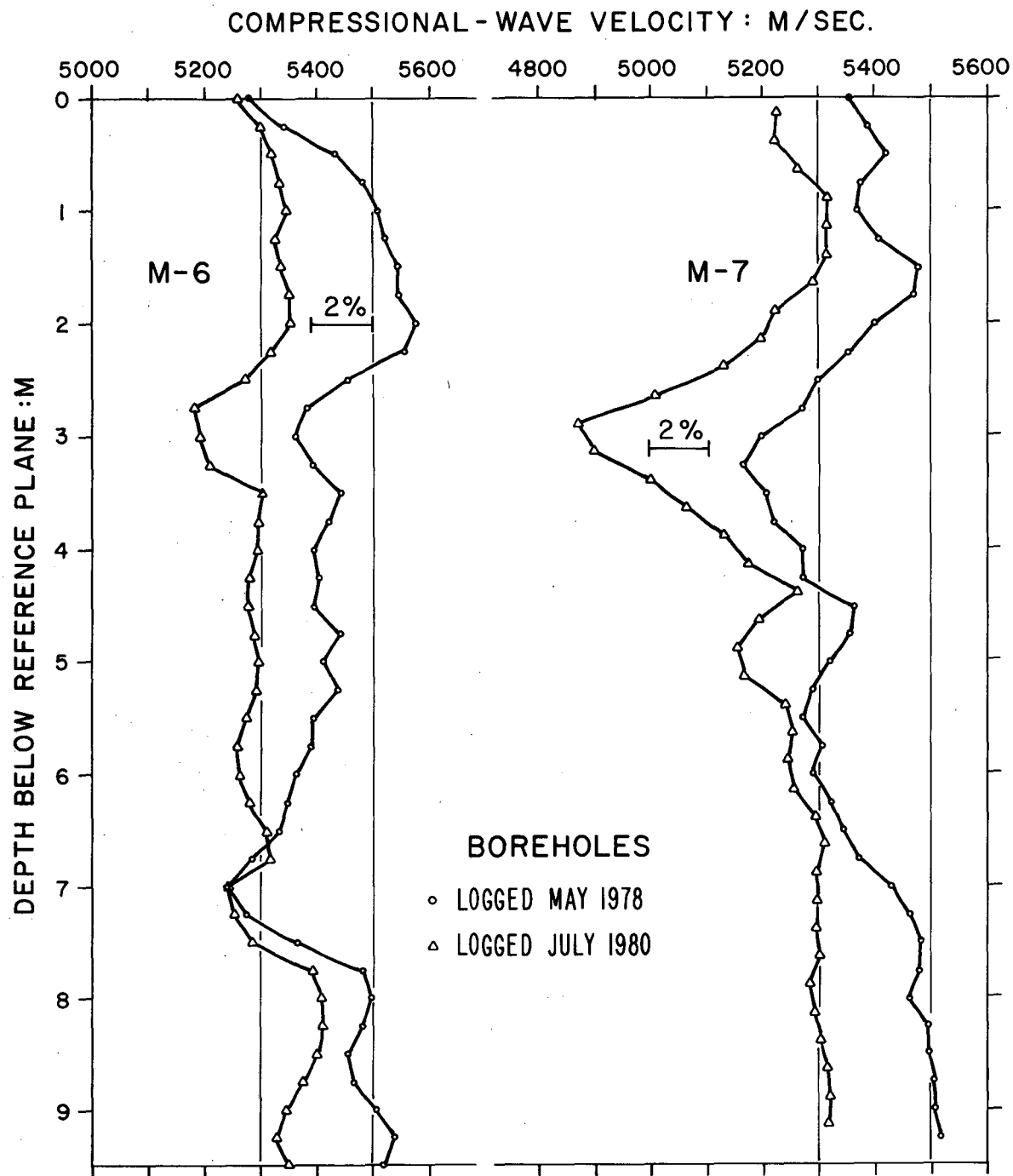
Fig. 5.20 Compressional wave velocities as function of depth in boreholes M6 and M7.
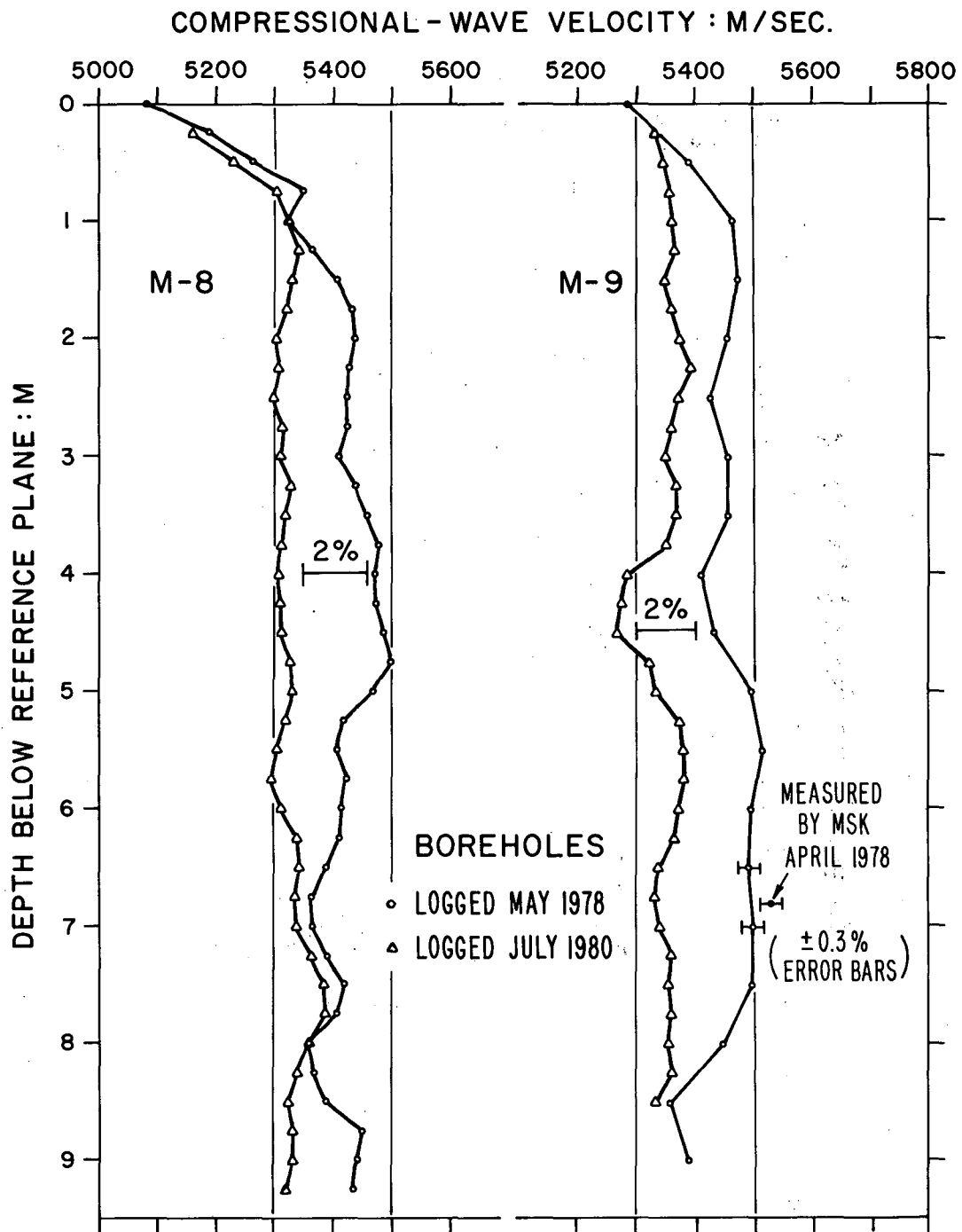
XBL 824-9037

Fig. 5.21 Compressional wave velocities as function of depth in boreholes M8 and M9.
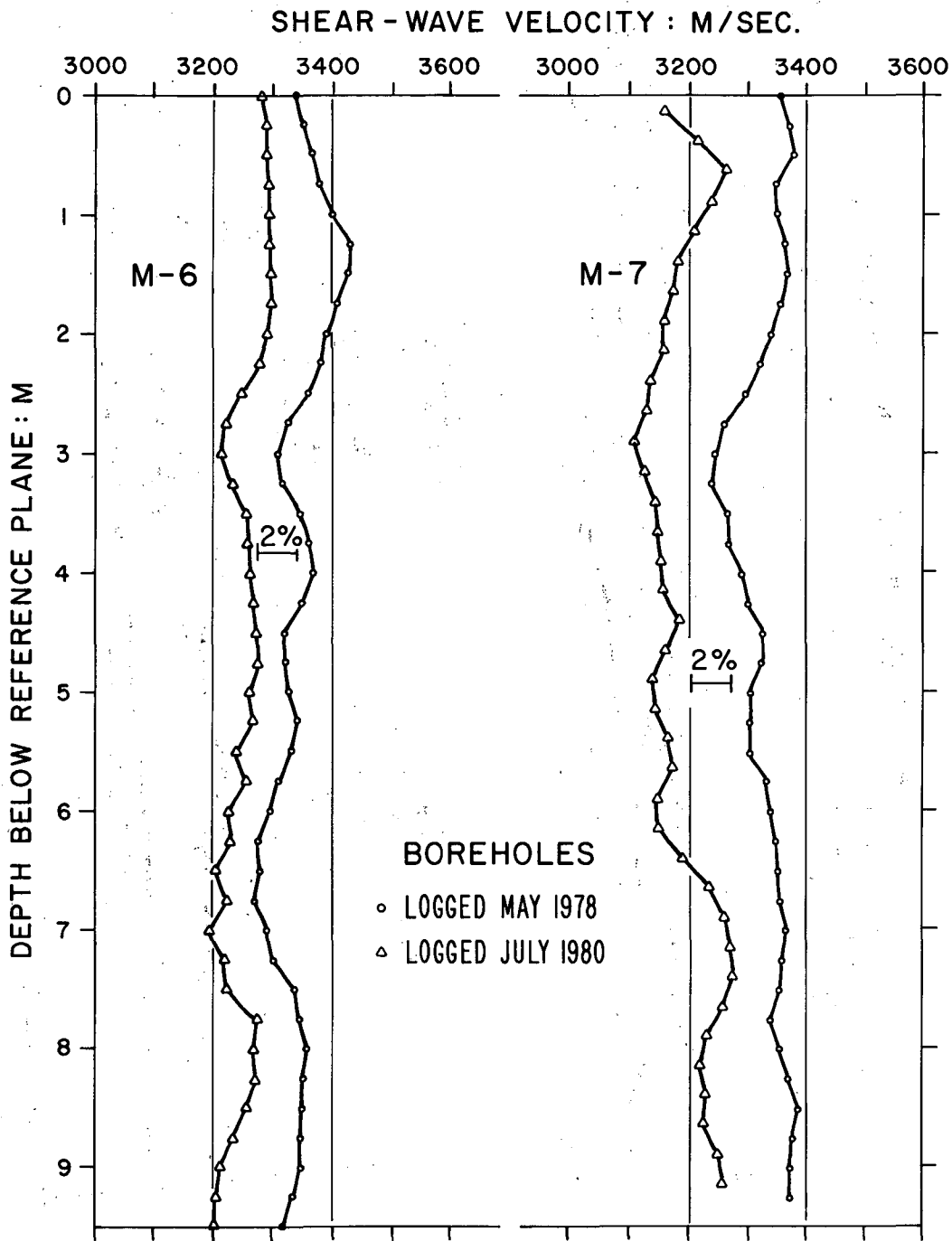
XBL 824-9036

Fig. 5.22 Shear wave velocities as function of depth in borehole M6 and M7.
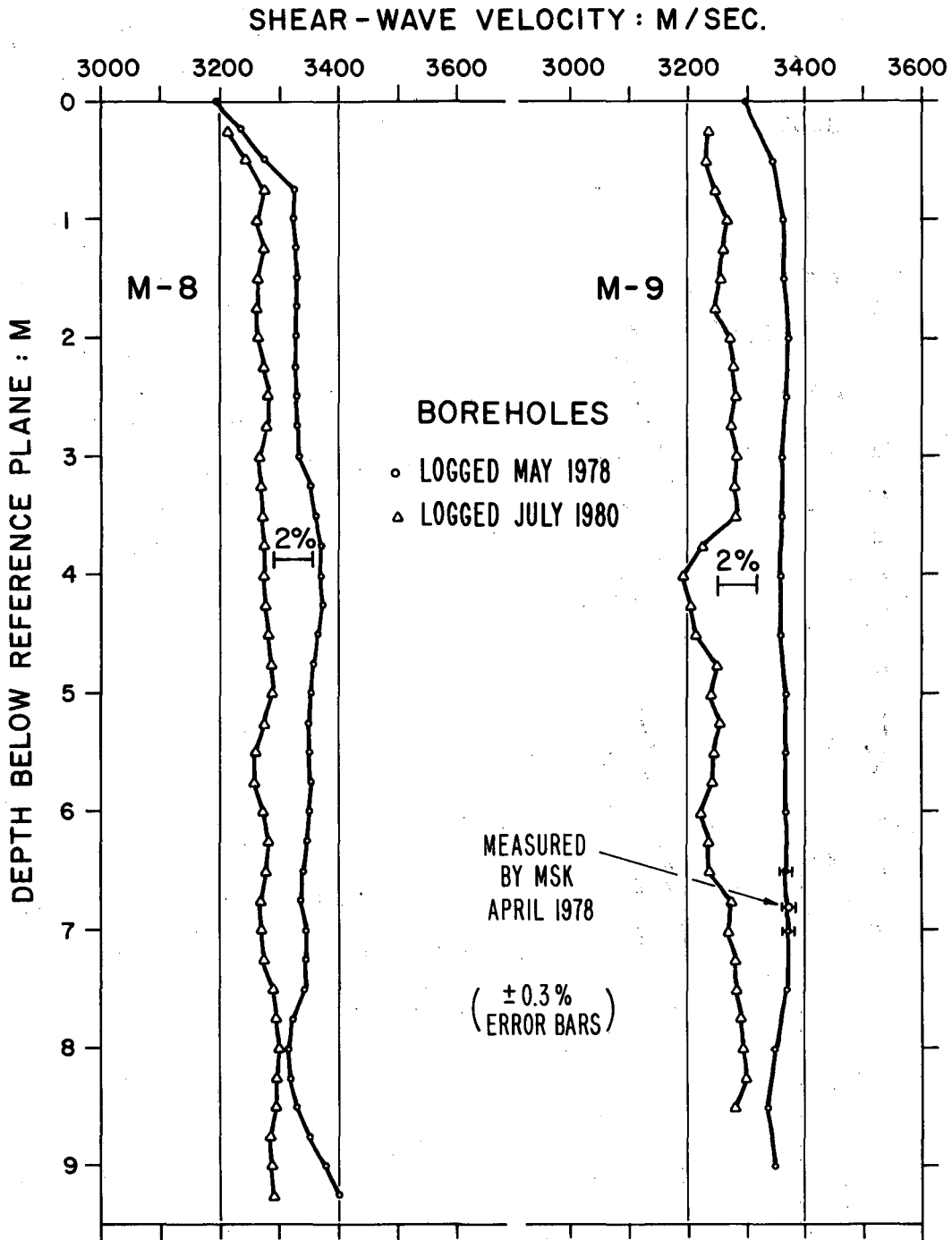
Fig. 5.23 Shear wave velocities as function of depth in boreholes M8 and M9.
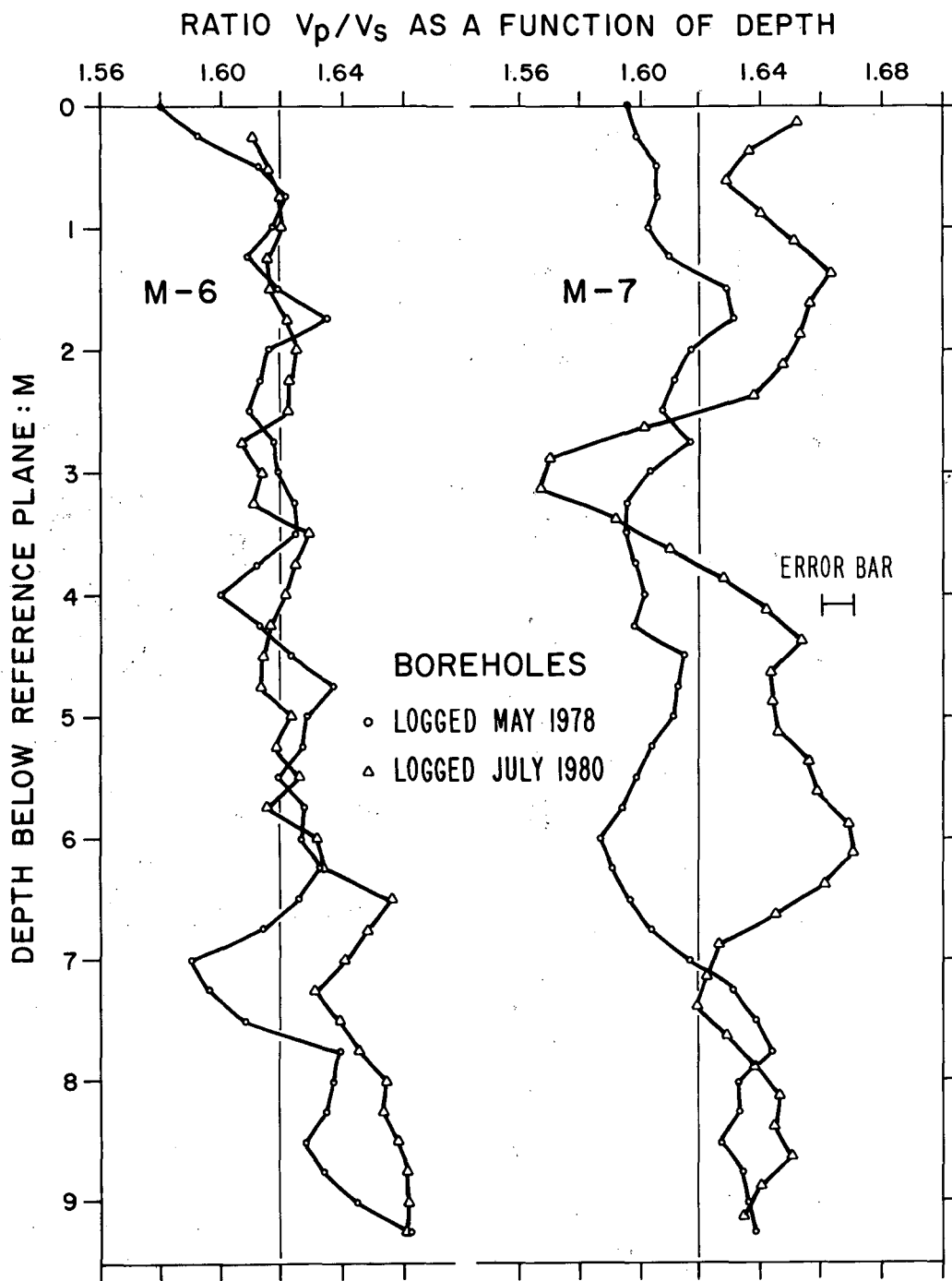
XBL 824-9034

Fig. 5.24 Ratio V_p / V_s as function of depth in boreholes M6 and M7.
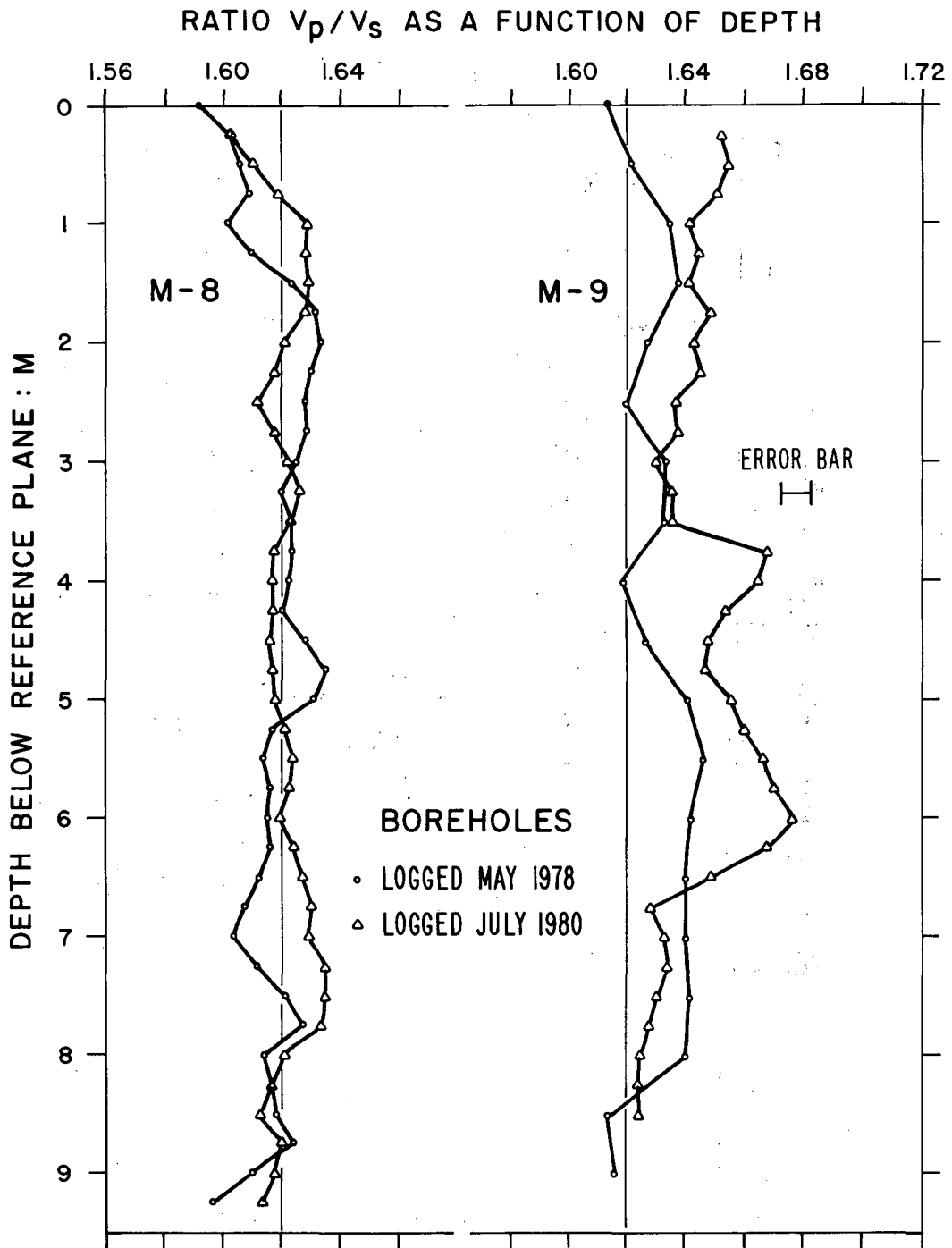
XBL 824-9033

Fig. 5.25 Ratio V_p / V_s as function of depth in boreholes M8 and M9.

XBL 824-9032

6. ATTENUATION EFFECTS

In This chapter attenuation of the P-waves transmitted between the boreholes in the H9 area will be discussed. The attenuation value, defined as Q^{-1}, where Q is the intrinsic quality factor for the path material, has been calculated for all the P-waveforms for which the velocities were obtained from the arrival times, as discussed in Chapter 5.

The process used to obtain the attenuation values from the field data for the rock *in situ* is a spectral ratio technique.

Introduction

The basic problem with a spectral ratio technique for field data is that it is difficult to obtain a reference signal, i.e., a signal which is used to form a spectral ratio with the signal in question. The quality of the result of the Q calculation with the spectral ratio technique depends on how well the properties for the reference is known. One way to calculate the Q for a rock is to use two paths with different transmission distances, assuming a constant Q for the two paths. Thus the signal at one distance becomes the reference signal. The amplitude spectrum for plane waves propagating in a homogeneous medium can be written as

$$A(f) = A_0 e^{i(kx - \omega t)}, \qquad [6.1]$$

(See Johnston and Toksoz 1981), where k is the wavenumber in the x direction and $\omega = 2\pi f$, where f is frequency. Attenuation can be described by assuming the wave number to be complex:

$$k = k_r + i\alpha \qquad [6.2]$$

to give

$$A(f) = A_0 e^{-\alpha x} e^{i(k_r x - \omega t)} \qquad [6.3]$$

where the spatial decay coefficient

$$\alpha = \frac{\pi f}{QV}, \qquad [6.4]$$

with the wave velocity $V = \omega / k_r$. Thus the spatial attenuation in the x direction is described by

$$A(x) = A_o e^{-\alpha x}. \qquad [6.5]$$

For two different positions for the receivers one obtains,

$$A(x_1) = A_0 e^{-\alpha x_1}$$

and

$$A(x_2) = A_0 e^{-\alpha x_2}.$$

Dividing and taking the natural logarithm

$$\ln\left[\frac{A(x_1)}{A(x_2)}\right] = -\alpha(x_1 - x_2) = \alpha\, \delta x. \qquad [6.6]$$

Over the frequency interval over which the linear regression is made for the field data (20-50 khz), there is a near-linear relationship between α and frequency, or, Q appear to be frequency independent. This results in the relationship $\alpha(f) = \gamma f$ or $\gamma = \frac{\pi}{VQ}$. This gives

$$\ln\left[\frac{A(x_1)}{A(x_2)}\right] = f(x_1 - x_2)\gamma = \frac{\pi f\, \delta x}{VQ}. \qquad [6.7]$$

If $\ln\left[\dfrac{A(x_1)}{A(x_2)}\right]$ is plotted as a function of f, the slope of the line will be

$s=(x_1-x_2)\gamma = \dfrac{\pi\delta x}{VQ}$. Thus γ is given by $\gamma = \dfrac{s}{(x_1-x_2)}$ and Q is given by

$$Q = \frac{\pi}{\gamma V} = \frac{\pi\delta x}{Vs}. \tag{6.8}$$

This formulation assumes in addition to a frequency independent Q, a common source and a uniform medium along both propagation paths x_1 and x_2. The latter is a fairly good assumption if the angle between the two paths is small or if the material is similar to a distance of x_2 along both paths. The two cross-sections used for establishing an average or reference Q_α were M7-M8 and M8-M6. The angle between the two cross-sections is 29° and the two cross-hole distances are 2.68 and 4.18 m, respectively. Figure 6.1 shows the spectra from the two cross-section. In Figure 6.2 the natural logarithm of the spectral ratios is shown as a function of frequency together with a least squares fit of a straight line to the data. When the signal is transmitted in a high-Q material, or when the ∇x is small, there is the risk that the Q estimate may become singular.

The reference spectrum used for all the spectral ratios calculations was that obtained from cross-section M7-M9 obtained just before the heater was turned off. The reason for using this spectrum is that, by inspection, it contains more high frequency energy than any other spectrum. The Q_α assigned to this spectrum is governed by the result obtained from the two cross-sections M7-M8 and M8-M6. A Q_α of 50 was chosen as a reasonable estimate for this standard. It transpires that the result is insensitive to the Q assigned to the standard. The Q_α obtained

under laboratory conditions for the Stripa quartz monzonite, as shown in Chapter 7, also indicate that $Q_\alpha=50$ is a reasonable estimate.

It would have been more satisfactory to utilize a reference spectrum from a standard material possessing a very high known Q-value. A possibility would have been to use an aluminum block of sufficient dimensions. Then the Q-values for the standard would be better defined and thus the determination of the absolute Q more certain. In this study the Q-values obtained in-field have been confirmed by similarly low Q-values determined from the complementary laboratory work.

6.1 Monitor Data

Using the standard described and the spectral-ratio technique, Q_α values for all the P-wave monitor data have been calculated. In figure 6.3 the data from the five lines, M7-M6, M8-M9, M8-M6, M7-M9, and the reference line are shown. Each cross bar represents one data point and at the same time indicates the standard deviation for the measurement at that point.

The standard deviation for the Q-value is based on a least squares linear fit of the natural logarithm of the spectral ratio as a function of frequency

$$y = a + bx, \qquad\qquad [6.9]$$

The data consist of a pair of measurements (x_i, y_i), assuming x to be the independent variable and y the dependent. In this case x = frequency and $y = \ln\left[\dfrac{A_1}{A_2}\right]$. The solution of the equations for minimizing the weighted sum of the deviation between the data and the straight line, Ψ^2,

is given by Bevington (1969) as :

$$a = \frac{1}{\Delta}\left[\sum x_i^2 \sum y_i - \sum x_i \sum x_i y_i\right], \qquad [6.10]$$

and

$$b = \frac{1}{\Delta}\left[N\sum x_i y_i - \sum x_i \sum y_i\right], \qquad [6.11]$$

where

$$\Delta = N\sum x_i^2 - \left(\sum x_i\right)^2 \qquad [6.12]$$

We assume that the uncertainties are instrumental and that the standard deviations σ_i for the data points y_i are all equal:, thus $\sigma_i = \sigma$. Then we can estimate the uncertainties from the data. The estimated standard deviation $\sigma_i = \sigma$ is

$$\sigma^2 \approx s^2 = \frac{1}{N-2}\sum\left[y_i - a - bx_i\right]^2 \qquad [6.13]$$

Then from Bevington (1969) the uncertainty in a and b are given by

$$\sigma_a^2 \approx \frac{\sigma^2}{\Delta}\sum x_i^2 \qquad [6.14]$$

and for the slope b of the straight line:

$$\sigma_b^2 \approx N\frac{\sigma^2}{\Delta} \qquad [6.15]$$

Where σ is given above. Knowing the uncertainties in the slope the uncertainties in γ are obtained. The uncertainties in x and γ for the

standard are not considered. However, they are not important in comparison with the uncertainties of the slope of the line from the linear regression analysis.

Thermal effects on attenuation

The results of the calculation the Q_α values for the P-waves are shown in Figure 6.3 The Q_α values for the reference line over the course of the experiment are also shown in Figure 6.3. Note that the reference line has a separate scale which has been shifted 13 units. This was done to avoid unnecessary cluttering of the figure. The reference line is between boreholes M9 and M6 at a depth of 1 m beneath the heater drift floor, as shown in Figure 3.1. The shape of the curve is similar to the curve obtained for the Q_α values as a function of time obtained for the the monitoring lines. This behavior was observed despite the fact that the reference line is 3 m above the heater midplane. In Figures 6.4 a and b, and Figures 6.5 a and b, the amplitude spectra are shown for the P-waves recorded in the H9 heater midplane throughout the experiment. The first amplitude spectrum in time is at the top of each figure. The vertical distance between each waveform does not represent equal time: the first third of the waveforms represent data taken over the first 400 days of the H9 experiment and the remaining two thirds data taken over the next 300 days which represents the period from the heater turn-off to the conclusion of the H9 experiment. The reason for this is that few data were collected immediately after the heater was turned on. During operation of the H9 heater data were collected on a bi-weekly basis. After the turn-off of the H9 heater, data were collected twice a day to ensure the capture of any transient events.

The first data points were taken 2 days before dewatering of the rock mass started 41 days before heater turn-on. In comparison with the velocity data obtained over the monitoring lines, the Q_α values shown in Figure 6.3 behave quite differently. There is a gradual long-term increase in the Q_α value during the entire course of the 398 days-long heater experiment showing no or little correlation with the operation of the heater. However, there are several dips in this long-term increase. Over the initial period of 100 days heating there is little or no increase in Q_α. Over the following 30 days the Q_α value increases between 25 % and 50 % depending on which line is being studied. Over the next 75 days the Q_α value decreases to a level just slightly above the initial level. The exception to this behavior is provided by the line M8-M9, which is farthest from the H9 heater. Over the next 60 days the Q_α values again increase. This behavior repeats itself three times in Figure 6.3, during the course of the heater experiment.

After the heater was turned off the Q_α values measured over the four lines show different modes of behavior. In line M7-M9 the Q_α values drop from a value of 22 at day 398 to a value of 12 14 days after the turn off of the heater at day 412. In the two lines M7-M6 and M8-M6 there is very little change for the 150 days which follow the heater turn-off. The Q_α values in line M8-M9 decrease first after the turn off until day 425 when the Q_α values increase to reach the same value at day 490 as before heater turn-off. After day 490 the Q_α values decrease slowly until day 580, when they decrease faster toward a value similar or below the value recorded prior to the heater test.

Effect of dewatering on monitor Q_α values

Dewatering of the 18 instrument holes started 41 days before heater turn-on. The dewatering data are presented in Figures 4.21-4.23. The water inflow increased in some of the boreholes when the heater was turned on. This higher level of inflow lasted between 70 - 100 days. The decrease of the inflow after 100 days coincides with an increase in the Q_α values which had been constant through the first 100 days of heating. There is no record of at which depth the water inflow occurred so no further conclusions can be drawn about the relationship between the Q_α values in the midplane and the behavior of the pore fluids.

Dewatering ceased at day 545, resulting in a change in the H9 heater midplane Q_α values. For the three lines M8-M6, M8-M9 and M7-M6 the onset of the decrease in the Q_α values is apparent. For line M7-M9 there is no decrease in Q following the termination of the dewatering. This is probably due to the large initial decrease in Q_α value following heater turn-off. The value obtained 150 days after the termination of the dewatering, which represents the last data point, is considerable smaller than the value at termination.

6.2   Survey Data

The calculated Q_α values from the 35 surveys in the 6 cross sections reveal the complexity of the interaction of the temperature increase, pore pressure, geology and direction of the propagation of the elastic waves. In this section all the surveys for each of the cross section will be discussed followed by sections on thermal effects on the attenuation. Finally a section on the effect from the dewatering on the Q_α values is presented.

Dewatering was performed daily in the U, T and C holes, shown in Figures 4.21 to 4.23, and Table 4.7. The bottom of these holes is at the level 30 on the abscissa on the depth/Q_α plot in Figures 6.6 to 6.11. The four monitoring boreholes were also dewatered (Table 4.6). The depth for this dewatering was 0.20 m below point 40 on the abscissa. The dates for which the M-boreholes were dewatered are also given in Table 4.6.

Observed attenuation changes

M7-M6 section

The Q_α values from the four surveys over the M7-M6 cross-section are shown in Figure 6.6. The curve marked "1" is the preheating curve. The most remarkable aspect of this curve, as with all the other preheating curves in the other five cross-sections, that there is no evidence for a related Q anomaly the low velocity zone found in the data. The Q_α values for the second survey (2) in this cross section at day 344 are maximum 2 m above the bottom of the M-holes. The third curve shows similar Q_α values to 2, but somewhat lower at depth than those for the second curves. The final survey, at day 701, has similar Q_α values to those recorded for the first survey.

M7-M8 section

For the second cross-section, M7-M8, the high Q_α values are also found in the lower part of the profile, as shown in Figure 6.7. Survey #2 at day 112 and survey #3 at day 348 are the two surveys which were performed over this cross-section during the operation of the heater. Note the result from survey # 2 in which despite 112 days of heating, the Q_α

values found in this cross-section did not change. No change occurred the first 112 days between the depths of the end points of the H9 heater despite thermal stresses of up to 50 MPa close to the heater borehole wall. Thus the Q_α values remained the same from day -44 to day 112. It is interesting to note that the Q_α values for the fourth survey (at day 425) are higher despite the fact that the heater had been turned off. It should a be noted that the increase in Q_α commenced at the lower end of the section and moved upwards. The Q_α values for the fourth survey also show a slight dip towards the lower end of the cross-section.

M8-M9 section

For the M8-M9 cross-section there appear to be more uniform changes of the Q_α value over the entire cross-section, as shown in Figure 6.8. In this section the temperature increase was moderate even at the closest point at the heater midplane level. The maximum temperature over this section was 45° C.

M6-M9 section

For cross-section M6-M9 the change in Q_α is small, as shown in Figure 6.9, but the change is still uniform with depth as in section M8-M9. This section, as is M8-M9, is a few meters from the H9 heater. The general behavior noted so far appears to prevail: i.e. that the first surveys show low Q_α values and that there is a slow increase with time, independent of the heater operation.

M8-M6 section

The two cross-sections where most of the survey data were collected where M8-M6 and M7-M9. The angle between the two cross-sections is 75°, and the distance between the holes in the two cross-sections is nearly identical, i.e. 4.181 and 4.202 m respectively. Furthermore, the temperature increase in the two sections is also very similar.

The Q_α values from 8 surveys from the M8-M6 cross-section are shown in Figure 6.10. The Q_α values for the four first surveys at days -44, -7, 20, and 111 changed very little. For the fifth survey, at day 118, there is a small but noticeable change, mainly between lines 30 and 39. The tendency for increasing Q_α values at the lower end of the cross-section continues for survey # 6 at day 341 and for survey # 7 at day 420. The maximum Q_α values for survey # 7 are found between lines 28 and 35. This represents a range of depths from 7 to 9 m below the floor of the drift. From a depth of 9 m to the bottom of the holes at 10 m the Q_α values tend to approach the ambient values. For survey # 6 and # 7 in Figure 6.10 there are also higher Q_α values between 1 and 2 m below the drift floor. The first data point below the drift floor which is at a depth of 0.9 m, shows a low value; this is probably caused by the blasting of the drift. The same effect is also noticeable in the velocity data from the same survey. An unexpected effect is seen in survey # 6 and # 7. The lowest Q_α values were found at the depth of the heater. For survey # 7 at day 420 the heater had been turned off, and in the same time interval the Q_α values began to increase between lines 17-24. The last survey (# 8), was performed at day 704. The Q_α values returned to the original ambient values both both above and below the H9 heater. Level with the heater the Q_α values are slightly higher in survey # 8 at day 704

than they were in survey # 1 at day -44.

M7-M9 section

The Q_α values from the M7-M9 cross-section, shown in Figure 6.11, also exhibit the complex behavior similar to that observed over the section M8-M6. There are however, a couple of features unique to this section. The Q_α values for the first four surveys at days -43, 0, 13 and at day 20 show no change. Survey # 1 has some features for which no explanation at this stage can be offered. The first survey at day -43 has higher Q_α values at the top and the bottom of the cross-section. The lowest values for survey # 1 correlate with the low-velocity zone. For survey # 5 at day 118 there is an increase of the Q_α value around line 32. In the sixth survey at day 349 the increase occurs at line 25. There is also a constant higher value of Q_α between lines 3 and 25 which is smaller but well sampled. For survey # 7 at day 419 the rock exhibited some very interesting behavior. The increase of Q_α values continues at the lower end of the cross-section below line 28. In the midplane of the heater the Q_α values dropped after the heater was turned off. This is the only cross-section where this was observed to occur. For survey # 8 the Q_α values returned to the original ambient values, except between lines 13 and 23 where low Q_α values were observed.

In Figure 6.12 two examples of amplitude spectra are shown for cross-section M8-M6 at two different times. Figure 6.12a shows the spectrum at day 341 when the H9 heater still was in operation and Figure 6.12b the spectrum at day 704. The difference in the spectral content, of which Q is a measure, is apparent. In Figure 6.13 the spectra from cross-section M7-M9 are shown. In Figure 6.13a the amplitude spectrum

from the survey during heater operation is shown. In Figure 6.13 b the survey performed at day 707 is shown, it also represents the last data collected over this cross-section.

Thermal effect on P-wave attenuation in the six cross section.

In this section the variations in attenuation of the P-waves observed in the cross hole surveys will be discussed. The thermal effects include a complex rock-fluid interaction when the temperature is raised from the ambient level. The highest temperatures were found between lines 8 and 25, between 2 and 6.25 m below the floor of the full-scale drift.

Gordon and Davis (1968) indicate that Q is generally independent of temperature at temperatures less than 150° C in dry rock. An increase in the attenuation at temperatures greater than 150°C in dry rock, as reported by Gordon and Davis (1968), is most likely due to thermal cracking of the rock caused by the differential thermal expansion of the different minerals. This suggests that the attenuation is not affected by the temperature *per se* up to temperatures encountered around the H9 heater. The small changes the Q_α values at depths between 2.25 and 6.25 m (line 9 and 25) during the operation of the heater as shown in Figures 6.6, 6.7, 6.10 and 6.11, should be noted. These figures show the cross sections which are closest to the heater and with the high temperatures shown in Figures 4.3, 4.4, 4.7 and 4.10. This is the level where the largest velocity increases were recorded. This points to the possibility that increased temperatures lower the Q_α values, or at least keep them constant, by decreasing the permeability so that the pore fluids cannot escape when they undergo thermal expansion. The higher thermal expansion of the pore fluids relative to the rock can even cause an

increase in the pore pressure. Heating of rock ahs been shown to decrease the permeability of granitic rock (Morrow *et al,* 1981) and to inhibited the drainage of the pore fluids. This phenomenon may have prevented closure of the water-filled fractures which exist above and below the heater. In only one case are the Q_α values clearly correlated with the operation of the heater. When the heater is turned off the Q_α values in the M7-M9 profile, as shown for survey # 7 in Figure 6.11, drop to low levels in the heater midplane. The low Q_α value is perfectly symmetric around the heater midplane, and is clearly connected with the effects of heating the rock. The low values are probably also associated with partial water saturation and possibly also as with thermally-induced cracking. In Figure 6.3 it is apparent that after the initial reduction in the Q_α values there is a period during which they increase. This is interpreted as occurring due to resaturation of the rock mass due to reduced porosity. An interesting effect is seen in Figure 6.11 at line 13 and at line 24, the depths of the two ends of the heater. Q increases from the low value at the heater midplane to a maximum value at these depths, and then decreases beyond these points. The reason for two peaks in Q_α values is speculative, but it appear possible that the sharp decrease in thermal stress upon turn-off of the H9 heater allowed water which was trapped above and below the heater to flow into the partially-saturated, relatively permeable zone at the heater midplane. This could have caused a decrease in the pore pressure around lines 13 and 24, and thus the fractures could close and the Q_α value increase. The central zone with very high attenuation is a good indicator of thermally-induced damage to rock and of the fractures already existing.

Effect of dewatering on survey Q_α values.

The large apparent effect of the dewatering on the attenuation of the P-waves was largely unexpected. The Q_α values for the first surveys in the six cross sections show no or little correlation with the P-wave velocities calculated from the arrival times of the compressional waves, or with the geological features mapped between the boreholes. In the four lines which pass close to the heater, M7-M6, M7-M8, M8-M6 and M7-M9 all show increasing Q_α values in the lower depth of the cross sections as time increases. The temperature increase in line 33 in section M7-M6 is shown in Figure 4.3 and it is seen that it does not exceed 10°C. This would indicate that the Q_α values recorded in the cross sections have no strict correlation with the elevated temperatures. When the dewatering of the rock mass is terminated the Q_α values also return to very near the values measured during surveys around day -44. In Nelson *et al.* (1982) it is reported that boreholes at the rear of the full-scale drift are subjected to a high in-flow of water throughout the the heater experiment. This can explain the small changes observed in Q_α, as it seems plausible that the magnitude of Q_α is mainly governed by the water content in the rock.

The Q_α values obtained in the heater midplane do not appear change over the first part of the heater experiment. Morrow *et al.* (1981), have shown that for a laboratory sample simulating a heated borehole and subjected to a temperature gradient with the borehole wall at a temperature of between 200° and 300° C, the permeability dropped by an order of magnitude over that measured under ambient temperature. Because of this low permeability the pore pressure was not able to dissipate, and so the Q_α values remained low. In Morrow *et al.* it is

shown that only 5 days after heater turn-on with a borehole tempera-
ture of 280°C, the permeability was reduced to 5 % of the original. Mor-
row *et al.* (1981) also reported that for a sample with a through-going
fracture there was an order of magnitude permeability decrease over a
period of a month when the temperature was elevated to 200° C. The
parallel-plate model analog for Darcy's law, discussed by Gale (1975), is
used to describe fluid flow in the case for which the permeability is
determined by the fractures rather than the porous matrix permeabil-
ity. Flow per unit crack length is given by

$$Q_f = (d^3 / 12v)(dP/dx) \qquad\qquad [6.16]$$

Where d is the separation between two parallel plates, v is the dynamic
viscosity, and $\dfrac{dP}{dx}$ is the pressure gradient in the x direction. Morrow *et
al.* (1981) tested this hypothesis on their sample and found that the
parallel-plate model was applicable to the hydrofractured surface they
used as the fracture in their experiment. As can be seen from the equa-
tion above, the permeability is proportional to the fracture width to the
third power.

Summary

It has been shown in this chapter how attenuation of ultrasonic P-
wave signals can be used to monitor with relatively high sensitivity the
effects of thermal and dewatering processes in an underground heating
experiment. It was shown that a low velocity zone seen clearly in the
data before heating does not have an accompanying anomaly in the Q_α
values. Q_α for the monitor data showed a gradual increase not corre-
lated strictly with the heater operation. There is a correlation between

Q_α variation and the termination of dewatering on day 545. Q_α values for the surveys stay fairly constant across the heater depths, but increase both above and below the heater. Again, their is no correlation between the increase of Q_α and the details of operation of the H9 heater. The attenuation of the P-waves continues to decrease in the deeper end of the cross section as long as the dewatering is continued. When the dewatering was stopped the Q_α in the survey cross sections returned to ambient values. The only place where a permanently lower Q_α was correlated with heating was in profile M7-M9 where the temperatures exceeded 130° C. This may be an important indication that this temperature was sufficient to induce extensive micro fracturing.
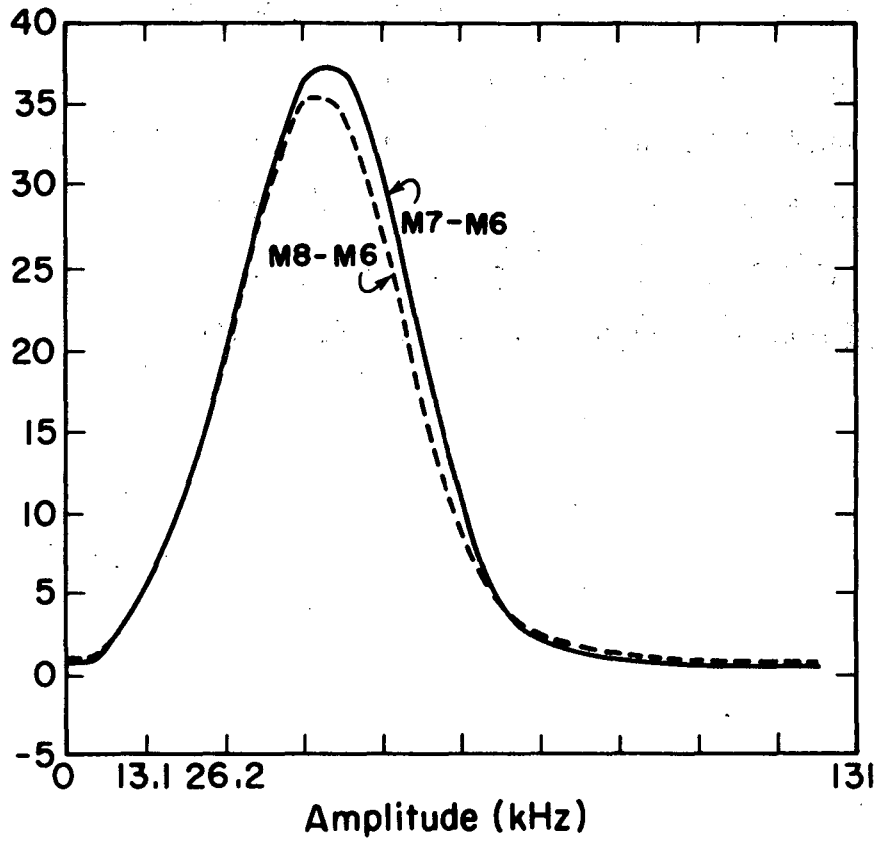
XBL838-2188

Fig. 6.1 0-125 kHz amplitude spectra for cross-section M8-M6, survey # 8 and cross-section M7-M6 survey # 3. The amplitude spectra are obtained by averaging all the signals in each cross-section.
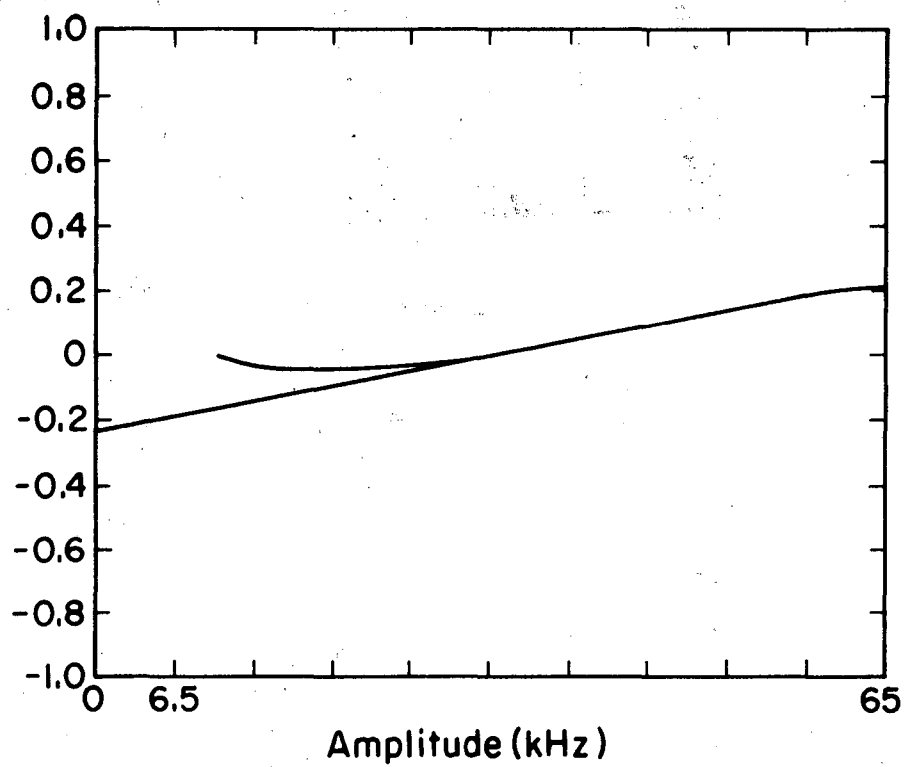
Fig. 6.2 Natural logarithm of the ratio of the amplitude spectra shown in Figure 6.1. The straight line is a least squares linear fit to the ratio for the values between 25 and 50 kHz.
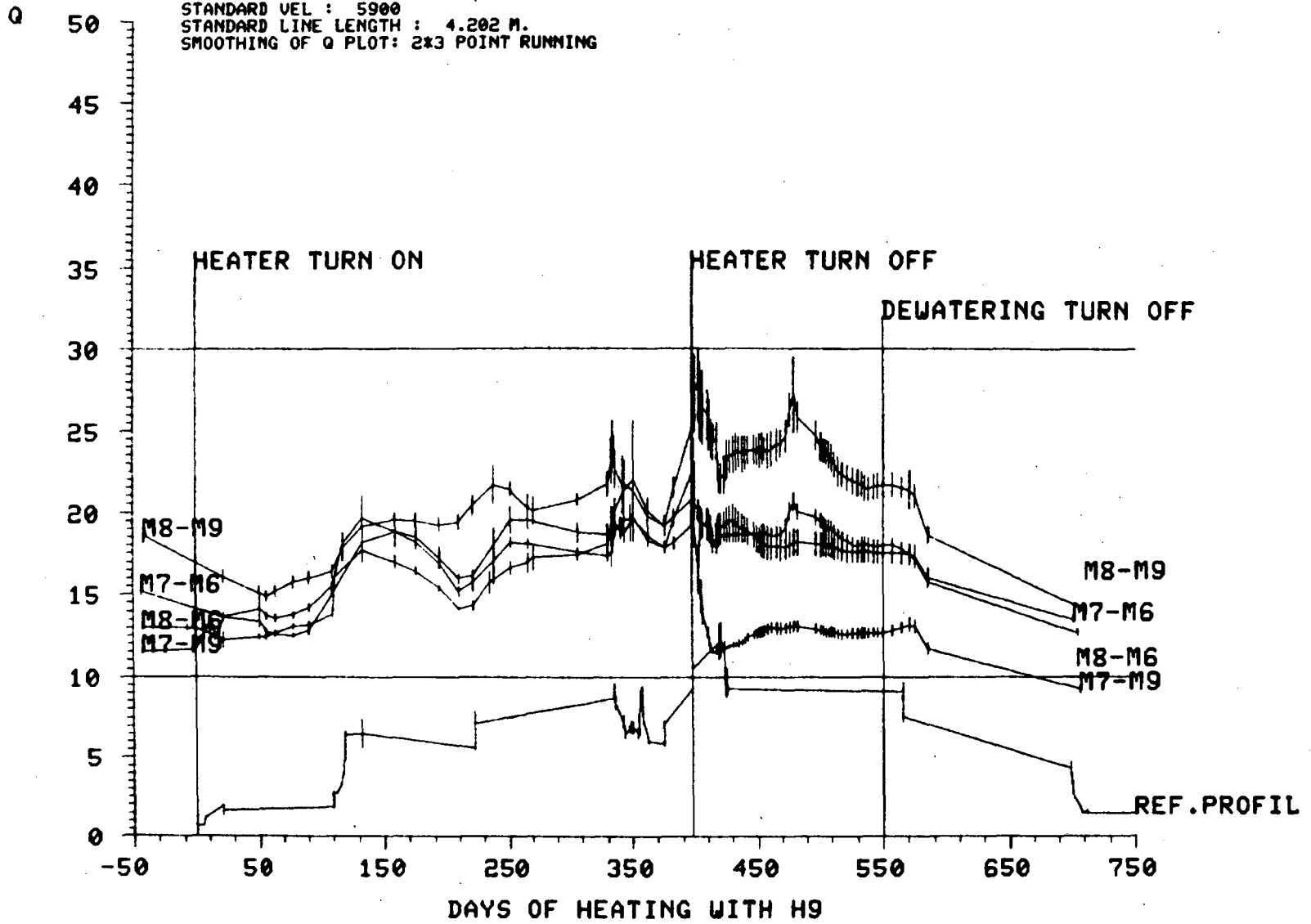
Fig. 6.3 Q_a for cross hole signals over four monitor lines in the heater midplane and for the reference line (Note that the scale for the reference line has a separate scale).

M7-M6,MON.P-WAVE SPECTRA,DE:0.33MS,7CE-CWIKO,SPECTOOTH,DAY:-44-+701,810415
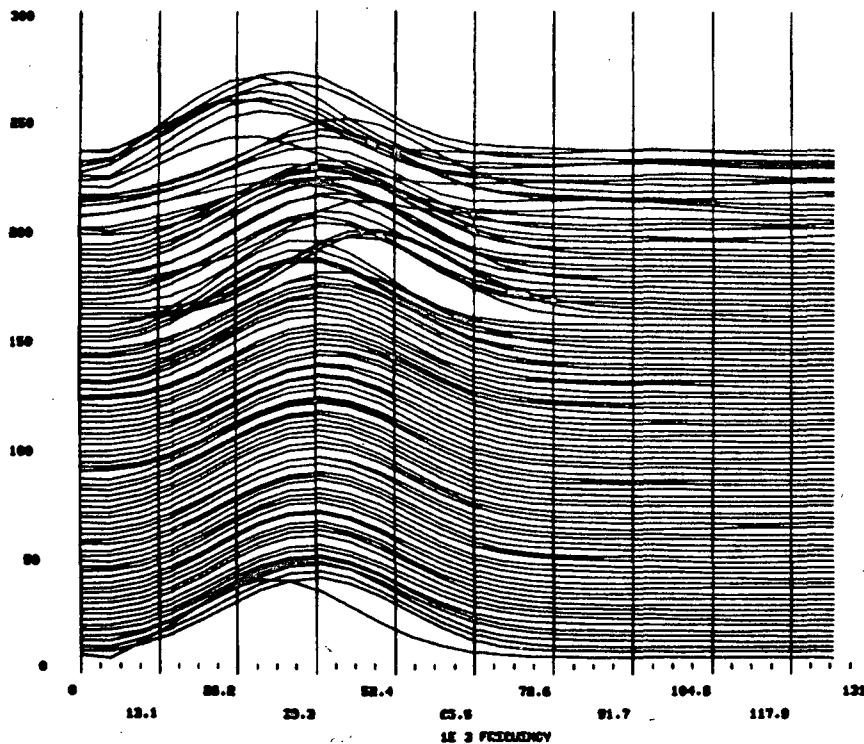
M8-M9,MONITOR, AMPLITUDE SPECTRA OF P-WAVES, DELAY:.690MS, AVE: 1-8, 4/26/81
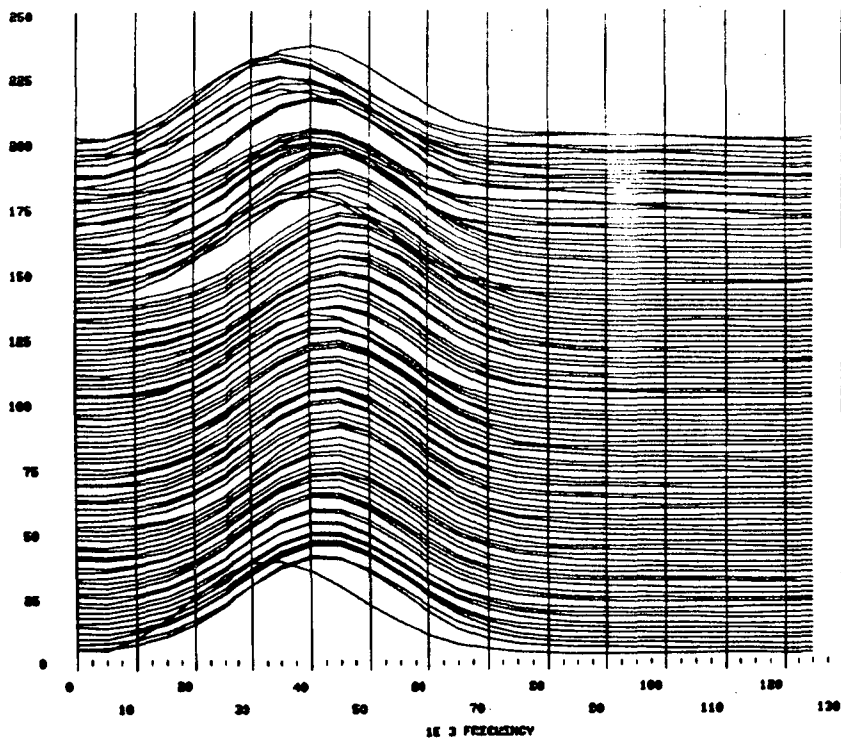
Fig. 6.4 0-125 kHz amplitude spectra for the monitor signals in lines M7-M6 and M8-M9 in the H9 heater midplane. The upper traces in each figure represent the amplitude spectra from the first P-waves recorded. In Table D:1.1 the day #, the Q-values and the P-wave velocities for each of the signals are given. In Table D:1.2 the corresponding values are given for cross section M8-M9.
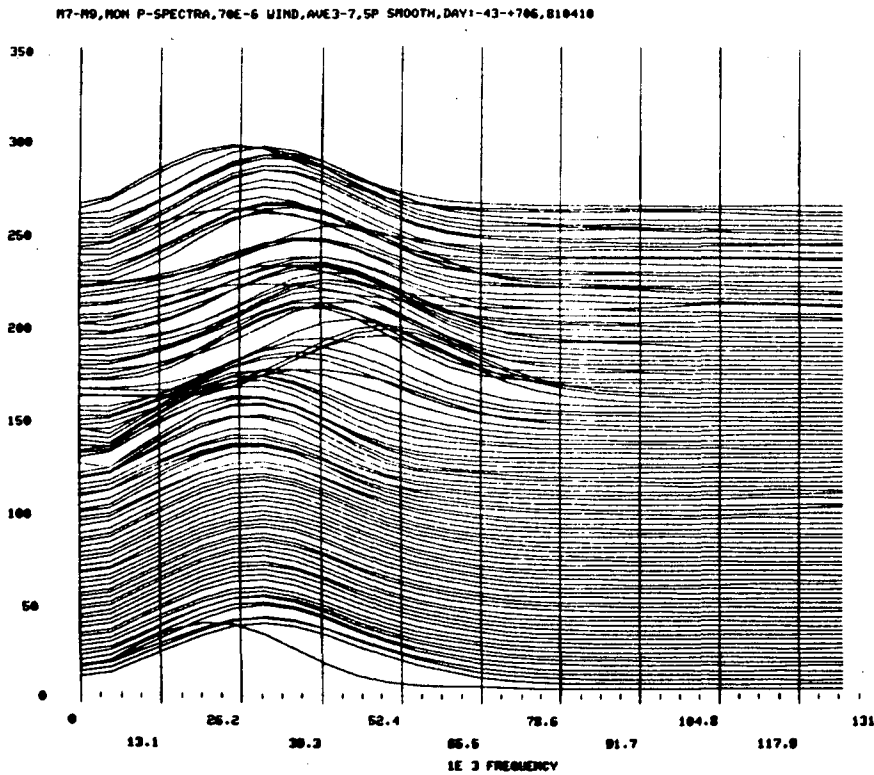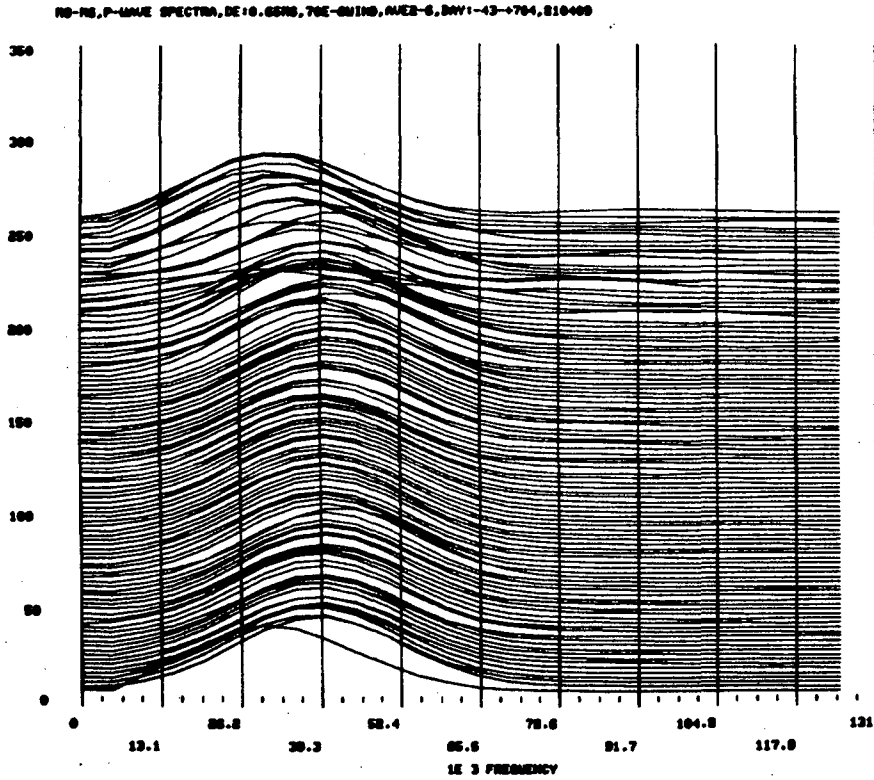
Fig. 6.5 Amplitude spectra for the monitor signals in lines M8-M6 and M7-M9 in the H9 heater mid-plane. The upper trace in each figure represent the amplitude spectra from the first P-waves recorded in each cross section. In Table D:1.3 the day #, Q values and P-wave velocities are given for cross section M8-M6 and the corresponding information for cross section M7-M9 is given in Table D:1.4.

CROSS SECTION : M7-M6
STANDARD FILE : M79PA.42
STANDARD Q : 50
STANDARD VEL : 5900
STANDARD LINE LENGTH : 4.202 M.
SMOOTHING OF Q PLOT: 2*3 POINT RUNNING

H9 HEATER, 3.6 KW

Fig. 6.6 Q_α for surveys in cross-section M7-M6 at Julian days -44(1), 344(2), 424(3) and 701(4).

Z=338.75 M.   LINENUMBER FROM DRIFTFLOOR:0.25 M BETWEEN POINTS   Z=348.75 M

CROSS SECTION : M7-M8
STANDARD FILE : M79PA.42
STANDARD Q : 50
STANDARD VEL : 5900
STANDARD LINE LENGTH : 4.202 M.
SMOOTHING OF Q PLOT: 2*3 POINT RUNNING

H9 HEATER, 3.6 KW

Z=338.75 M.   LINENUMBER FROM DRIFTFLOOR:0.25 M BETWEEN POINTS   Z=348.75 M
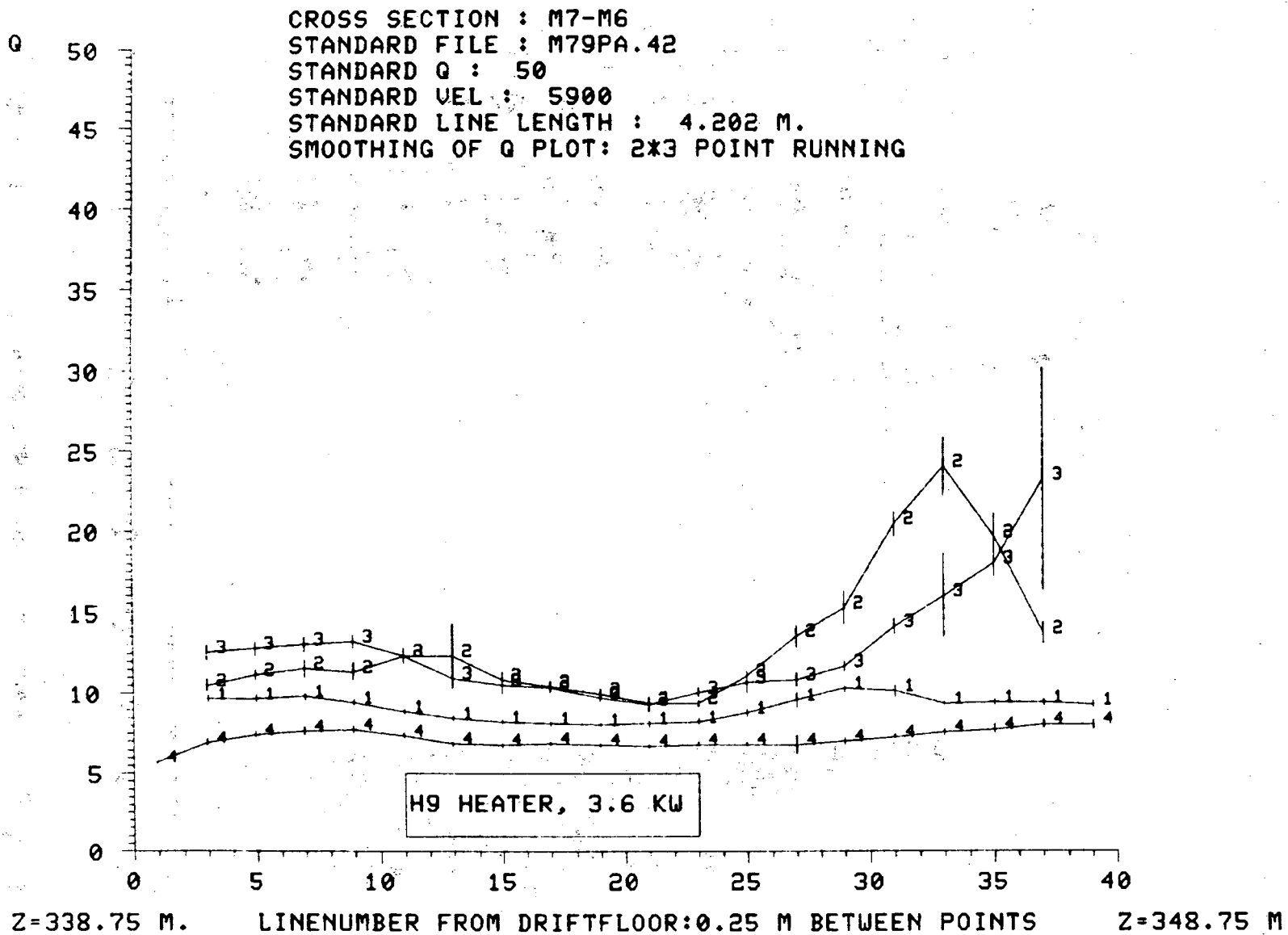
Fig. 6.7 Q_a for surveys in cross-section M7-M8 at Julian days -44(1), 112(2), 348(3), 425(4) and 708(5).

CROSS SECTION : M8-M9
STANDARD FILE : M79PA.42
STANDARD Q : 50
STANDARD VEL : 5900
STANDARD LINE LENGTH : 4.202 M.
SMOOTHING OF Q PLOT: 2*3 POINT RUNNING

H9 HEATER, 3.6 KW

Z=338.75 M.   LINENUMBER FROM DRIFTFLOOR:0.25 M BETWEEN POINTS   Z=348.75 M
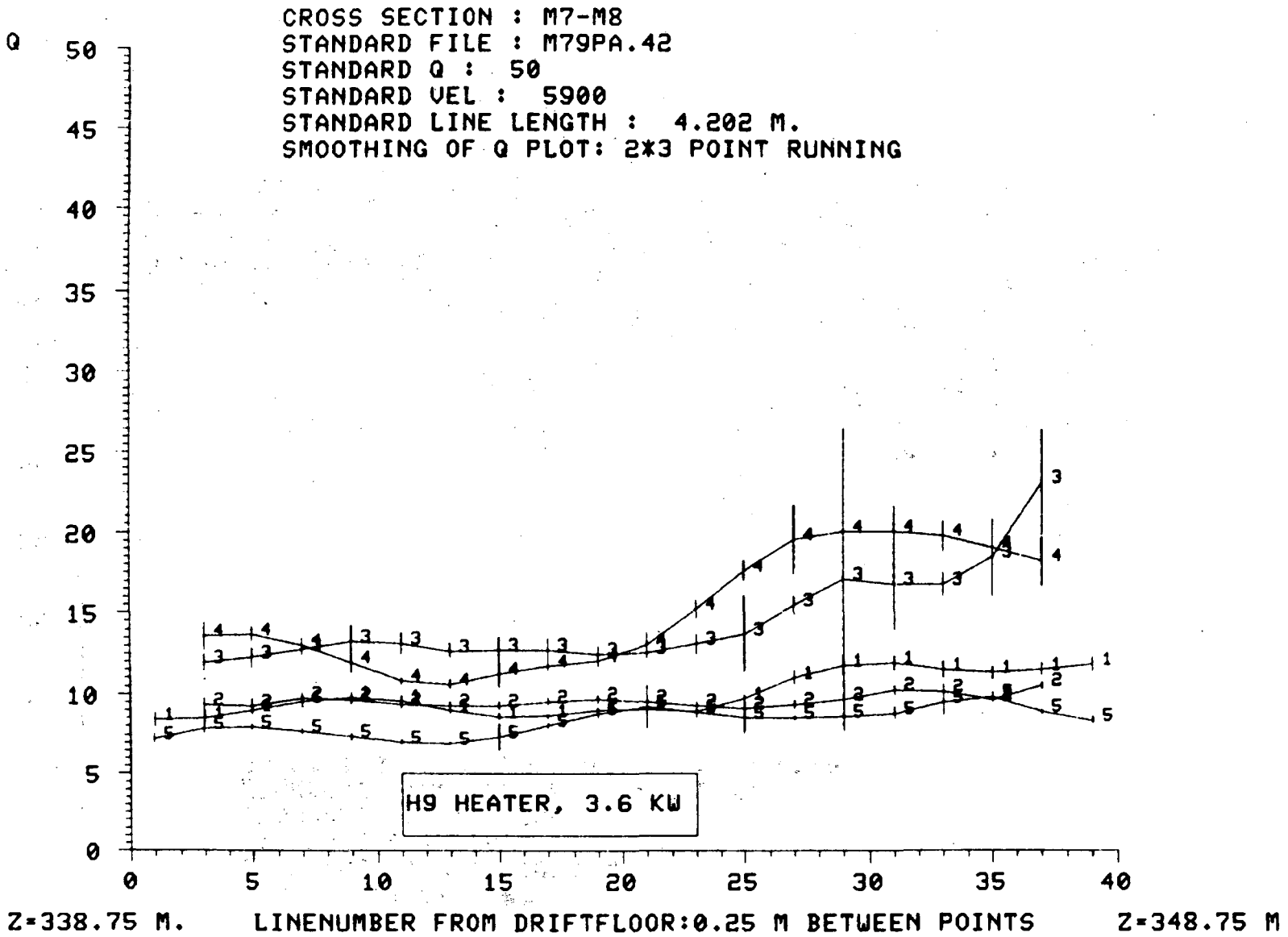
Fig. 6.8 Q_a for surveys in cross section M8-M9 at Julian days -42(1), 118(2), 343(3), 425(4) and 711(5).
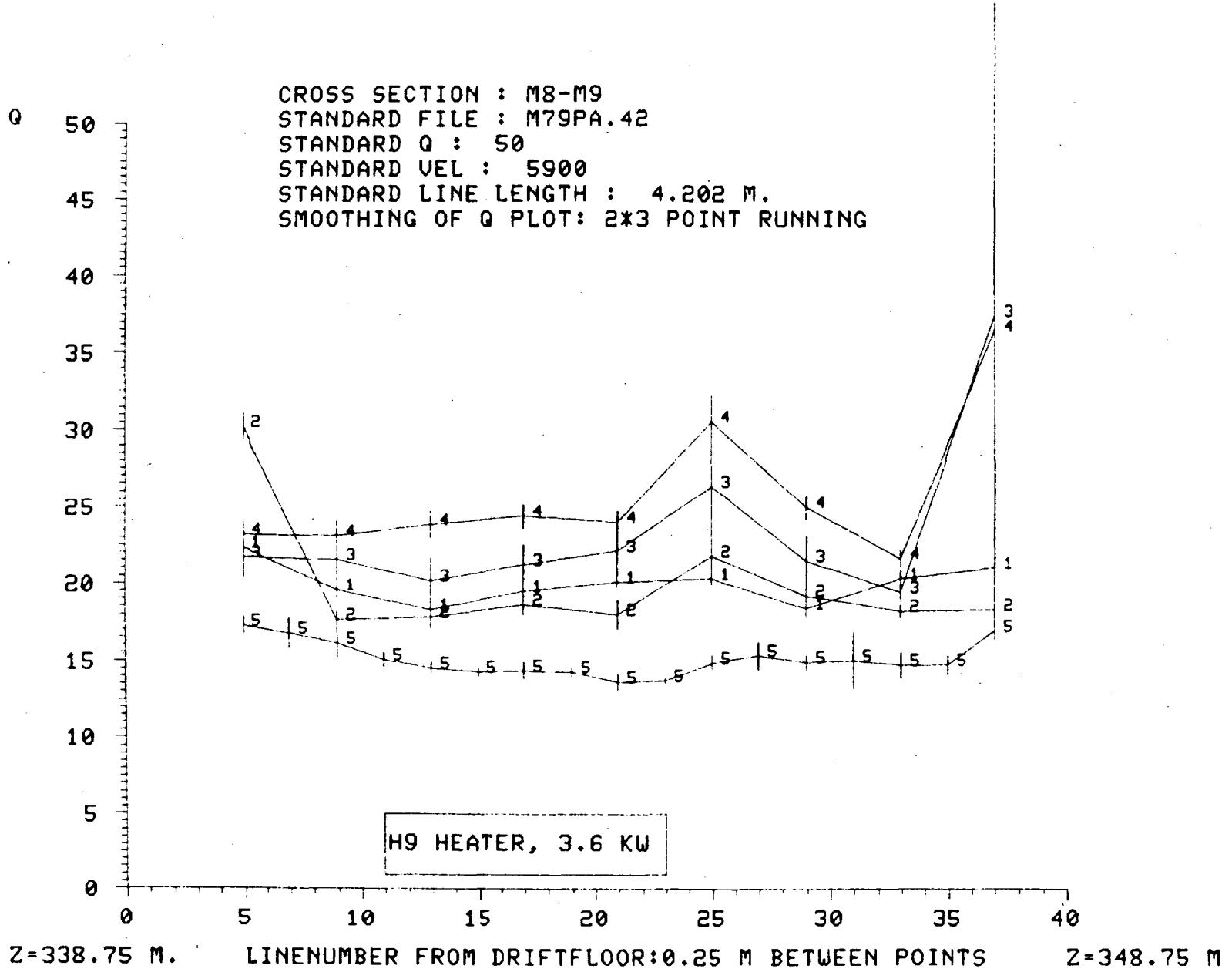
CROSS SECTION : M6-M9
STANDARD FILE : M79PA.42
STANDARD Q : 50
STANDARD VEL : 5900
STANDARD LINE LENGTH : 4.202 M.
SMOOTHING OF Q PLOT: 2*3 POINT RUNNING

H9 HEATER, 3.6 KW

Z=338.75 M.   LINENUMBER FROM DRIFTFLOOR:0.25 M BETWEEN POINTS   Z=348.75 M

Fig. 6.9 Q_a for surveys in cross-section M6-M9 at Julian days -42(1), 119(2), 343(3), 426(4) and 710(5).
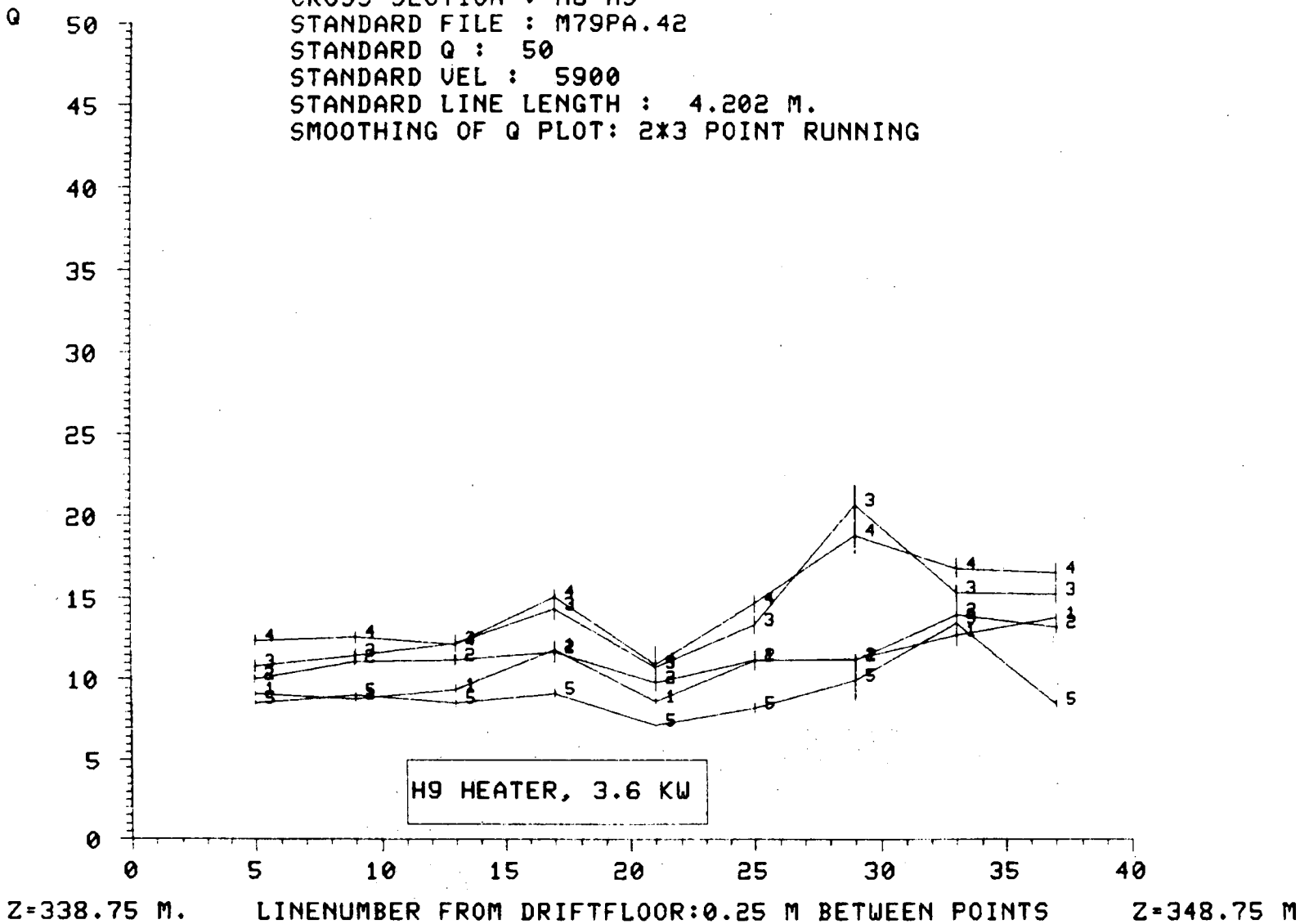
CROSS SECTION : M8-M6
STANDARD FILE : M79PA.42
STANDARD Q : 50
STANDARD VEL : 5900
STANDARD LINE LENGTH : 4.202 M.
SMOOTHING OF Q PLOT: 2*3 POINT RUNNING

H9 HEATER, 3.6 KW

Z=338.75 M.   LINENUMBER FROM DRIFTFLOOR:0.25 M BETWEEN POINTS   Z=348.75 M
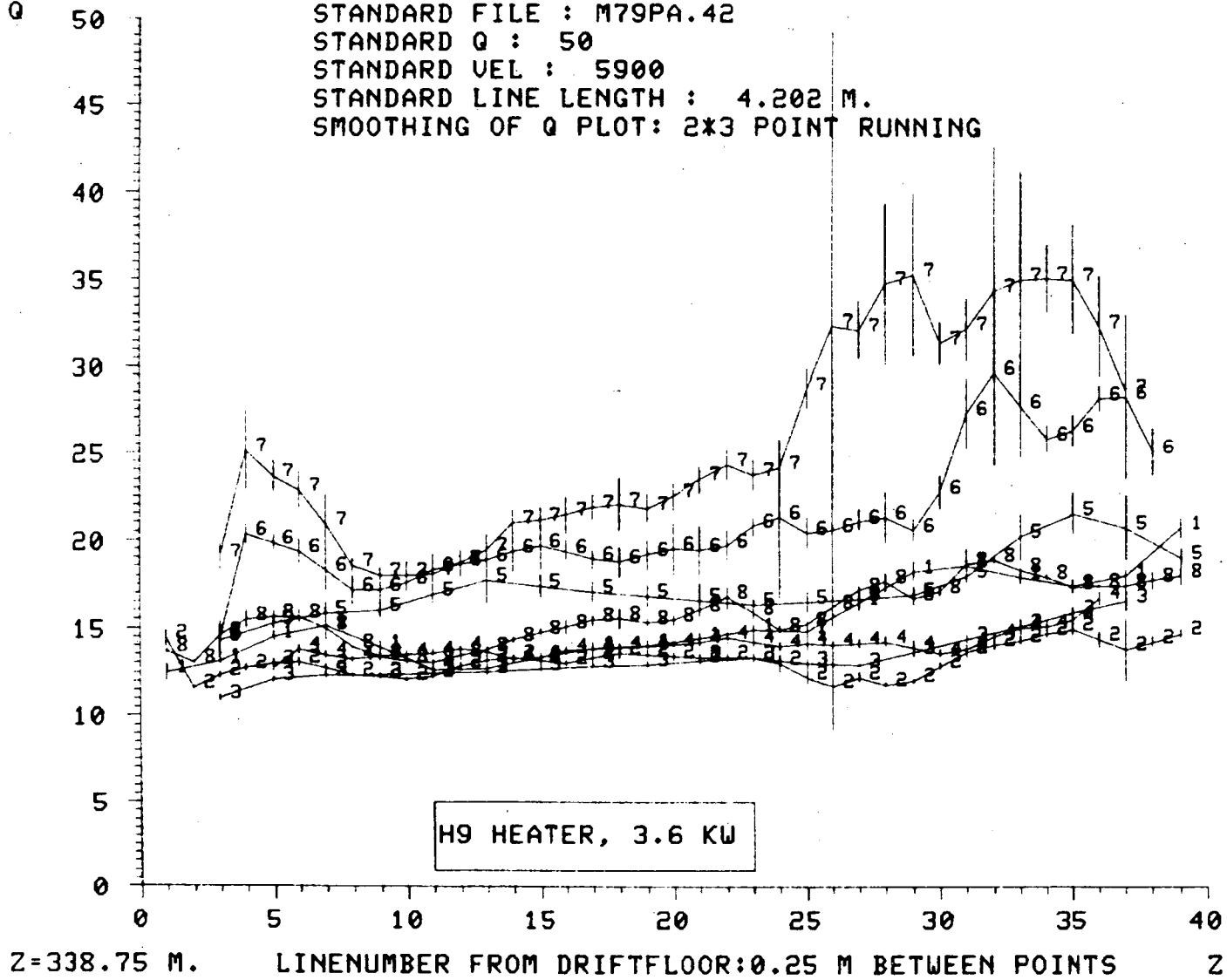
Fig. 6.10 Q_a for surveys in cross-section M8-M6 at Julian days -4-4(1), -7(2), 20(3), 111(4), 118(5), 341(6), 420(7) and 704(8).

CROSS SECTION : M7-M9
STANDARD FILE : M79PA.42
STANDARD Q : 50
STANDARD VEL : 5900
STANDARD LINE LENGTH : 4.202 M.
SMOOTHING OF Q PLOT: 2*3 POINT RUNNING

H9 HEATER, 3.6 KW

Z=338.75 M.   LINENUMBER FROM DRIFTFLOOR:0.25 M BETWEEN POINTS   Z=348.75 M

Fig. 6.11 Q_a for surveys in cross-section M7-M9 at Julian days -43(1), 0(2), 13(3), 20(4), 111(5), 349(6), 419(7) and 707(8).

184
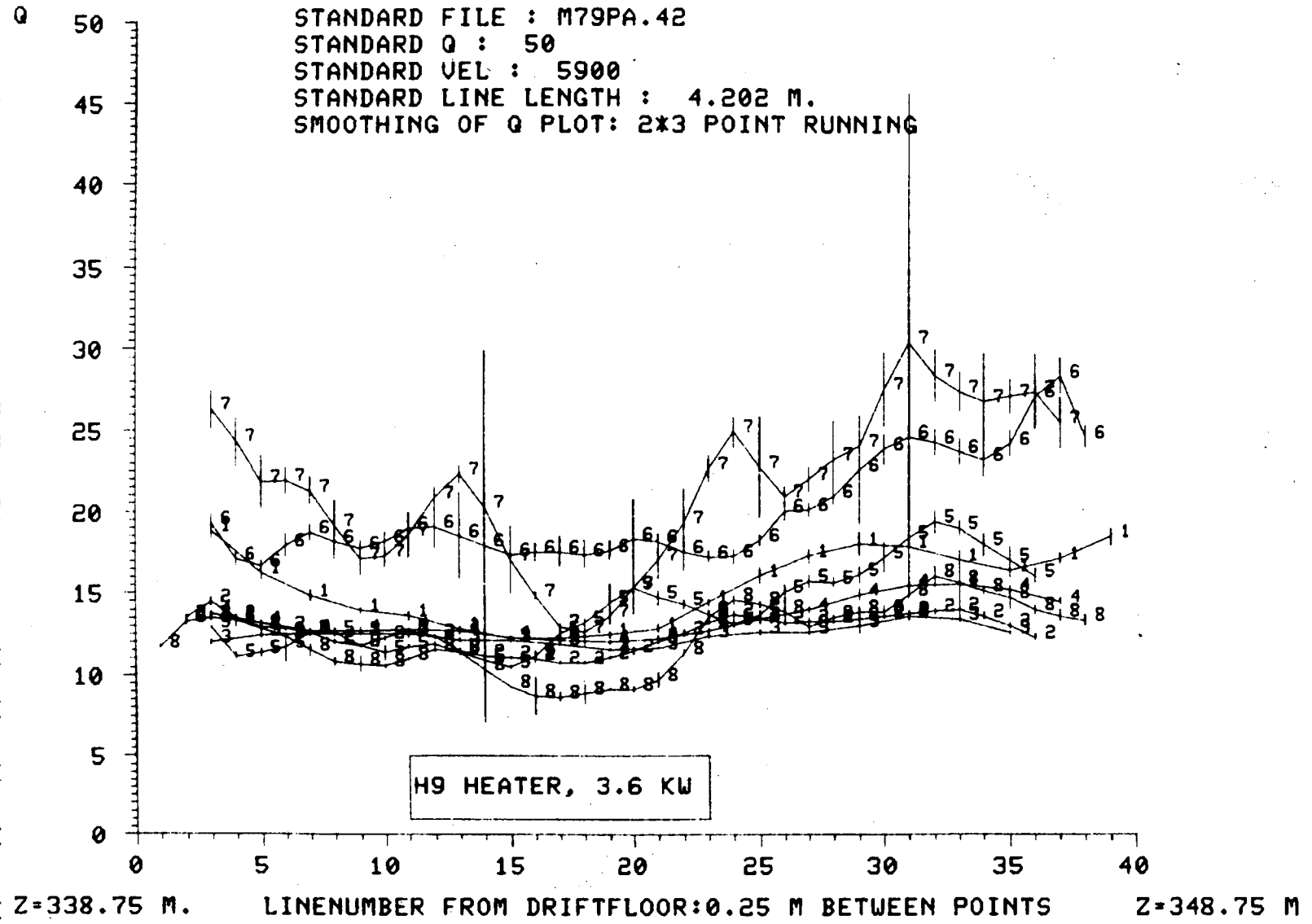
M8-M6, SURVEY #8, DAY# 341, 31 JULY 1979, P-WAVE AMPLITUDE SPECTRA
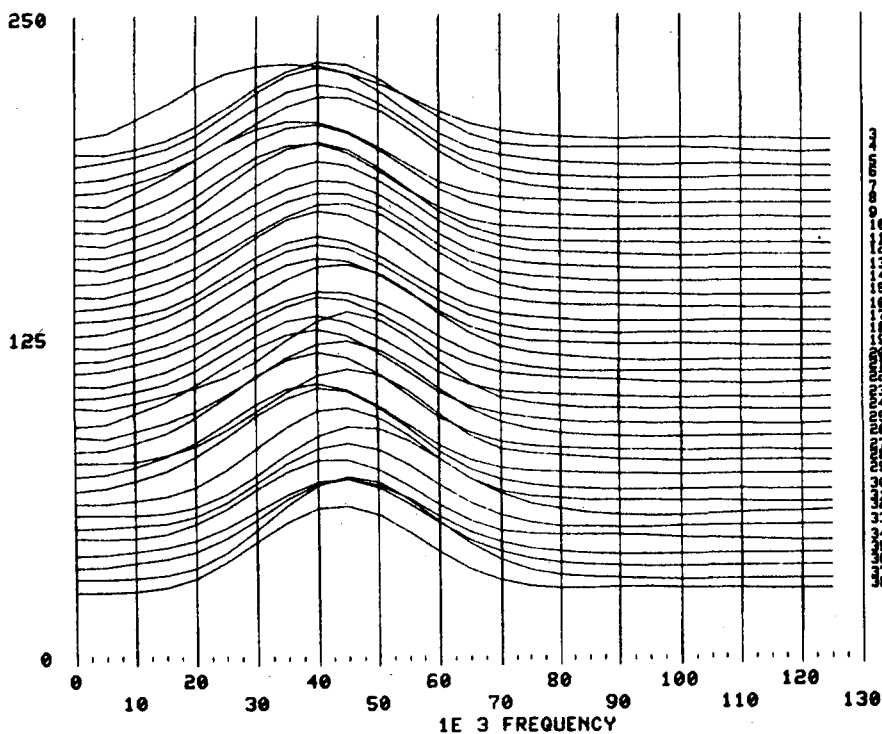
M8-M6, SURVEY #10, DAY# 704, 28 JULY 1980, P-WAVE AMPLITUDE SPECTRA
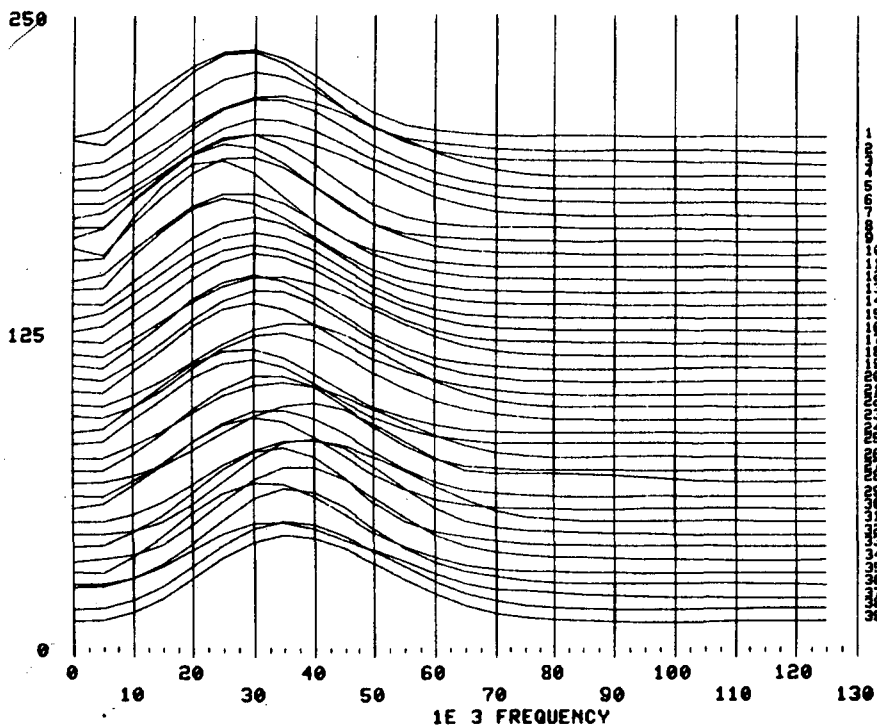
Fig. 6.12a Amplitude spectra for cross-section M8-M6 survey # 8, 349 days after heater turn on. Each line represents the relative distance along the cross-section. 6.12b Amplitude spectra for cross-section M8-M6 survey # 10, 704 days after turn on of the H9 heater.

M7-M9, SURVEY #9, DAY# 349, 8 AUGUST 1979, P-WAVE AMPLITUDE SPECTRA

M7-M9, SURVEY #11, DAY# 707, 30 JULY 1980, P-WAVE AMPLITUDE SPECTRA
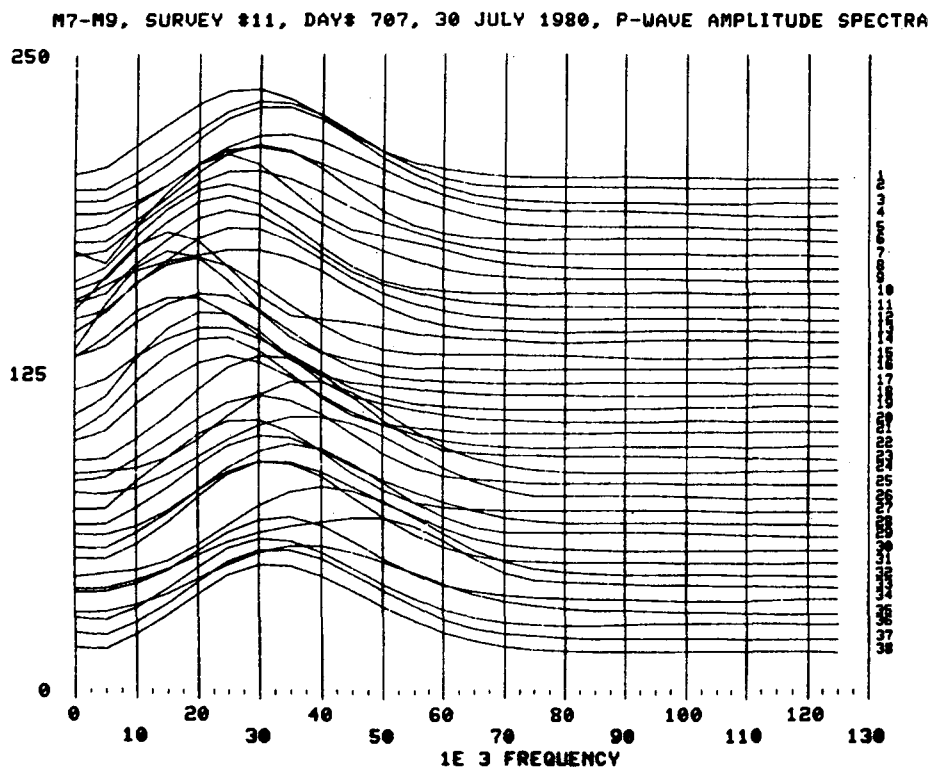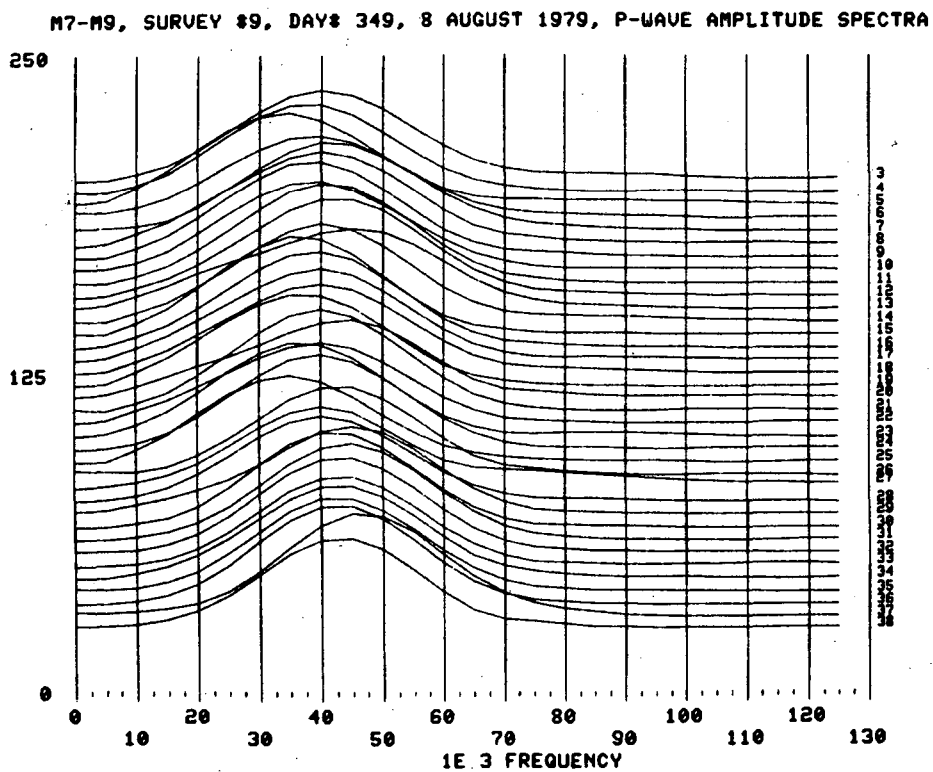
Fig. 6.13 a Amplitude spectra for cross-section M7-M9 survey # 9, 349 days after the heater turn on. The distance between each line represents a vertical spacing of 0.25 m. 6.13b Amplitude spectra for cross-section M7-M9, survey # 11, 707 days after the H9 heater was turned on.

7. LABORATORY DATA

A number of cyclic uniaxial compression tests were conducted on specimens of Stripa granite, during which the propagation of compressional and transverse waves was studied. The travel-times were measured and waveforms digitized for each test at 16 uniaxial stresses in the range 2.5 MPa to 51 MPa, and returning to 2.5 MPa. This was done for 11 specimens, both dry and water-saturated. Eight of the specimens were from the H9 heater area and 3 from the H10 area. P- and S-wave travel-times and waveforms were also collected for two of the specimens from the H9 area over a range of saturations from zero to 100 %. Laboratory testing of the granitic rock played an important role in the acoustic work performed during the Stripa experiment. Despite the considerable degree of control achieved during the field experiment on parameters such as length of transmission path, fracture density, fracture position and water flow, several parameters remained which were not well controlled. These included important factors such as saturation, field stresses, thermal stresses and pore pressure. The laboratory work has provided the necessary control for V_p, V_s, Q_α and Q_β for different stresses and saturation levels.

7.1 Introduction

Specimen were selected to represent rock in two orthogonal directions. The reason being that the two main profiles M7-M9 and M8-M6 are 75° apart. Fortunately, horizontal drill-holes from the extensometer drift were drilled approximately parallel to the two sections, as indicated in Figures 1.7 and 1.8. Appreciable differences in the velocities and the

elastic moduli were recorded for the different specimens. Eight speci-
mens came from the H9 area, as shown in Figure 7.1. Four of the speci-
mens come from boreholes parallel to the M8-M6 cross section (Figure
7.2) and four came from boreholes which are parallel to the M7-M9 cross
section (Figure 7.3). In Figures 7.1 to 7.3 the exact position is given
from which each of the core specimens were recovered. Three of the
specimens come from the H10 area: specimen # 3 from borehole E29
(Figure 7.4) which was drilled before the heater experiment for the
installations of instruments. Two of the specimens are from the DBEX-1
drill hole indicated in the same figure. This borehole was drilled after
completion of the heater experiment to investigate the possible damage
on the rock from the heating. Results from this investigation have been
reported by Flexser *et al.* (1982).

Assuming that a material is isotropic, homogeneous and elastic it is
possible, knowing the density, to determine the elastic moduli by
measuring the compressional (P) and transversal (S) wave velocities.
This procedure has been used here to determine the moduli as a func-
tion of uniaxial stress for the 11 cylindrical core specimens.

In addition to the elastic moduli it proved important also to obtain
values of the P and S-wave attenuation as a function of stress and
saturation in the laboratory in order to verify the low Q-values (for gran-
itic rocks) calculated from the field data using the spectral ratio tech-
nique (Chapter 6).

In this chapter a method to perform and handle spectral ratio cal-
culations on large volumes of data with a mini-computer will be
presented. Both the field and the laboratory data represent elastic-wave
propagation phenomena, and so are handled principally in the same way.

The large difference in the frequency band used: for the field data 25 - 50 khz and for the laboratory data 0.5 - 1.0 MHz, make it necessary to use windows of different lengths. For each set of data the first step was to digitize the waveforms several times and then to average them to improve the signal-to-noise ratio.

Assuming that Q (the Quality factor) which is related to the attenuation coefficient α by

$$A(f) = A_0 e^{-\alpha x} = A_0 e^{-\frac{\pi f x}{VQ}} \qquad [7.1]$$

and

$$Q = \frac{\pi f}{\alpha V} \qquad [7.2]$$

is independent of frequency, a procedure described by Toksoz *et al.* (1979) has been used to calculate Q_α and Q_β where α refers to compressional waves and β to transversal waves (see details in Chapter 6). Computer programs have been developed for a PDP 11-34 with a Digital Processing Oscilloscope (DPO) which make it possible to calculate both the moduli and the Q-values interactively.

7.2 Experimental Method

The moduli can be calculated from the P and S wave velocities and the density of the rock using the following relations ships;

$$V_p = \left[\frac{K_d + 4/3 G_d}{\rho} \right]^{\frac{1}{2}} \qquad [7.3]$$

and

190

$$V_s = \left[\frac{G_d}{\rho} \right]^{\frac{1}{2}} \qquad\qquad [7.4]$$

where K_d = dynamic bulk modulus, G_d = dynamic shear modulus ρ = density. The following relationships have been used to calculate the dynamic values of Poisson's ratio and the moduli:

$$v_d = \left[\frac{V_p^2/V_s^2 - 2}{2(V_p^2/V_s^2 - 1)} \right] \qquad\qquad [7.5]$$

and

$$E_d = 2(1 + v_d)\rho V_s^2 \qquad\qquad [7.6]$$

where v_d = Poisson's ratio and E_d = Youngs modulus. Using the following relationships the shear and the bulk modulus have been calculated :

$$G_d = \frac{E_d}{2(1 + v_d)} \qquad\qquad [7.7]$$

and

$$K_d = \frac{E_d}{3(1 - 2v_d)} \qquad\qquad [7.8]$$

The method consists of transmitting ultrasonic waves through a specimen by a transmitter mounted at one end of the cylindrical core and a receiver mounted at the other end of the specimen, as shown in Figure 7.5a. In Figure 7.5b the average values of V_p and V_s for 21 specimen from the full-scale drift is shown. The specimen were tested under six different uniaxial loads (Paulsson and King 1980). In Figure 7.5c the dynamic moduli calculated from the velocities in previous figure are

shown. The static modulus was obtained simumtaneously and the difference between static and dynamic modulus is indicated in Figure 7.5c. It is shown that for dry specimen the static and dynamic modulus agree very well. When the specimen are saturated the dynamic moduli increase and the static moduli decrease. In order to calculated the Q-values an aluminum standard was used with the same geometry and dimensions as the core specimens. For these experiments a standard cylinder made of rolled aluminum was used, with Q_α and Q_β equal to approximately 2000. The actual values of Q_α and Q_β for the aluminum are probably higher: measurements made by the resonant bar technique indicate values of 10^4 for Q_α and Q_β (King: 1982 personal communication). However, the error introduced using 2000 rather than 10^4 for a specimen with a $Q_\alpha = Q_\beta = 50$ and a compressional velocity of $V_p = 5900 m/s$ is less than 2%, and it shows a Q-value which is lower than the correct value. With Q_s being the Q value for the standard, the two values considered here are $Q_{s1} = 2000$ and $Q_{s2} = 10000$. The compressional velocity for the aluminum was found to be $V_p = 6362$. The P-wave velocity in this example is 5900 m/s. Using $\gamma = \dfrac{\pi}{Q \times V_p} \gamma_r$ for the specimen is $\gamma_r = 1.0649 \times 10^{-5}$ with the Q for the rock being set to 50. Using the equation $s = (\gamma_r - \gamma_{s1,2})x$ s_1 for standard 1 = 8.32×10^{-7} and s_1 for standard 2 = 8.48×10^{-7}. γ_{r1} is the γ obtained for the first γ_{s1} using $\gamma_r = \left[\dfrac{s_{1,2}}{x} + \gamma_s \right]$ with the γ_s being the γ for Q=2000. so now we find:

$$\gamma_{r1} = 1.0649 \times 10^{-5}$$

giving

$$Q = 50$$

and for

$$\gamma_{r2} = 1.0846{\times}10^{-5}$$

giving

$$Q = 49.1$$

The ultrasonic pulses transmitted through the rock specimens were generated by a stacked system of P and S wave piezoelectric crystals mounted in an aluminum housing, as shown in Figure 7.5a. The transducer system has been described by King (1970). Aluminum is a suitable material because it has a similar acoustic impedance to granite thus little energy is reflected from the transducer - specimen interface. The transducers and the core specimens were mounted in a Carver press and subjected to unconfined uniaxial loading.

Wyllie *et al.* 1958 showed that for competent rock at low axial stresses the wave propagation behavior is similar for both uniaxial and hydrostatic loading at the same stress levels. While it appears to not be a disadvantage to have only uniaxial loading while the propagation properties of a core specimen are investigated, that is apparently not true for investigations of the attenuation properties. In an analysis of Q_β data in this study it is apparent that uniaxial stress fails to close the fractures which affect the axially transmitted shear waves. For investigating the attenuation properties it is a serious disadvantage to not have confining stress but it was the only equipment available for this work. When the saturated specimens were tested a large discrepancy was noted between the P-wave velocities on the loading cycle and those

measured during the unloading cycle. This can be explained by the following behavior: when the specimen is compressed the water is squirted out of the fractures; when the specimen is unloaded the fractures open, and thus become only partially saturated.

The press used had a maximum range of 0 - 11.0 tonnes, which results in a 0 - 51 MPa uniaxial stress on the specimens tested. This is approximately 25 % of the uniaxial strength of the Stripa granite reported by Swan (1978) as 207.6 ± 31.4 MPa at 20° C. The value was reported to be constant at temperatures to 150° C. The uniaxial strength was defined by the peak of the stress strain curve for uniaxial stress.

For the aluminum standard, P and S wave signals were obtained under 10 MPa axial stress. In Figure 7.6 the P and S waves for the aluminum standard are shown. Also shown are the truncated waves and the their amplitude spectra. These spectra were then used for all the laboratory work described in this thesis. In Figure 7.7 a similar set of data is shown for specimen # 1 in a dry condition. The ratio between the spectra obtained from the aluminum cylinder and the granite specimens for both the P and the S waves give the result is shown in Figure 7.8. These spectral ratios are plotted on a semi-logarithmic scale. The frequency band used for the Q_α and Q_β calculations is 0.5 - 1.0 MHz. A linear regression is applied to the data over this frequency interval. This is a similar technique to the one discussed for the field measurements in Chapter 6.

The amplitude of plane waves for a standard and for a test specimen have been given in Chapter 6 and the same procedure is followed for the signal obtained in the laboratory test.

When $\ln\left[\dfrac{A_1}{A_2}\right]$ is plotted as a function of f, γ_2 is obtained from the slope of the line by s = slope,

$$s = (\gamma_2 - \gamma_1)x \qquad\qquad [7.9]$$

which leads to

$$\gamma_2 = \frac{s}{x} + \gamma_1 \qquad\qquad [7.10]$$

This method is suitable for specimens with a relatively low Q (i.e. the slope of s is large). When Q increases, the slope of the line is small and the determination of Q become more uncertain.

The error bars on the Q-plots relate to the uncertainties in the coefficients for the least-squares fit of a straight line to the data between 0.5 and 1.0 MHz. This has been discussed in detail in Chapter 6.

7.3 Experimental Procedures

The velocity measurements were made by measuring the delay of the impulse arrival relative to the trigger from the pulsing unit. A Tektronix Digital Processing Oscilloscope (DPO) with a digital delay trace was used to measure the arrival time of the signals. In Figure 3.3 a block diagram of the signal analysis system is shown. In order to correct for instrument delay, the transducers were clamped together in face-to-face contact and the times of arrival of P and for S-waves were recorded. The instrument delay for P-waves was found to be 5.47×10^{-6} s and for S-waves 9.41×10^{-6} s. These values were subtracted from all laboratory arrival times, and they should also be taking into account when the arrival times are read from the digitized traces in this chapter and in

Appendix E.3.

The times of wave arrival were measured to an accuracy of $\pm 20 \times 10^{-9}$ seconds or $\pm 0.1\%$. The specimen lengths were carefully measured to $\pm 10 \times 10^{-6}$ meter.

No correction was made for the shortening of the specimen during compression, but using an E of 70 GPa it is easily shown that the axial strain corresponding to an axial stress of 51 MPa is 7.3×10^{-4}. For a specimen length of 80 mm this corresponds to a change in length of 0.06 mm. This change in length is less than 0.1 %, and can therefore be neglected. The P and S waveforms for each axial load were digitized twice and then averaged before the signal was stored on a floppy disc. This was done automatically at each increment of axial load. The arrival times for the P- and the S- waves were also recorded from the digital display on the DPO and were used to calculate the velocities. Each specimen was tested at 16 increments of load. It is important that the original signal is digitized and stored, because it is then possible to post-process the data in different ways to reach the optimum result. An example of 16 waveforms which have been digitized and stored on floppy disc is shown in Figures 7.9 a and b. The P-waveforms are from specimen Stripa # 2: the upper figure is for the specimen after it was dried in a convection oven for 48 hours at 70° C. Figure 7.9b, is for the specimen after it had been saturated. In Table 7.1 the load, the corresponding uniaxial stress, the seismic velocities and the moduli are given for specimen # 2 in a dry and saturated state. The saturation procedure is as follows: the specimen is put in a vacuum chamber for 48 hours in approximately 5 millitorrs vacuum; then water is allowed to submerge the specimen in the chamber; finally the specimen is left under vacuum for at

least a further 24 hours. The saturation procedure is a well established procedure which yields high degree of saturation.

For the first experiments described in this chapter the specimens were dried in a convection oven at $70°$ C. This procedure probably did not dry out the specimen more than down to 20-30 % saturation. This will be discussed later when the results of an experiment for which the velocities and the attenuation as a function of saturation are investigated.

One of the experiments concerned an investigation of the velocities and attenuation of P and S-waves as a function of saturation. Specimens # 1 and # 2 were first saturated according to the procedure described above and then tested in this saturated state. The specimens were carefully weighed when they were saturated. Table 7.2 gives the values for specimen # 1 and Table 7.3 gives the values for specimen # 2. The specimens were weighed between each step and the saturation was determined by:

$$S[\%] = \left[1 - \left[\frac{W_s - W_i}{W_s - W_d}\right]\right] \times 100 \qquad [7.11]$$

where W_s is the weight of the specimen saturated, W_d the weight dry and W_i the weight of the specimen before each test. The specimens were tested again after 2 hours of drying in a room atmosphere. For a complete timetable of the testing see Table 7.4 for specimen # 1 and Table 7.5 for specimen # 2. The specimens up to and including test # 4 were dried in room atmosphere with an unknown but rather high humidity, as the laboratory is in Berkeley which has a coastal climate. After this test the drying out process was accelerated by putting the specimens in a

				Saturation experiment for Specimen # 1
Test	Date	time	Hours	Comment
1	820915	12:00	0	Fully saturated
2	820915	14:00	2	Drying in room atm.
3	820915	22:00	10	Drying in room atm.
4	820916	10;30	22.5	Drying in room atm.
5	820916	22:00	34	In the dessicator with $CaSo_4$
6	820919	13:00	97	- " -
7	820930	10:30	363	In 100% humidity
8	820929	10:00	338.5	In 100% humidity
9	820924	9:30	218.5	In room humidity
10	820923	10:30	195.5	48 h in a oven held at 70° C
11	821004	20:00	468.5	72 h in a vacuum oven at 75° C
12	821019	10:00	770.5	13 days in 50 millitorr vacuum

Table 7.4

dessicator with Dririte, (a common drying agent). The terminal dryness for Dririte is 0.005 milligram of H_2O per liter gas at 24° C. The dessicator was used to speed up the process, but after 72 hours in the dessicator the specimens had only lost 10 % of their water content. The specimens were then put into a convection oven for 48 hours, which represents the same drying process all the specimens normally underwent before testing. The saturation recorded after this treatment was 40% and 23 % saturation for # 1 and # 2, respectively. This shows that even a drying in a convection oven at 70° C will not yield a

Saturation experiment for Specimen # 2				
Test	Date	Time	Hours	Comments
1	820915	12:00	0	Fully saturated
2	820915	15:00	2	Drying in room atm.
3	820915	22:00	10	Drying in room atm.
4	820916	10:30	22.5	Drying in room atm.
5	820916	21:30	33	In the dessicator with $CaSo_4$
6	820919	15:00	99.5	- " -
7	821001	10:00	382.5	In 100% humidity
8	820930	11:30	360	In 100% humidity
9	820924	8:00	212.5	In room humidity
10	820922	11:30	168	48 h in an oven held at 70°C
11	821004	9:00	453.5	72 h in a vacuum oven at 75° C
12	821019	11:00	771.5	13 days in 50 millitorr vacuum

Table 7.5

sufficiently satisfactory dryness. The specimens were tested, (test # 10) and then put into a container with 100 % humidity to increase the saturation. The specimens regained weight and then Tests # 9, # 8 and # 7 were performed. Before Test # 11 the specimens were put into a vacuum oven maintained at 75° C and a low ($\approx$50 millitorr) vacuum. This process reduced the saturation levels to 6% for both specimens. This method appears to provide an effective method to dry the specimens and it also gives a saturation level which is constant in the specimens. Before the final test, the specimens were put into a high vacuum

chamber under a 50 millitorr vacuum for 14 days. The weight recorded after this drying process also serves as the reference weight. There certainly are traces left of water, but in terms of effective weight that should play little part in determining the saturation level. There is, however probably still a mono-molecular layer of adsorbed water in the fine cracks.

The waveforms recorded for the laboratory tests are degraded by the presence of ringing and sidewall reflections occurring some time after the first arrival. The average wave-length for the frequencies lying between 0.5-1.0 MHz is 8 mm for P-waves and 4 mm for the S-waves. With a circular vibrating source of diameter d $\sim=\sim$ 22 mm an ultrasonic beam was generated which can be approximated by a plane wave in the specimen tested for P-wave with a velocity of 5900 m/sec and a frequency of 0.75 MHz, giving a ratio of $\frac{d}{\lambda} = 2.75$ and for S-waves with a velocity of 3200 m/sec and a frequency of 0.75 MHz, $\lambda = 4$ mm giving a ratio of $\frac{d}{\lambda} = 5.50$. King (1980) has shown that by using the Fraunhofer formula a half-beam width obtained for P-waves such that

$$\Theta_\alpha = arcsin\left(1.22\frac{\lambda_p}{d}\right) = 26^o \qquad [7.12a]$$

and for S-waves

$$\Theta_\beta = arcsin\left(1.22\frac{\lambda_s}{d}\right) = 13^o \qquad [7.12b]$$

This means that the plane-wave assumption is reasonable and that problems with sidewall reflections should be minor. To reduce possible degradation of the signal which is used for attenuation analysis even

further the signal is truncated with a half cosinee window with a duration of $4\times10^{-6}sec$. The earliest time at which a sidewall reflection arrives after the primary arrival is 2.7 μ s but then the amplitude of the window is only 0.2 (out of 1.0) so it will reduce the reflected energy to a very small fraction of the total energy in the window. An example of the window and the waveforms is shown in Figure 7.7. The signals in figure 7.7 b and e are the truncated P-waves and S-waves from Figures 7.7 a and d respectively. For S-waves a separate problem is encountered. S-wavetrains contain a certain amount of parasitic P-wave energy, so the problem is to maximize the S-wave energy/P-wave energy ratio. For S-waves a window of 3 micro seconds was chosen after experimenting with a set of five different windows. The reference point for this window is the crossover point of the S-wave with the zero-amplitude line, an example of which is shown in Figure 7.7 d. From this point and to the left a half-cosinee window is used, with a length of 1 μs and to the right of this point a window of 2 μs length is used. The total duration of the window is therefore 3 μs, with the center of the "bell" centered were the maximum energy of the S-wave is expected to be. The waveforms were digitized in a 512-point long array. The truncated waveforms were Fourier-transformed with a standard FFT routine which is part of the software package in the Tektronix 1200 signal processor system used. The result of this transform is shown in Figure 7.7 c and f. Figure 7.7 c shows the P-wave results and in Figure 7.7 f the corresponding S-wave results. In Figure 7.9 a are shown the P-wave arrivals for specimen # 2 in it's dry state at different stress levels. In Figure 7.9 b are shown the P-wave arrivals for the same specimen in a saturated state. Line # 10 in these figures represents the arrival at the highest stress, which is reflected in

the shortest arrival time.

In Figure 7.10 a and b are shown the signals from Figure 7.9 truncated with the cosinee windows shown in Figure 7.7 b and 7.7 e. In Figure 7.11 a the spectra for the test on the dry specimen are shown, and in Figure 7.11 b for the same specimen in it's saturated state. Note how the frequency content changes in the signals as the stress is applied. In Table 7.6 the loads for each of the 16 spectra are given and the corresponding uniaxial stresses. This table provides the key for all laboratory tests showing 16 test levels if stress.

In Figure 7.12 a and b the corresponding S-wave arrivals are shown. In Figure 7.13 a and b the truncated S-waves are shown. The spectra for the truncated S-waves are shown in Figure 7.14 a and b. The velocities calculated for these specimens are given in Appendix E.1, together with the velocities for the other 9 specimens. The waveforms for the remaining specimens are given in Appendix E.2 and the truncated waveform in Appendix E.3. The spectra for all the specimens are shown in Appendix E.4.

7.4 Sample Preparation

In Table 7.7 the 11 specimens tested are listed. The weights listed for the specimens include the weight of the lead discs, shown in Figure 7.5a, the latter amounts to 0.647 gram. The lead discs were employed to provided god acoustic contact between the transducer holders and the rock specimen. The specimens are all from a 76 mm-diameter horizontal borehole drilled from the extensometer drift with a triple-tube core barrel. The core diameter from this barrel is 52 mm which represents the diameter of the test specimens.

Loads and uniaxial stresses for the 16 test stress levels		
#	load	Uniaxial stress, σ_{ua}
	[tonnes]	[MPa]
1	0.5	2.3
2	1.0	4.7
3	2.0	9.3
4	3.0	14.0
5	4.0	18.7
6	5.0	23.4
7	6.0	28.0
8	7.0	32.7
9	9.0	42.1
10	11.0	51.4
11	9.0	42.1
12	7.0	32.7
13	5.0	23.4
14	3.0	14.0
15	1.0	4.7
16	0.5	2.3

Table 7.6

All the core, with the exception of specimen # 4 and # 5, were taken from core recovered before the heater experiments. Specimens # 4 and 5 were taken from core obtained from the drill-back experiment, conducted after completion of the heater test, described by Flexser *et al.*

(1982). The maximum temperature reached where specimen # 4 was situated was 130° C. The specimen was taken 1.45 m from the H10 heater. Specimen # 5 was 0.75 m from the heater, where a temperature of 200° C was reached. The DBEX-1 borehole was situated 0.5 m above the heater midplane, as shown in Figure 7.4.

		Stripa core specimen			
speci-men no.	Heater area	Bore-hole name	Distance from collar [m]	Weight satu rated [gr]	Weight dry [gr]
1	H9	E21	11.77-11.85	437.303	436.934
2	H9	E24	11.38-11.46	452.353	451.871
3	H10	E29	9.56-9.64	---	---
4	H10	DBEX-1	10.49-10.57	---	---
5	H10	DBEX-1	10.72-10.80	---	---
6	H9	E22	10.12-10.20	430.710	430.430
7	H9	E22	11.62-11.70	456.443	455.800
8	H9	E22	5.41-5.49	447.783	447.442
9	H9	E25	9.72-9.80	454.863	454.412
10	H9	E25	13.09-13.17	444.323	443.918
11	H9	E25	13.17-13.25	444.323	443.918

Table 7.7

The core was cut with a diamond saw to a length of 80 mm, and the flat-ends were ground with a diamond wheel so they were smooth and parallel to within 0.001 mm.

7.5 Calibration of the spectral ratio technique

To test the reliability of the spectral ratio technique a set of 51 mm diameter perspex cylinders 7.622, 5.080, and 2.544 cm long were tested. First Q_α for the 7.622 cm long specimen was calculated with the aluminum standard previously discussed as standard. For this test Q_α was found to be 74 ± 6.5. The next test used the technique with two specimens with same attenuation but with two different lengths. The shortest of the perspex specimens was used as standard and Q_α was calculated by taking the spectral ratio between the spectrum from the P-wave signals from the 2.544 cm specimen and the 7.622 and 5.080 cm specimens. For this test the same relationships described in Chapter 6 were used. Inserting the γ value obtained in

$$Q_\alpha = \frac{\pi}{\gamma V_p} \qquad\qquad [7.13]$$

Q_α for the perspex is obtained. This operation was performed twice with the 7.622 cm and the 5.080 cm specimens, in both cases using the 2.54 cm specimen as the "standard". The results are shown in Table 7.8.

These Q-values agree very well with the value of 66±2.2 reported for perspex by Sears and Bonner (1981). However results obtained in this work do not shown any strong frequency dependence between 0.5 and 1.0 MHz as Sears and Bonner suggested. In Figure 7.44 the spectra for the aluminum standard and the three perspex samples are shown, and in Figure 7.45 the spectral ratio between the aluminum standard and the

Q_α for P-waves in perspex						
Specimen	Specimen length (cm)	Specimen vel. (m/s)	Stand-ard	Stand-ard length (cm)	Stand-ard vel. (m/s)	Q_α
perspex	7.622	2734	alum.	7.622	6362	74 ±6.5
perspex	7.622	2734	perspex	2.544	2738	71 ±0.5
perspex	5.080	2741	perspex	2.544	2738	66 ±2.0

Table 7.8

7.622 cm specimen. This indicates a good fit between the actual curve and the least squares linear fit.

7.6 Results

7.6.1 P-wave attenuation

In Figure 7.17 Q_α values for Stripa specimen # 1 are shown as a function of axial stress. In Figure 7.17a the specimen is dry. In this test "dry" refers to the specimen condition after it had been in a convection oven for 48 hours at 70° C. Figure 7.17b shows the results for the same specimen tested saturated. The values obtained during the loading part of the uniaxial test of the saturated specimen are not very different from form the values obtained during the loading part of the test when the specimen was in a dry state. During the unloading part of the test on the saturated specimen the Q_α values drop considerably compared with when the load was increased. The reason probably is that when the

unconfined, plastic-wrapped specimen is compressed uniaxially at a stress of 50 MPa micro-fractures close and squeeze out the water. During the unloading part of the cycle the fractures open again and the specimen becomes partially saturated. In Figure 7.18a results from the test of specimen # 2 are shown under the same conditions as for specimen # 1 in 7.17a. The large differences in the results between the two specimens should be noted. Q_α values for specimen # 2 are less than half those obtained for Specimen # 1. Q_α values for specimen # 1 reach their maximum at an axial load of 23 MPa, and then start to decrease due to opening of the micro-fractures which are parallel to the maximum stress. For Specimen # 2 there is a small but noticeable increase of Q_α over the whole test range, indicating very different fracture orientations. Micro-fractures for the specimen # 1 were oriented such that their aperture decreased with stress. Lockner *et al.* (1977) show that P-wave amplitudes decreased with increased aperture; the reverse is true as well.

In specimen # 2 the fractures must be oriented in a different direction. From Figure 2.2 it can be seen that there is a preferential direction of the macroscopic fractures. Now this test shows that there is preferential direction of the microscopic fractures as well. The pole of the macroscopic fractures is perpendicular to the direction of borehole E25 from which specimen # 2 comes. This means that the fracture planes are parallel to the core axis, and that the compression of the specimen is parallel to these fracture. It is easily realized that in such a model the fracture tends to open rather than close under uniaxial stress. Borehole E21 from which specimen # 1 is taken certainly is not perpendicular to the major pole in Figure 2.2. The angle between the E21 core

and the major pole is approximately 35°. This difference in angle is evidently large enough to cause the difference in behavior of the two specimens indicated in Figure 7.17 a and Figure 7.18 a.

Q-values for specimens 3, 4, and 5 obtained from the H10 area yield further information on the influence of microfractures and their aspect ratios on attenuation. These results suggest a possible dominant mechanism for the attenuation of elastic waves in a rock such as the Stripa quartz monzonite. In Figure 7.19a and b Q_a values from specimen # 3 from borehole E29 are shown. In Figure 7.19a the Q_a values are shown when the specimen is dry, and in Figure 7.19b the Q_a values are shown for the saturated specimen. In Figure 7.19a the maximum Q_a for the loading part of the cycle is reached at a uniaxial stress of 18.6 MPa. At this point the Q_a value decreases to a local minimum and then Q_a increases again as the load increases. An interesting phenomenon occurs when the rock is unloaded. The Q_a value increases at first with decreasing stress. This indicates that unloading of the rock causes fractures parallel to the axis of loading to close. In Figure 7.20a results for specimen # 4 are shown. Specimen # 4 was obtained 1.45 m from the H10 heater where the temperature reached 130°C during that experiment. An interesting observation in Figure 7.20 a is that the behavior for the Q_a curve is similar in that there are two maxima at uniaxial stress of 23 MPa and 51 MPa. The Q-value for a uniaxial stress of 51 MPa is 67, while for Specimen # 3 it was 53. In Figure 7.20b the difference between the specimen dry and saturated is very apparent. The fully saturated specimen attenuates the signal less, indicating that a fully saturated specimen can have a higher Q_a value for P-waves than the same specimen dry. For specimen # 5 in Figures 7.21a and b an

unexpectedly high Q_α was found at high stresses. Note the change in scale on the ordinate to accommodate the high Q_α values. The Q_α value reached a maximum of 240 at a uniaxial stress of 51 MPa. The Q_α at a uniaxial stress of 2.3 MPa was no higher for this specimen than the others, and on reducing the axial stress Q_α returns to almost exactly the same value as it had originally. This is the rock specimen that was subjected to 200° C. Temperatures of this magnitude caused additional fractures parallel to the borehole wall, as shown by Flexser *et al.* (1982), or perpendicular to the thermal gradient which is very steep in this area, during the operation of the H10 heater. The high Q_α value suggest the extension of existing fractures rather than creating new ones. Any extension at fracture tips decreases the aspect ratios for these fractures, thus making the fractures easier to close with a normal stress.

Flexser *et al.* (1982) reported that fine fractures oriented tangentially to the H10 heater hole were found in rock which had spalled from the borehole wall. The maximum depth of the decrepitation observed was 8 cm with an average of 1.7 cm. It is clear from evidence provided by specimen # 4 and # 5 1.45 and 0.75 m from the H10 heater borehole respectively, that there is a strong P-wave attenuation effect to at least 0.75 m and a noticeable effect to 1.45 m from the borehole. The observation that the fractures created are tangential to the borehole (i.e. perpendicular to the axis of both boreholes E29 and DBEX-1) agrees well with the observation that P-waves show a large increase in Q_α with the application of stress in the specimens closest to the heater, while the Q_β for the S-waves do not show a similar effect. The S-wave particle motion is parallel to the fractures, and thus would not be affected by the length of the fracture. Flexser *et al.* (1982) also reported that microfracturing

could not be detected in thin sections from core recovered from distances from the heater larger than 8 cm. However, microfractures were visible in the thin sections made from the pieces of rock which fell from the borehole wall due to decrepitation. This shows that micro-fracturing did occur and that the Q values are sensitive to this kind of fracturing.

Johnston (1978) reported that thermal cycling of Westerly granite yielded lower velocities but higher Q-value. This agrees very well with the results obtained for the three-specimen suit from the H10 area. Simmons and Cooper (1978) reported an increase in porosity made up of low aspect ratio cracks for thermally-cycled Westerly granite. There is no contradiction implied in this insofar that the porosity under low stresses might be larger but the micro-fractures close more readily with the application of stress. The pressure at which a crack closes is given by

$$P_c = \frac{\pi \alpha E}{4(1-v^2)} \qquad [7.14]$$

where E= Young's modulus, v= Poisson's ratio and α is the crack aspect ratio. It is clearly seen that when the crack length increases, the aspect ratio α decreases and the stress necessary to close the fractures decreases.

Simmons and Cooper (1976) found that the effect of heating rocks at a rate of less than $1° C/min$ created what they called thermal cycling cracks. In Westerly granite the crack porosity increases exponentially with temperature:

$$c = 10^{-3.75+(2.24\times10^{-3})T_m} \qquad [7.15]$$

where T_m is the maximum temperature $in°$C. This shows that the crack

porosity doubles for each increase in 140° C.

Simmons and Cooper (1976) used a differential strain analysis technique and concluded that most of the cracks formed were those that closed at low pressures (i.e. low aspect ratio cracks). This conclusion agrees well with the results reported here. Simmons and Cooper indicated that heating of the specimens caused thermal cracks near the grain boundaries of the minerals comprising the rock. Their model indicates that thermal heating extends the length of the fracture along the grain boundaries, possibly by connecting several micro-fractures. Thus a new and larger fracture is formed which effectively forms a lower aspect ratio fracture. The latter would help explain the seemingly contradictory finding that thermally-induced fractures in specimens results in higher Q_α values for P-waves, at least at high stress levels.

The quartz content of the Stripa quartz monzonite 37.1 % and because of the high thermal expansion coefficient of quartz this would imply that there would be a very large increase in the crack porosity when the rock is thermally cycled. Simmons and Cooper found the crack porosity to increase considerably for Westerly granite which has a quartz content of 22 %. The larger quartz content in the Stripa quartz monzonite does imply a larger degree of fracturing at elevated temperatures.

7.6.2 S-wave attenuation

In Figures 7.22 - 7.26 the S-wave Q_β value curves for Specimens # 1 - 5 are shown. The most notable aspect of these curves is the small variation encountered. The S-wave is polarized perpendicular to the direction both of the direction of propagation and of the application of the

compression stress. Lockner *et al.* (1977) showed that the amplitude for such S-waves decreases with stress. The same behavior is observed in the data reported here. In Figure 7.22a for Specimen # 1 in it's dry state the highest Q_β value is found at an axial stress of 9.3 MPa and Q_β decreases at higher stresses. In Figures 7.22b for the same specimens saturated the Q_β value decreases for the range of uniaxial stress from 2.3 MPa to 51 MPa. For specimen # 2 in it's dry state, shown in Figure 7.23a, there is an increase in Q_β from 14 to 30, a 114 % increase. For the saturated case Q_β remains relatively constant after a small initial increase. During the unloading part of the test cycle, there are indications that the the specimen becomes partially saturated from the low Q_β value compared with the loading part of the curve.

Q_β values for specimen # 3 in Figure 7.24a in the dry state show a 55 % gradual increase over the range of uniaxial stresses from 2.3 MPa to 51 MPa. In the saturated state Q_β decreases after reaching a maximum at a uniaxial stress of 28 MPa, as indicated in Figure 7.24b. Specimen # 4 in Figure 7.25a in the dry state behaves in the same manner as specimen # 3. In the saturated state (Figure 7.25b) the specimen becomes partially saturated during unloading.

For specimen # 5 in the dry state the decrease in the S-wave Q_β value over the range of actual stresses from 2.3 MPa to 50 MPa is 50 %, as indicated in Figure 7.26a. This is the specimen that was recovered from the area around the H10 heater that reached $200°$ C at radial distance of 0.75 m from the center of the H10 heater. In the saturated state, shown in Figure 7.26 b, there was little change in Q_β except that the specimen appears to become partially saturated at unloading.

Saturation experiment

In Table 7.2 and 7.3 the results from an important experiment detailing the combined effects of changes in axial stress and water saturation are tabulated. P and S-wave velocities are shown in Figure 7.27 for specimen # 1 and Figure 7.28 for Specimen # 2, at four different axial stresses as a function of saturation. Both the P and the S-wave velocities appear to depend linearly on the degree of saturation at all the four axial stresses plotted. This is an important finding which tends to confirm the analysis of the P-wave velocities made in Chapter 5. The finite viscosity of water in thin cracks increases the shear modulus, as is seen in the higher S-wave velocities with increasing saturation.

The porosity of the two specimens are found to be 0.90 % and 0.95 % for Specimen # 1 and 2 respectively. The porosity is almost identical, for both specimens. Despite this there are large differences in the behavior of the two specimens, which is mirrored in the differences observed between the P and S-wave velocities. In Figures 7.29 - 7.32 the moduli are shown, calculated from the P and the S-wave velocities and the bulk density.

In Figures 7.33 and 7.34 the P-waveforms are shown for specimen # 1 for four different uniaxial stresses at 12 different saturation conditions for each of the stresses. In Figure 7.35 - 7.36 the P-waveforms for Specimen # 2 are shown. and The sequency of stresses applied is from an axial stress of 5 MPa for Figure 7.35a, 10 MPa for Figure 7.35b, 20 MPa for Figure 7.36a and 30 MPa for Figure 7.36b. It is interesting to observe the change in waveform with time and to see how the frequency content of the signals changes. It is clear from the figures that the degree of saturation has a much greater effect at low axial stresses.

In Figures 7.37 and 7.38 the S-waveforms are shown for Specimen # 1 under the same conditions as noted above. The velocity decrease with decreasing saturation is quite obvious. In Figures 7.39 and 7.40 the S-waveforms for Specimen # 2 are shown. Again the effect of saturation is clearly seen. The change with stress is not as apparent as in the P-wave case.

In Figures 7.41 and 7.42 the Fourier amplitude spectra are shown for the P-waves from specimen # 2. Shown in this figure are the dramatic changes in frequency content of the signals as the saturation is varied. The change in frequency content over the range of saturation tests is as large with change in stress level from 5 to 30 MPa.

The change in Q results from a change in the spectral ratio with frequency. In Figure 7.43a the two ratios are shown for Specimen # 2 going from fully saturated (line # 1) to 78 % partially saturated (line # 2).

In Figure 7.43 b the same effect is seen for the S-waves. In Figure 7.44 the Q_α and Q_β values from Specimen # 1 show the relationship between the saturation and the attenuation. The Q_α values vary between 50 and 90, depending on the stress when the specimen is fully saturated. The attenuation decreases rapidly with decreasing saturation. The minimum occurs between 70 and 80 % saturation for P-waves. For the case of a uniaxial stress of 5 MPa the attenuation decreases monotonically with saturation. For the higher axial stresses there is an increase in Q_α with decreasing saturation. This is particularly obvious for a uniaxial stress of 30 MPa. For Q_β in Figure 7.44 b the attenuation increases when the specimen goes from fully saturated to 93 % saturated. Below 93 % saturation Q_β increases continually down to a saturation of 6 %. At zero % saturation the Q_β value is lower again.

For Specimen # 2 the behavior from fully saturated to partially saturated is the same as for specimen # 1. The attenuation reduces monotonically to a saturation of 66 % and then it remains more or less constant as the saturation is reduced still further. This occurs despite the large decrease in V_p. For Q_β in Figure 7.45b the attenuation correlates well the uniaxial stress. For uniaxial stresses of 5 MPa and 10 MPa, a minimum in Q_β occurs at a saturation of 63 %. For a uniaxial stress of 20 MPa there is a monotonic decrease of Q_β.

For a uniaxial stress of 30 MPa there is a small decrease in Q_β as the saturation is reduced to 30 %. On reducing the saturation further to zero, there is a drop in Q_β from 42 to 27.

7.7 Summary

In this chapter a set of laboratory tests have been described which confirm the low Q-values obtained from the field data. Large differences in the change of attenuation with applied uniaxial stress is correlated with the inferred direction of microfractures. Q_β changes less with applied stress than does Q_α. This can be explained by the closing of fractures which are perpendicular to the stress direction and opening of fractures which are parallel to the uniaxial stress direction. Q_α is most sensitive to fractures perpendicular to the direction of propagation while Q_β is most affected by fractures which are parallel to the direction of propagation. The results from the test of the drill-back specimen from the heated rock in the H10 heater area show the sensitivity of attenuation of inferred low aspect ratio fractures. The result indicate that by observing the behavior of P and S-wave attenuation with changing stress applied in different directions, Q-values calculated for elastic

waves can be used in a diagnostic analysis for thermal cracking which is not detectable by an optical analysis of thinsections. Saturated specimen yield higher Q_α values than do dry. The difference in Q_β between saturated and dry specimen is small. For the saturation experiment V_p and V_s were found to be to the first order linearly dependent on the saturation. Attenuation for different saturations in the two specimens varied greatly. With some exceptions, Q_α and Q_β for both specimen reached their maximum values at full saturation. Q_α for specimen # 1 fully vacuum dried was considerably higher than the value fully saturated for a high axial stress. In most cases for the lowest Q_α and Q_β were found at saturation levels of 60 %. This test support the earlier conclusion that in specimen # 1 the microfractures are more perpendicular to the core axis than in specimen # 2.

SPECIMEN\FILE :STRPD2.2

DATE :3 SEPTEMBER, 1982

LENGTH OF SPECIMEN : .081928 METER.

DIAMETER OF SPECIMEN : 5.1689 CENTIMETER

NUMBER OF LOADS : 16

DENSITY OF SPECIMEN : 2605 KG/M^3

LOAD	PRESSURE	P-WAVE VEL	S-WAVE VEL	YOUNGS M	BULK M	SHEAR M	PO. RA
(TONS)	(MPA)	(M/S)	(M/S)	(MPA)	(MPA)	(MPA)	
.5	2.33671	4989.52	3180.43	61.0168	29.7191	26.35	.157813
1	4.67342	5017.02	3189.1	61.5182	30.2441	26.4938	.160991
2	9.34683	5032.43	3217.91	62.2657	30.0064	26.9746	.154153
3	14.0203	5114.11	3264.06	64.1848	31.1261	27.754	.156318
4	18.6937	5245.07	3325	67.05	33.2656	28.7999	.164068
5	23.3671	5379.38	3378.47	69.834	35.7379	29.7337	.174323
6	28.0405	5469.16	3419.37	71.8278	37.3895	30.4578	.179136
7	32.7139	5550.68	3459.34	73.6999	38.7187	31.156	.182755
9	42.0607	5661.92	3511.7	76.2908	40.6761	32.125	.187405
11	51.4076	5733.24	3542.07	77.8731	42.0492	32.6829	.191342
9	42.0607	5701.32	3522.27	77.0065	41.5842	32.3186	.191363
7	32.7139	5600	3480.37	74.8045	39.6203	31.5544	.185327
5	23.3671	5461.87	3405.15	71.411	37.4388	30.2052	.182099
3	14.0203	5235.02	3303.55	66.4755	33.485	28.4295	.169128
1	4.67342	5020.1	3189.1	61.555	30.3245	26.4938	.161687
.5	2.33671	4977.4	3174.27	60.7507	29.5403	26.248	.157244

Table 7.1a Results from laboratory testing specimen # 2 in a dry state after a drying period in a convection oven at 70°C for 48 h.

SPECIMEN\FILE :STPDU2.DAT

DATE :3 SEPTEMBER, 1982

LENGTH OF SPECIMEN : .081928 METER.

DIAMETER OF SPECIMEN : 5.1689 CENTIMETER

NUMBER OF LOADS : 16

DENSITY OF SPECIMEN : 2611 KG/M^3

LOAD	PRESSURE	P-WAVE VEL	S-WAVE VEL	YOUNGS M	BULK M	SHEAR M	PO. RA
(TONS)	(MPA)	(M/S)	(M/S)	(MPA)	(MPA)	(MPA)	
.5	2.33671	5814.62	3423.65	75.5731	47.4713	30.6046	.234671
1	4.67342	5835.33	3422.22	75.7058	48.1353	30.579	.237871
2	9.34683	5864.57	3430.82	76.2083	48.8233	30.7328	.23985
3	14.0203 -	5877.19	3439.46	76.5748	49.0036	30.8879	.239561
4	18.6937	5894.1	3462.72	77.4207	48.9645	31.307	.236474
5	23.3671	5902.59	3480.37	78.025	48.7994	31.627	.233518
6	28.0405	5923.93	3490.75	78.5239	49.2055	31.816	.234033
7	32.7139	5932.51	3514.71	79.3189	48.8077	32.2542	.229538
9	42.0607	5949.75	3542.87	80.2906	48.7504	32.7502	.225504
11	51.4076	5967.08	3571.4	81.3204	48.5632	33.3031	.220912
9	42.0607	5958.4	3551.28	80.6446	48.792	32.9268	.224529
7	32.7139	5932.51	3516.22	79.3639	48.8508	32.2819	.22923
5	23.3671	5856.18	3486.3	77.7833	47.2309	31.7348	.225521
3	14.0203 -	5697.36	3440.91	74.991	43.5343	30.9138	.212904
1	4.67342	5502.22	3359.08	70.8789	39.765	29.451	.202926
.5	2.33671	5513.32	3359.08	70.9909	40.0845	29.461	.204828

Table 7.1b Results from laboratory testing specimen # 2 in a fully saturated state. The specimen was first subjected to 10 microns vacuum for 48 h and then submerged in distilled water for 24 hours.

SPECIMEN\FILE :STDAT2.WET

DATE :26 OCTOBER, 1982

LENGTH OF SPECIMEN : .079045 METER. DIAMETER OF SPECIMEN : 5.1791 CENTIMETER

NUMBER OF LOADS : 4

DENSITY OF SPECIMEN :

2626	2626	2626	2625	2625
2625	2625	2624	2624	2624
2623	2623 KG/M^3			

POROSITY : .897748 %

THE UNIAXIAL STRESS IS : 5 MPA

WEIGHT	SATURATION	P-WAVE VEL	S-WAVE VEL	YOUNGS M	BULK M	SHEAR M	PO. RA
(GRAMS)	(%)	(M/S)	(M/S)	(GPA)	(GPA)	(GPA)	
437.283	100	5979	3475	78	52	32	.245083
437.243	93	5890	3490	78	48	32	.229525
437.206	86	5778	3459	77	46	31	.220666
437.173	80	5720	3413	75	45	31	.223514
437.162	78	5691	3412	75	44	31	.219508
437.095	67	5626	3375	73	43	30	.218875
437.063	61	5590	3355	72	43	30	.218501
437.023	54	5485	3342	71	40	29	.204772
436.983	47	5501	3344	71	40	29	.206974
436.943	40	5505	3344	71	40	29	.20762
436.743	6	5374	3249	67	39	28	.211922
436.708	0	5305	3241	66	37	28	-------

THE UNIAXIAL STRESS IS : 9 MPA

WEIGHT	SATURATION	P-WAVE VEL	S-WAVE VEL	YOUNGS M	BULK M	SHEAR M	PO. RA
(GRAMS)	(%)	(M/S)	(M/S)	(GPA)	(GPA)	(GPA)	
437.283	100	5979	3478	78	52	32	.244404
437.243	93	5903	3512	78	48	32	.226195
437.206	86	5834	3484	78	47	32	.22285
437.173	80	5791	3450	77	46	31	.224819
437.162	78	5757	3438	76	46	31	.222797
437.095	67	5703	3422	75	44	31	.21875
437.063	61	5634	3390	73	43	30	.216363
437.023	54	5551	3390	73	41	30	.202711
436.983	47	5559	3378	72	41	30	.207243
436.943	40	5570	3379	72	41	30	.208801
436.743	6	5448	3289	69	40	28	.213083
436.708	0	5326	3253	67	37	28	.20261

THE UNIAXIAL STRESS IS : 19 MPA

WEIGHT	SATURATION	P-WAVE VEL	S-WAVE VEL	YOUNGS M	BULK M	SHEAR M	PO. RA
(GRAMS)	(%)	(M/S)	(M/S)	(GPA)	(GPA)	(GPA)	
437.283	100	5979	3504	80	51	32	.238516
437.243	93	5934	3530	80	49	33	.226107
437.206	86	5890	3513	79	48	32	.223909
437.173	80	5864	3485	78	48	32	.226893
437.162	78	5842	3478	78	47	32	.225622
437.095	67	5791	3459	77	46	31	.222569
437.063	61	5728	3435	76	45	31	.219131
437.023	54	5662	3423	75	43	31	.211941
436.983	47	5670	3423	75	43	31	.213239
436.943	40	5670	3422	75	43	31	.213629
436.743	6	5574	3323	71	43	29	.224477
436.708	0	5578	3302	70	43	29	.230365

THE UNIAXIAL STRESS IS : 28 MPA

WEIGHT	SATURATION	P-WAVE VEL	S-WAVE VEL	YOUNGS M	BULK M	SHEAR M	PO. RA
(GRAMS)	(%)	(M/S)	(M/S)	(GPA)	(GPA)	(GPA)	
437.283	100	5979	3541	81	50	33	.229807
437.243	93	5957	3541	81	49	33	.22664
437.206	86	5925	3534	80	48	33	.224067
437.173	80	5912	3521	80	48	33	.225197
437.162	78	5894	3507	79	48	32	.226069
437.095	67	5851	3496	78	47	32	.222354
437.063	61	5799	3476	77	46	32	.21965
437.023	54	5745	3465	77	46	32	.213056
436.983	47	5753	3468	77	45	32	.214474
436.943	40	5753	3461	76	45	31	.216431
436.743	6	5666	3381	73	44	30	.223593
436.708	0	5602	3337	72	43	29	.225105

Table 7.2 Results from saturation experiment on specimen # 1.

```
SPECIMEN\FILE :STDAT2.UET

DATE :27 OCTOBER, 1982

LENGTH OF SPECIMEN : .081928 METER.  DIAMETER OF SPECIMEN : 5.1689 CENTIMETER

NUMBER OF LOADS : 4

DENSITY OF SPECIMEN :
       2631         2630         2630         2630         2630
       2629         2629 2629    2629         2629         2628
       2628         2628 KG/M^3

POROSITY :  .949747 %
```

THE UNIAXIAL STRESS IS : 5 MPA

WEIGHT (GRAMS)	SATURATION (%)	P-WAVE VEL (M/S)	S-WAVE VEL (M/S)	YOUNGS M (GPA)	BULK M (GPA)	SHEAR M (GPA)	PO. RA
452.353	100	5852	3401	76	50	30	.24501
452.218	78	5451	3309	70	40	29	.208256
452.17	70	5252	3292	67	35	28	.176514
452.143	66	5105	3237	64	32	28	.163699
452.121	63	5098	3214	64	32	27	.170181
452.043	50	4974	3195	62	29	27	.148761
452.028	48	4932	3187	61	28	27	.141803
451.953	36	4814	3183	59	25	27	.11155
451.918	30	4752	3182	58	24	27	.0937929
451.871	23	4733	3171	58	24	26	.0929625
451.763	6	4608	3138	55	21	26	.0676624
451.725	0	4552	3116	54	20	26	.0587805

THE UNIAXIAL STRESS IS : 9 MPA

WEIGHT (GRAMS)	SATURATION (%)	P-WAVE VEL (M/S)	S-WAVE VEL (M/S)	YOUNGS M (GPA)	BULK M (GPA)	SHEAR M (GPA)	PO. RA
452.353	100	5865	3422	77	49	31	.241825
452.218	78	5510	3337	71	41	29	.210266
452.17	70	5369	3293	68	38	29	.198473
452.143	66	5212	3252	66	34	28	.18187
452.121	63	5215	3269	66	34	28	.176279
452.043	50	5101	3246	64	31	28	.159852
452.028	48	5057	3234	63	31	28	.153927
451.953	36	5054	3228	63	31	27	.155509
451.918	30	4868	3243	61	25	28	.100854
451.871	23	4845	3240	60	25	28	.0957026
451.763	6	4772	3194	59	24	27	.0940541
451.725	0	4695	3176	57	23	26	.0784116

THE UNIAXIAL STRESS IS : 19 MPA

WEIGHT (GRAMS)	SATURATION (%)	P-WAVE VEL (M/S)	S-WAVE VEL (M/S)	YOUNGS M (GPA)	BULK M (GPA)	SHEAR M (GPA)	PO. RA
452.353	100	5890	3461	78	49	32	.236235
452.218	78	5733	3441	76	45	31	.218584
452.17	70	5642	3400	74	43	30	.215078
452.143	66	5510	3369	72	40	30	.201472
452.121	63	5499	3355	71	40	30	.203454
452.043	50	5401	3322	69	38	29	.195586
452.028	48	5330	3321	69	36	29	.182794
451.953	36	5317	3298	68	36	29	.187178
451.918	30	5215	3275	66	34	28	.174569
451.871	23	5215	3268	66	34	28	.176705
451.763	6	5086	3238	64	31	28	.159011
451.725	0	5076	3234	64	31	27	.158235

THE UNIAXIAL STRESS IS : 28 MPA

WEIGHT (GRAMS)	SATURATION (%)	P-WAVE VEL (M/S)	S-WAVE VEL (M/S)	YOUNGS M (GPA)	BULK M (GPA)	SHEAR M (GPA)	PO. RA
452.353	100	5920	3489	79	49	32	.233791
452.218	78	5865	3533	80	47	33	.215189
452.17	70	5802	3503	78	46	32	.21331
452.143	66	5713	3473	77	44	32	.206949
452.121	63	5693	3463	76	43	32	.206467
452.043	50	5619	3427	74	42	31	.204025
452.028	48	5558	3424	74	40	31	.194314
451.953	36	5543	3392	73	40	30	.20057
451.918	30	5433	3376	71	38	30	.185579
451.871	23	5447	3370	71	38	30	.189943
451.763	6	5337	3326	69	36	29	.182462
451.725	0	5265	3336	68	34	29	.164737

Table 7.3 Results from saturation experiment on specimen # 2.
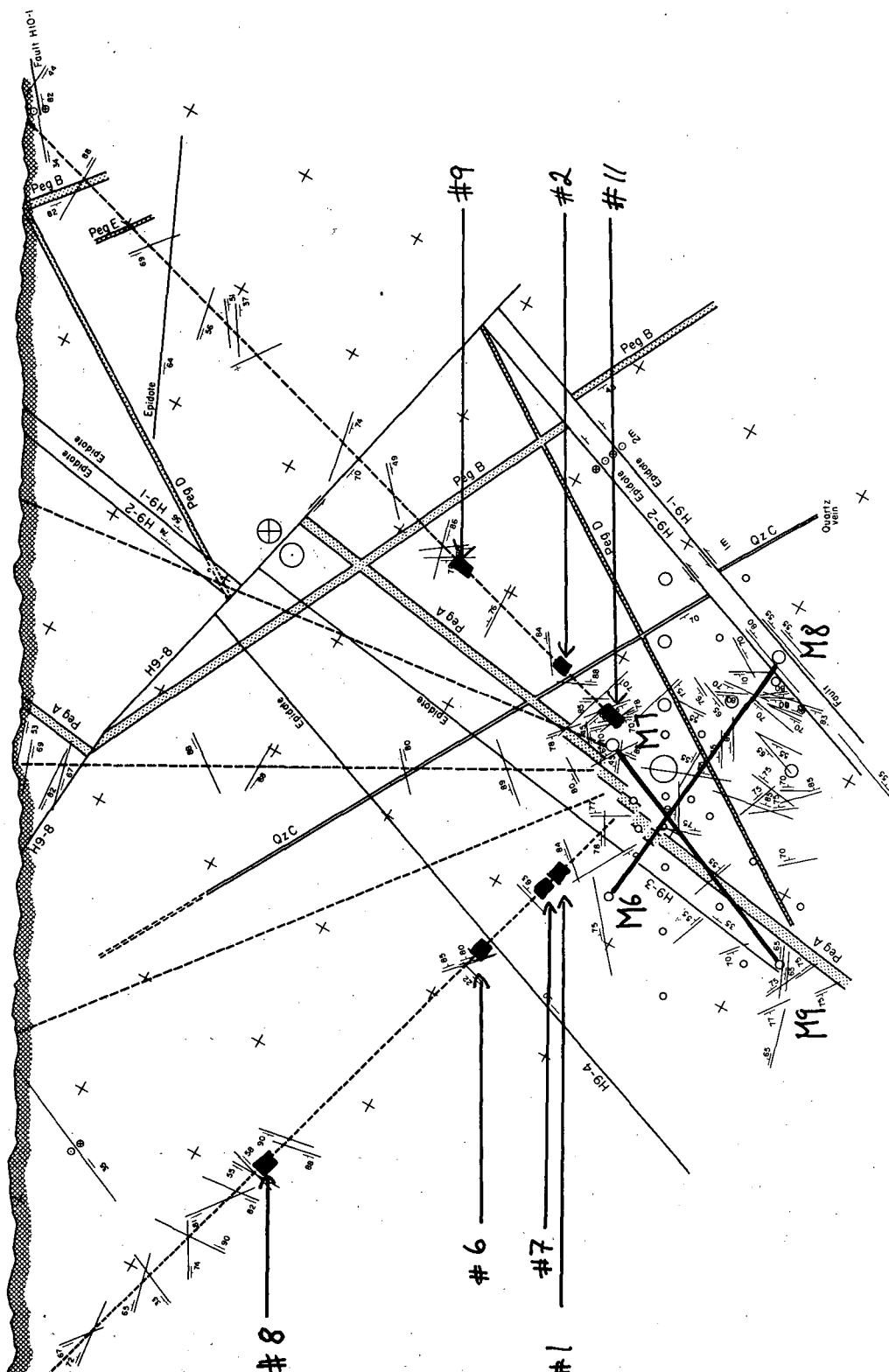
Fig. 7.1 H9 heater midplane borehole and fracture map showing the location of specimens 1,2,6,7,8,9,10 and 11. Also shown are the major dikes and faults at elevation of H9 heater midplane, based on extrapolation from nearby surfaces and core data. Short lines with dip symbols show projected intercepts of calcite-bearing fractures. Upthrown (downthrown) sides of faults are designated by head (tail) of arrows. Part of mine coordinate system is shown on 2 m centers.
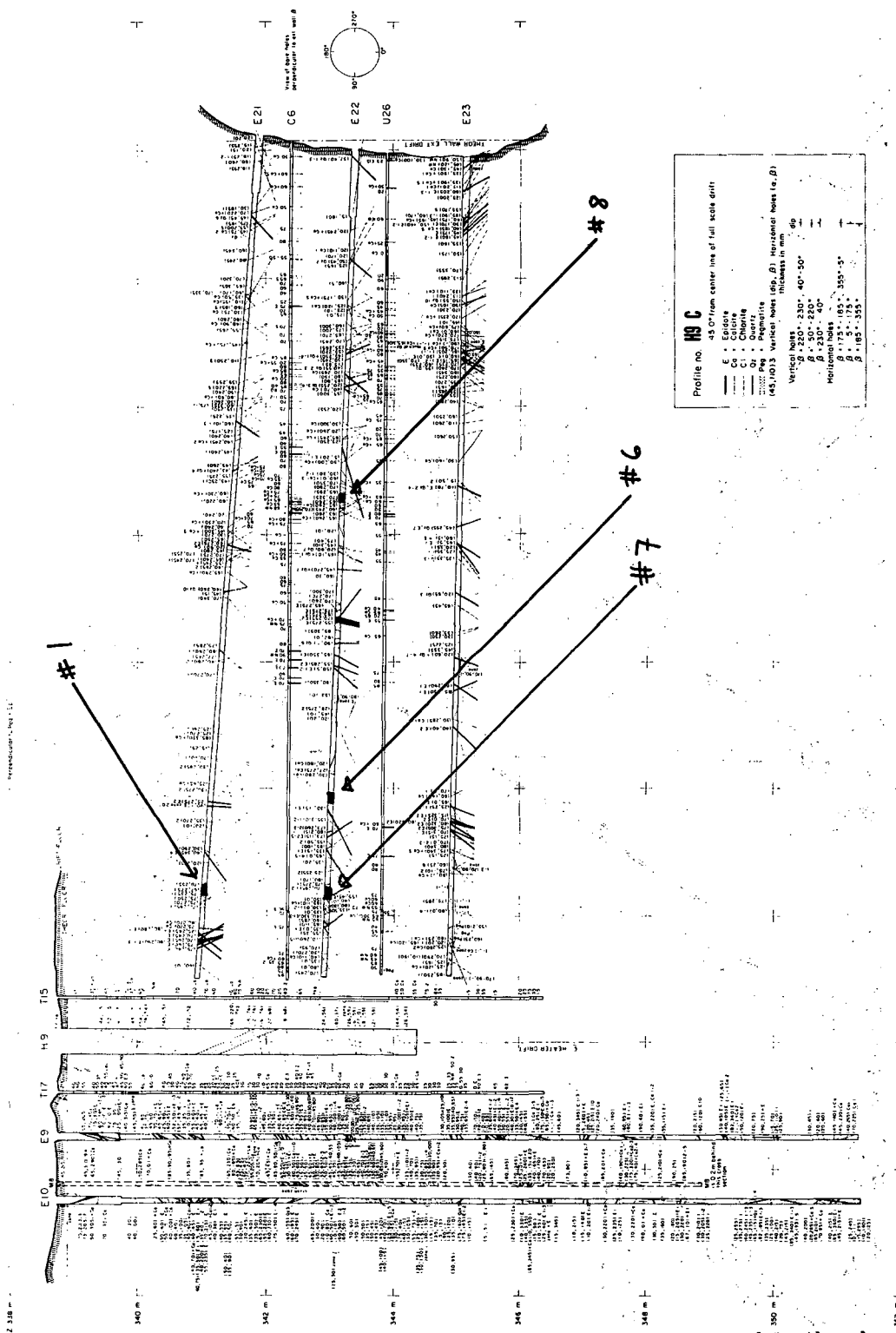
Fig. 7.2 Vertical cross section H9 C showing location of specimen 1,6,7 and 8. Also shown are the mapped fractures in the core from the boreholes in the cross section. Boreholes E10, E9, T17, H9 and T15 were drilled from the full scale drift. Boreholes E21, C6, E22, U26 and E23 were drilled from the extensometer drift.
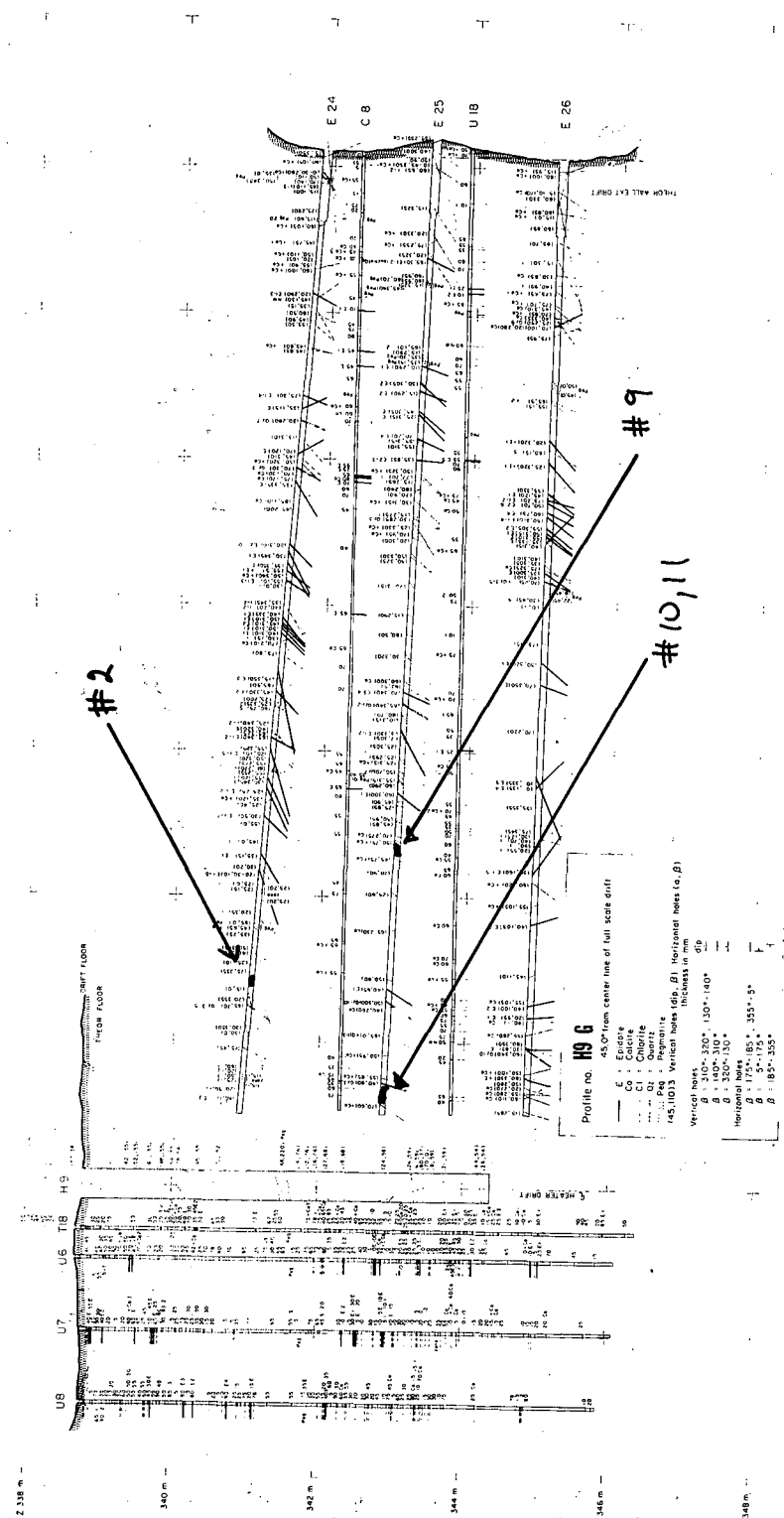
Fig. 7.3 Vertical cross section H9 G showing location of specimen 2,9,10,11. Also shown are the mapped fractures in the core from the boreholes in the cross section. Boreholes U8, U7, U6, T18 and H9 were drilled from the full scale drift. Boreholes E24, C8, E25, U18 and E26 were drilled from the extensometer drift.
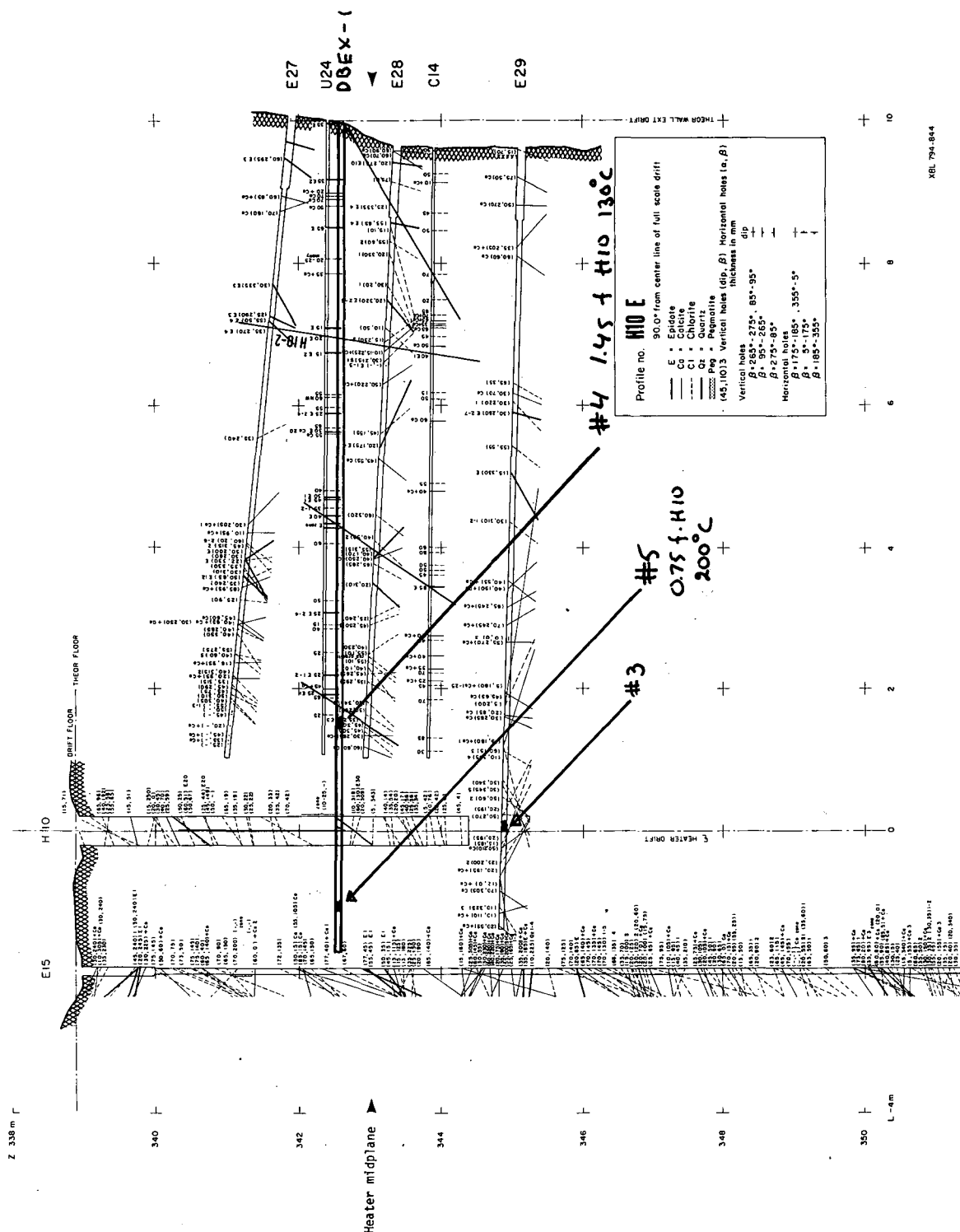
Fig. 7.4 Vertical cross section H10 E showing location of specimen 3,4 and 5. Also shown are the mapped fractures in the core from the boreholes in the cross section. Boreholes E 15 and H10 are drilled from the full scale drift. Boreholes E27, U24, DBEX-1, E28, C14 and E29 were drilled from the extensometer drift.

222

RECEIVER

BNC ELECTRICAL
CONNECTOR

LUCITE
ALUMINIUM
P-WAVE TRANS.
ALUMINIUM
S-WAVE TRANS.

CYLINDRICAL
ROCK
SPECIMEN

SHEAR-WAVE
TRANSDUCER ACTION

COMPRESSIONAL-WAVE
TRANSDUCER ACTION

LEAD FOIL DISC

S-WAVE TRANS.
ALUMINIUM
P-WAVE TRANS.
ALUMINIUM
LUCITE

TRANSMITTER

FULL SCALE

XBL 813-2711
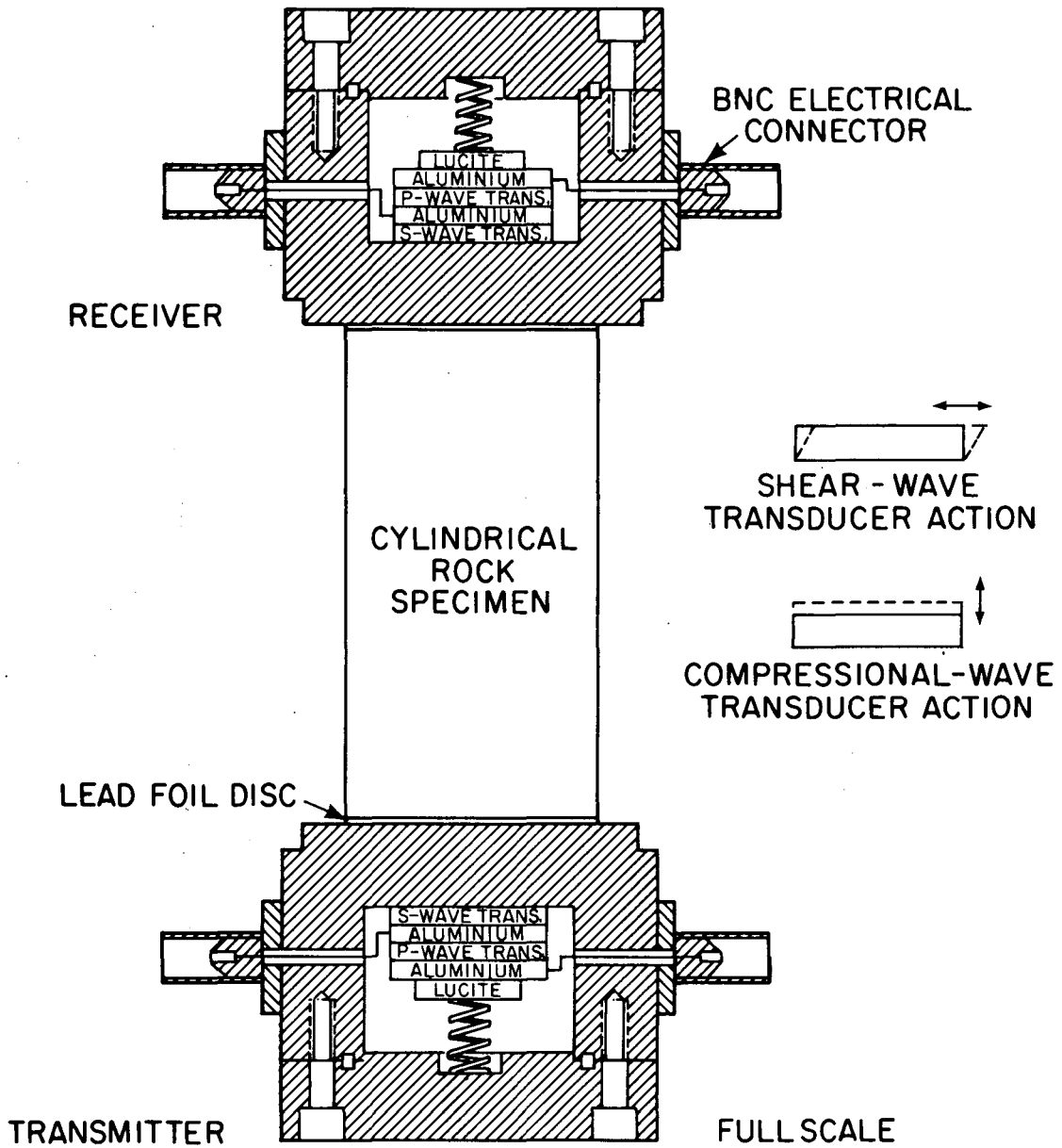
Fig. 7.5a Cross section through transducers used in the laboratory experiment. The load is applied on the top and bottom of the assembly. For the test the core specimen has the same diameter as the transducer, to create uniformal stress in the specimen.

ACOUSTIC VELOCITIES: STRIPA GRANITE,
DRY AND WATER-SATURATED
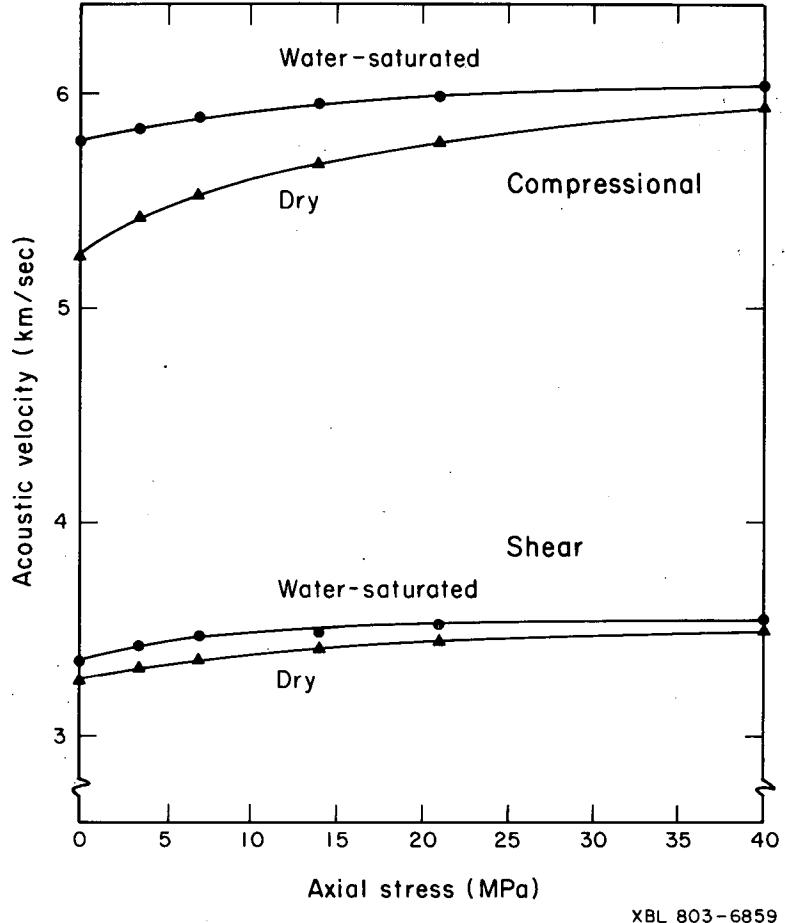
XBL 803-6859

Fig. 7.5b Acoustic velocities of the Stripa Granite dry and water saturated (From Paulsson and King , 1980).
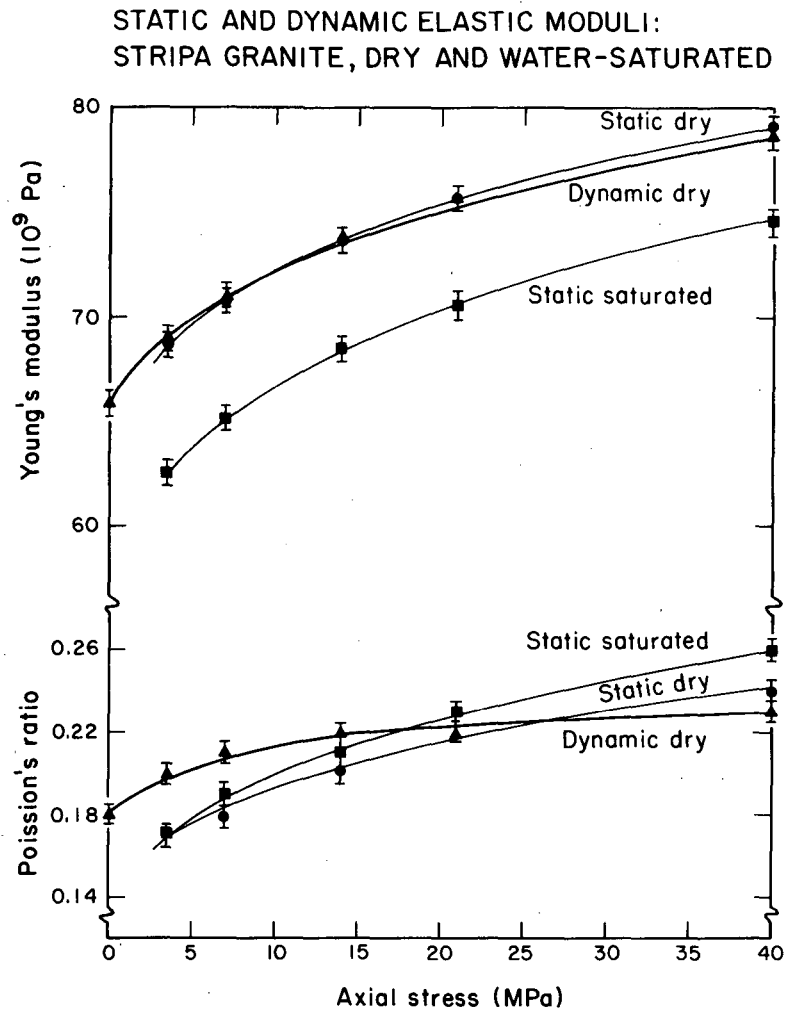
Fig. 7.5c Static and dynamic Youngs moduli and Poisson's ratio as function of uniaxial stress.
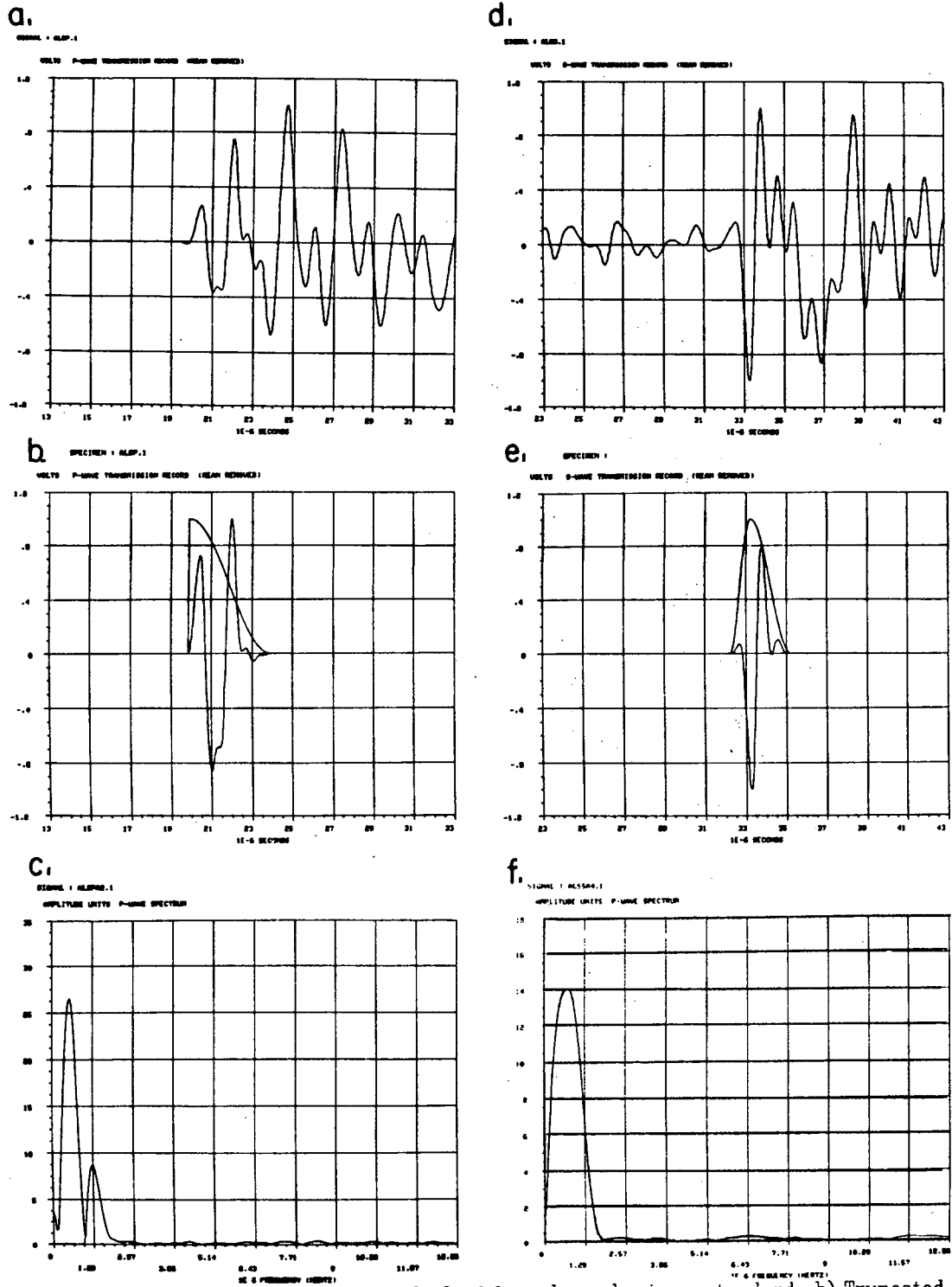
Fig. 7.6 a) P-waveform transmitted through the 7.7 cm long aluminum standard. b) Truncated P-waveform from the aluminum standard. c) Fourier amplitude spectrum of the truncated P-waveform from the aluminum standard. d) S-waveform transmitted through the 7.7 cm long aluminum standard. e) Truncated S-waveform from the aluminum standard. f) Fourier amplitude spectrum of the truncated S-waveform from the aluminum standard.
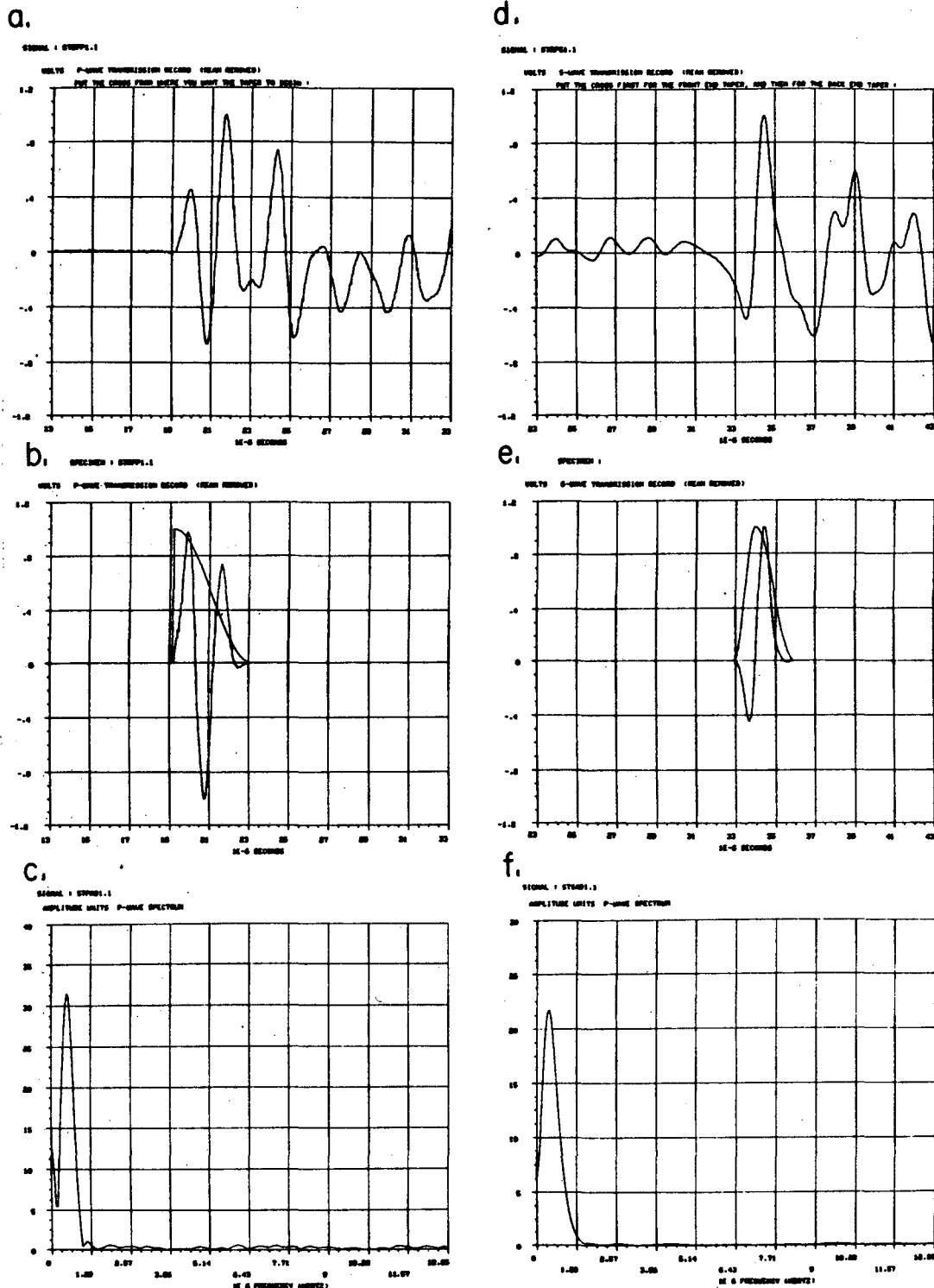
Fig. 7.7 a) P-waveform from specimen #1, under σ_{ua} = 2.3 MPa. b) Truncated P-waveform with a 4×10^{-6} sec. half cosine window. c) Fourier amplitude spectrum of the truncated P-waveform from specimen #1. d) S-waveform from specimen #1, under σ_{ua} = 2.3 MPa. e) Truncated S-waveform with a $1+2\times10^{-6}$ sec. half cos window. f) Fourier amplitude spectrum of the truncated S-waveform from specimen #1.

a

LINE : STRIPA 81, DRY, M8-M6, E21, 821109
DATE : 9 NOUEMBER, 1982
STANDARD : ALSPA2.1
STANDARD Q : 2000
STANDARD VEL : 6362
SMOOTHING : 0

IE 6 FREQUENCY (HERTZ)

b

LINE : STRIPA 81, DRY, S-WAVES, WINDOW:1+2E-6 SEC, 821109
DATE : 9 NOUEMBER, 1982
STANDARD : ALSSA4.1
STANDARD Q : 2000
STANDARD VEL : 3201
SMOOTHING : 0

IE 6 FREQUENCY (HERTZ)
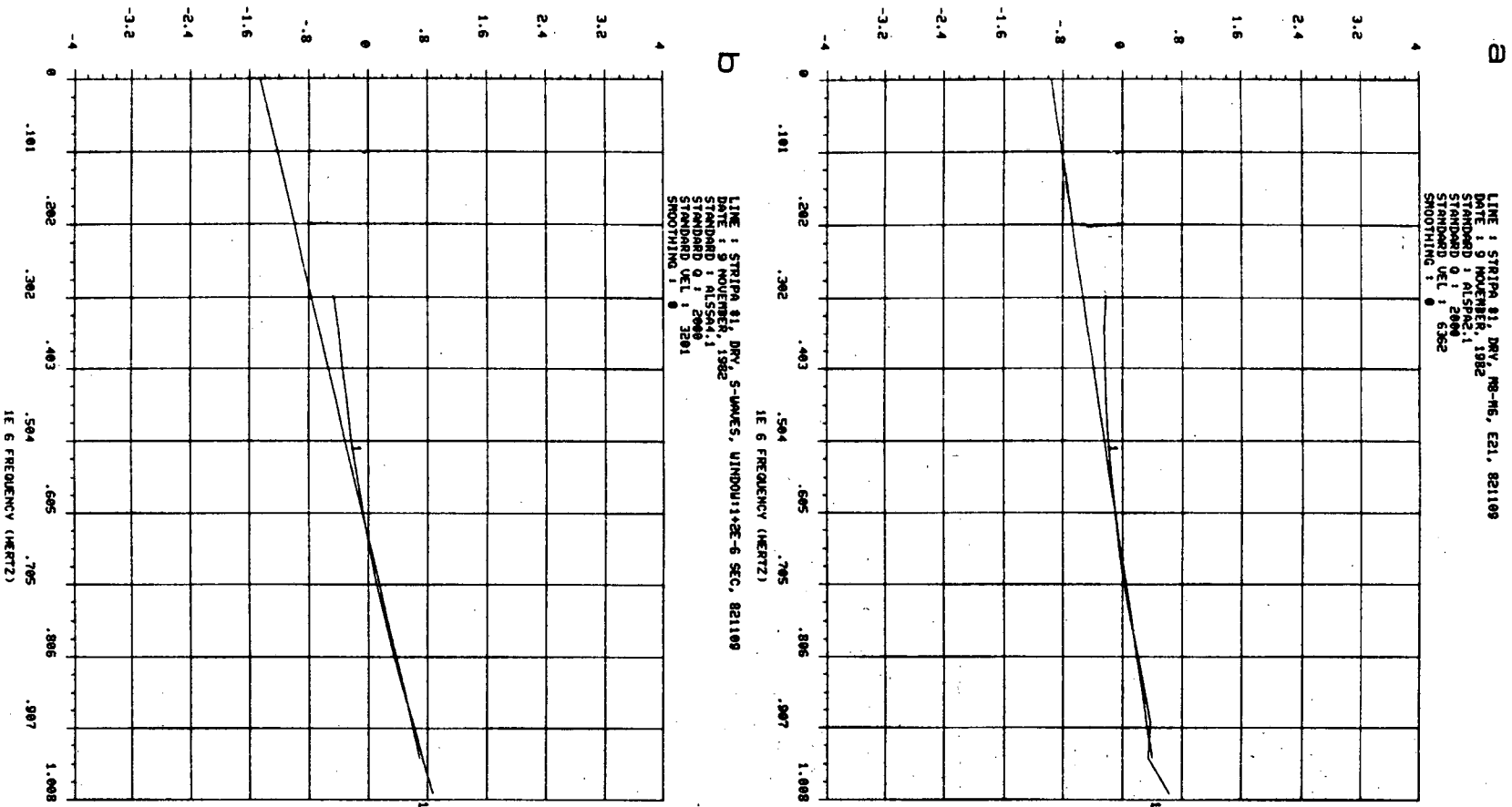
Fig. 7.8 a) Spectral ratio between the amplitude spectra of the P-waves from the aluminum standard and the specimen #1. Least squares fit to a straight line between the frequencies 0.5 and 1.0 MHz. The slope of the line determines the Q-value. b) Spectral ratio between the amplitude spectra of the S-waves form the aluminum standard and the specimen #1.
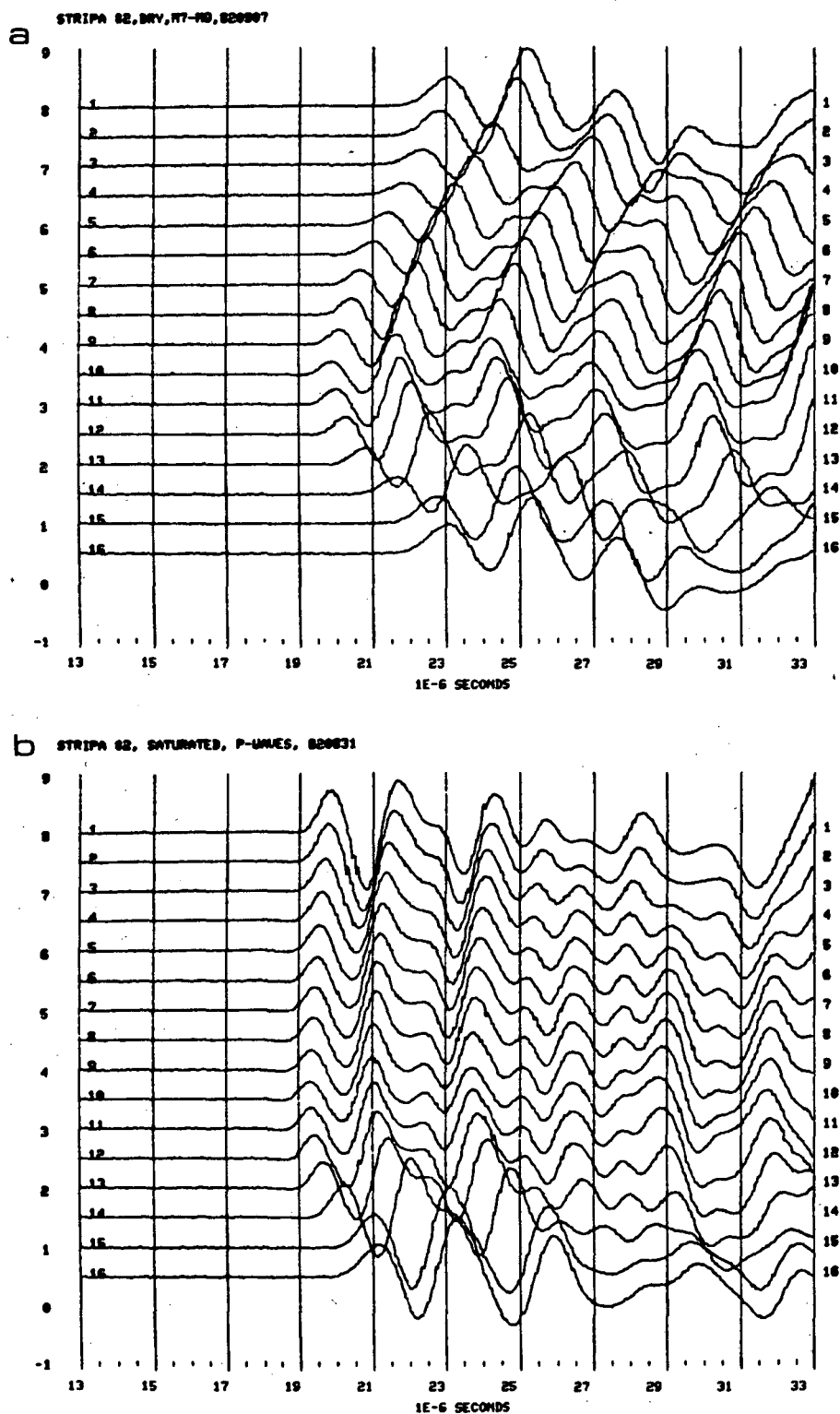
Fig. 7.9 a) P-waves from the specimen #2 dried in a convection oven at 70° C for 48 hours, at a load cycle from 2.3 MPa to 51 MPa and back to 2.3 MPa. b) P-waves from specimen #2 saturated using a 5 millitorr vacuum, from a complete load cycle from 2.3 MPa to 51 MPa and back to 2.3 MPa.
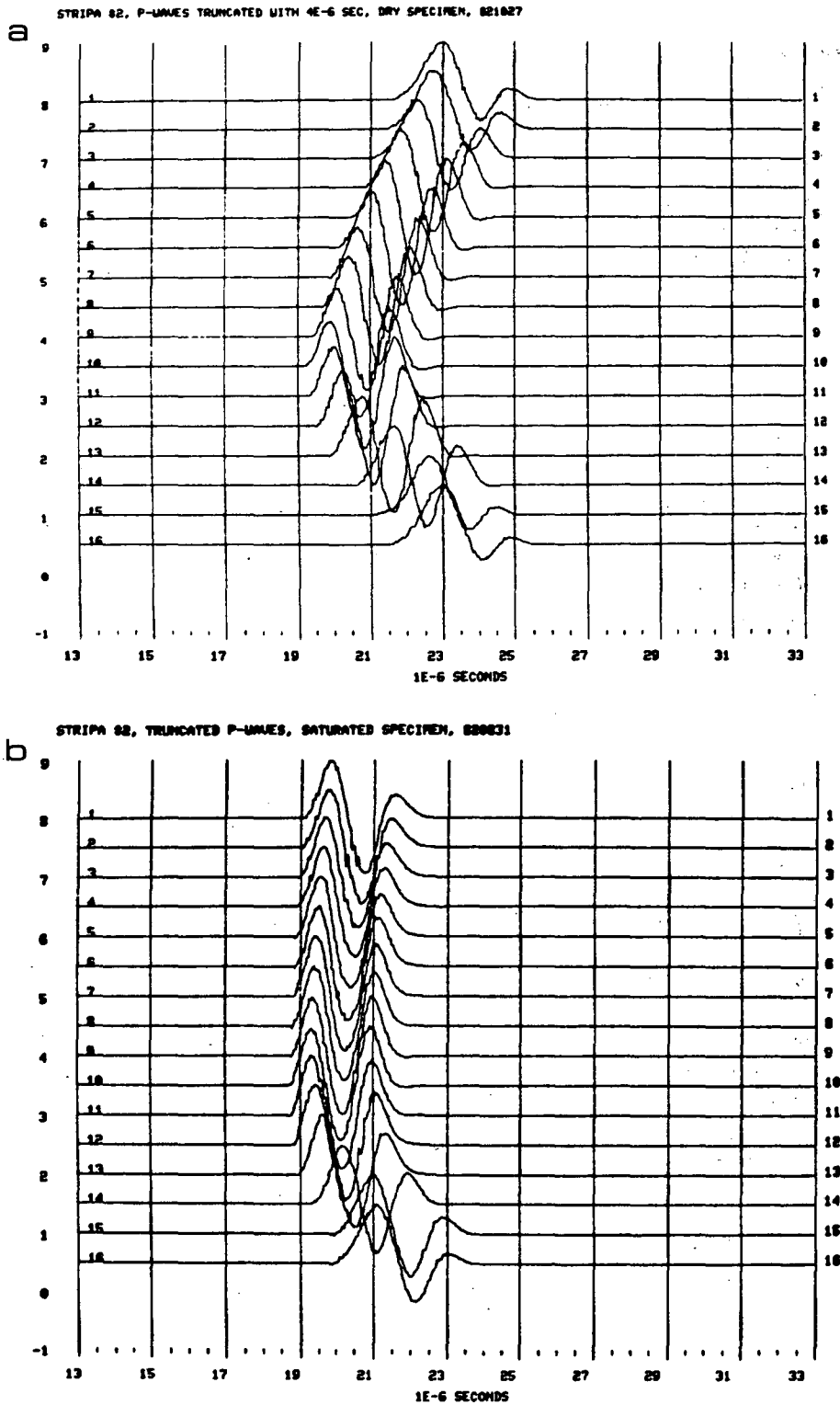
Fig. 7.10 a) Truncated P-waves from specimen #2 under a load cycle from 2.3 MPa to 51 MPa back to 2.3 MPa. Specimen dried in a convection oven at 70° C for 48 hours. b) Truncated P-waves from specimen #2 under a load cycle from 2.3 MPa to 51 MPa back to 2.3 MPa. Specimen saturated using a 5 millitorr vacuum and distilled water.

a

1E 6 FREQUENCY

b

1E 6 FREQUENCY
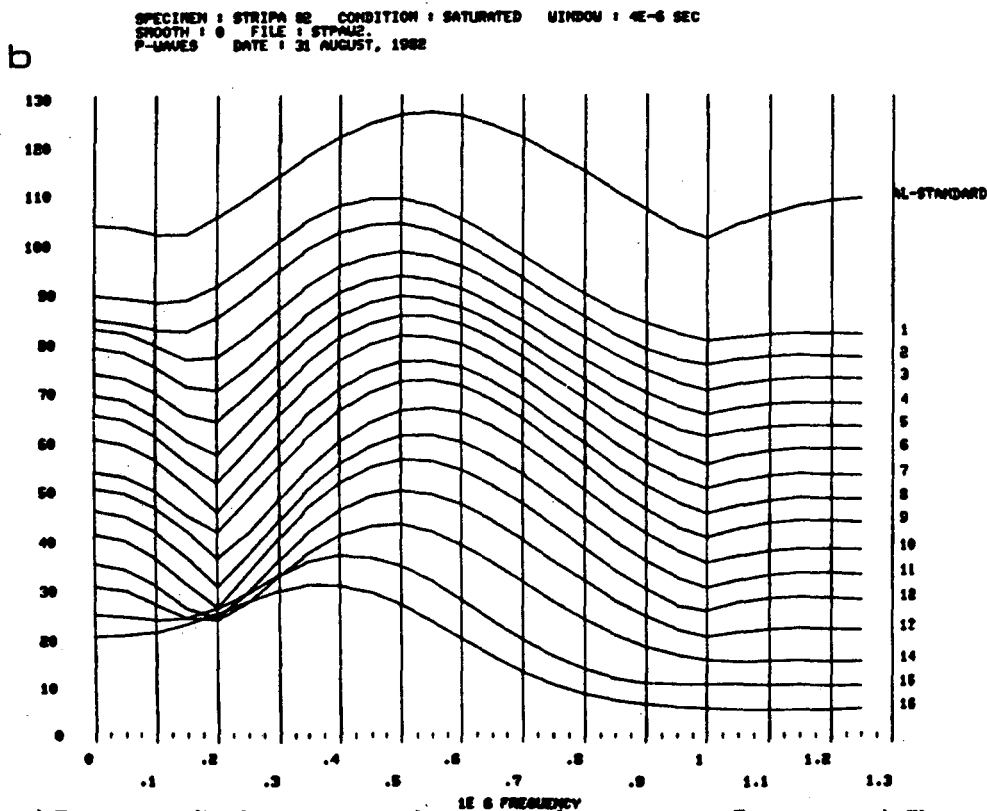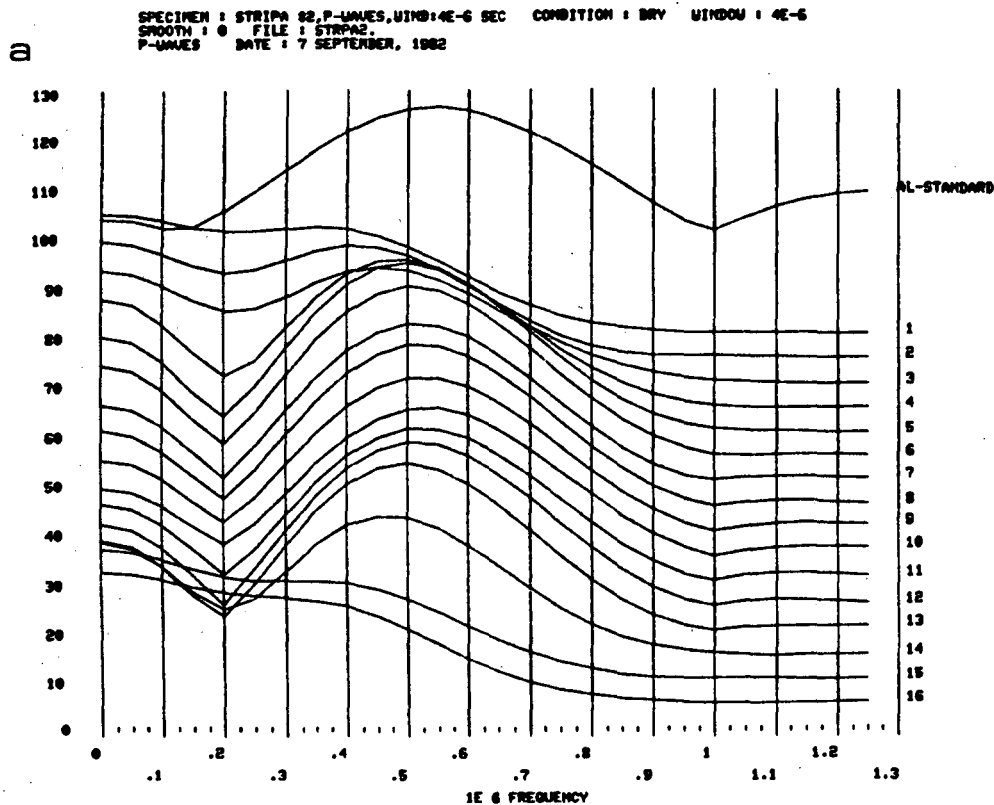
Fig. 7.11 a) Fourier amplitude spectra for the truncated waveforms in Figure 7.10 a), The specimen has been dried in a convection oven for 48 hours at 70° C. b) Fourier amplitude spectra for the truncated waveforms in Figure 7.10 b), the specimen was saturated by evacuating down to 5 millitorr vacuum for 24 hours and then submerge the specimen in distilled water for 24 hours.

a STRIPA 82,S-WAVES,DRY,820907

b STRIPA 82, SATURATED, S-WAVES, 820831
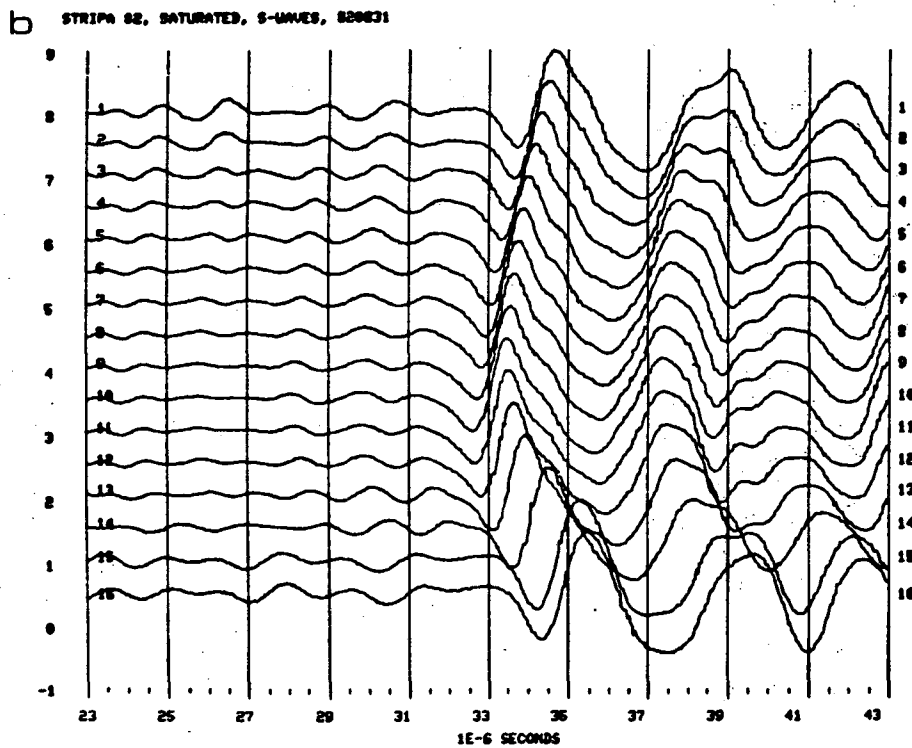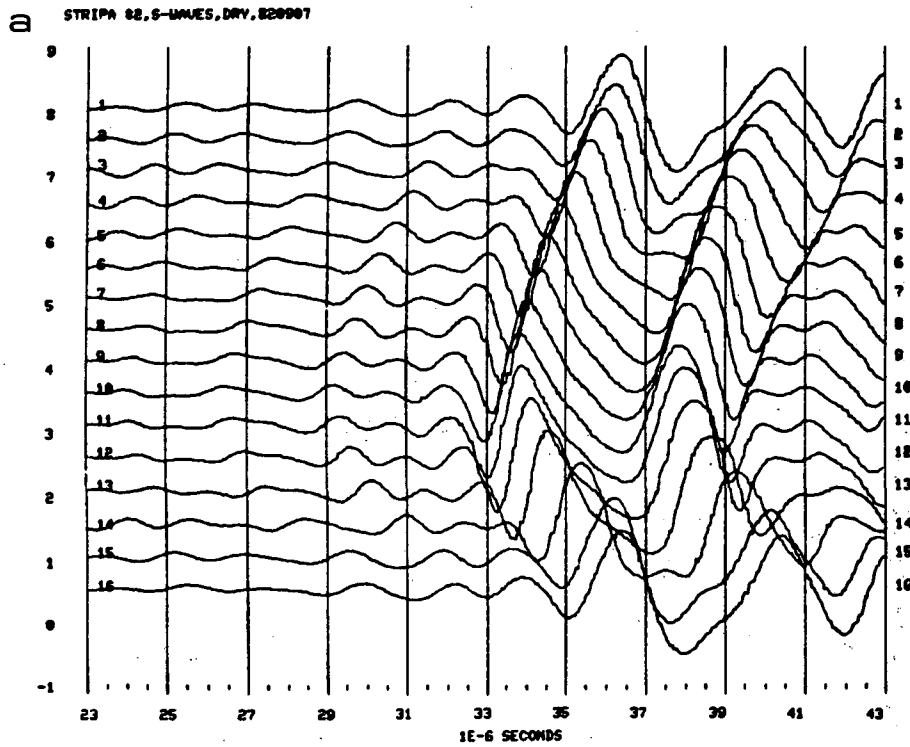
Fig. 7.12 a) S-waves for a complete load cycle from 2.3 MPa to 51 MPa for specimen #2. The specimen was dried in a convection oven at 70° C for 48 hours. b) S-waves for a complete load cycle from 2.3 MPa to 51 MPa for specimen #2. The specimen was saturated by first evacuating the specimen to 5 millitorr and then submerge the specimen in distilled water for 24 hours.
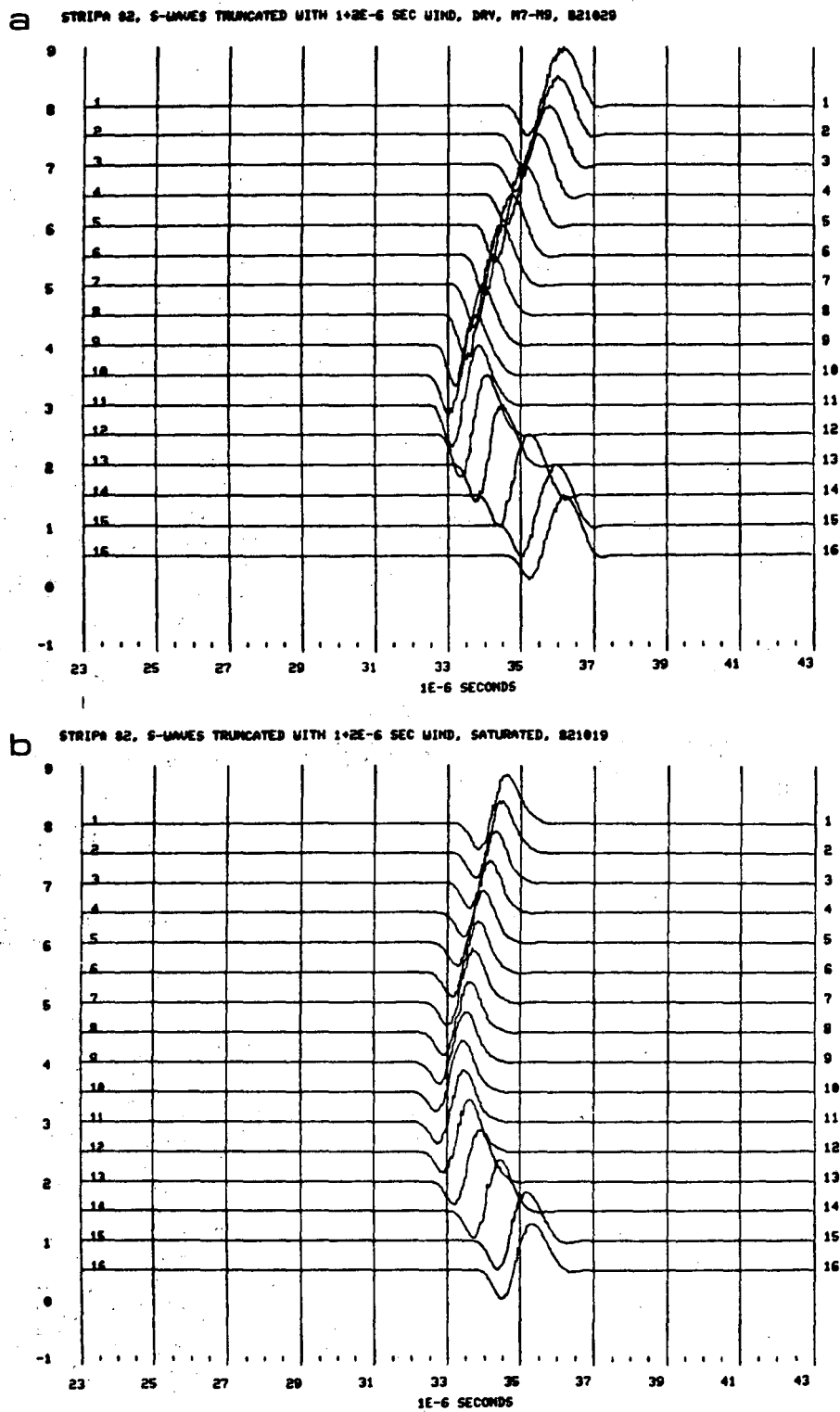
Fig. 7.13 a) Truncated S-waves for a complete load cycle from 2.3 to 51 MPa for specimen #2. The specimen was dried in a convection oven at 70° C for 48 hours. b) Truncated S-waves for a complete load cycle from 2.3 MPa to 51 MPa for specimen #2. The specimen was saturated.

a

b
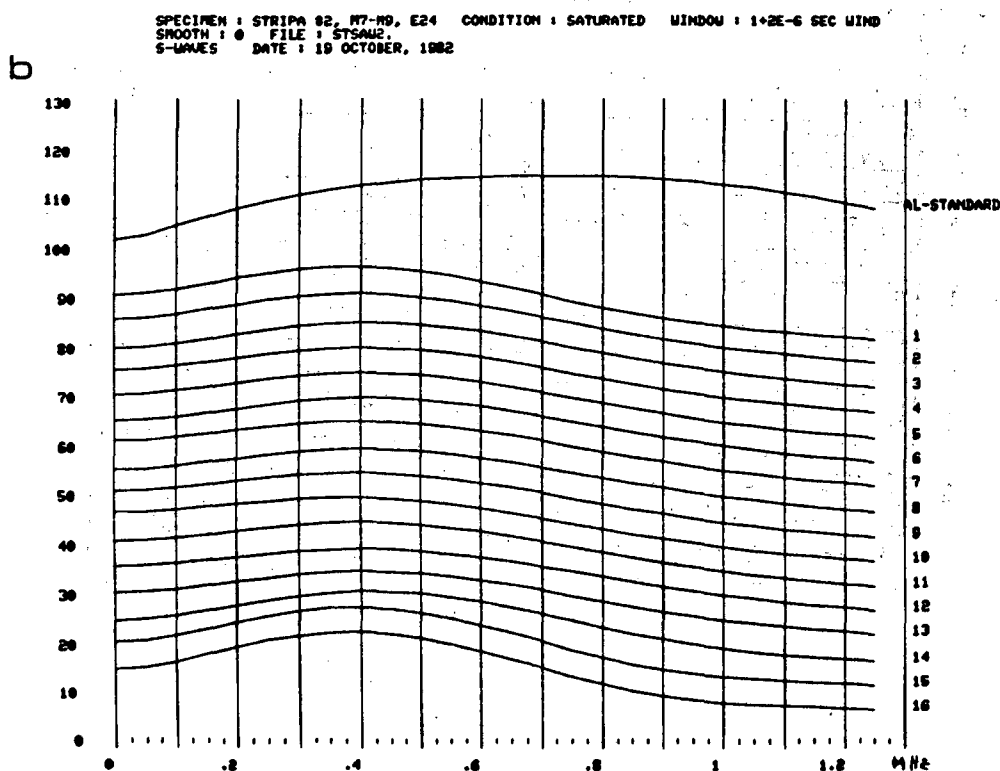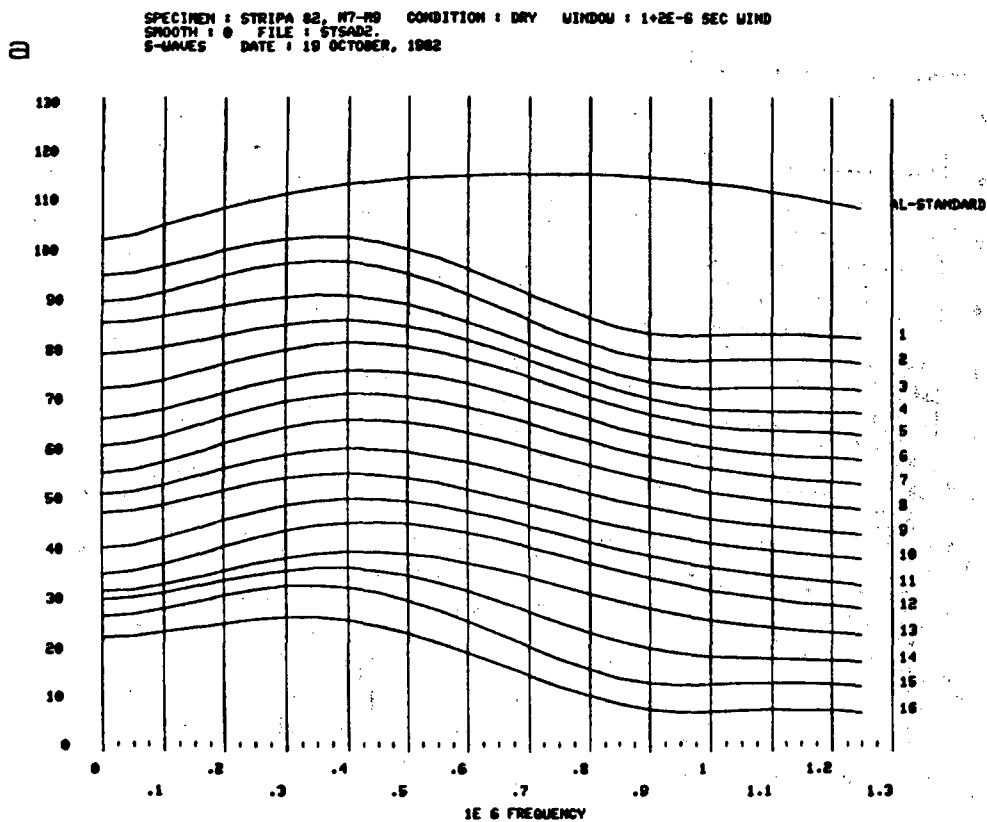
Fig. 7.14 a) Fourier amplitude spectra for the truncated S-waves in Fig. 7.13 a). The spectra are from a complete load cycle from 2.3 MPa to 51 MPa uniaxial stress for the specimen dried in a convection oven at 70° C for 48 hours. b) Fourier amplitude spectra for the truncated S-waves in Fig. 7.13 b). The spectra are from a complete load cycle from 2.3 MPa to 51 MPa uniaxial stress for the specimen saturated under a 5 millitorr vacuum.
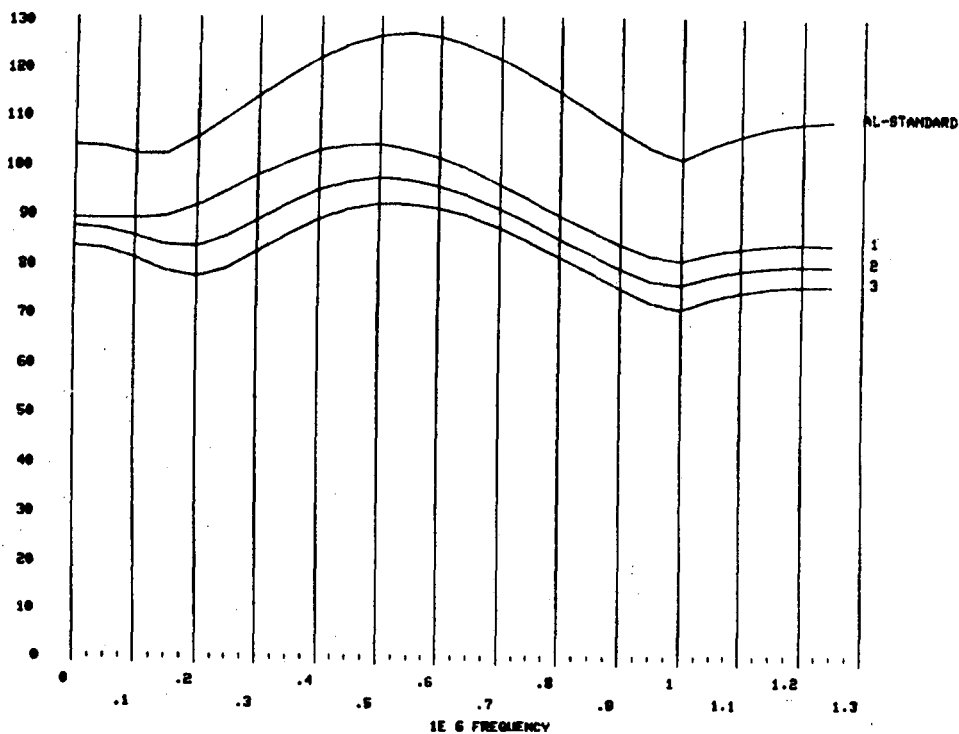
Fig. 7.1 5 Amplitude spectra for the aluminum standard and three perspex specimen 7.622, 5.080 and 2.544 cm long.

Fig. 7.16 Spectral ratio between the spectra from the aluminum standard and the 7.622 cm long perspex specimen.

Fig. 7.17 a) Q_α for specimen #1 in a dry state as function of uniaxial stress. b) Q_α for specimen #1 in a saturated state as function of uniaxial stress.

a

```
Q FOR UNIAXIAL STRESS ON CORE
SPECIMEN FILE : STPQD2.1
SPECIMEN : STRIPA #2, R7-R9, DRY
STANDARD FILE : ALSPA2.1
STANDARD Q : 2000
STANDARD VEL : 6362
STANDARD LENGTH : .07622 M.
SMOOTHING OF Q PLOT: 283 POINT RUNNING
```

SPECIMEN : STRIPA #2, R7-R9, DRY

#	STRESS	Q-VALUE	VELOCITY
1	2.33671	15.5261	4989.52
2	4.67342	20.2859	5017.02
3	9.34683	25.3258	5032.43
4	14.0203	28.1668	5114.11
5	18.6937	31.2199	5245.07
6	23.3671	32.5284	5379.38
7	28.0405	32.9886	5469.16
8	32.7139	35.6856	5550.68
9	42.0607	39.0354	5661.92
10	51.4076	39.0265	5733.24
11	42.0607	34.6695	5701.32
12	32.7139	29.7182	5600
13	23.3671	25.1293	5461.87
14	14.0203	20.7835	5235.02
15	4.67342	16.8511	5020.1
16	2.33671	14.4213	4977.4

b

```
Q FOR UNIAXIAL STRESS ON CORE
SPECIMEN FILE : STPQD2.W1
SPECIMEN : STRIPA #2, SATURATED
STANDARD FILE : ALSPA2.1
STANDARD Q : 2000
STANDARD VEL : 6362
STANDARD LENGTH : .07622 M.
SMOOTHING OF Q PLOT: 283 POINT RUNNING
```

SPECIMEN : STRIPA #2, SATURATED

#	STRESS	Q-VALUE	VELOCITY
1	2.33671	26.5204	5914.62
2	4.67342	28.8483	5935.33
3	9.34683	35.05	5864.57
4	14.0203	41.3289	5877.19
5	18.6937	47.0337	5894.1
6	23.3671	51.0116	5902.59
7	28.0405	54.2097	5923.93
8	32.7139	57.9033	5932.51
9	42.0607	61.882	5949.75
10	51.4076	62.3429	5967.08
11	42.0607	50.1075	5958.4
12	32.7139	39.1667	5932.51
13	23.3671	32.4016	5856.18
14	14.0203	23.6902	5697.36
15	4.67342	16.88	5502.22
16	2.33671	14.9725	5513.32

Fig. 7.18 a) Q_α for specimen #2 in a dry state as function of uniaxial stress. Table of test number, uniaxial stress, Q-value and V_p. b) Q_α for specimen #2 in a saturated state as function of uniaxial stress. Table of test number, uniaxial stress, Q-value and V_p.

```
Q FOR UNIAXIAL STRESS ON CORE
SPECIMEN FILE : STPQD3.3
SPECIMEN : STRIPA #3,P-WAVES,H10,E29,DRY,WIND:.5-1.0,4E-6
STANDARD FILE : ALSPA2.1
STANDARD Q : 2000
STANDARD VEL : 6362
STANDARD LENGTH : .07622 M.
SMOOTHING OF Q PLOT: 2X3 POINT RUNNING
```

	STRESS	Q-VALUE	VELOCITY
1	2.3207	13.4122	5586.92
2	4.6414	20.1853	5586.92
3	9.28279	29.6143	5629.54
4	13.9242	43.3742	5680.76
5	18.5656	52.2035	5716.76
6	23.207	49.7023	5749.15
7	27.8484	41.2087	5773.68
8	32.4898	39.6081	5798.43
9	41.7726	44.0609	5827.57
10	51.0553	52.6492	5848.56
11	41.7726	68.8618	5835.95
12	32.4898	77.2879	5802.57
13	23.207	59.0359	5777.79
14	13.9242	35.8817	5712.74
15	4.6414	21.2706	5625.64
16	2.3207	12.2419	5598.48

UNIAXIAL STRESS [MPA]


```
Q FOR UNIAXIAL STRESS ON CORE
SPECIMEN FILE : STPQD3.W1
SPECIMEN : STRIPA #3, SATURATED
STANDARD FILE : ALSPA2.1
STANDARD Q : 2000
STANDARD VEL : 6362
STANDARD LENGTH : .07622 M.
SMOOTHING OF Q PLOT: 2X3 POINT RUNNING
```

	STRESS	Q-VALUE	VELOCITY
1	2.3207	29.1797	5865.46
2	4.6414	35.7219	5891
3	9.28279	43.2898	5921.08
4	13.9242	46.2008	5934.06
5	18.5656	46.1736	5942.75
6	23.207	47.5223	5947.11
7	27.8484	53.5949	5955.83
8	32.4898	62.2204	5960.21
9	41.7726	66.7252	5964.58
10	51.0553	53.934	5968.97
11	41.7726	44.0076	5968.97
12	32.4898	44.6555	5955.83
13	23.207	46.1874	5951.47
14	13.9242	42.9844	5934.06
15	4.6414	36.2729	5882.46
16	2.3207	29.0093	5865.4f

UNIAXIAL STRESS [MPA]

Fig. 7.19 a) Q_α for specimen #3 from the borehole E29 in the H10 area as function of uniaxial stress. The specimen is dry. b) Q_α for P-waves for specimen #3 from borehole E29 in the H10 area as function of uniaxial stress. The specimen is dry. Table of the test number, stress, Q-value and the V_p.

a

Q FOR UNIAXIAL STRESS ON CORE
SPECIMEN FILE : STPQD4.1
SPECIMEN : STRIPA 84, DRILLBACK 1.45 FROM H10, 4E-6 SEC WINDOW, DRY
STANDARD FILE : ALSPA2.1
STANDARD Q : 2000
STANDARD VEL : 6382
STANDARD LENGTH : .07622 R.
SMOOTHING OF Q PLOT: 2X3 POINT RUNNING

#	STRESS	Q-VALUE	VELOCITY
1	2.30043	27.0577	5555.36
2	4.60086	27.933	5571.28
3	9.20171	33.799	5623.65
4	13.8026	43.1047	5672.87
5	18.4034	53.171	5710.35
6	23.0043	60.2431	5744.09
7	27.6051	56.2131	5773.94
8	32.206	47.8941	5799.78
9	41.4077	55.2781	5838.96
10	50.6094	67.6116	5856.55
11	41.4077	66.3418	5838.96
12	32.206	59.6696	5812.78
13	23.0043	50.4111	5765.38
14	13.8026	39.4633	5693.63
15	4.60086	29.4693	5591.3
16	2.30043	21.09	5563.3

UNIAXIAL STRESS [MPA]

b

Q FOR UNIAXIAL STRESS ON CORE
SPECIMEN FILE : STPQD4.U1
SPECIMEN : STRIPA 84, SATURATED
STANDARD FILE : ALSPA2.1
STANDARD Q : 2000
STANDARD VEL : 6382
STANDARD LENGTH : .07622 R.
SMOOTHING OF Q PLOT: 2X3 POINT RUNNING

SPECIMEN : STRIPA 84, SATURATED

#	STRESS	Q-VALUE	VELOCITY
1	2.30043	31.1109	5969.81
2	4.60088	34.3431	5987.59
3	9.20171	43.0403	5909.96
4	13.8026	55.731	5914.46
5	18.4034	73.7951	5923.46
6	23.0043	86.2646	5937.77
7	27.6051	75.6928	5932.49
8	32.206	84.999	5941.56
9	41.4077	100.638	5950.65
10	50.6094	100.594	5959.77
11	41.4077	99.5909	5948.1
12	32.206	83.9837	5937.62
13	23.0043	76.8996	5923.46
14	13.8026	55.7830	5896.51
15	4.60088	37.2164	5852.15
16	2.30043	30.528	5812.78

UNIAXIAL STRESS [MPA]

Fig. 7.20 a) Q_α for specimen #4 from borehole DBEX-1 at he isotherm of 130° C. The specimen is dry and the Q_α is a function of the uniaxial stress. Table of the test number, stress, Q-value and the V_p. b) Q_α for specimen #4 from borehole DBEX-1 at the isotherm 130° C. The specimen is saturated and the Q_α is a function of the uniaxial stress. Table of the test number, stress, Q-value and the V_p.

Plot a header:
Q FOR UNIAXIAL STRESS ON CORE
SPECIMEN FILE : STPQD5.1
SPECIMEN : STRIPA 85, DRILLBACK 0.75 FROM H10, 4E-6 WINDOW, DRY
STANDARD FILE : ALSPA2.1
STANDARD Q : 2000
STANDARD VEL : 6362
STANDARD LENGTH : .07622 M.
SMOOTHING OF Q PLOT: 283 POINT RUNNING

#	STRESS	Q-VALUE	VELOCITY
1	2.31275	20.7849	5539.86
2	4.62551	26.1807	5555.45
3	9.25101	37.5962	5567.21
4	13.8765	52.7536	5610.73
5	18.502	78.6316	5654.94
6	23.1275	133.964	5691.64
7	27.753	192.124	5728.81
8	32.3786	207.099	5753.86
9	41.6296	213.951	5791.86
10	50.8806	242.198	5821.76
11	41.6296	237.604	5808.9
12	32.3786	186.727	5766.47
13	23.1275	131.483	5724.66
14	13.8765	73.2487	5642.82
15	4.62551	37.6406	5551.55
16	2.31275	18.0851	5532.1

UNIAXIAL STRESS [MPA]

Plot b header:
Q FOR UNIAXIAL STRESS ON CORE
SPECIMEN FILE : STPQD5.W1
SPECIMEN : STRIPA 85, DRILLBACK 0.75 H10, SATURATED
STANDARD FILE : ALSPA2.1
STANDARD Q : 2000
STANDARD VEL : 6362
STANDARD LENGTH : .07622 M.
SMOOTHING OF Q PLOT: 283 POINT RUNNING

#	STRESS	Q-VALUE	VELOCITY
1	2.31275	27.0879	5900.07
2	4.62551	39.1529	5900.07
3	9.25101	48.4945	5908.91
4	13.8765	54.9975	5913.33
5	18.502	69.6773	5917.77
6	23.1275	88.4461	5922.21
7	27.753	91.1986	5931.1
8	32.3786	78.5396	5940.03
9	41.6296	75.3765	5944.5
10	50.8806	71.9174	5953.47
11	41.6296	69.1865	5944.5
12	32.3786	58.032	5935.56
13	23.1275	46.4687	5922.21
14	13.8765	38.5723	5904.49
15	4.62551	31.1412	5860.65
16	2.31275	23.3876	5856.31

UNIAXIAL STRESS [MPA]

Fig. 7.21 a) Q_α for specimen #5 from borehole DBEX-1 in the H10 area at the *in situ* isotherm of 200° C. The specimen is dry and the Q_α is a function of uniaxial stress. Table of test number, uniaxial stress, Q-value and V_p. b) Q_α for specimen #5 from borehole DBEX-1 in the H10 area at the isotherm 200° C. The specimen is saturated and the Q_α is a function of uniaxial stress. The table is showing the test number, uniaxial stress [MPa], Q-value and the V_p.

Fig. 7.22 a) Q_β for specimen #1 in a dry state. b) Q_β for specimen #1 in saturated state.

a

Q FOR UNIAXIAL STRESS ON CORE
SPECIMEN FILE : STSQD2.3
SPECIMEN : STRIPA #2, DRY, M7-M9,E24, .5-1.0 MHZ,
STANDARD FILE : ALSSA4.1
STANDARD Q : 2000
STANDARD VEL : 3201
STANDARD LENGTH : .07622 M.
SMOOTHING OF Q PLOT: 253 POINT RUNNING

SPECIMEN : STRIPA #2, DRY, M7-M9,E24, .5-1.0 MHZ.

#	STRESS	Q-VALUE	VELOCITY
1	2.33671	13.9441	3180.43
2	4.67342	14.1517	3189.1
3	9.34683	15.7312	3217.91
4	14.0203	18.898	3264.06
5	18.6937	22.44	3325
6	23.3671	25.4638	3378.47
7	28.0405	27.6574	3419.37
8	32.7139	28.776	3458.34
9	42.0607	29.2475	3511.7
10	51.4076	29.8206	3542.07
11	42.0607	30.4867	3522.27
12	32.7139	29.8207	3480.37
13	23.3671	25.8818	3405.15
14	14.0203	20.0062	3393.55
15	4.67342	15.5897	3189.1
16	2.33671	12.5064	3174.27

UNIAXIAL STRESS [MPA]

b

Q FOR UNIAXIAL STRESS ON CORE
SPECIMEN FILE : STSQU2.3
SPECIMEN : STRIPA #2, SATURATED, E24, WINDOW 1+2E-6 SEC, M7-M9
STANDARD FILE : ALSSA4.1
STANDARD Q : 2000
STANDARD VEL : 3201
STANDARD LENGTH : .07622 M.
SMOOTHING OF Q PLOT: 253 POINT RUNNING

SPECIMEN : STRIPA #2, SATURATED, E24, WINDOW 1+2E-6 SEC, M7-M9

#	STRESS	Q-VALUE	VELOCITY
1	2.33671	27.764	3423.65
2	4.67342	31.0458	3422.22
3	9.34683	32.7424	3430.82
4	14.0203	33.3345	3439.46
5	18.6937	33.8106	3462.72
6	23.3671	34.266	3480.37
7	28.0405	34.2648	3490.75
8	32.7139	33.5755	3514.71
9	42.0607	32.8106	3542.07
10	51.4076	32.8878	3571.4
11	42.0607	33.7381	3551.28
12	32.7139	34.0884	3516.22
13	23.3671	31.8734	3486.3
14	14.0203	27.5	3448.91
15	4.67342	23.2843	3359.08
16	2.33671	20.1279	3359.08

UNIAXIAL STRESS [MPA]

Fig. 7.23 b) Q_β for specimen #2 in a dry state. b) Q_β for specimen #2 in a saturated state.

a

Q FOR UNIAXIAL STRESS ON CORE
SPECIMEN FILE : STSQD3.3
SPECIMEN : STRIPA 83, S-WAVES TRUNCATED WITH 1+2E-6 SEC WIND, E20/H10, 821019
STANDARD FILE : ALSSA4.1
STANDARD Q : 2000
STANDARD VEL : 3201
STANDARD LENGTH : .07622 M.
SMOOTHING OF Q PLOT: 2&3 POINT RUNNING

#	STRESS	Q-VALUE	VELOCITY
1	2.3207	19.9125	3307.99
2	4.6414	22.556	3318.81
3	9.28279	24.3006	3354.46
4	13.9242	25.6002	3373.98
5	18.5656	26.6142	3392.31
6	23.207	27.1302	3416.58
7	27.8484	27.8312	3429.57
8	32.4898	29.1918	3444.12
9	41.7726	31.0883	3461.75
10	51.0553	31.8939	3470.63
11	41.7726	31.0545	3460.27
12	32.4898	29.7808	3444.12
13	23.207	27.9201	3413.71
14	13.9242	25.0501	3371.18
15	4.6414	22.0924	3332.43
16	2.3207	19.8571	3313.39

UNIAXIAL STRESS [MPA]

b

Q FOR UNIAXIAL STRESS ON CORE
SPECIMEN FILE : STSQD3.3
SPECIMEN : STRIPA 83, S-WAVES TRUNCATED WITH 1+2E-6 SEC WIND, SATURATED, H10/E20
STANDARD FILE : ALSSA4.1
STANDARD Q : 2000
STANDARD VEL : 3201
STANDARD LENGTH : .07622 M.
SMOOTHING OF Q PLOT: 2&3 POINT RUNNING

#	STRESS	Q-VALUE	VELOCITY
1	2.3207	28.6068	3472.11
2	4.6414	33.4943	3475.09
3	9.28279	36.9137	3481.05
4	13.9242	38.2027	3490.03
5	18.5656	38.1581	3503.58
6	23.207	37.9254	3512.68
7	27.8484	38.1013	3518.77
8	32.4898	37.8173	3524.88
9	41.7726	36.6626	3538.71
10	51.0553	36.6161	3538.71
11	41.7726	37.319	3535.63
12	32.4898	38.3171	3523.35
13	23.207	39.0275	3566.61
14	13.9242	37.348	3488.53
15	4.6414	32.9313	3458.8
16	2.3207	27.3272	3449.98

UNIAXIAL STRESS [MPA]

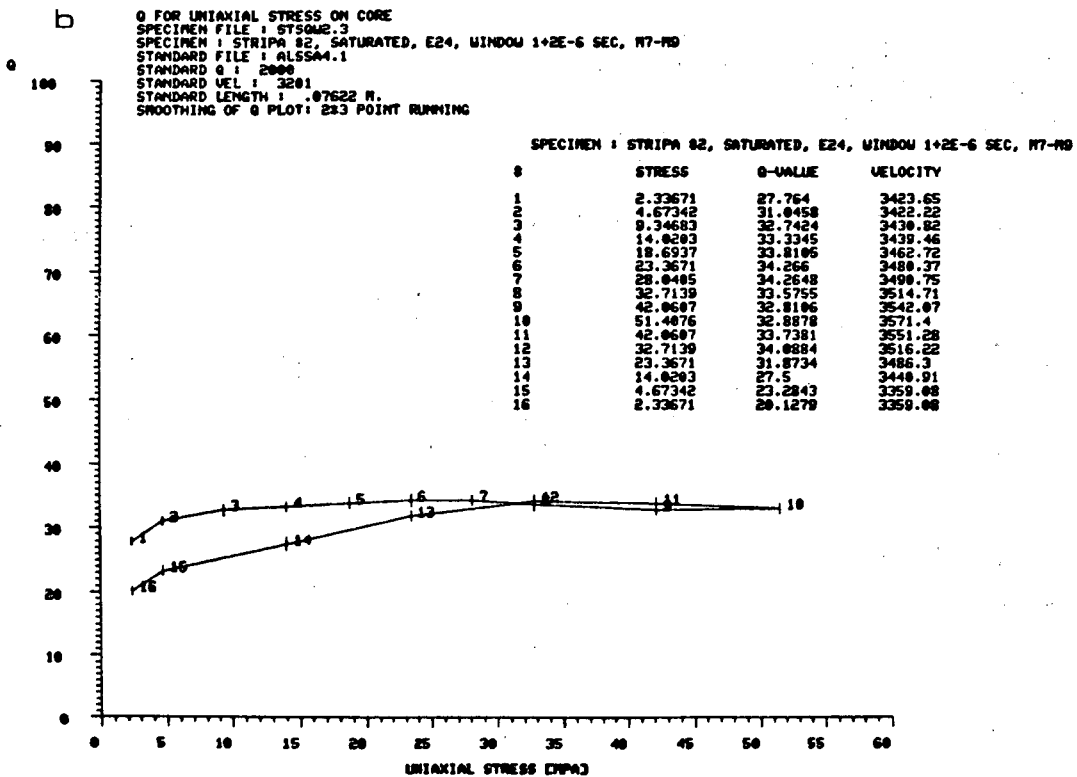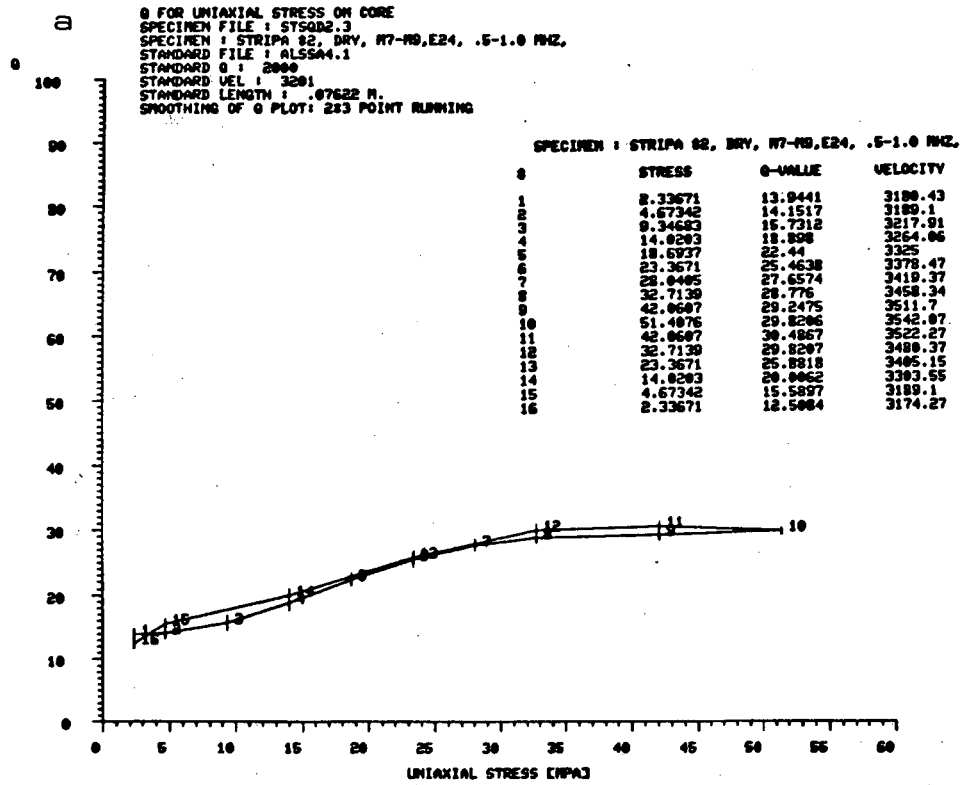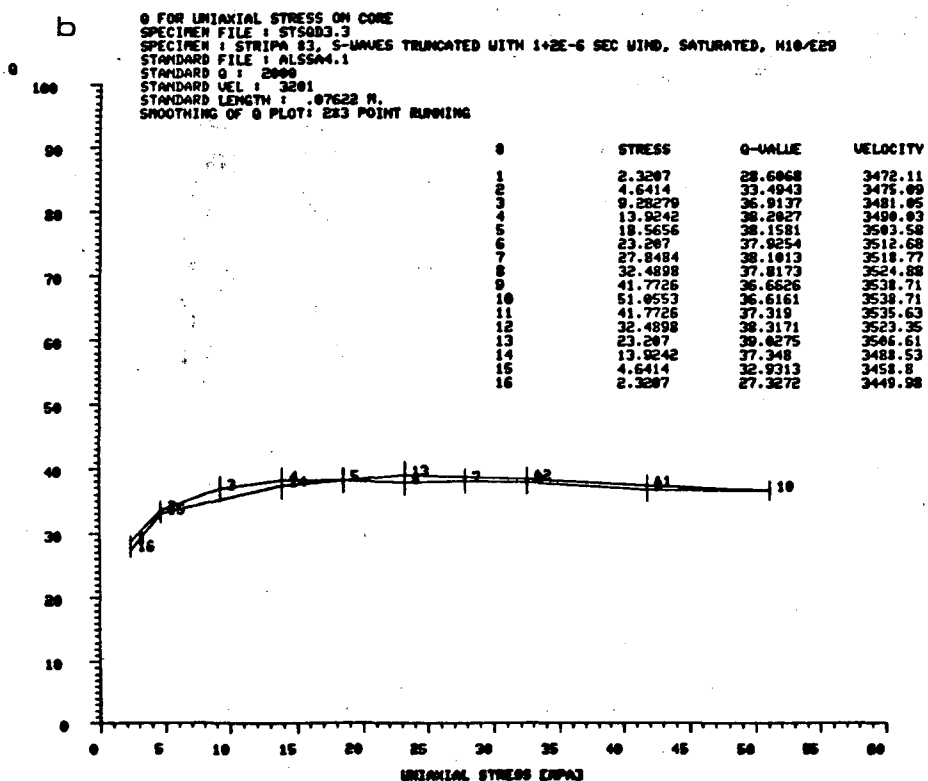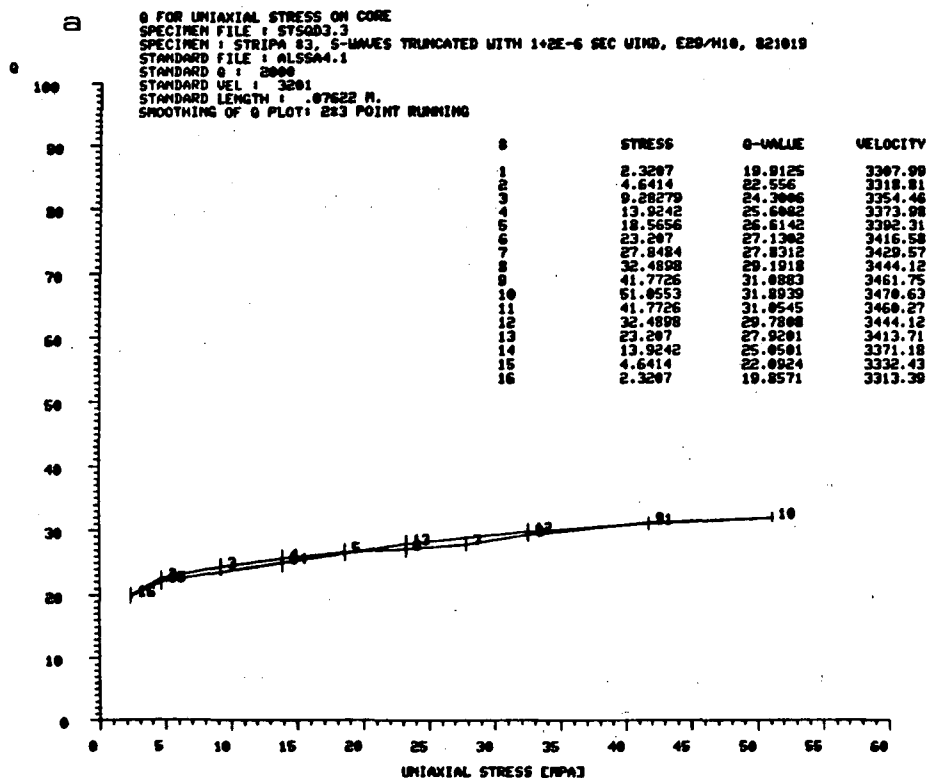Fig. 7.24 a) Q_β for specimen #3 in a dry state. b) Q_β for specimen #3 in a saturated state.

Fig. 7.25 a) Q_β for specimen #4 in a dry state. b) Q_β for specimen #4 in a saturated state.

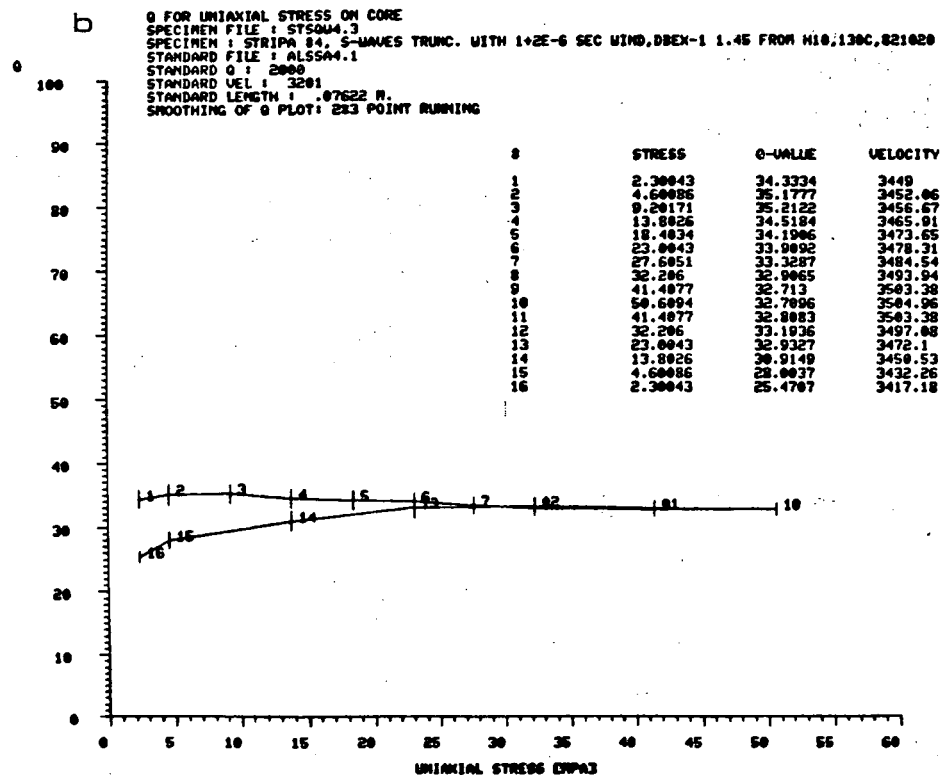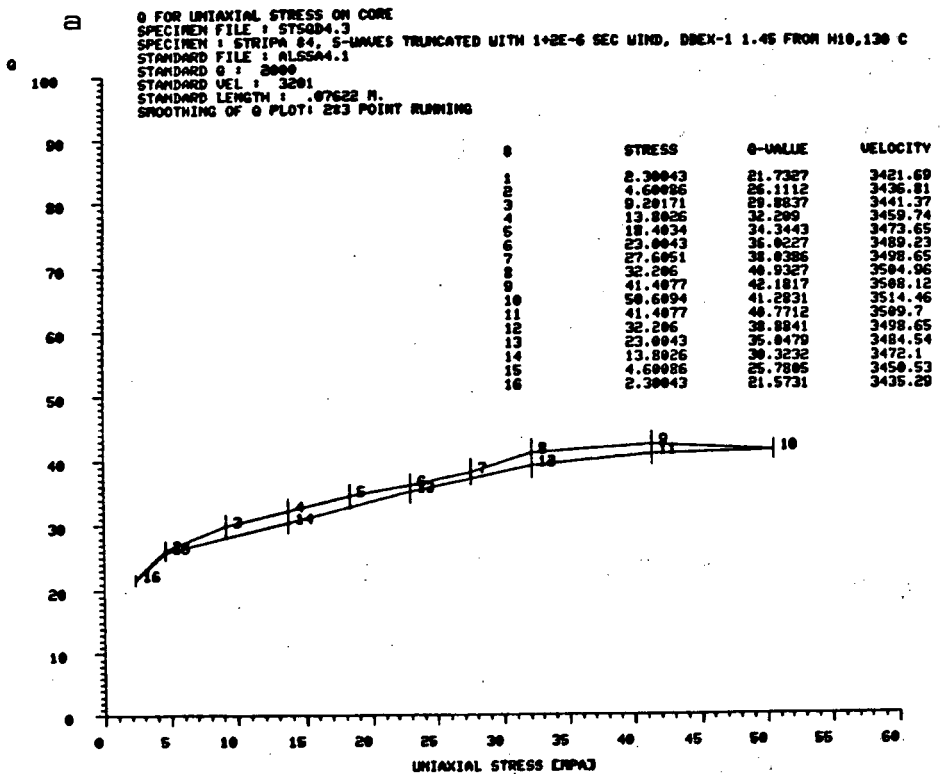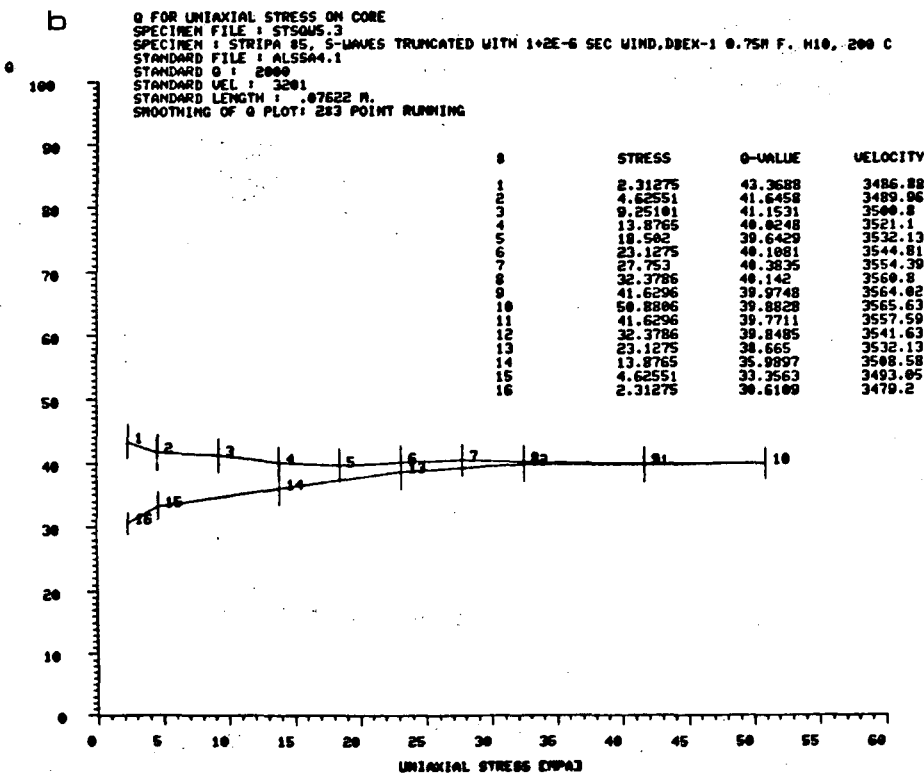Fig. 7.26 a) Q_β for specimen #5 in a dry state. b) Q_β for specimen #3 in a saturated state.

a

POROSTIY : .897748 %

SATURATION (%)

b

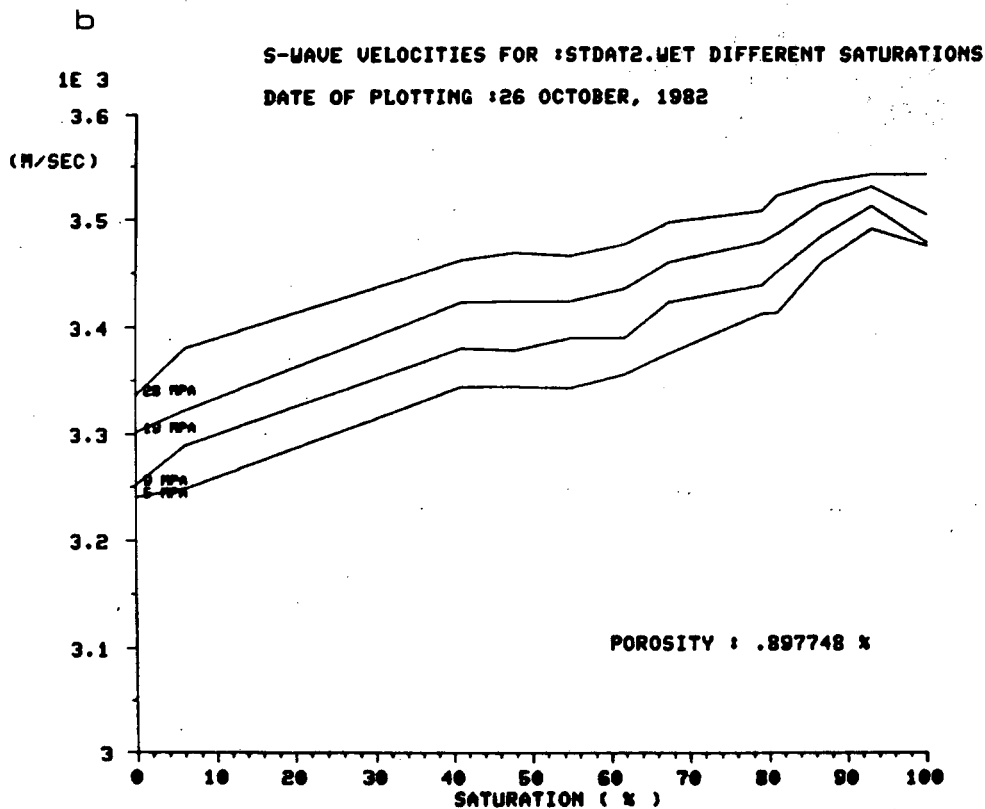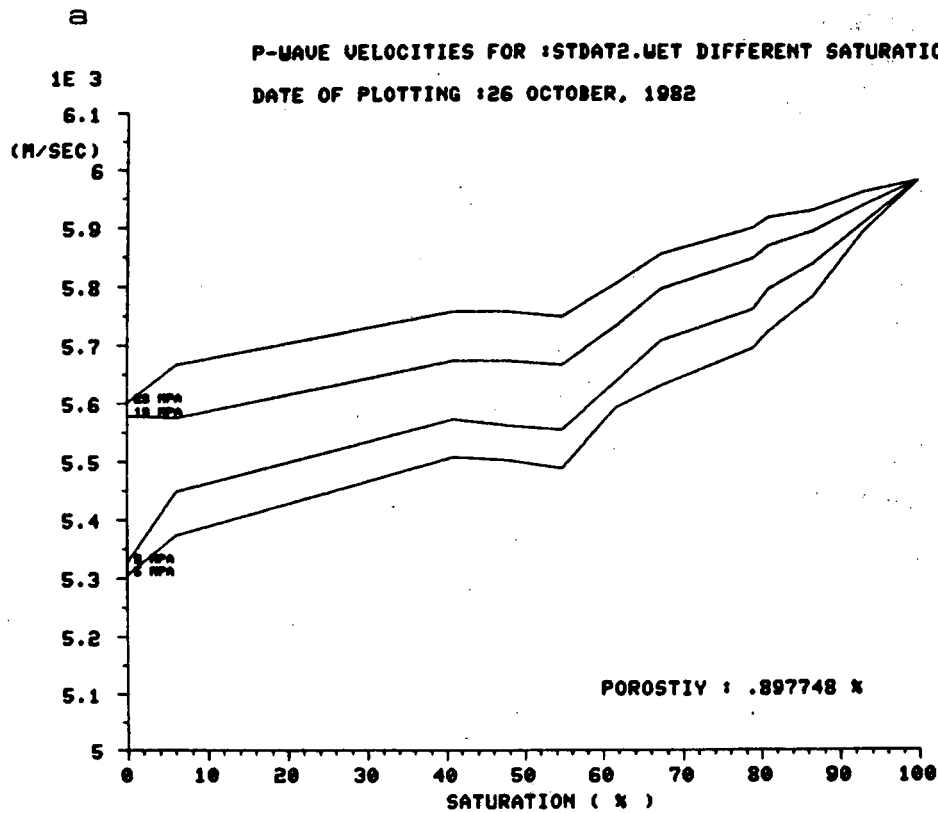POROSITY : .897748 %

SATURATION (%)

Fig. 7.27 a) V_p for specimen #1 for saturation ranging from 100 % to 0 % under 4 uniaxial stresses, 5, 10, 20 and 30 MPa. b) V_s for specimen #1 for saturation ranging from 100 % to 0% for 4 uniaxial stresses σ_{ua} of 5, 10, 20 and 30 MPa.

a

b

S-WAVE VELOCITIES FOR :STDAT2.WET DIFFERENT SATURATIONS
DATE OF PLOTTING :27 OCTOBER, 1982

Fig. 7.28 a) V_p for specimen #2 for saturation ranging from 100% to 0% for 4 uniaxial stresses σ_{ua} of 5, 10, 20 and 30 MPa. b) V_s for specimen #2 for saturation ranging from 100 % to 0% for 4 uniaxial stresses σ_{ua} of 5, 10, 20 and 30 MPa.
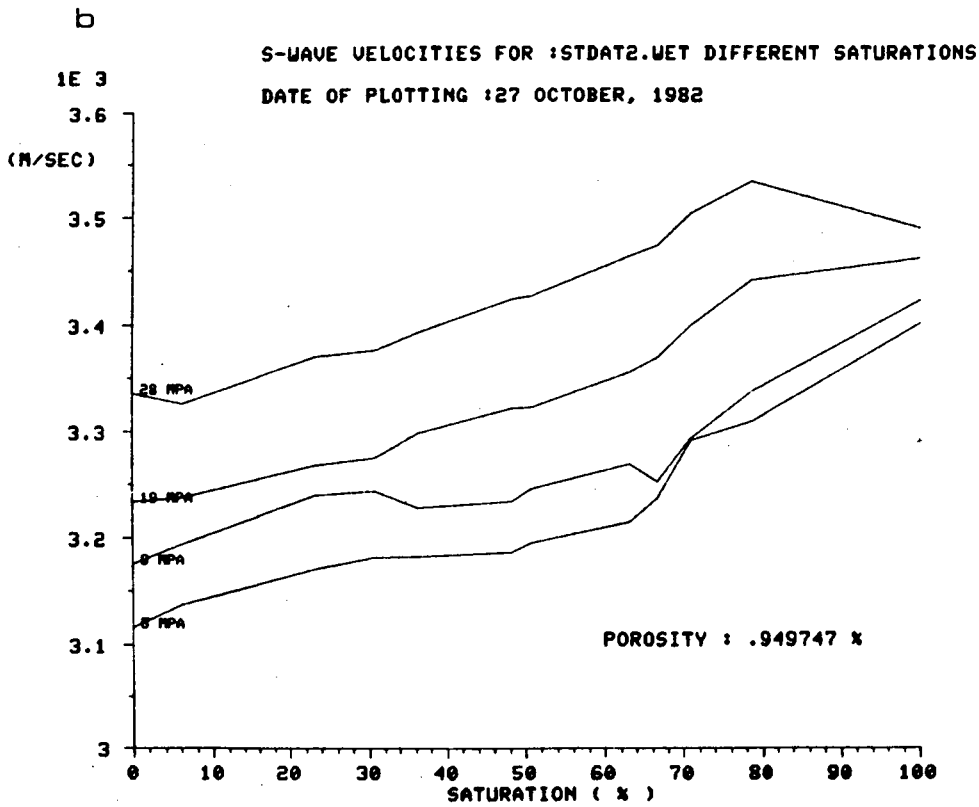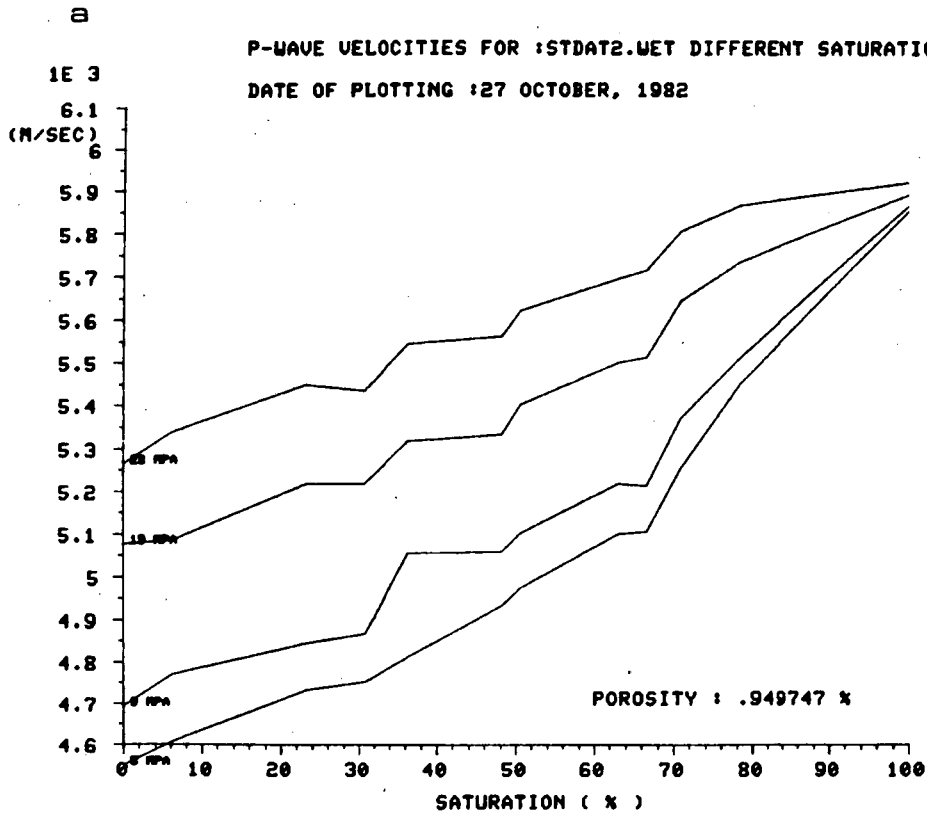
a

POISSONS RATIO FOR :STDAT2.WET DIFFERENT SATURATIONS

1E-3

DATE OF PLOTTING :26 OCTOBER, 1982

300

250

10 MPA
20 MPA
30 MPA

5 MPA

200

150

100

50

POROSITY : .897748 %

0

0   10   20   30   40   50   60   70   80   90   100

SATURATION (%)

b

YOUNGS MODULUS FOR :STDAT2.WET DIFFERENT SATURATIONS

(GPA) 85

DATE OF PLOTTING :26 OCTOBER, 1982

80

75

20 MPA
10 MPA

70

10 GPA
5 MPA

65

POROSITY : .897748 %

60

0   10   20   30   40   50   60   70   80   90   100

SATURATION (%)

Fig. 7.29 a) Poisson's ratio for specimen #1 as function of saturation for four differents stresses, 5, 10, 20 and 30 MPa. b) Youngs modulus for specimen #1 as function of saturation for four different stresses, 5, 10, 20 and 30 MPa.

a

POISSONS RATIO FOR :STDAT2.WET DIFFERENT SATURATIONS

DATE OF PLOTTING :27 OCTOBER, 1982

POROSITY : .949747 %

SATURATION (%)

b

YOUNGS MODULUS FOR :STDAT2.WET DIFFERENT SATURATIONS

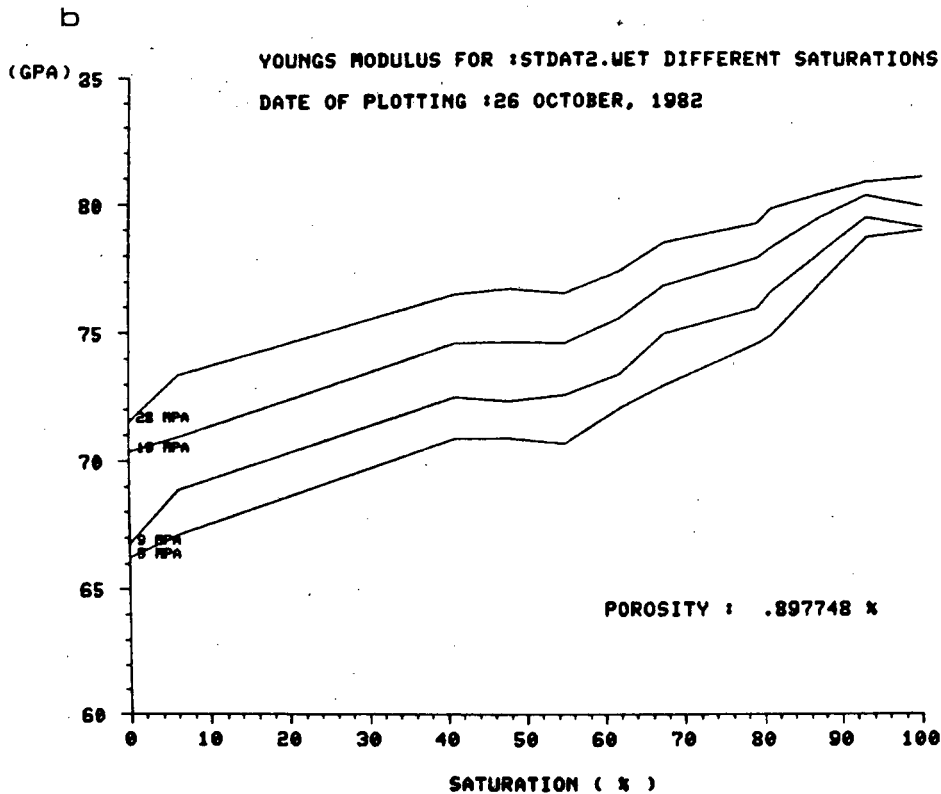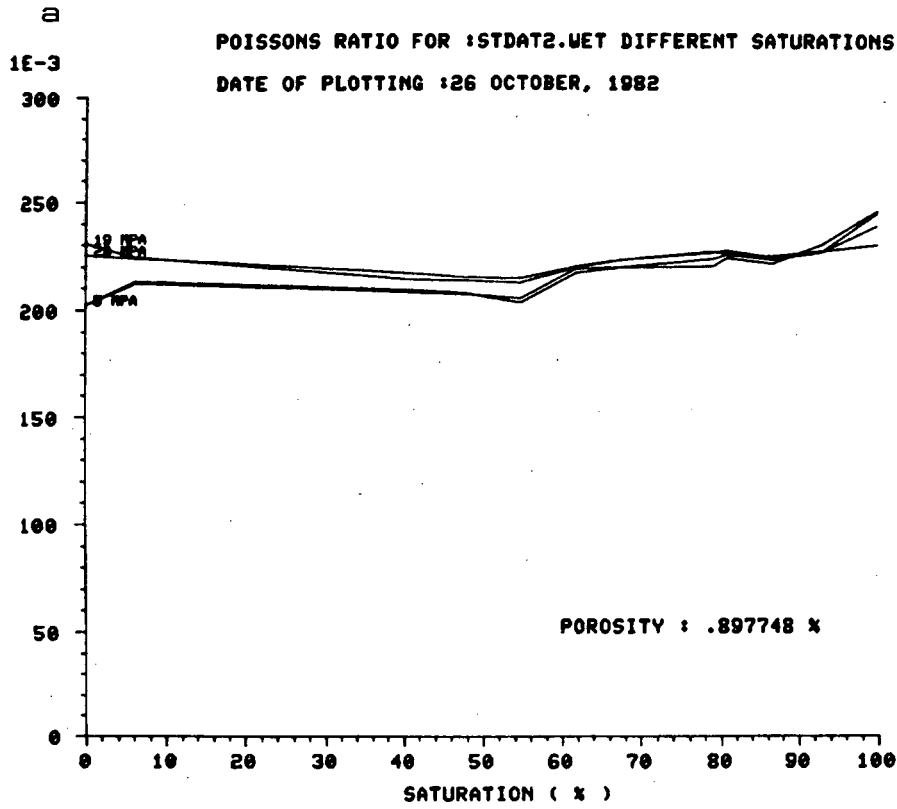DATE OF PLOTTING :27 OCTOBER, 1982
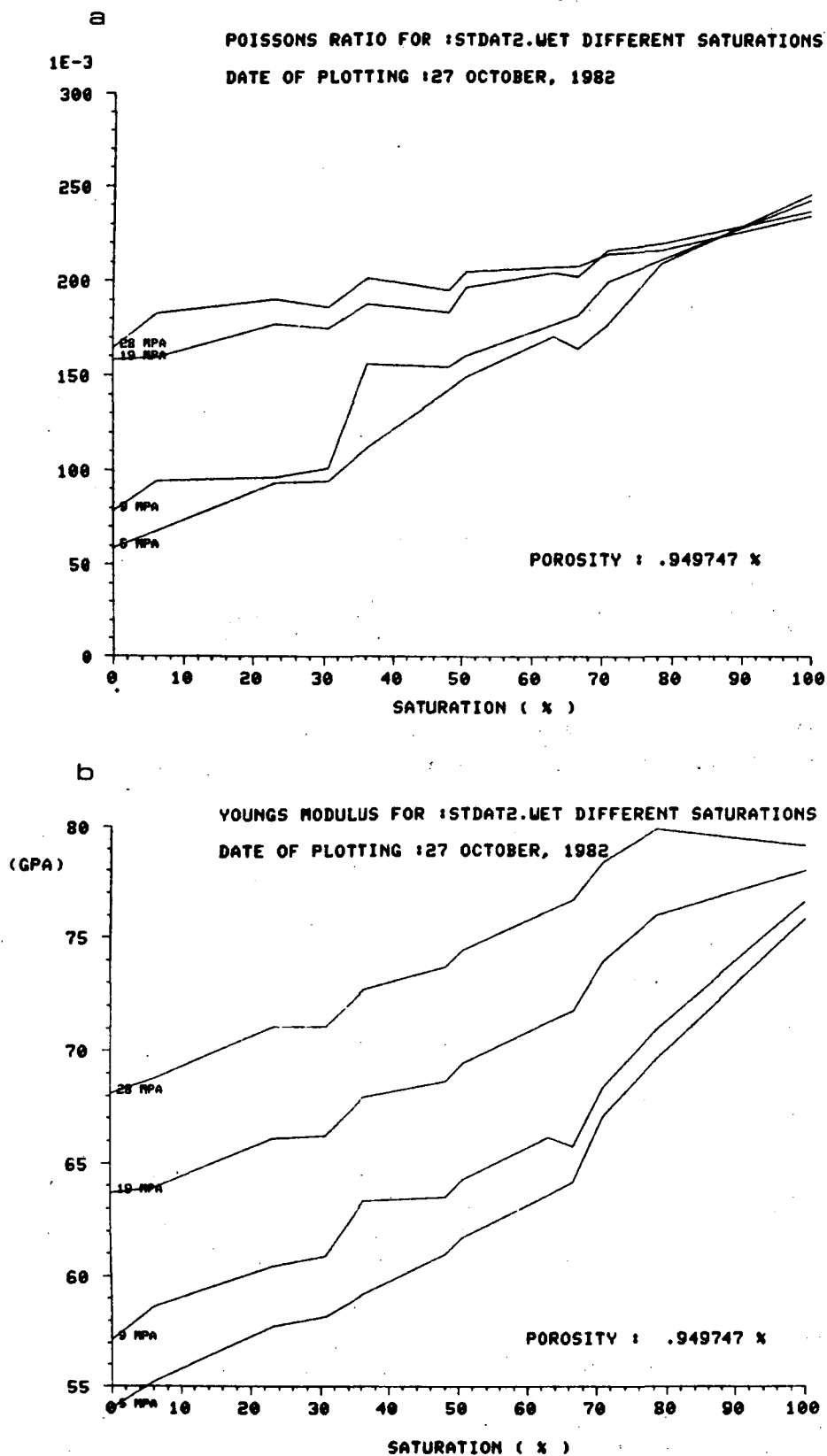
POROSITY : .949747 %

SATURATION (%)

Fig. 7.30 a) Poisson's ratio for specimen #2 as function of saturation of four different stresses, 5, 10, 20 and 30 MPa. b) Youngs modulus foe specimen #2 as function of saturation for four different stresses, 5, 10, 20 and 30 MPa.

a

BULK MODULUS FOR :STDAT2.WET DIFFERENT SATURATIONS

DATE OF PLOTTING :26 OCTOBER, 1982

(GPA) 55

POROSITY : .897748 %

SATURATION (%)

b

SHEAR MODULUS FOR :STDAT2.WET DIFFERENT SATURATIONS

DATE OF PLOTTING :26 OCTOBER, 1982

(GPA) 35

POROSITY : .897748 %

SATURATION (%)

Fig. 7.31 a) Bulk modulus for specimen #1 as function of saturation for four different stresses, 5, 10, 20, and 30 MPa. b) Shear modulus for specimen #1 as function of saturation for four different stresses, 5, 10, 20 and 30 MPa.

a **BULK MODULUS FOR :STDAT2.WET DIFFERENT SATURATIONS**

DATE OF PLOTTING :27 OCTOBER, 1982

b **SHEAR MODULUS FOR :STDAT2.WET DIFFERENT SATURATIONS**
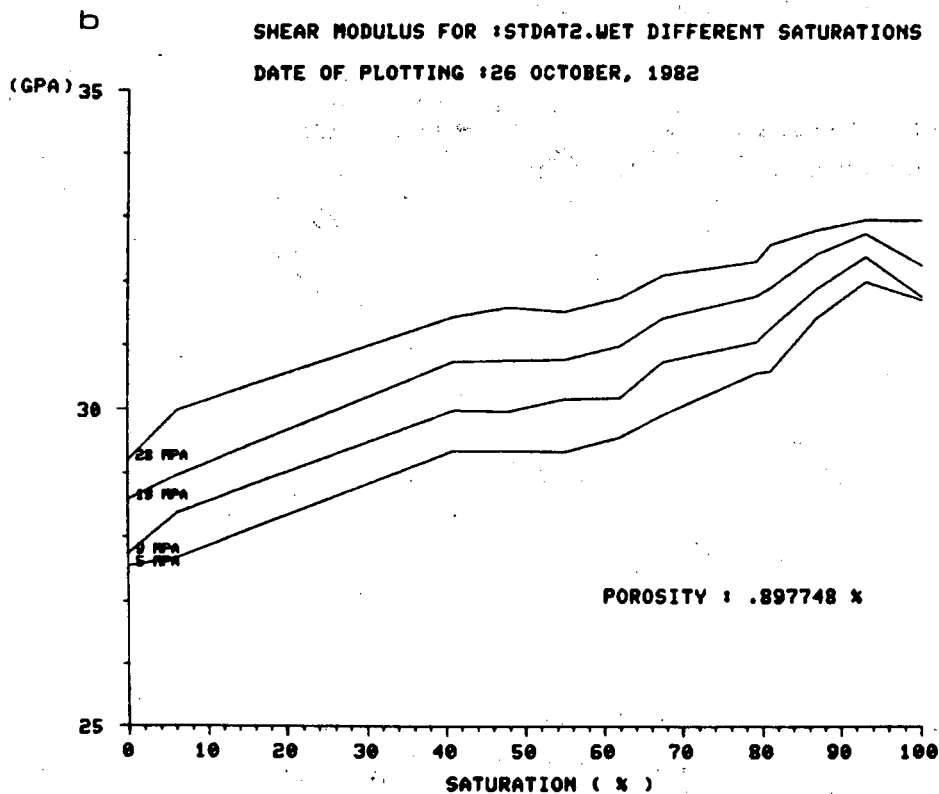
DATE OF PLOTTING :27 OCTOBER, 1982

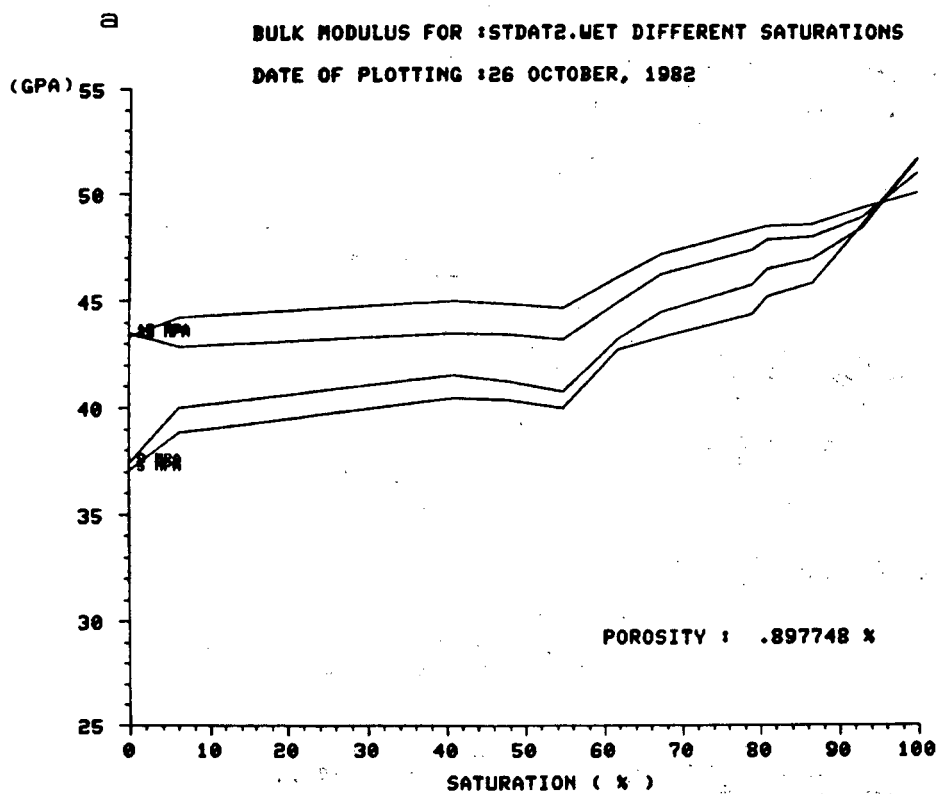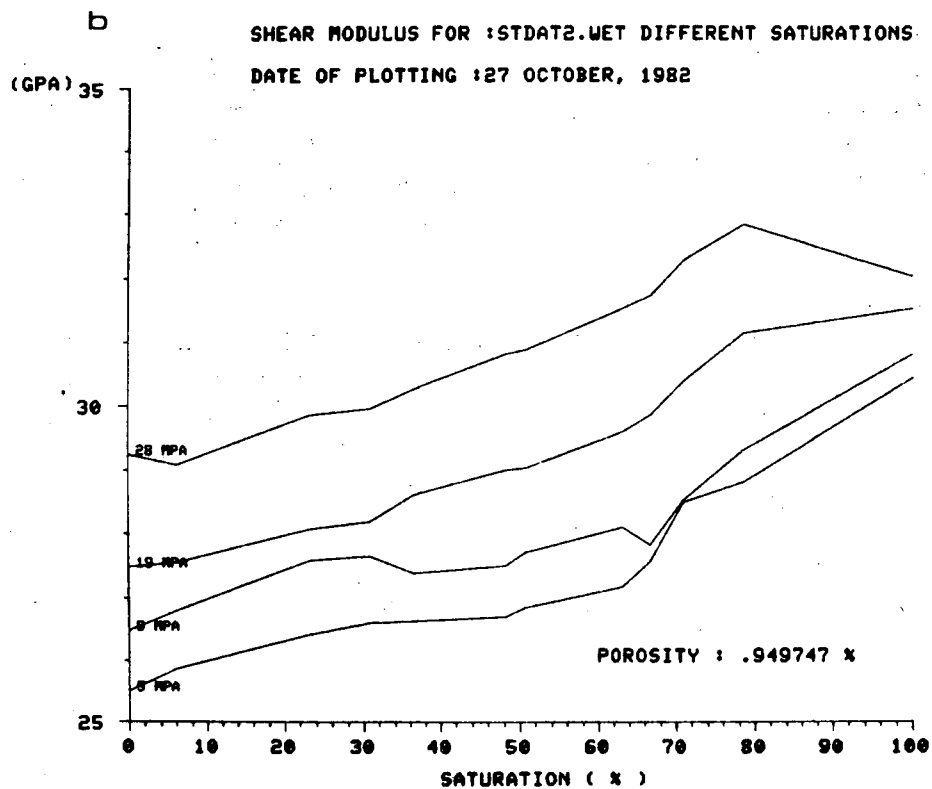

Fig. 7.32 a) Bulk modulus for specimen #2 as function of saturation for four different stresses, 5, 10, 20 and 30 MPa. b) Shear modulus for specimen #2 as function of saturation for four different stresses, 5, 10, 20 and 30 MPa.
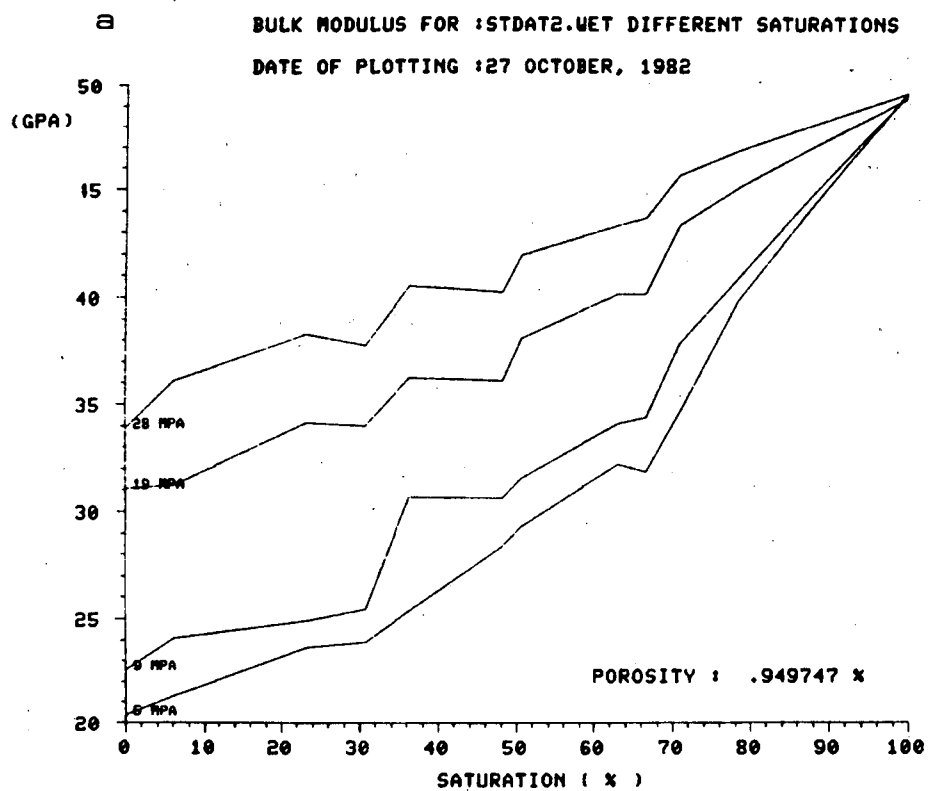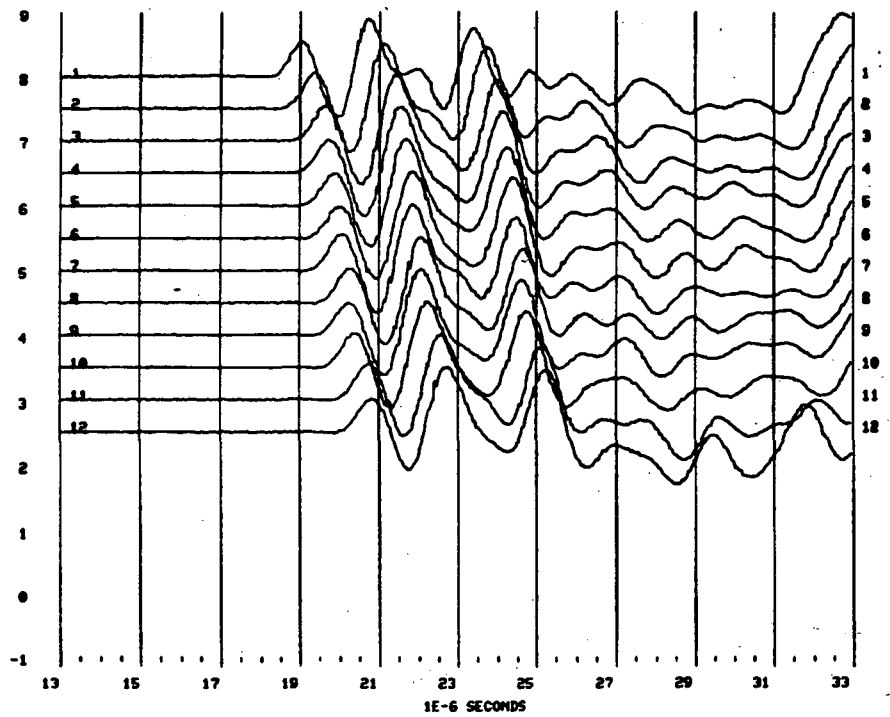
Fig. 7.33 a) P-waveforms for specimen #1 over saturation range from 100 to 0 % under σ_{ua} = 5 MPa.
b) P-waveforms for specimen #1 over saturation range from 100 to 0 % under σ_{ua} = 10 MPa.

a

STRIPA 81, SATURATED -> DRY, 20 MPA UNIAXIAL STRESS, P-WAVES, 821026

1E-6 SECONDS

b

STRIPA 81, SATURATED -> DRY, 30 MPA UNIAXIAL STRESS, P-WAVES, 821026

1E-6 SECONDS

Fig. 7.34 a) P-waveforms for specimen #1 over saturation range from 100 to 0% under $\sigma_{ua} = 20$ MPa.
b) P-waveforms for specimen #1 over a saturation range from 100 to 0% under $\sigma_{ua} = 30$ MPa.

a

STRIPA #2, SAT -> DRY, 5 MPA UNIAXIAL STRESS, P-WAVES 821025

1E-6 SECONDS

b

STRIPA #2, SAT -> DRY, 10 MPA UNIAXIAL STRESS, P-WAVES, 821025

1E-6 SECONDS

Fig. 7.35 a) P-waveforms for specimen #2 over saturation range from 100 to 0% under σ_{ua} = 5 MPa.
b) P-waveforms for specimen #2 over saturation range from 100 to 0% under σ_{ua} =10 MPa.

a

STRIPA 82, SAT -> DRY, 20 MPA UNIAXIAL STRESS, P-WAVES, 821026

b

STRIPA 82, SAT -> DRY, 30 MPA UNIAXIAL STRESS, P-WAVES, 821026
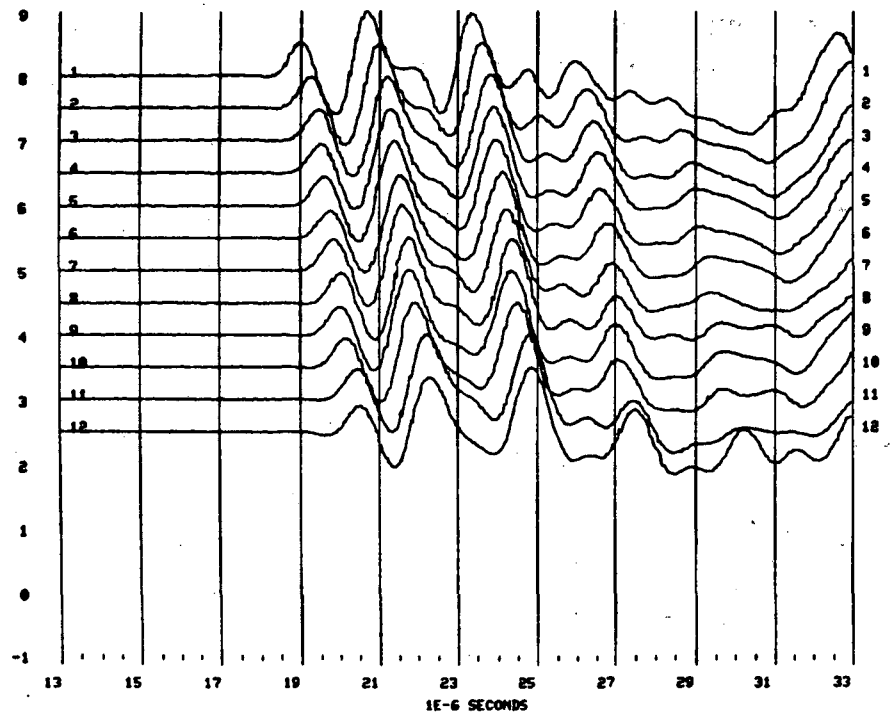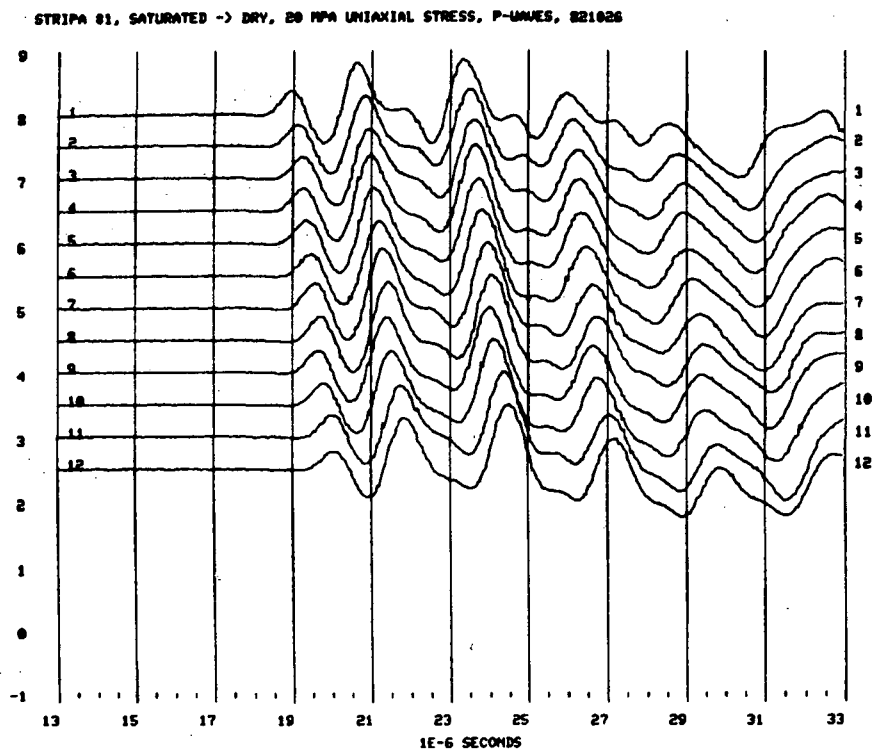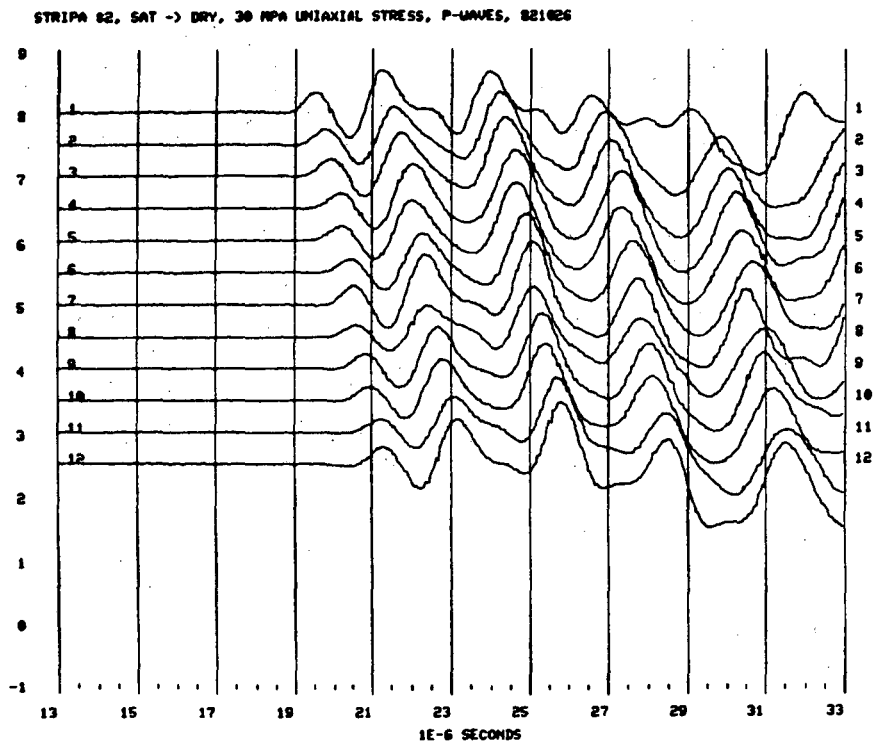

Fig. 7.36 a) P-waveforms for specimen #2 over saturation range from 100 to 0 % under σ_{ua} = 20 MPa. b) P-waveforms for specimen #2 over saturation range from 100 to 0 % under σ_{ua} = 30 MPa.
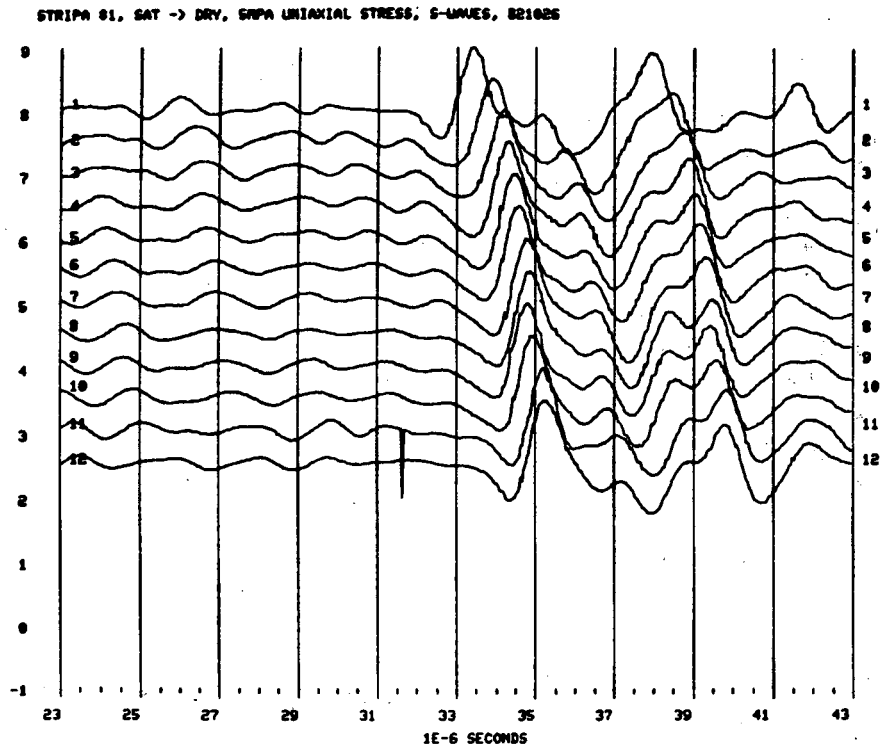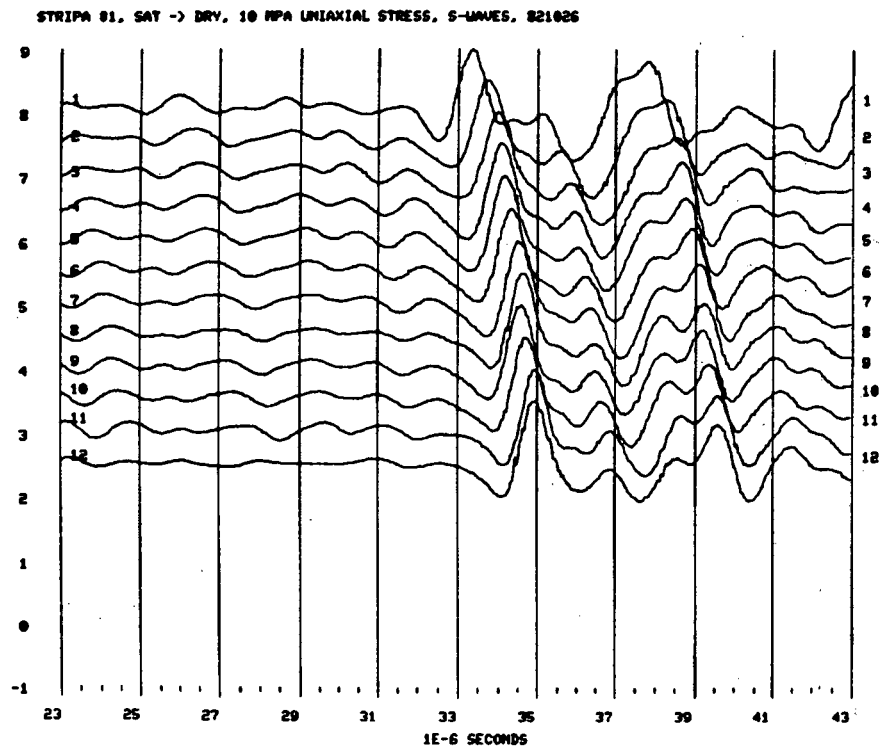
Fig. 7.37 a) S-waveforms for specimen #1 over saturation range from 100 to 0% under σ_{ua} = 5 MPa.
b) S-waveforms for specimen #1 over saturation range from 100 to 0 % under σ_{ua} = 10 MPa.

a

STRIPA 81, SAT -> DRY, 20 MPA UNIAXIAL STRESS, S-WAVES, 821026

b

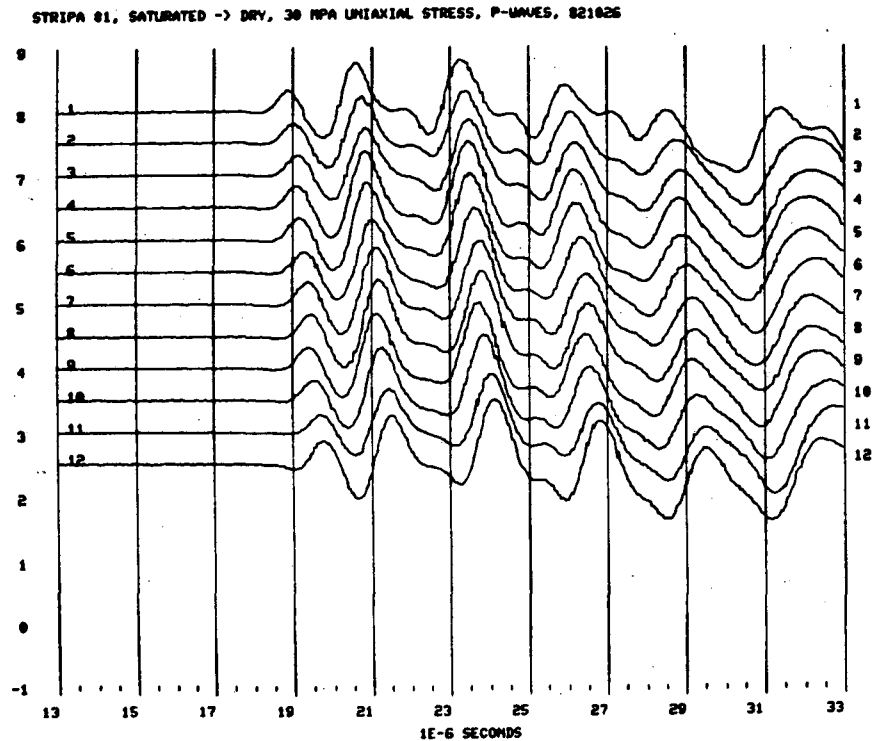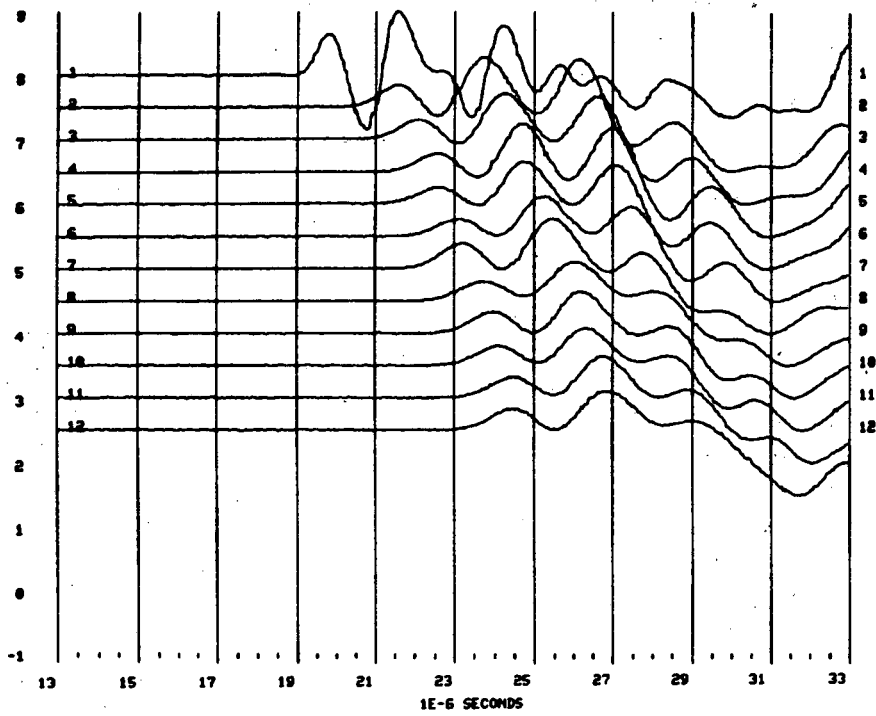STRIPA 81, SAT -> DRY, 30 MPA UNIAXIAL STRESS, S-WAVES 821026
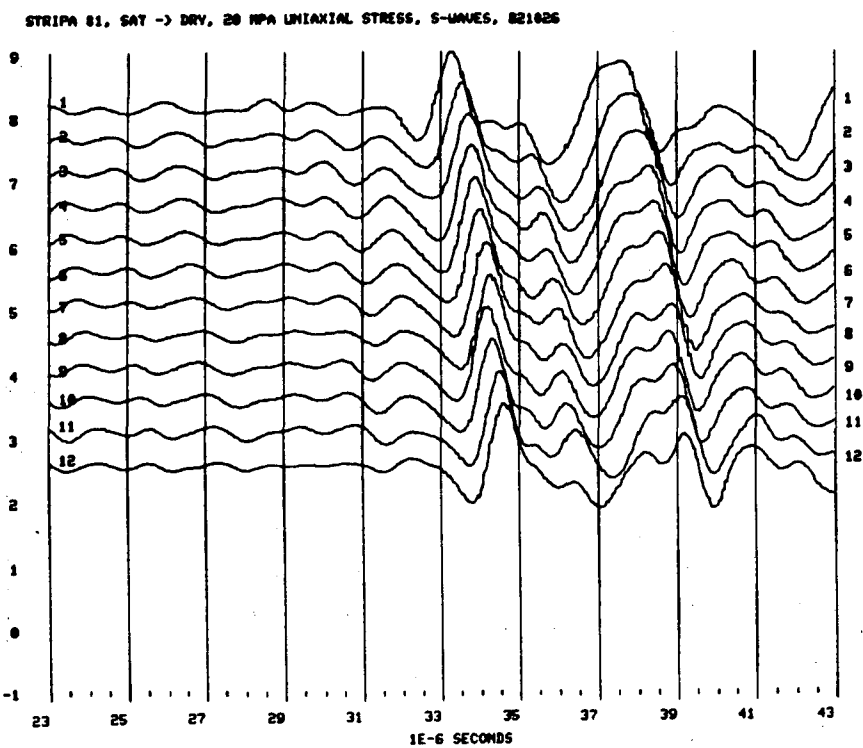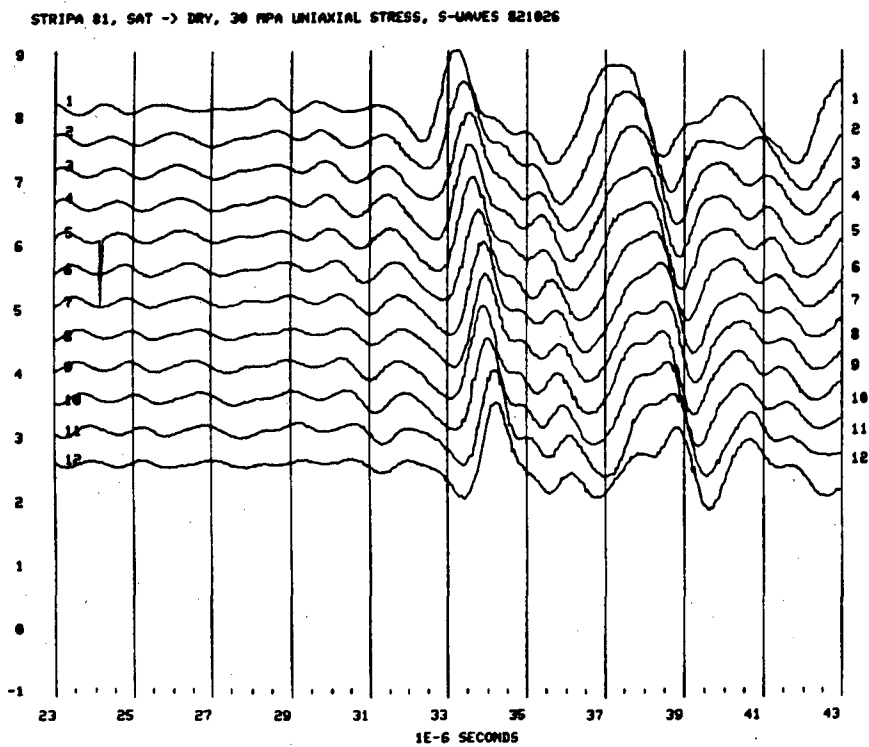
Fig. 7.38 a) S-waveforms for specimen #1 over saturation range from 100 to 0% under σ_{ua} = 20 MPa. b) S-waveforms for specimen #1 over saturation range from 100 to 0% under σ_{ua} = 30 MPa.

258

Fig. 7.39 a) S-waveforms for specimen #2 over saturation range from 100 to 0% uncer σ_{ua} = 5 MPa.
b) S-waveforms for specimen #2 over saturation range from 100 to 0% under σ_{ua} =10 MPa.

a

STRIPA 82, SAT -> DRY, 20 MPA UNIAXIAL STRESS, S-WAVES, 821026

b

STRIPA 82, SAT -> DRY, 30 MPA UNIAXIAL STRESS, S-WAVES, 821026
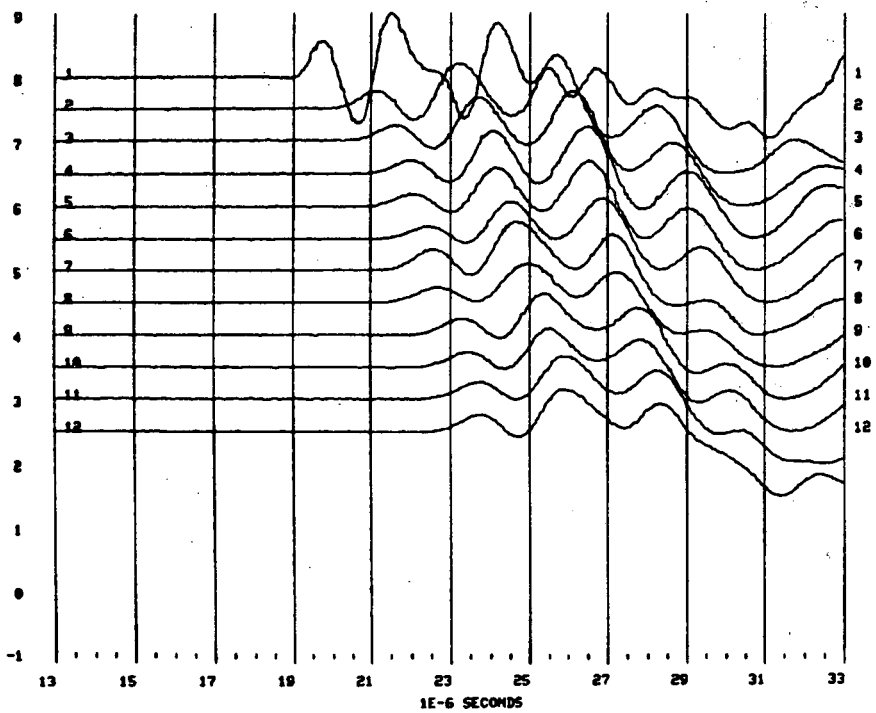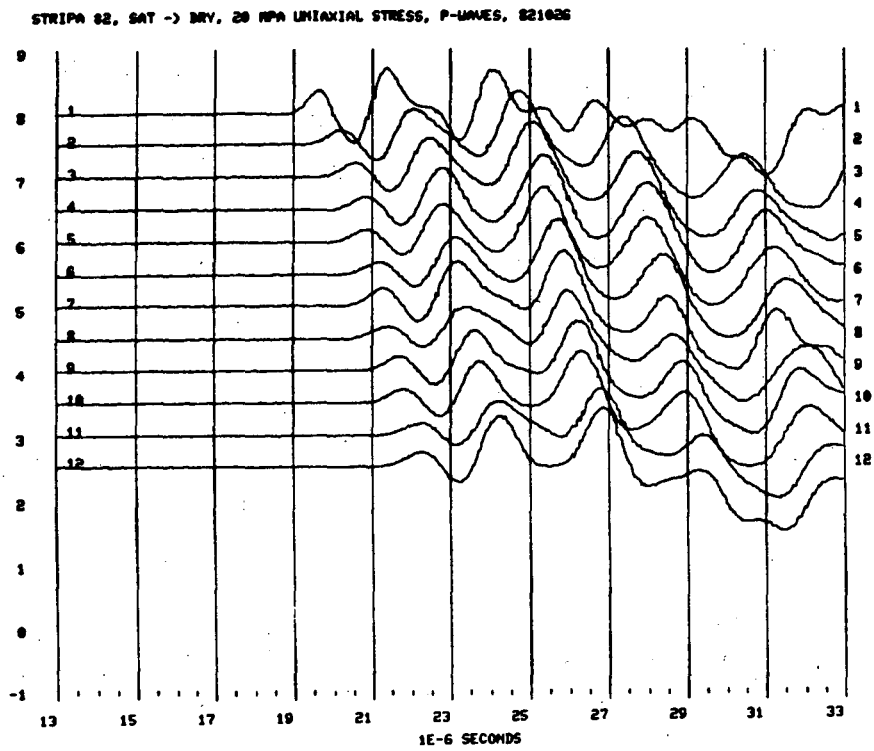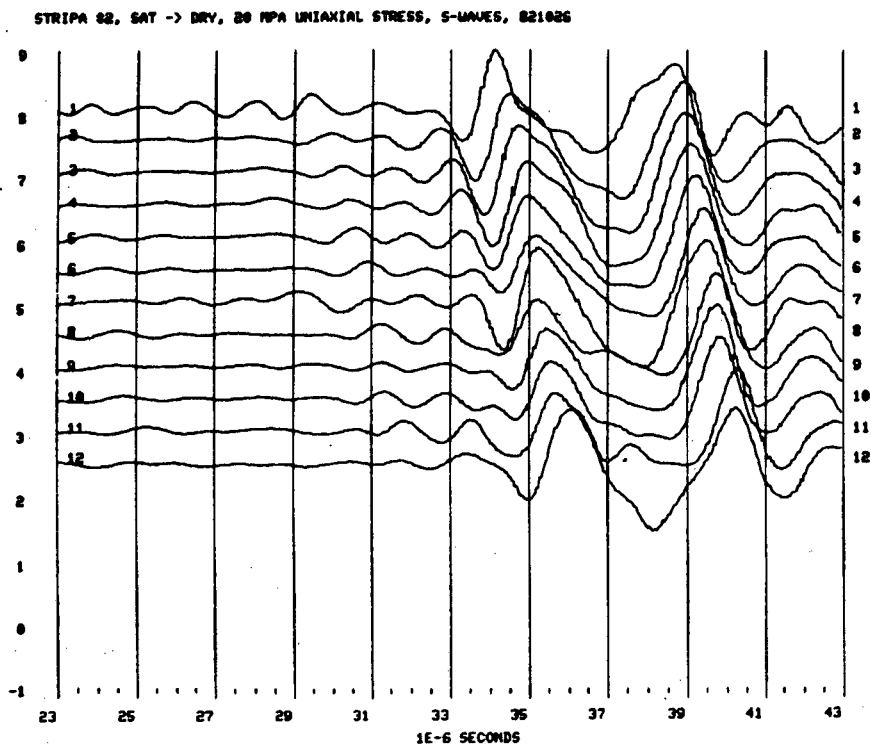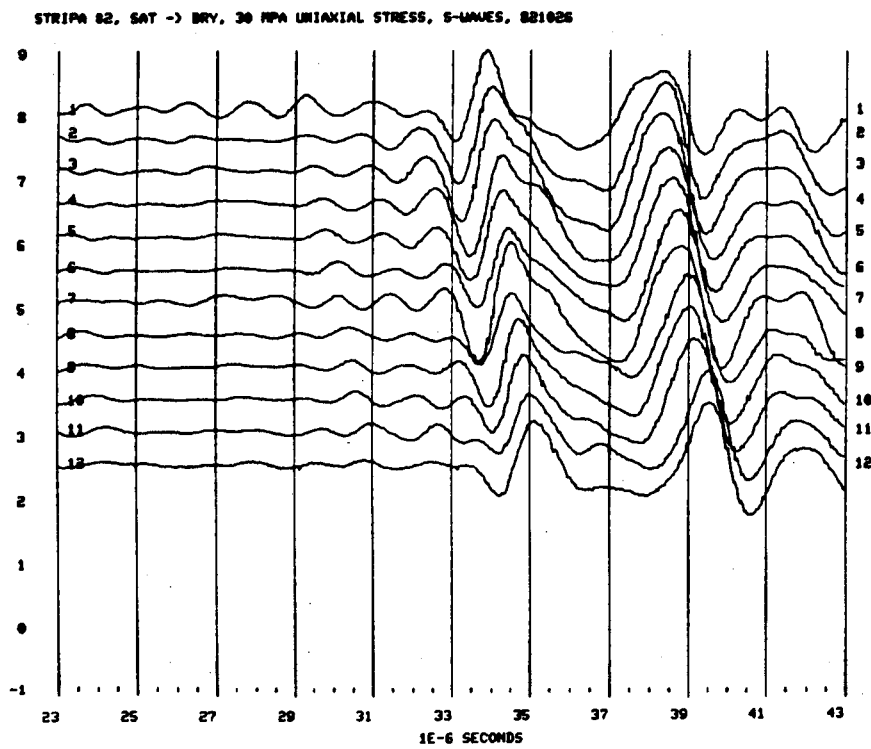

Fig. 7.40 a) S-waveforms for specimen #2 over saturation range from 100 to 0% under σ_{ua} = 20 MPa.
b) S-waveforms for specimen #2 over saturation range from 100 to 0% under σ_{ua} = 30 MPa.
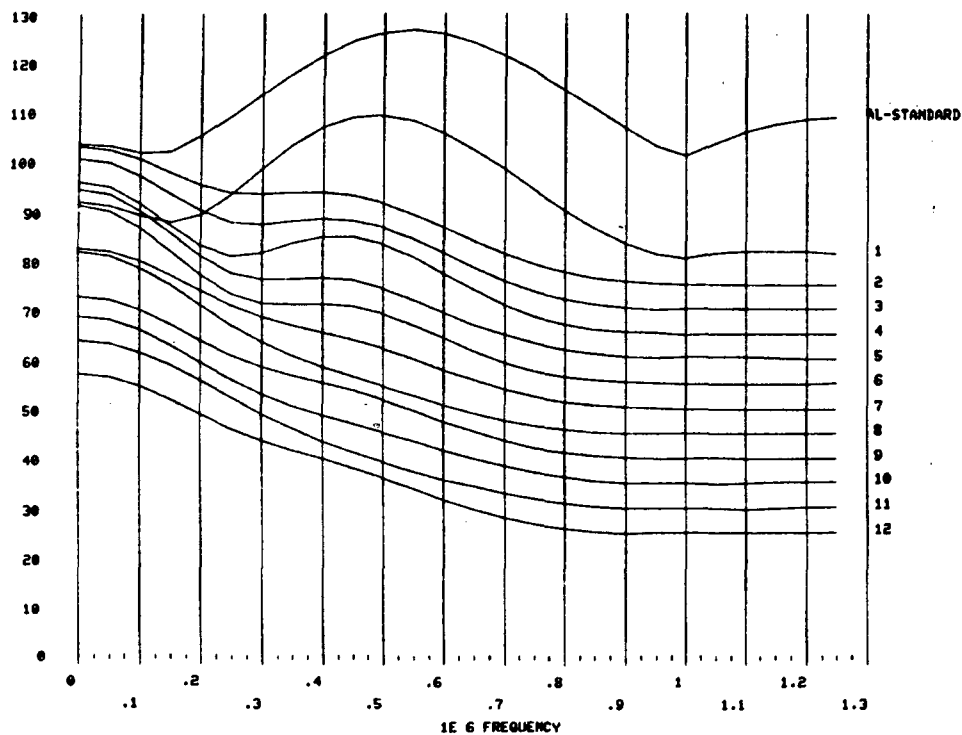
Fig. 7.41 a) Fourier amplitude spectra from specimen #2 over a saturation range from 100 to 0 % under σ_{ua} = 5 MPa. b) Fourier amplitude spectra from specimen #2 over a saturation range from 100 to 0 % under σ_{ua} = 10 MPa.

a

SPECIMEN : STRIPA 82, E24, M7-M9   CONDITION : SAT -> DRY   WINDOW : 4E-6 SEC
SMOOTH : 0   FILE : STPA20.
P-WAVES   DATE : 27 OCTOBER, 1982
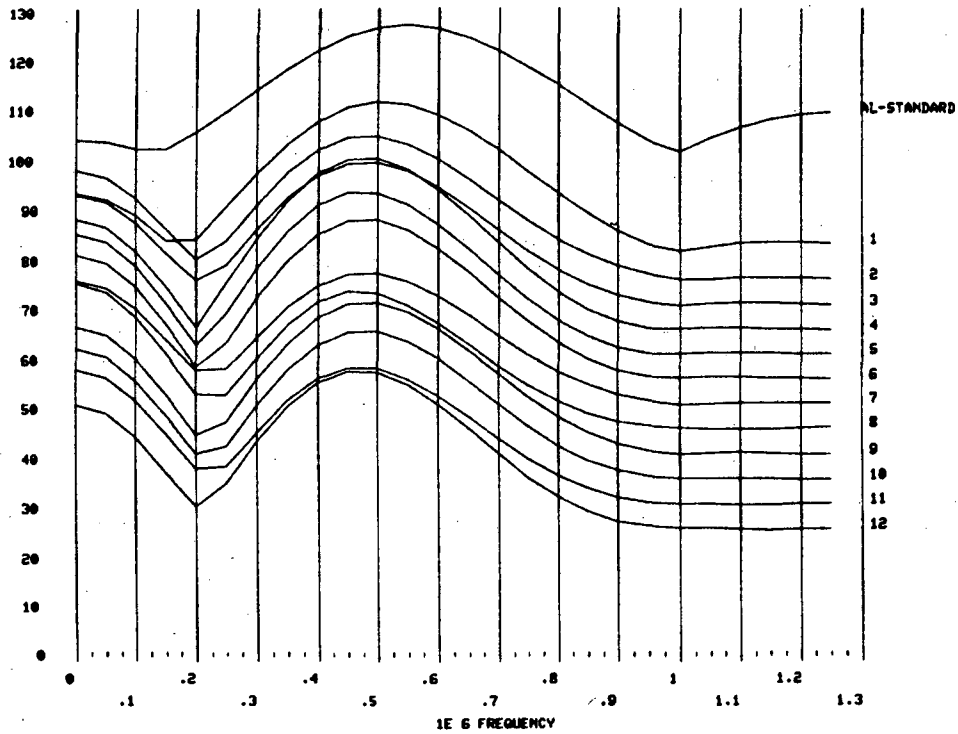
b

SPECIMEN : STRIPA 82, E24, M7-M9   CONDITION : SAT -> DRY   WINDOW : 4E-6 SEC
SMOOTH : 0   FILE : STPA30.
P-WAVES   DATE : 27 OCTOBER, 1982
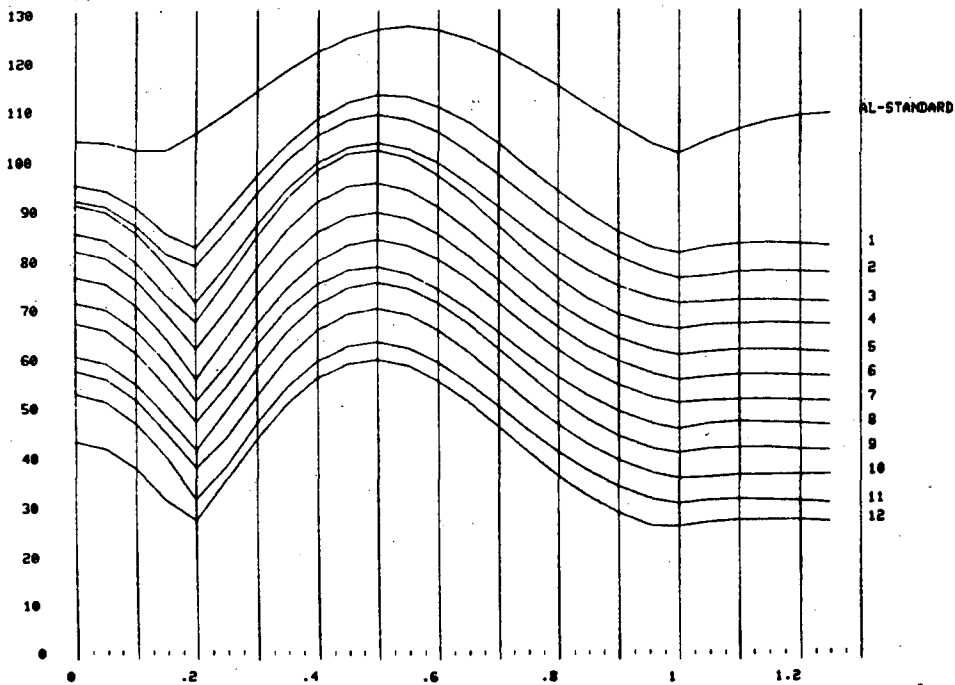
Fig. 7.42 a) Fourier amplitude spectra from specimen #2 over a saturation range from 100 to 0 % under σ_{ua} = 20 MPa. b) Fourier amplitude spectra from specimen #2 over saturation range from 100 to 0 % uncer σ_{ua} = 30 MPa.
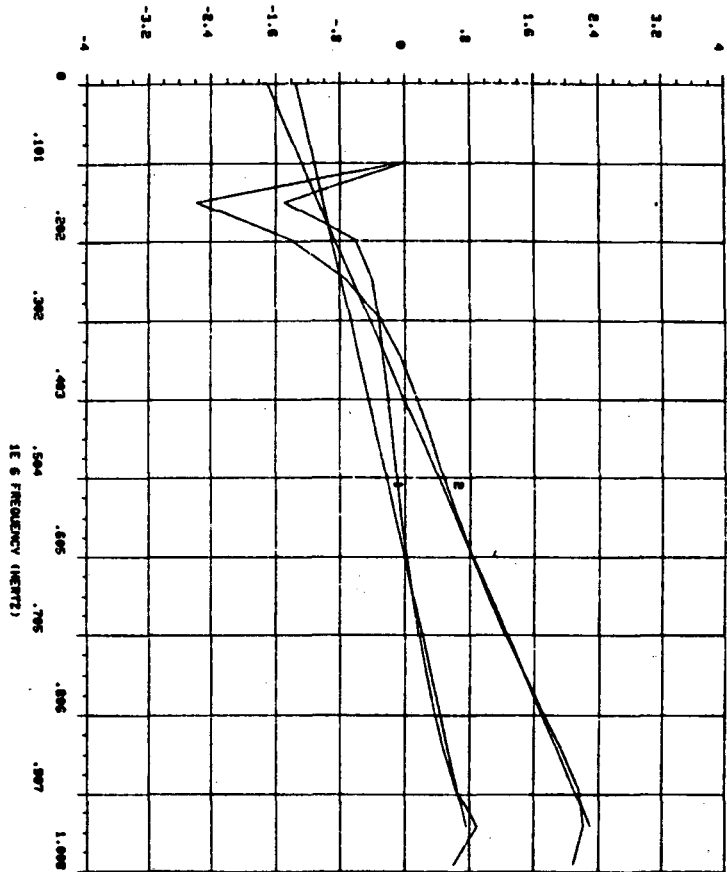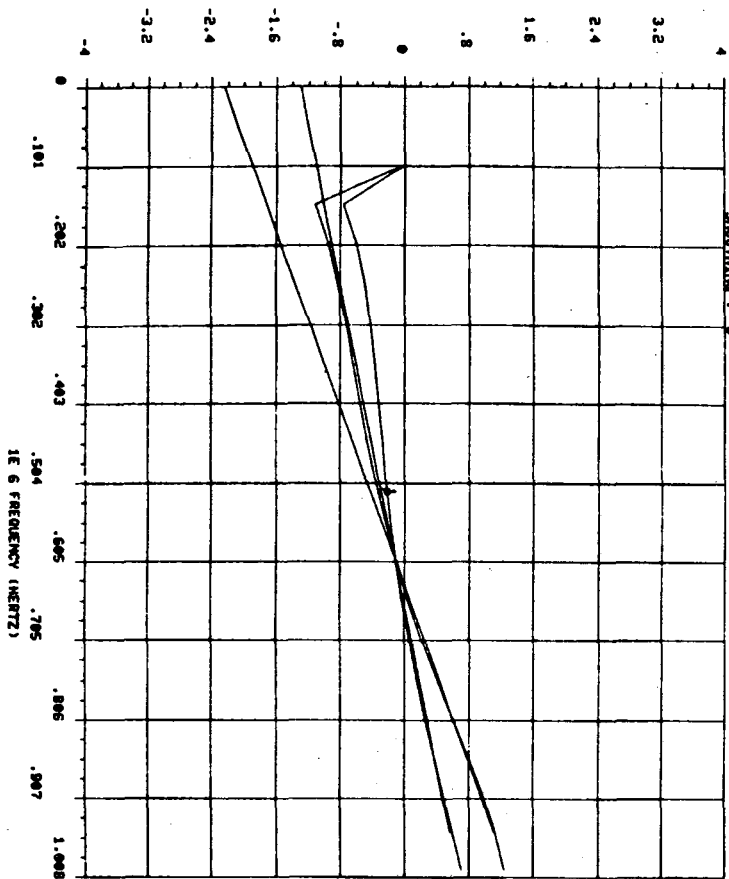
Fig. 7.43 a) Spectral ratios for specimen # 2 at 100 % and 78% saturation showing the change in slope when the Q_α value change from 19 to 12. b) Spectral ratios for S-waves transmitted through specimen #2 at 100 % and 78 % saturation showing the change in slope when the Q_β change from 38 to 25.
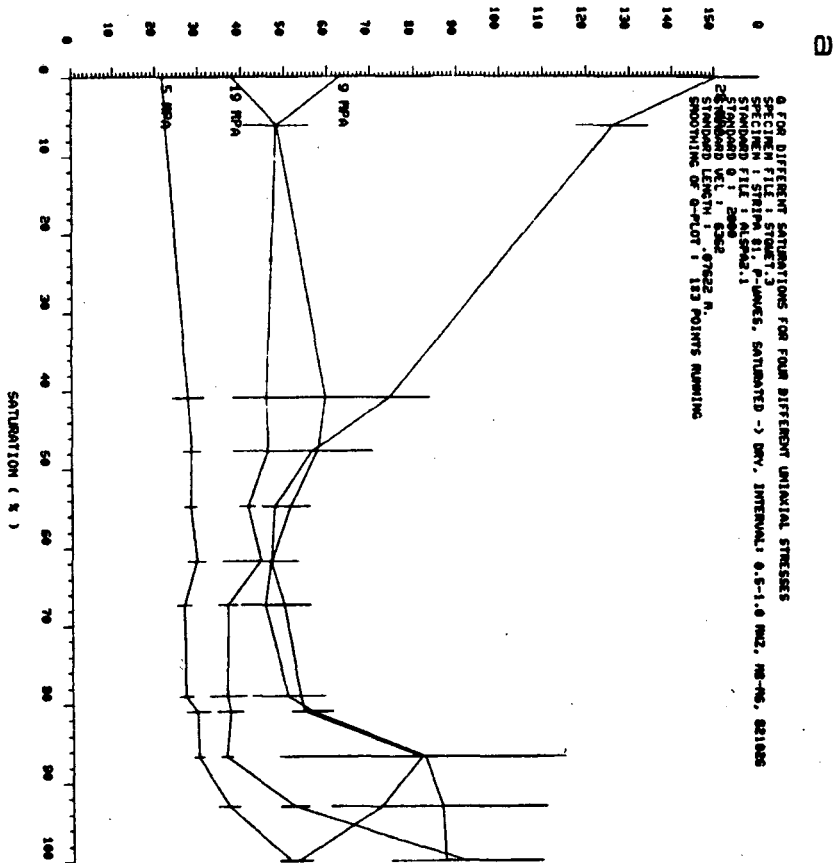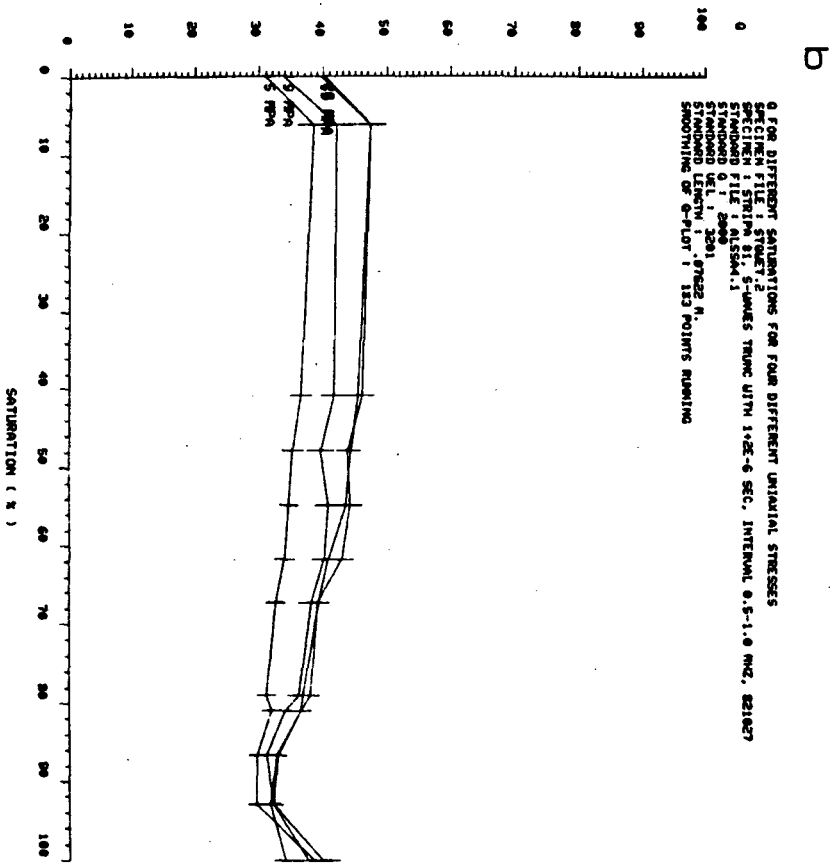
Fig. 7.44 a) Q_α for Stripa specimen #1 from borehole E21, which is parallel to cross section M8-M6. Saturation range from 100 % to 0% and the four uniaxial stresses, σ_{ua} are 5, 10 20 and 30 MPa. b) Q_β for Stripa specimen #1 from borehole E21, which is parallel to cross section M8-M6. Saturation range from 100 to 0% and the four uniaxial stresses, σ_{ua} are 5, 10, 20 and 30 MPa.

S—Waves   P—Waves

#	SATURATION (%)	Q-VALUE	VELOCITY (M/S)		#	SATURATION (%)	Q-VALUE	VELOCITY (M/S)
UNIAXIAL STRESS : 5					UNIAXIAL STRESS : 5			
1	100	38	3474		1	100	50	5979
2	93	29	3489		2	93	36	5890
3	86	29	3459		3	86	29	5778
4	80	31	3412		4	80	29	5719
5	78	31	3411		5	78	26	5690
6	67	32	3375		6	67	26	5625
7	61	33	3355		7	61	29	5590
8	54	34	3342		8	54	27	5485
9	47	35	3343		9	47	28	5500
10	40	36	3343		10	40	27	5504
11	6	38	3248		11	6	22	5373
12	0	30	3240		12	0	21	5305
UNIAXIAL STRESS : 9					UNIAXIAL STRESS : 9			
1	100	40	3477		1	100	91	5979
2	93	32	3511		2	93	51	5903
3	86	31	3483		3	86	36	5833
4	80	34	3450		4	80	36	5790
5	78	36	3438		5	78	36	5757
6	67	38	3421		6	67	36	5703
7	61	44	3389		7	61	44	5633
8	54	40	3389		8	54	41	5550
9	47	39	3377		9	47	45	5558
10	40	41	3379		10	40	45	5570
11	6	42	3289		11	6	47	5447
12	0	33	3252		12	0	62	5326
UNIAXIAL STRESS : 19					UNIAXIAL STRESS : 19			
1	100	37	3503		1	100	86	5979
2	93	32	3530		2	93	86	5934
3	86	32	3513		3	86	81	5890
4	80	36	3485		4	80	55	5863
5	78	36	3477		5	78	50	5842
6	67	39	3459		6	67	44	5790
7	61	40	3435		7	61	46	5727
8	54	43	3423		8	54	50	5662
9	47	44	3423		9	47	57	5670
10	40	45	3421		10	40	59	5670
11	6	47	3322		11	6	48	5574
12	0	39	3301		12	0	37	5578
UNIAXIAL STRESS : 28					UNIAXIAL STRESS : 28			
1	100	34	3541		1	100	52	5979
2	93	31	3541		2	93	71	5956
3	86	32	3533		3	86	81	5925
4	80	36	3520		4	80	53	5912
5	78	37	3506		5	78	53	5894
6	67	39	3496		6	67	49	5850
7	61	42	3476		7	61	46	5799
8	54	44	3465		8	54	47	5744
9	47	43	3468		9	47	56	5752
10	40	46	3460		10	40	74	5752
11	6	47	3384		11	6	126	5666
12	0	40	3336		12	0	150	5602

Tables for figures 7.44 a and b.

Fig. 7.45 a) Q_α for Stripa specimen #2 from borehole E25, which is parallel to cross section M7-M9. Saturation range from 100 to 0% and the four uniaxial stresses, σ_{ua}, are 5, 10, 20 and 30 MPa. b) Q_β for Stripa specimen #2 from borehole E25, which is parallel to cross section M7-M9. Saturation range from 100 to 0% and the four uniaxial stresses, σ_{ua} are 5, 10, 20 and 30 MPa.

S—Waves					P—Waves			

| #	SATURATION (%)	Q-VALUE	VELOCTIV (M/S)		#	SATURATION (%)	Q-VALUE	VELOCTIV (M/S)
UNIAXIAL STRESS : 5					**UNIAXIAL STRESS : 5**			
1	100	38	3474		1	100	50	5979
2	93	29	3489		2	93	36	5890
3	86	29	3459		3	86	29	5778
4	80	31	3412		4	80	29	5719
5	78	31	3411		5	78	26	5690
6	67	32	3375		6	67	26	5625
7	61	33	3355		7	61	29	5590
8	54	34	3342		8	54	27	5485
9	47	35	3343		9	47	28	5500
10	40	36	3343		10	40	27	5504
11	6	38	3248		11	6	22	5373
12	0	30	3240		12	0	21	5305
UNIAXIAL STRESS : 9					**UNIAXIAL STRESS : 9**			
1	100	40	3477		1	100	91	5979
2	93	32	3511		2	93	51	5903
3	86	31	3483		3	86	36	5833
4	80	34	3450		4	80	36	5790
5	78	36	3438		5	78	36	5757
6	67	38	3421		6	67	36	5703
7	61	40	3389		7	61	44	5633
8	54	40	3389		8	54	41	5550
9	47	39	3377		9	47	45	5558
10	40	41	3379		10	40	45	5570
11	6	42	3289		11	6	47	5447
12	0	33	3252		12	0	62	6326
UNIAXIAL STRESS : 19					**UNIAXIAL STRESS : 19**			
1	100	37	3503		1	100	86	5979
2	93	32	3530		2	93	86	5934
3	86	32	3513		3	86	81	5890
4	80	36	3485		4	80	55	5863
5	78	36	3477		5	78	50	5842
6	67	39	3459		6	67	44	5790
7	61	40	3435		7	61	46	5727
8	54	43	3423		8	54	50	5662
9	47	44	3423		9	47	57	5670
10	40	45	3421		10	40	59	5670
11	6	47	3322		11	6	48	5574
12	0	30	3301		12	0	37	5578
UNIAXIAL STRESS : 28					**UNIAXIAL STRESS : 28**			
1	100	34	3541		1	100	52	5979
2	93	31	3541		2	93	71	5956
3	86	32	3533		3	86	81	5925
4	80	36	3528		4	80	53	5912
5	78	37	3506		5	78	53	5894
6	67	39	3496		6	67	49	5850
7	61	42	3476		7	61	46	5799
8	54	44	3465		8	54	47	5744
9	47	43	3468		9	47	56	5752
10	40	46	3460		10	40	74	5752
11	6	47	3384		11	6	126	5666
12	0	40	3336		12	0	150	5602

Tables for figures 7.45 a and b.

8.   DISCUSSION

In a discussion of this series of experiments it is important to ascertain and discriminate between first-order and second-order effects of some physical property or change in physical property. In addition to the thermal load on the rock and the subsequent increase in the stress with related effects on cracks, the pore fluid, which in all cases is water, has a higher coefficient of thermal expansion than that of the rock and adds its own effects to the overall system response to heating. The Stripa granite, typical of rocks which are being considered as host rock for nuclear waste repositories, is a low permeability rock. The low permeability does not allow the increasing pore-fluid pressure to dissipate by flow when the rock mass is subjected to rapid heating (Figures 4.1a-4.1d) with the associated thermal expansion of the rock and the water.

In addition to the initial low permeability the effect of heating is to form a zone with even lower permeability around the heater. Where the water can be drained from the rock, which is the case around the boreholes, the fractures close due to thermal expansion of the rock and the associated compressive stress throughout the medium. The water inflow data support this hypothesis. These data show a large increase in water inflow to the holes just after the heater was turned on, as the water was expelled from the fractures adjacent to the boreholes. This fracture closure model explains the low Q_α values near the heater, a zone where permeability is decreased due to high compression to levels where dissipation of the pore water pressure takes a longer time than at greater distances from the heater. Morrow *et al.* (1981), showed that the permeability of heated granite dropped between 1 and 2 orders of magnitude for both intact specimens and specimens with a through-

going fracture. The rate of the permeability decrease depended on the temperature with higher rates at higher temperatures. For the 200°C case the permeability dropped one order of magnitude over one month.

8.1 Pore Pressure and Thermal Hydrofracturing.

In a recent paper, Palciauskas and Domenico (1982) show that in a saturated, low-porosity rock of low permeability which is subjected to rapid heating, micro-hydrofracturing will occur as a result of the increased pore pressure. In the following section, a model of the changes in effective stress caused by heating will be given.

In the following calculation it will be assumed that the fluid mass in the rock around the heater is constant, i.e. the permeability is so low that other effects dominate. From Figures 4.1a to 4.1d and Figures 4.21 to 4.23 it is clear that the thermal load increases the temperatures very quickly around the heater while the water inflow in the boreholes changes slowly. The modal composition of the granite was given in Chapter 2; based on the minerals present and their ratios some estimates of the moduli are given in table 8.1. This is based on the treatment proposed by Simmons and Wang (1971). The values given in table 8.1 are the mean of the calculated averages for aggregates based on Voight and Reuss schemes. The values are in all cases calculated for room temperature.

The moduli given in table 8.1 are the volume averaged values for the polycrystalline grains. The value for the plagioclase is for a mineral with 56 % Anorthite.

For any further consideration of the influence of the pore fluids it is necessary to define the coefficients which are important in the analysis.

Red Stripa Quartz Monzonite							
Mineral	Vol. [%]	E [Mbar]	G [Mbar]	ν	K_s [Mbar]	β_s $[Mbar]^{-1}$	V_s [km/s]	V_p [km/s]
Quartz	37.1	0.957	0.451	0.063	0.364	2.746	4.123	6.035
Plag.	32.0	0.889	0.344	0.295	0.721	1.387	3.570	6.616
Microc.	22.2	0.731	0.287	0.278	0.547	1.828	3.337	6.013
Mu+Chl	8.7	0.788	0.317	0.253	0.522	1.916	3.330	5.778
Vol.av.	100.0	0.870	0.369	0.202	0.533	1.876	3.703	6.194

Table 8.1

The following coefficients are valid in an undrained saturated case.

$$\frac{1}{K_u} = \beta_u = \frac{1}{V_b}\left[\frac{\partial V_b}{\partial \sigma}\right]_{P,T} \qquad [8.1]$$

$$\alpha_b = \frac{1}{V_b}\left[\frac{\partial V_b}{\partial T}\right]_{\sigma,P} \qquad [8.2]$$

and

$$\alpha_m = \frac{1}{m}\left[\frac{\partial m}{\partial T}\right]_{\sigma,P} \qquad [8.3]$$

where V_b is the bulk volume. K^{-1}_u is the compressibility for an undrained rock, α_b the expansivity of the bulk volume for different temperatures at constant stress and pressure. α_m is the coefficient which reflects the change in the fluid mass at constant stress and pressure. This constant includes the effect on the fluid from both pore and fluid expansivities. These constants can be expressed in terms of the sum of the weighted effect on the pore and solid fractions of the total volume.

$$\frac{1}{K_u} = \beta_u = (1-\psi_{un})\,\beta_s + \psi_{un}\beta_p \qquad [8.4]$$

$$\alpha_b = (1 - \psi_{un}) \, \alpha_s + \psi_{un} \, \alpha_p \qquad\qquad [8.5]$$

and

$$\alpha_m = \psi_{un} (\alpha_f - \alpha_p) \qquad\qquad [8.6]$$

where β_u is the compressibility for the undrained rock, α the expansivity, and the subscripts p,s and f refers to the pores, the solid material, and the porefluid, respectively. ψ_{un} is the unconnected porosity as defined in Tables 5.3 and 8.2. This is the porosity used in all calculations. For all the calculations in this report it is assumed that the rock mass is fully saturated.

To calculate the temperature dependence of the pore pressure P, stress σ, strain ε, and porosity ψ, it is necessary to specify a the following isothermal coefficients, following Palciauskas and Domenico (1982) and Biot (1941).

The four coefficients of interest are ζ, H, R and Φ. Of the four Φ is not independent and is defined as

$$\frac{1}{\Phi} = \frac{1}{R} - \frac{\zeta}{H} \qquad\qquad [8.7]$$

The definition of ζ is given by Biot (1941) and Nur and Byerlee (1971), and is a proportionality constant between the pore and the bulk volume changes at constant P and T.

$$\zeta = 1 - \frac{K_{dr}}{K_s} \qquad\qquad [8.8]$$

where K_s is the bulk modulus of the solid polycrystalline material.

$\frac{1}{H}$ is defined by Biot (1941) as the pore compressibility, and $\frac{1}{K_{dr}}$ the compressibility of the drained rock. With ζ defined as a proportionality constant it can be written $\zeta = \frac{K_{dr}}{H}$ and from this we can write

$$\frac{1}{H} = \frac{1}{K_{dr}} - \frac{1}{K_s} = \beta_{dr} - \beta_s \approx \beta_p \qquad [8.9]$$

as shown by Palciauskas and Domenico (1982).

The coefficient $\frac{1}{R}$ is a measure of the change of the water content for a given change in fluid pressure. Biot (1941) defined $\frac{1}{\Phi}$ as a measure of the amount of water which can be forced into a material under pressure while the volume of the material is kept constant.

$$\frac{1}{R} = \beta_p + \psi_{un}(\beta_f - \beta_s) \qquad [8.10]$$

and

$$\frac{1}{\Phi} = \psi_{un}(\beta_f - \beta_s) + \frac{\beta_s \beta_p}{\beta_{dr}} \qquad [8.11]$$

The β_f which is the fluid compressibility, as an average between ambient and $80°$ C, is set to 0.05 $kbar^{-1}$, which is obtained from Figure 4.24.

In Table 8.2 the coefficients used in this section are given with a brief explanation and comment.

The apparent porosity is estimated in Chapter 5 of this report as 0.2 %. This agrees well with a value of 0.3 % for the Stripa granite which is reported by Nelson et $al.$ (1979). The total porosity is estimated to be 1.5 %, as reported in Table 5.4. The value of 0.9 % porosity reported for two of the specimens in this paper in Chapter 7 was obtained after the

Coefficients used for the pore pressure calculations				
Variable	Description	Num.value	Unit	Source of data
β_f	compress of fluid	50	$Mbar^{-1}$	Nelson (1982)
β_p	compress of pores	0.547	$Mbar^{-1}$	$\beta_{dr} - \beta_s$
β_s	compress of solid	1.876	$Mbar^{-1}$	Table 8.1
α_f	expansivity of fluid	5×10^{-4}	C^{-1}	Nelson (1982)
α_p	expansivity of pores	22×10^{-6}	C^{-1}	$= \alpha_b$
α_m	Changes in the fluid	6.21×10^{-6}	C^{-1}	$\psi_{un}(\alpha_f - \alpha_p)$
α_b	cub thermal exp coeff	22×10^{-6}	C^{-1}	Myer & Rachiele
K_d	bulk mod.(drained)	0.413	Mbar	P & K (1980)
β_d	compress.(drained)	2.423	$Mbar^{-1}$	P & K (1980)
K_s	bulk mod.poly.crysta.	0.533	Mbar	Table 8.1
E_{dr}	Young's modulus at $\sigma_{ua} = 14 MPa$ dry	0.743	Mbar	P & K (1980)
ν	Poissons ratio	0.20	-	P & K (1980)
K_c	constrained bulkmodulus	0.826	Mbar	$= K_{dr} + \frac{4}{3} G_{dr}$
β_c	constrained compressibility	1.210	$Mbar^{-1}$	
G_{dr}	shear modulus	0.310	Mbar	P & K (1980)
K_u	Undrained	0.537	Mbar	
β_u	Undrained	1.864	$Mbar^{-1}$	$(1-\psi_{un})\beta_s + \psi_{un}\beta_p$
ζ	Prop const. between pore and bulk vol changes at constant P and T	0.22	-	$1 - \dfrac{K_{dr}}{K_s}$
ψ_t	Total porosity	1.5	%	Table 5.4
ψ_c	Connected porosity	0.2	%	Table 5.4
ψ_{un}	Unconnected porosity	1.3	%	Table 5.4
$\dfrac{1}{\Phi}$	Undrained	1.05	$Mbar^{-1}$	$\psi_{un}(\beta_f - \beta_s) + \dfrac{\beta_s \beta_p}{\beta_{dr}}$
$\dfrac{1}{H}$	Drained	0.547	$Mbar^{-1}$	$\approx \beta_p$
$\dfrac{1}{R}$	Undrained	1.17	$Mbar^{-1}$	$\beta_p + \psi_{un}(\beta_f - \beta_s)$
$\left(\dfrac{\partial P}{\partial T}\right)_{m,\sigma}$	Constant fluid mass	5.30	$bars\,^{\circ}C$	$= R\alpha_m$
$\left(\dfrac{\partial P}{\partial T}\right)_{m,\epsilon}$	Constant bulk volume	10.52	$bars\,^{\circ}C$	$= \Phi(\zeta\alpha_b + \alpha_m)$

P&K in this table
refer to Paulsson & King (1980)

Table 8.2

specimen had been dried out in a vacuum chamber under a 10 millitorrs vacuum for 14 days. The numerical average for the two specimens is 0.93 %. The porosity value, ψ_{un}, used in this paper, and given in Table 8.2, for calculating the heat effect on the effective stress is 1.3 % which probably is close to the true total porosity as that includes the porosity of larger fractures which were not included in the laboratory specimen. The density is reported for saturated samples to be 2611 kg/m^3. For an axial stress of 14 MPa, Paulsson and King (1981) reported an Young's modulus of 0.743 Mbars, Poisson's value of 0.20. Myer and Rachiele (1982) reported a cubic thermal expansion coefficient α_b of $22 \times 10^{-6} C^{-1}$ at temperatures of $60^\circ C$ and a confining pressure of 15 MPa. The shear and the bulk moduli are obtained from the relationships:

$$G_{dr} = \frac{E_{dr}}{2(1+\nu)} \qquad [8.12]$$

and

$$K_{dr} = \frac{E_{dr}}{3(1-2\nu)} \qquad [8.13]$$

An equation which describes the changes in the fluid mass content in a nonisothermal porous medium was given by Biot (1941) as

$$\frac{(m-m_o)}{\rho_o} = \frac{P}{R} + \frac{\sigma}{H} - \alpha_m (T-T_o) \qquad [8.14]$$

where m is the mass of the porefluid per unit volume of the medium. R is one of Biot's elastic constants and ρ_o is the density.

Under conditions of constant fluid mass, which appears to be a reasonable assumption after the initial expulsion of water around the

heater, the constant stress case for the pressure dependence on temperature can be found by setting $m - m_o$ to zero in Eq. [8.14] and from this one obtains

$$(\partial P / \partial T)_{m,\sigma} = R\ \alpha_m \qquad\qquad [8.15]$$

For the case of a change in the fluid-mass content, Palciauskas and Domenico (1982) give the following expression

$$\frac{(m - m_o)}{\rho_o} = \zeta \varepsilon + \frac{P}{\Phi} - \zeta(\alpha_b + \frac{\alpha_m}{\zeta})\ (T - T_o) \qquad\qquad [8.16]$$

with $\zeta = \frac{K}{H}$. By setting $m - m_o$ to zero the following expression is obtained for the constant bulk volume case

$$(\partial P / \partial T)_{m,\varepsilon} = \Phi\ (\zeta \alpha_b + \alpha_m) \qquad\qquad [8.17]$$

The coefficients α_m and α_b reflects changes in the fluid mass content at constant stress and pressure, and the response of the bulk volume to changes in temperature at constant stress and pressure respectively. The coefficients are given by

$$\alpha_m = \psi_{un} (\alpha_f - \alpha_p) \qquad\qquad [8.18]$$

and

$$\alpha_b = (1 - \psi_{un})\alpha_s + \psi_{un}\ \alpha_p \qquad\qquad [8.19]$$

where the α_f is the fluid expansivity. The value used in these calculations is $5 \times 10^{-4} C^{-1}$ which is an average value for the range of temperature to $80^{\circ}C$ as seen in Figure 4.24. The pore expansivity α_p is assumed to be the equal to the polycrystalline expansivity α_s. In Table 8.3 the

cubic thermal expansion coefficients for polycrystalline materials are given (after Walsh, 1973) where it is shown that $\alpha_b \approx \alpha_s$.

Cubic thermal expansion coefficient		
α_b (Theoretical) $[10^{-4}C^{-1}]$	α_s (Vol. averaged) $[10^{-4}C^{-1}]$	α_b (Experimental) $[10^{-4}C^{-1}]$
Al_2O_3 14.9	14.9	15.6
TiO_2 23.9	23.6	23.5
$CaCO_3$ 11.0	13.8	24±12
SiO_2 32.7	33.4	36.5

Table 8.3

For field situations there are both volume and stress changes when a thermal load is applied. Therefore, the displacement field and the stress distribution should be derived from the stress equilibrium equation as described by Palciauskas and Domenico (1982). For computations this equation is expressed in terms of displacements, fluid pressure and temperature through an equation given by Nadai (1963) as

$$\varepsilon = \frac{\sigma}{K_{dr}} + \frac{P}{H} + \alpha_b \, (T - T_o) \qquad [8.20]$$

where ε is the volumetric strain, σ the mean stress, α_b is the coefficient of cubical thermal expansion. K_{dr} is the bulk modulus defined as $E_{dr}/3(1-2\nu)$. If the temperature distribution around a heater is described as $T(x,y,x,t)$ whichs tends to a constant T_o at infinite distance. For a deformation where the curl of the displacement field is equal to

zero, the volume dilatation due to the thermal stress can be shown to be (Landau and Lifshitz, 1959),

$$\varepsilon = (K + \tfrac{4}{3}G)^{-1}\left[\zeta P_i + K\alpha_b T_i\right] \tag{8.21}$$

where P_i and T_i are the increase of the pressure and temperature over ambient.

The first part of the last equation is the definition of β_c which is the confined compressibility. For an undrained case, P is determined by Eq. [8.16] by setting $m = m_o$ giving

$$\varepsilon = -\left[\frac{P}{\zeta\Phi}\right] + \left[\alpha_b + \frac{\alpha_m}{\zeta}\right]T \tag{8.22}$$

Now it is possible to derive the excess pressure P, the volume dilatation ε and the hydrostatic changes in the ambient stress, as a function of temperature and the parameters of the medium. Combining the last two equations gives

$$\frac{P}{T} = \frac{\alpha_b K_c \zeta\Phi + \Phi\alpha_m K_c - K_{dr}\alpha_b \zeta\Phi}{(\zeta^2\Phi + K_c)} \tag{8.23}$$

and rearranging

$$\frac{P}{T} = \frac{K_c \Phi(\alpha_b \zeta + \alpha_m) - K_{dr}\alpha_b \zeta\Phi}{(\zeta^2\Phi + K_c)} \tag{8.24}$$

and now add and subtract $K_{dr}\Phi(\alpha_b\zeta + \alpha_m)$ to Eq. [8.24] and from Eq. [8.17] we obtain

$$\frac{P}{T} = \left[\frac{K_c - K_{dr}}{\zeta^2\Phi + K_c}\right]\left[\frac{\partial P}{\partial T}\right]_{m,\varepsilon} \times \alpha_m K_{dr}\Phi \tag{8.25}$$

and using Eq.[8.7] to obtain the expression for R

$$R = \Phi \frac{H}{H + \zeta\Phi}$$ [8.26]

and rearranging the second term in [8.26]

$$\frac{\alpha_m K_{dr} \Phi}{\zeta^2\Phi + K_c}$$ [8.27]

and multiply and divide with Eq. [8.26] which gives

$$\frac{\alpha_m R K_{dr} (H + \zeta\Phi)}{H(\zeta^2\Phi + K_{dr})}$$ [8.28]

and dividing with H and from earlier $\zeta = \dfrac{K_{dr}}{H}$ to obtain

$$\frac{R\alpha_m (K + \zeta^2\Phi)}{\zeta^2\Phi + K_{dr}}$$ [8.29]

and from Eq. [8.15] the expression for $R\alpha_m$ is given and combining the second term with [8.25] yields

$$\frac{dP}{dT} = \left[\frac{(\Phi\zeta^2 + K_{dr})}{(\Phi\zeta^2 + K_c)}\right]\left[\frac{\partial P}{\partial T}\right]_{m,\sigma} + \left[\frac{(K_c - K_{dr})}{(\Phi\zeta^2 + K_c)}\right]\left[\frac{\partial P}{\partial T}\right]_{m,\varepsilon}$$ [8.29]

The temperature change also alters the bulk volume of the medium which is given by;

$$\frac{d\varepsilon}{dT} = \left[\frac{(\zeta^2\Phi + K_{dr})}{\zeta\Phi(\zeta^2\Phi + K_c)}\right]\times\left[\left[\frac{\partial P}{\partial T}\right]_{m,\varepsilon} - \left[\frac{\partial P}{\partial T}\right]_{m,\sigma}\right]$$ [8.30]

and then the change in the hydrostatic stress for this model is described

by,

$$\frac{d\sigma}{dT} = -(K_c - K_{dr})\times(\frac{d\varepsilon}{dT})$$
[8.31]

The result of applying the Stripa data to these equations is given in Table 8.4

Volume dilatation, Fluid Pressure and Hydrostatic stress per unit Temperature for the Stripa quartz monzonite	
$\frac{d\varepsilon}{dT}$, $10^{-5\circ}C^{-1}$	1.312×10^{-5}
$\frac{dP}{dT}$, $bars^\circ C^{-1}$	7.77
$\frac{d\sigma}{dT}$, $bars^\circ C^{-1}$	-5.42
$\frac{d\sigma_{eff}}{dT}$, $bars^\circ C^{-1}$	2.4

where 1000 bars = 100 MPa

Table 8.4

From Table 8.4 it is clear that the pore pressure P increases faster than the compressive stress σ with temperature. The effective stress defined as the confining stress minus the pore pressure decrease with $2.4^\circ C^{-1}$ bars when the temperature is increased. The measured pore pressure in a borehole in the floor of the extensometer drift is 7.5 bars (Birgersson and Neretnieks, 1982) from which the large effect of the temperature is easily realized.

The minimum stress has been measured as approximately 45 bars, Doe *et al.* (1981). The pore pressure is reported as approximately 10 bars in boreholes in an adjacent drift, Nelson and Wilson (1980). If the pore pressure had followed the hydrostatic gradient the pore-pressure would have been 35 bars but Gale *et al.* (1982) report that the hydraulic gradient is lower than the hydrostatic pressure line. The mine acts as a hydraulic sink and causes the pore pressure to decrease in the mine surroundings. This would yield a minimum effective stress of 35 bars. Doe (1981) also reports the intermediate stress as 77 bars and the maximum principal stress from the extensometer-fullscale drifts as between 199 and 241 bars. The effective intermediate stress is then 67 bars and the effective maximum stress is between 189 and 231 bars.

The tensile strength of the Stripa granite is reported by Swan (1978) as 150 bars. Assuming that the effective stress is decreasing at a rate of 2.4 bars C^{-1}, as shown in Table 8.4, a temperature of approximately $77^0 C$ would be required to hydrofracture the rock assuming that a pore pressure of 150 + 35 bars had to created. The pore pressure gradient as function of temperature is shown in Figure 8.1 where also the principal stresses, after Doe *et al.* (1981), are shown together with the tensile strength. In a recent experiment the pore pressure was measured in a vertical borehole drilled from the extensometer drift, shown in Figure 1.7. A pore pressure of 7.3 bars was measured 11 m below the floor of the drift (Birgersson and Neretnieks, 1982). The inflow of the borehole was observed to be 168 ml/day. The inflow reported is similar to what was found in the M9 borehole in the full-scale drift. If this pore pressure had been used instead of 10 bars the temperature for thermal hydrofracturing had been raised only with $1^o C$.

8.2 Behavior of the rock mass inferred from the V_p and Q_α.

Both the velocity data, which are presented in Chapter 5, and the attenuation data, which are presented in Chapter 6, show major changes throughout the experiment. There is however, a difference in the response times to various stimuli between the velocities and the attenuation of compressional waves recorded in the monitoring lines in the heater midplane. The reason for this must be the different sensitivity of these parameters to different physical processes. There are two dominant processes which continue during the length of the experiment. The first is the heating of the rock mass; the second is the dewatering of the rock mass by the 22 diamond-drilled boreholes. While 95 % of the ultimate temperature increase 0.20 m from the heater was reached 62 days after turn-on of the heater, the dewatering process extended throughout the entire experiment and the rate of water extraction was in most boreholes fairly constant throughout the experiment. The two measured quantities, the P-wave velocity, V_p, and the attenuation of P-waves, Q_α, are both sensitive to changes in stress and saturation. The compressional wave velocities are very sensitive to changes in stress in the region 0 - 200 bars. In this interval the fractures are in the process of closing. The attenuation Q_α is more sensitive to the final process of fracture closure when the surfaces are in physical contact.

Velocity and attenuation changes in the heater midplane.

The seismic signals recorded have traveled several meters, and have thus traversed regions having different states of stress and saturation. The velocity and the attenuation must then be average values over the distances traveled. To obtain the mean temperature over the

monitoring lines as a function of time, the radial temperature function has been projected on the four monitor lines shown in Figure 3.1 at 100 equally spaced points on a line connecting the boreholes to obtain the mean temperatures for all the days when seismic data were gathered. In this way the V_p, Q_α and the temperature are mean values over the same space. Change in the mean temperature over the four lines with time is shown in Figure 8.2 and the data are also tabulated in Appendix C:1. The highest mean temperature was found over line M8-M6, followed by M7-M9 and M7-M6. The lowest mean temperature of 38°C, at day 398 after the turn on of the H9 heater, was found over the line M8-M9. The highest recorded temperature increase in this line is 35°C, which is only 35 % of the highest temperature increase in the line M8-M6. The sharp increase of the average temperature after heater turn-on should be noted. For three of the four lines, 95 % of the total mean temperature increase was reached after 80 days of heating. The time constants for the cooling curves are approximately the same as for heating for all the four lines.

Thermal expansion caused by the heating increases the compressive stress. In the absence of pore fluids the response would simply be that the existing fractures close and and as a result, the compressional and transversal velocities would increase. The attenuation would also decrease (i.e. increase in Q), which is shown in a number of laboratory investigations on dry rock.

As practically all rock is saturated to some degree at depths which are under consideration for the storage of high level nuclear waste, the presence of pore fluids must be considered. The water table in the area is approximately 10 m below the surface level around the Stripa mine. This means that the rock in the test area was fully saturated at the

beginning of the heater experiment and before dewatering of the rock mass around the heaters.

The V_p for the monitor lines, as shown in Figure 5.1 have a regular behavior with temperature. The V_p increase 5-10 % from the ambient levels, depending on the direction of transmission. The V_p decrease upon turn off of the heater. For at least one line, M7-M9, the post-heating values are clearly lower than the values observed prior to the experiment.

The variation of Q_α calculated over the four heater mid-plane monitor lines is less regular than that for the velocities. This can, however, be explained first by an increase of the pore pressure to the point where the tensile strength of the rock or an adjacent fracture is reached, and subsequently by a decrease in the pore fluid pressure as it expands into the newly created pore space. In the first case there is a decrease in effective stress and in the second an increase.

In Chapter 5 it was concluded that the P-wave velocity as function of the temperature was well approximated with a linear function of some slope which depended on the direction of the cross section. The function obtained in chapter 5 was from data gathered at a particular day (398) thus eliminating changes in other parameters such as saturation or pore pressure. The P-wave velocity and P-wave attenuation data presented in this section are from a period extending 700 days and are therefore also affected by other processes occurring during this time. In Figure 8.3a the P-wave velocities in line M7-M6 for a period spanning from 44 days before the heater was turned on to 403 days after the 3.6 kW heater was turned off after 398 days of operation. The P-wave velocities increase with increasing temperature. When the heater was turned

off the velocity at first decreased and then showed an increase, particularly after the dewatering of the rock mass was terminated. The Q-values for the M7-M6 line in Figure 8.3b show no linear correlation with temperature. The Q_α values stay constant until the maximum mean temperature is reached, and then over the main part of the experiment, when the mean temperature changes very little, increase by 8 units from an initial value of 13. When the heater is turned of the Q_α values stay constant at this higher level and do not go back to the original value until 151 days after the dewatering of the rock mass is terminated.

In line M8-M9 the difference between the behavior between the P-wave velocities and the attenuation of P-waves is even more apparent, as shown in Figure 8.4. In this figure the effect of terminating the dewatering on the P-wave velocities and the attenuation is especially apparent. After the initial increase of the velocities in this line, there is a leveling off and even a decrease of V_p as the temperature is increasing. This might be due to the build up of the pore pressure in this area due to the heating. The increased pore pressure would decrease the effective stress. The temperature increase is less rapid in this line due to the distance form the heater and it is therefore not surprising that other processes play relatively larger roles. At the turn off of the heater, the decrease of the mean temperature in this line, as seen in Figure 8.2, is more rapid than the corresponding increase at turn on. The slope down from a high temperature - high velocity state is here very linear with a slope similar to the initial temperature-velocity function after H9 heater turn on. Incidentally, the slope for the temporal variation of velocity with temperature in line M8-M9 is very similar to the spatial variation of velocity with temperature in cross section M7-M6, as seen in Figure

5.15a. The two lines M8-M9 and M7-M6 are parallel as seen in Figure 5.6. This observation tends to confirm the hypothesis that the velocity gradient with increasing temperature is a function of direction. The linear part of the temperature-velocity plot represents 100 days of data after the turn off of the heater. Finally during the following 200 days the velocity values return to values similar to the initial. To sum up the events in this line:

1. V_p increases linearly with temperature immediately after turn on.

2. V_p levels off and decreases because of an increase in σ_p due to retarded flow.

3. V_p decreases as the mean temperature decreases

4. V_p increases as fractures are closing due to a decrease in the pore pressure.

Using the V_p value at day 501, when the velocities have decreased after cool down but before they have increased due to fracture closure, along with a second value at day 711 the change in the porosity can be calculated. In table D:1.2 in Appendix D:1, the two P-wave velocity values, 5809 m/s and 5855 m/s, can be used with the equations given in Chapter 5 to calculate the porosity change due to termination of the dewatering. Subtracting the first porosity from the second one finds the change in the part of the path which is water to be 11.6 mm. In Jaeger and Cook (1979) a relationship between length and width of a very flat crack under plane stress, modeled by an elliptical semicylinder is given by

$$\frac{v}{c} = \frac{2\,\sigma}{E}$$
[8.32]

where v is the semi minor-axis and c the semi major-axis, σ is the stress change and E the polycrystallin Youngs modulus in Table 8.1. The linear Equation [8.32] make it possible to form

$$\sum_1^n \frac{v}{c} = \frac{2\sigma}{E} \qquad [8.33]$$

and

$$\frac{\sum_1^n v_i}{\sum_1^n c_i} = \frac{2\sigma}{E} \qquad [8.34]$$

and identifying $\sum v_i$ = 11.6 mm as the total closure of the fractures in the path. By using the pore pressure increase of 67 bars for an increase in the temperature of $28°C$, given in Figure 8.1, and the Young's modulus of 0.870 Mbar from Table 8.1, c is found to be 38 m. This is the total length of the fractures effected by the pore pressure change between boreholes M8 and M9. The average aspect ratio using the total fracture width over the total fracture length is found to be 1.5×10^{-4}. This is a value similar to what is reported for a Westerly granite by Cheng and Toksoz (1979).

In Figure 8.5 the data are presented for the line M8-M6 and the corresponding data from line M7-M9 are shown in Figure 8.6. In these two lines, which are $75°$ apart as seen in Figure 4.20, the magnitudes of the velocity change in response to temperature are very different. For both M8-M6 and M7-M9 the velocity-temperature relationships are very close to those found for the spatial case, shown in Figure 5.17a and b. In both Figures 8.5 and 8.6 it is apparent that the process discussed for

line M8-M9 is influencing the data. The attenuation also changes in these two lines but, as previously discussed for M7-M6 and M8-M9, there is an increase of Q_α only after the temperatures have approached their final values. For M8-M6 the Q_α values stay constant as the temperature decreases from a mean value of 65°C, at day 398 after heater turn-on, back to the ambient level of approximately 10°C. For M7-M9 the Q_α values are constant as the mean temperature increases, then follow the common pattern of increase while the temperature is at the maximum level. After the heater was turned off however, the Q-values in this line decreased. The final decrease, as also seen in some other lines, brings the final Q value to a level lower than that recorded prior to the heater experiment. This suggests that at a distance of 0.2 m from the heater borehole wall substantial damage of the rock is occurring due to heating.

Permanent velocity and attenuation changes in six vertical cross section near the heater.

A temperature of 77°C should increase the pore pressure sufficiently to hydrofracture the intact Stripa rock, assuming a constant fluid mass. This temperature is reached in four cross-sections; M7-M6, M7-M8, M8-M6 and M7-M9, as can be seen in Figures 4.3, 4.4, 4.7 and 4.8. Over all of these sections, which had temperatures in excess of 75°C, lower velocities were recorded post-heating compared to those measured prior the heater experiment.

Damage to rock lying outside the 75°C isotherm, however, is also indicated by the lower velocities measured in cross section M8-M9, as seen in Figure 5.9. A plausible explanation is the low tensile strength of

the rock due to the presence of calcite fractures which are seen in the rock mass adjacent to the H9 heater. If the effective stress is 35 bars prior to the heater experiment, an effective stress decrease of 2.4 $bars^{o}C^{-1}$ will reduce to zero the effective stress at an temperature increase of approximately 15°C. Such a temperature increase occurs within a radial distance from the H9 heater of 3.5 m. With low tensile strength calcite fractures, fracturing could occur at larger temperature increases than 15°C. Their are no experiments reported which investigate the tensile strength of the fractures in the Stripa pluton. There are, however, fractures in the drift area which are open and thus should have a very low tensile strength derived from only the bridges which connect the fracture surfaces. Other fractures such as the epidote fractures encountered probably have a tensile strength approaching the unfractured rock. The system of different fractures between the M-boreholes can be seen in Figures 2.5-2.10. A more thorough analysis of the fracture system in the full scale drift is provided by Paulsson *et al.* (1982).

The Q_{a} values for M7-M9, as seen in Figure 6.11, show a low Q_{a} zone at the heater level. This low Q_{a} zone was not found in the data taken prior to the heater experiment. The temperatures reached 130° C over part of this section, a level which is higher than that attained in any other section.

Comparing plots of the 80°C isotherms for the M8-M6 and the M7-M9 cross sections (Figures 4.7 and 4.8) it is apparent that the area covered by this isotherm is larger in the latter case. This is a likely reason for the larger interval over which the P-wave velocities were depressed in the final survey, which showed lower P-wave velocities post-heating

compared with pre-heating. The velocity anomalies are also skewed upwards from the heater midplane and a similar shape is found in the velocity difference plot between the first and last surveys. The only zone with lower Q_α values post-heating compared with pre-heating is across the heater in the cross section M7-M9. This section is only 0.20 m from the heater, while the M8-M6 section is 0.30 m from it. This indicates that the damaged zone from heating extends at least 0.20 m but not as much as 0.30 m from the heater. These V_p and Q_α data also give an indication of the different sensitivity of the two quantities. V_p is sensitive to a widening of existing fractures, resulting in a larger fraction of the path which is water. The Q_α values are sensitive to an increased number of fractures, as seen in cross section M7-M9 at the level of the heater (Figure 6.11). This is also discussed in Chapter 7. The Q_α values are not otherwise sensitive to relatively small changes in aperture of already existing fractures. The Q_α value is sensitive of an increase of touching asperities as this seems to be decreasing the attenuation significantly.

8.3 Velocity and attenuation as functions of fracture width.

An experiment was conducted to investigate the effect of a water filled fracture on P- and S-wave velocities and P-wave attenuation. One of the specimens used in the work presented in Chapter 7 was fractured into two parts using a two thin stainless steel rods and a laboratory press applying the rods perpendicular to the axis of the core so the fracture would be parallel to the end surfaces of the core. A bicycle inner tube was then slipped over the two core halves with the valve of the inner tube across the fracture. By applying tap water at a pressure of 3.4 bars the two halves were separated as much as 5 mm when the plates

on the laboratory press were separated from each other. This was first done with the tensile fracture in a rough state with all the asperities intact to simulate the closure of a natural fracture. To complete the investigation, the rough end surfaces were also ground smooth and parallel to within 0.001 mm and the specimen was tested with the same procedure as above. The P- and S-wave velocities from the specimen with rough fracture surfaces are shown in Figure 8.7. From this figure it can be seen that both the P-wave and S-wave velocities are linear functions of the width of a macroscopic fracture. In Figure 8.8a the P-waveforms from the test of the specimen with rough fracture surfaces are shown and in Figure 8.8b the P-waveforms from the specimen with smooth end surfaces are shown. The only apparent difference is the shorter travel-time for the specimen with smooth fracture surfaces as the grounding of the ends shorten the specimen. In Figure 8.9a and b the truncated P-waveforms are shown. In Figures 8.10a and b the P-wave amplitude spectra are shown and finally, in Figure 8.11a and b, the computed Q_a values are given. The Q_a values increase slowly as the fracture gap is decreasing from 5 to 1 mm. The "dip" in the curve is a resonance phenomenon. For the application of these laboratory data on the field results this "dip" is not important because the wavelength for the field experiment was 20 times the wavelength in the laboratory. The resonance is caused by the wavelength/fracture width ratio. For the same thing to happen for the field data the fracture have to be approximately 10 mm thick and filled with water. Such fractures do not exist in the area where the H9 experiment is conducted.

The sharp increase of Q_a when the fracture close from 0.5 mm to 0 is of interest. This increase apparently occurs when the asperities come

into contact.

## 8.4 Summary

In this chapter it was shown that for a constant fluid case the pore pressure in the Stripa granite increases with temperature at $2.4 bars\,^{o}C^{-1}$. Hydrofracturing would occur at $77^{o}C$ for the intact rock and at much lower temperatures in existing fractures.

From the monitor data a linear relationship between temperature and velocity was found. The gradient was dependent on the direction of the line with the smallest gradient in the inferred ambient σ_{max} direction.

There is no linear correlation between the temperature and the attenuation of the cross-hole signals. Q values increase after the maximum temperature has been reached, indicating that the long term effect of fracture closure due to decreasing pore pressure affects attenuation by a gradual increase in asperity contact as the fractures close.

The main result from the survey data is that V_p is sensitive to the fraction of water in the path and therefore is sensitive to opening of existing or new fractures. Q_α is not very sensitive to opening of existing fractures but correlates well with creation of additional fractures and also correlate well with an inferred increase in the contact area of fracture surfaces.
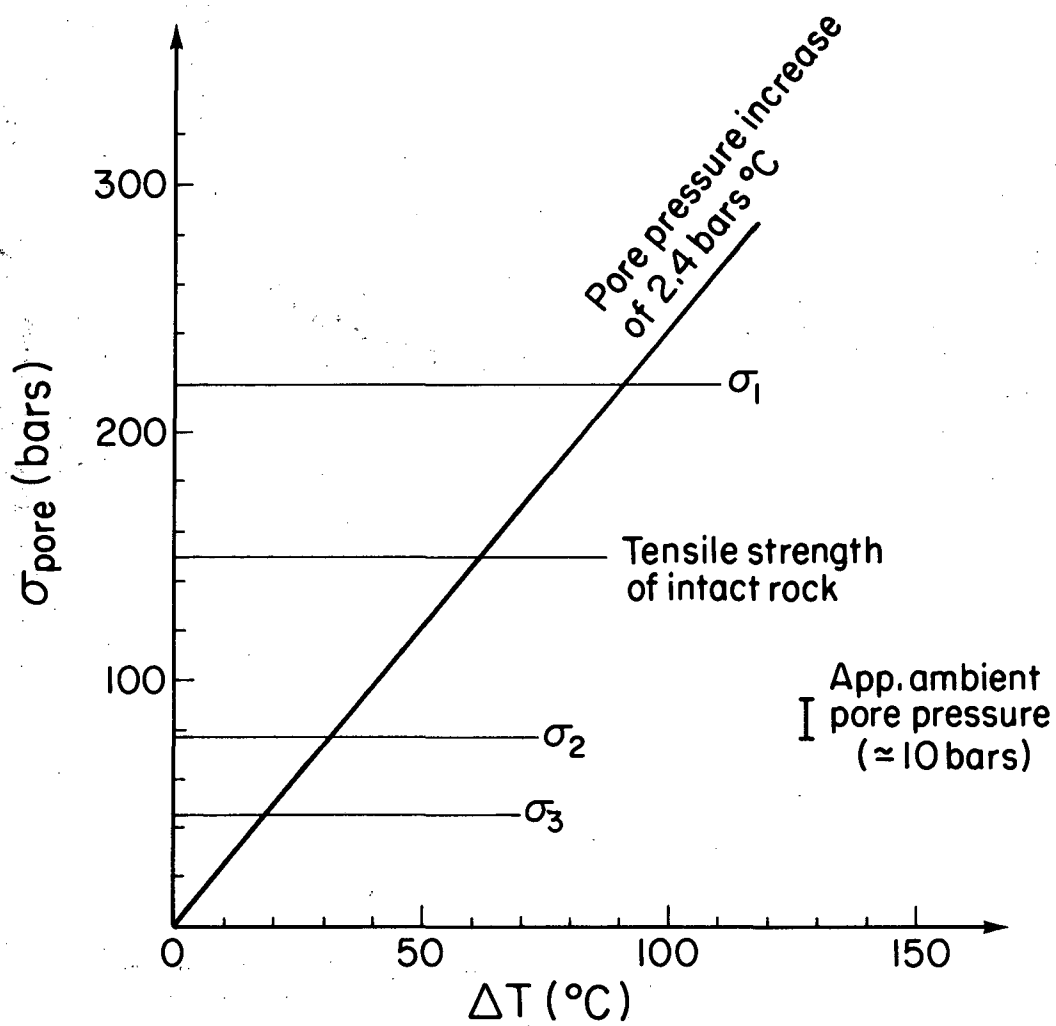
Fig. 8.1 Pore pressure increase with temperature for the Stripa quartz monzonite under a constant fluid mass situation. Also shown are the principal stresses and the tensile strength of the Stripa rock.
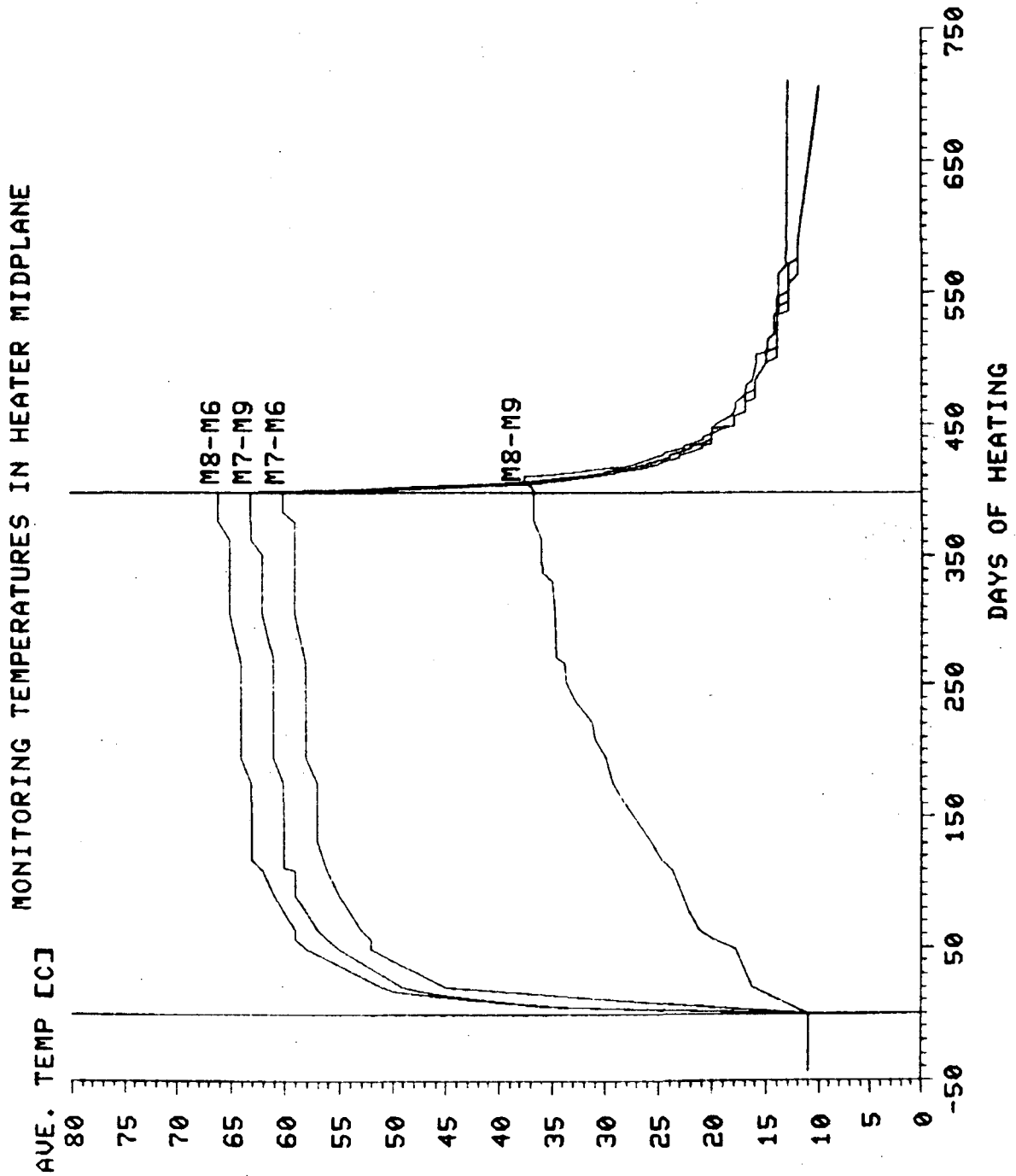
Fig. 8.2 Mean spatial temperatures over the four monitor lines from day -45 to day 710 of the H9 heater experiment. Day 0 indicates the day the heater was turned on and day 398 the day the heater was turned off.
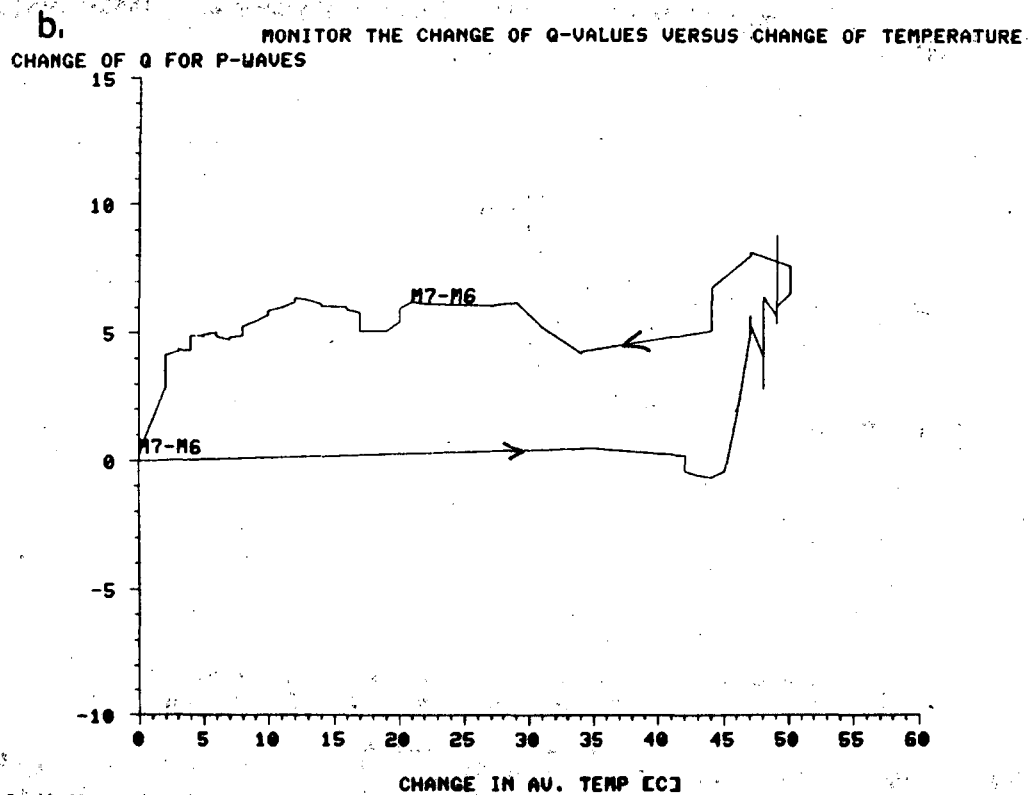
a.

MONITOR THE CHANGE OF VELOCITY VERSUS CHANGE OF TEMPERATURE

b.

MONITOR THE CHANGE OF Q-VALUES VERSUS CHANGE OF TEMPERATURE

Fig. 8.3 a) Change in compressional wave velocity V_p as function of change in mean temperature in line M7-M6. b) Change in attenuation of compressional waves as function of change in mean temperature in line M7-M6. The termination of the dewatering is marked with an arrow in Figures a and b. The turn off of the heater is obvious by the onset of the decrease in temperature.

a.

MONITOR THE CHANGE OF VELOCITY VERSUS CHANGE OF TEMPERATURE

P-VEL CHANGE [M/S]

b.

MONITOR THE CHANGE OF Q-VALUES VERSUS CHANGE OF TEMPERATURE

CHANGE OF Q FOR P-WAVES

CHANGE IN AV. TEMP [C]

Fig. 8.4 a) Change in compressional velocity V_p as function of mean temperature in line M8-M9. b) Change in attenuation of compressional waves as function of change in mean temperature in line M8-M9 The termination of the dewatering is marked with an arrow in Figures a and b. The turn off of the heater is obvious by the onset of the decrease in temperature.
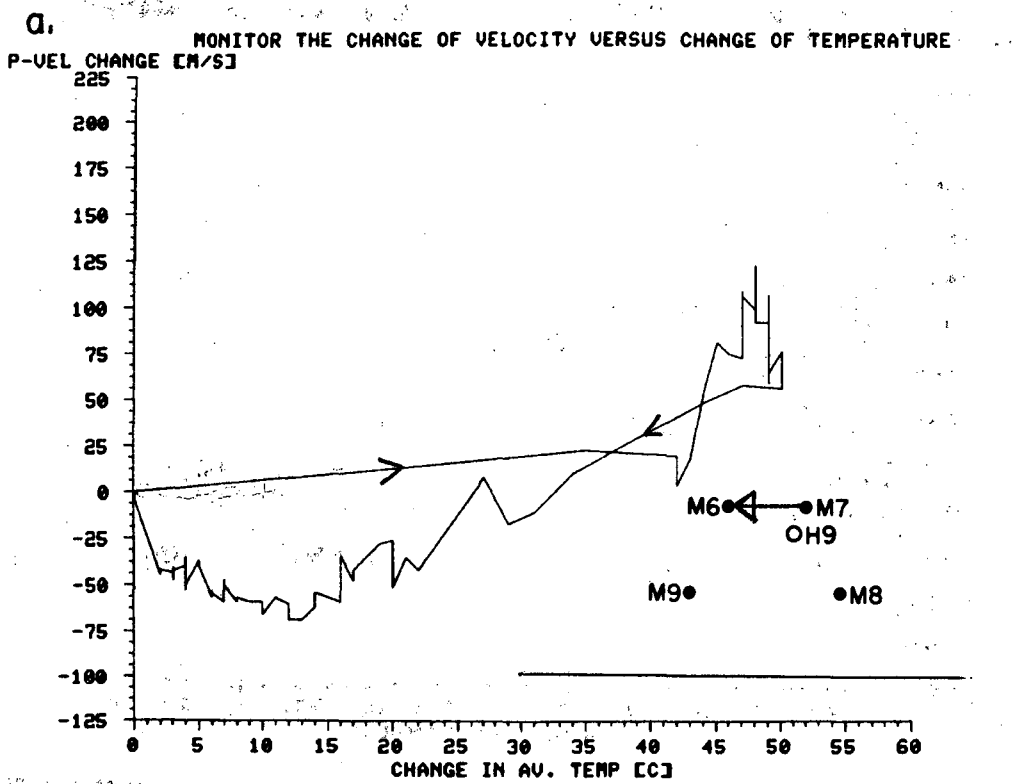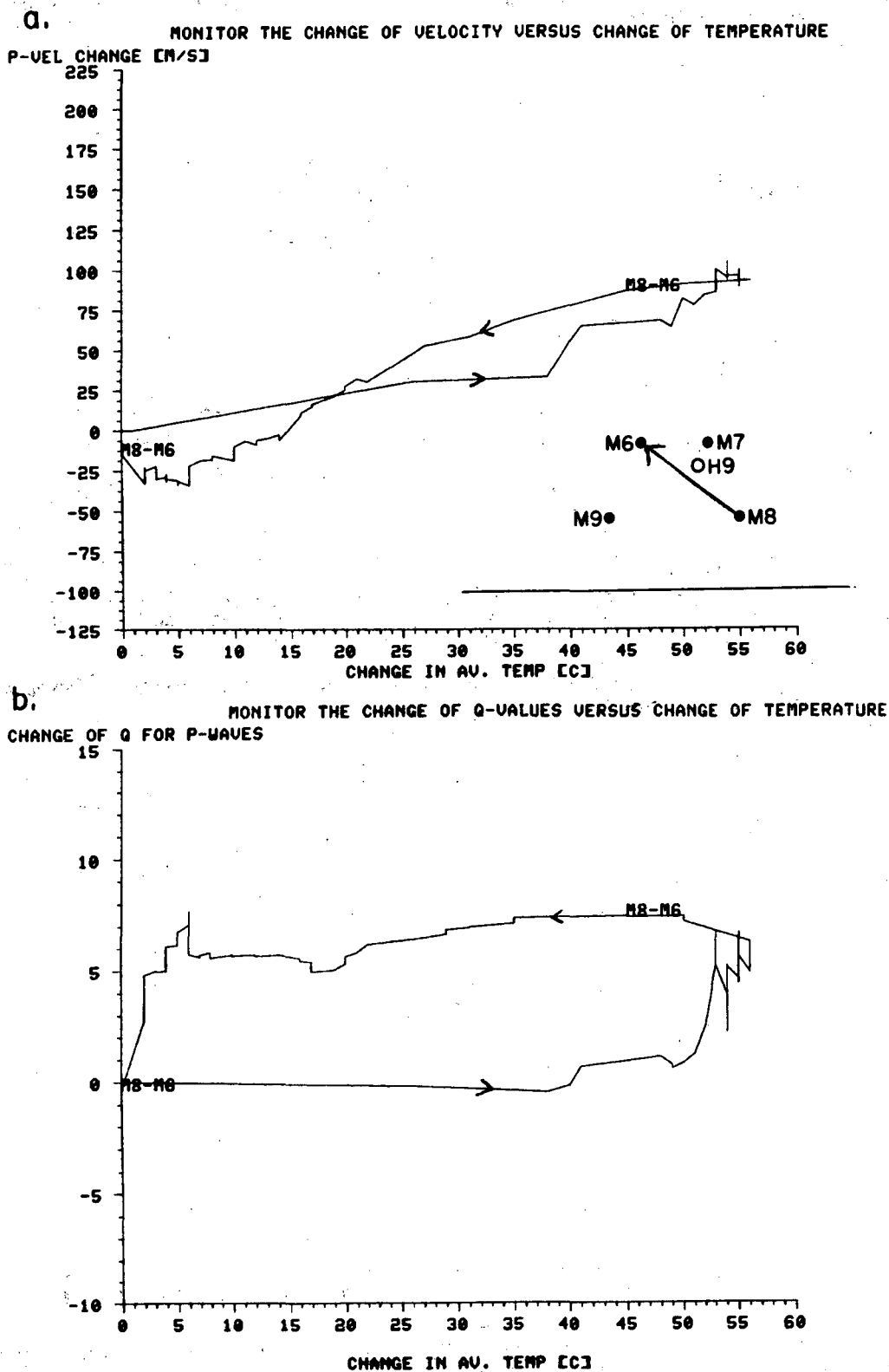
Fig. 8.5 a) Change in compressional wave velocity V_p as function of change in mean temperature in line M8-M6. b) Change in attenuation of compressional waves as function of change in mean temperatures in line M8-M6. The termination of the dewatering is marked with an arrow in Figures a and b. The turn off of the heater is obvious by the onset of the decrease in temperature.
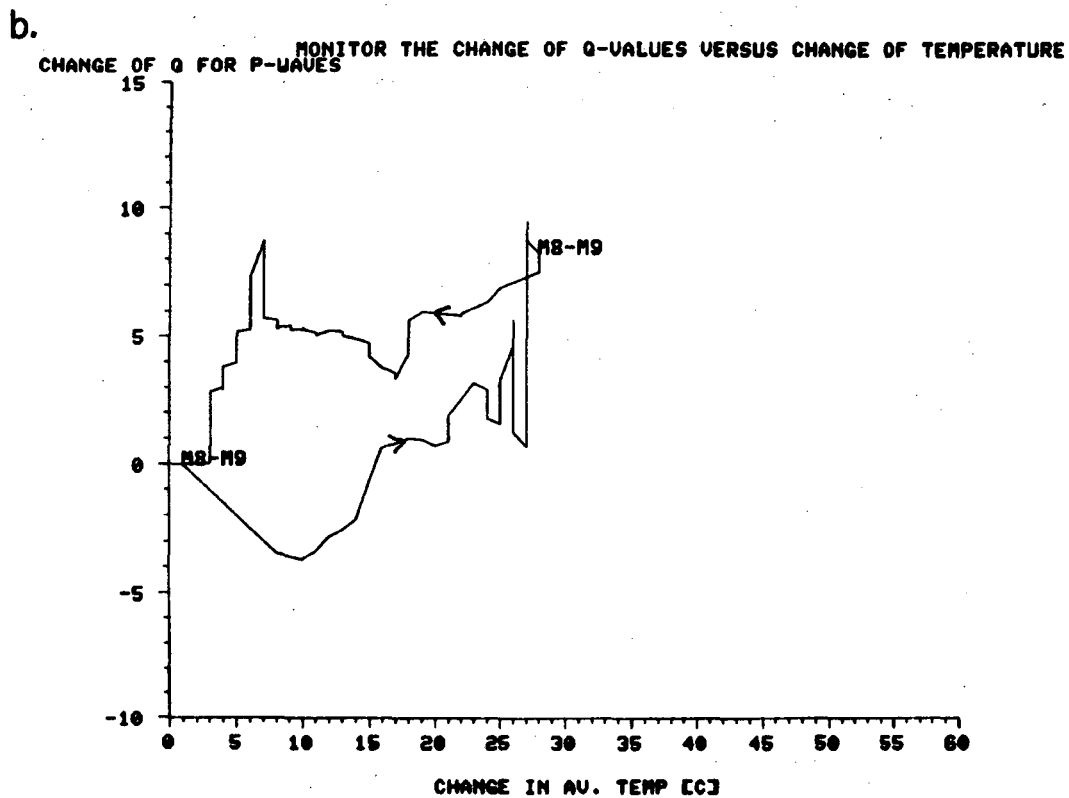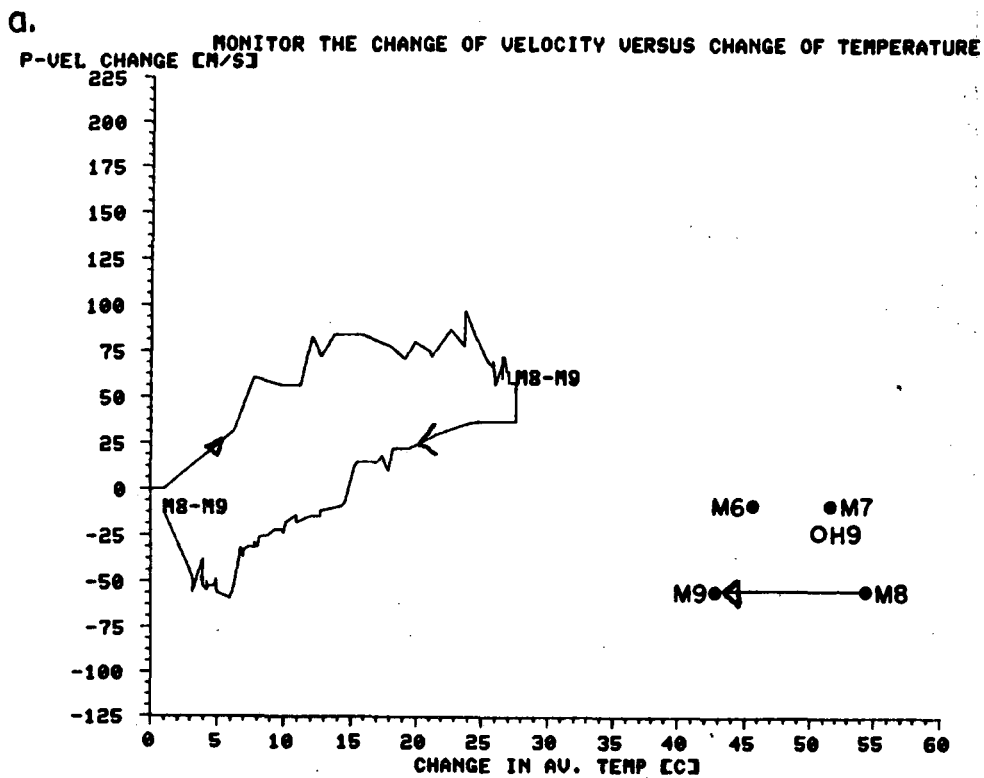
Fig. 8.8 a) Change in compressional wave velocity V_p as function of change in mean temperature over line M7-M9. b) Change in attenuation of compressional waves as function of change in mean temperatures over line M7-M9. The termination of the dewatering is marked with an arrow in Figures a and b. The turn off of the heater is obvious by the onset of the decrease in temperature.
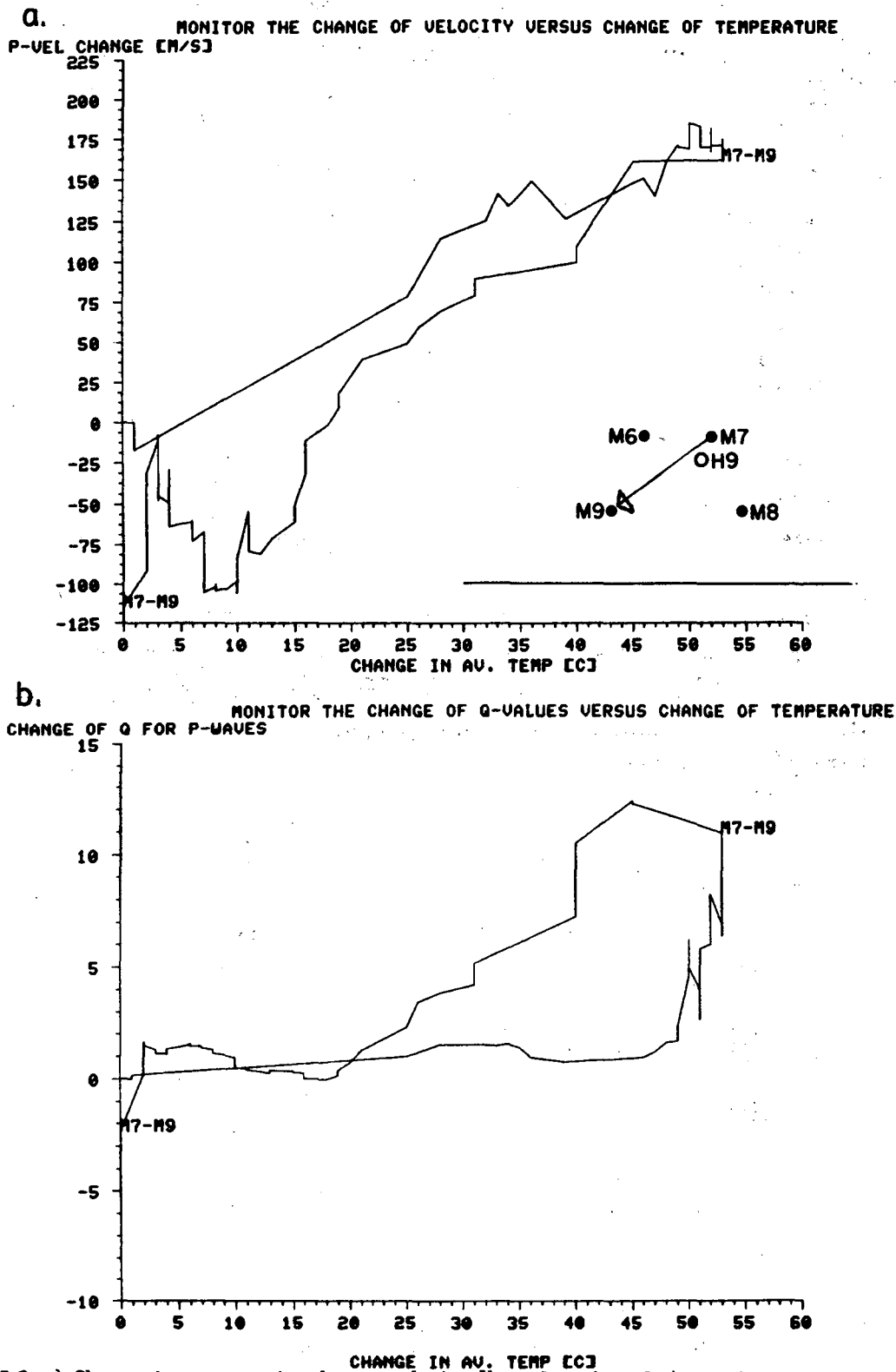
P-WAVE AND S-WAVE VELOCITIES :GAP8PO.DAT FOR FRACTURE WIDTH
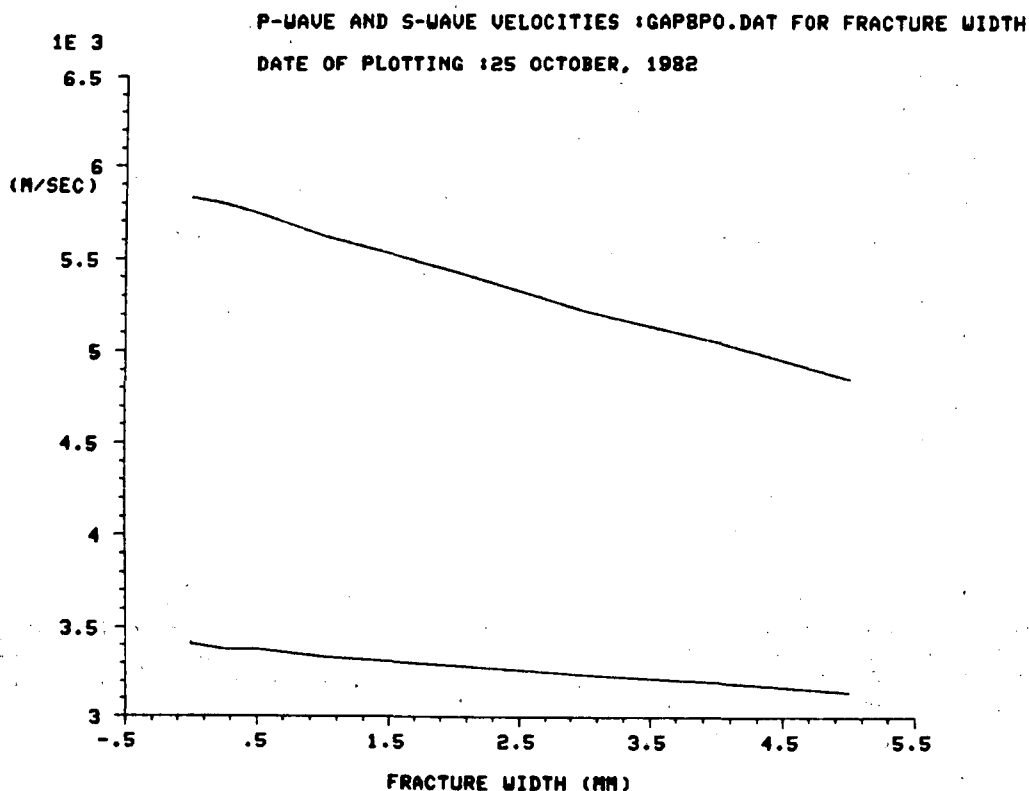
DATE OF PLOTTING :25 OCTOBER, 1982

Fig. 8.7 P and S-wave velocities in a specimen with an artificially induced tensile fracture. P and S-wave velocities as function of fracture width from 5 to 0 mm. Also shown is the table of the numerical results from the test.

SPECIMEN\FILE :GAP8PO.DAT

DATE :25 OCTOBER, 1982

LENGTH OF SPECIMEN : .071374 METER.

DIAMETER OF SPECIMEN : 5.1841 CENTIMETER

NUMBER OF LOADS : 9

DENSITY OF SPECIMEN : 2611 KG/M-3

PORE PRESS.	FRAC. WIDTH	P-WAVE VEL	S-WAVE VEL	YOUNGS M	BULK M	SHEAR M	PO. RA
(MPA)	(MM)	(M/S)	(M/S)	(GPA)	(GPA)	(GPA)	
.34	5	4846.07	3141.67	58.6291	26.9566	25.7708	.137609
.34	4	5041.74	3196.52	62.1034	30.798	26.6786	.16392
.34	3	5208.26	3236.47	64.8439	34.36	27.3495	.185468
.34	2	5423.06	3290.31	68.3337	39.0989	28.2671	.208714
.34	1	5619.1	3336.74	71.3769	43.6797	29.0705	.227651
.34	.5	5740.74	3377.54	73.5883	46.334	29.7857	.235298
.34	.25	5794.82	3378.49	74.9607	47.9406	29.8025	.242526
.5	0	5826.45	3408.5	75.2202	48.1913	30.3343	.239855
.5	0	5821.7	3416.66	75.4251	47.8529	30.4797	.237302

Table 8.5 P- and S-wave velocities and calculated moduli for a change in the fracture aperture from 5.0 to 0.0 mm.

STRIPA 88, FRACTURE WIDTH VARY FROM 5 -> 0 MM, SATURATED, 821024
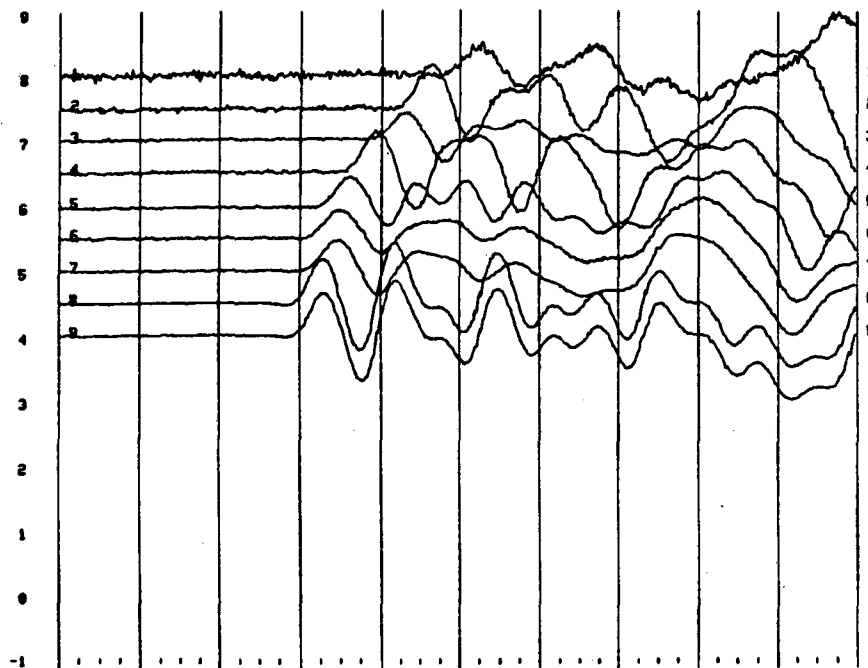
Fig. 8.8 a) P-waveforms for a specimen with an induced tensile fracture as function of fracture width. Trace # 1 is for the fracture width of 5 mm, # 2 of 4 mm, # 3 of 3 mm, # 4 of 2 mm, # 5 of 1 mm, # 6 of 0.5 mm, # 7 of 0.25 mm and for # 8 and # 9 the fracture is in contact but the pore pressure is lower for line # 9, as shown in Table 8.5 in Figure 8.7.

STRIPA 88, FRACTURE GAP: 5->0 MM, POLISHED FRAC.SUR., 821025

1E-6 SECONDS
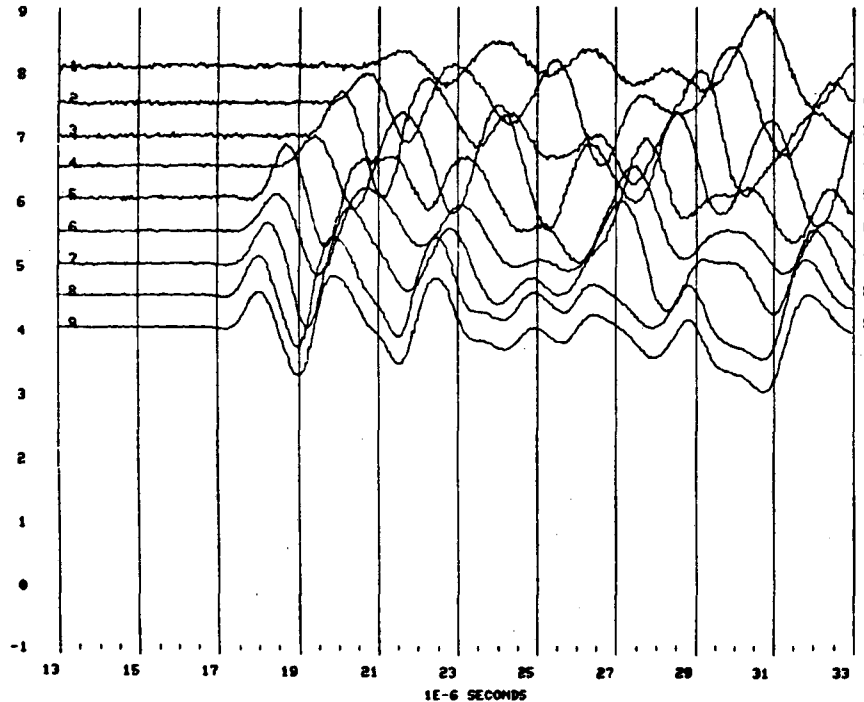
Fig. 8.8 b) P-waveforms for the same test of the same specimen with the end surfaces of the specimen with the induced tensile fracture ground smooth with a diamond wheel. The advancement in arrival time comparing trace # 1 in this figure with trace # 1 in Figure 8.8a is due to the shortening of the specimen after grounding the surfaces.

a.

b.

STRIPA 88, P-WAVES TRUNC. WITH 2E-6 SEC WIND, FRAC.WIDTH 5->0 MM, 821025
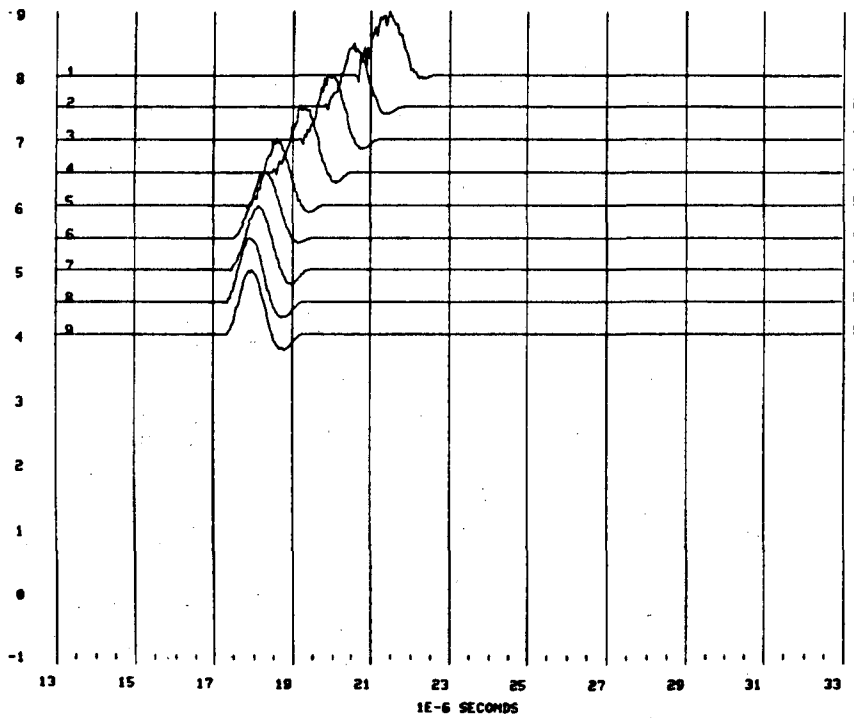
Fig. 8.9 a) Truncated waveforms from specimen in Figure 8.8 a. b) Truncated waveforms from specimen in Figure 8.8 b.

Fig. 8.10 a) P-wave Fourier amplitude spectra (0 - 1.25 MHz) for specimen with tensile fracture with rough fracture surfaces. b) P-wave Fourier amplitude spectra for specimen with tensile fracture with smooth grounded fractures surfaces.

a₁

Q FOR FRACTURE WIDTH ON CORE SAMPELS
SPECIMEN FILE : GPQD81.1
SPECIMEN : STRIPA 88, SPEC. WITH FRACTURE, WIDTH VARYING FROM 5 -> 0 MM, TRUNC.WIND:2E-6 S
STANDARD FILE : ALSPA3.1
STANDARD Q : 2000
STANDARD VEL : 6362
STANDARD LENGTH : .07622 M.
SMOOTHING OF Q-PLOT: 033 POINT RUNNING

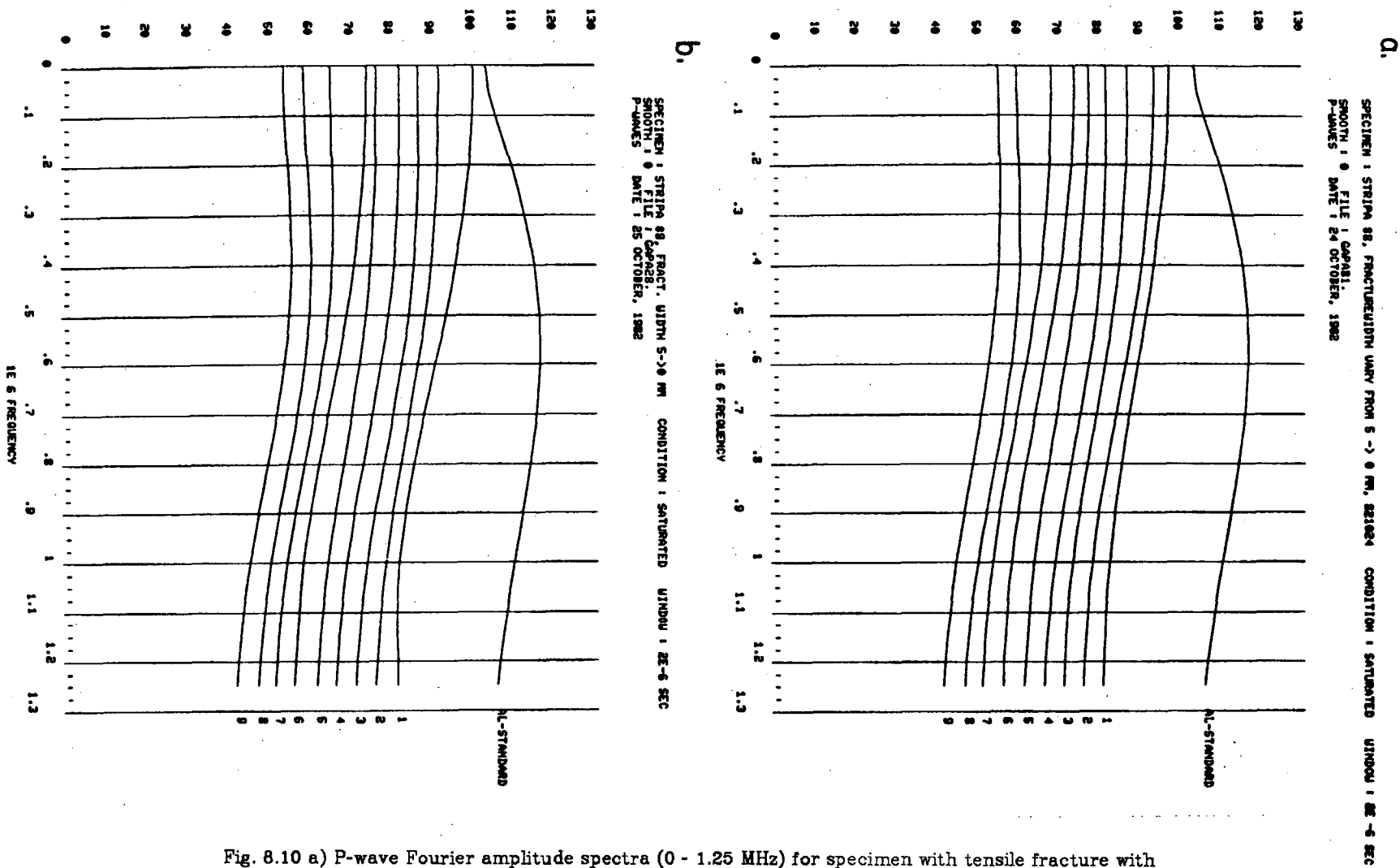| 8	FRAC.WIDTH	Q-VALUE	VELOCITY
1	5	21.6537	4846.32
2	4	23.43	5151.03
3	3	24.5834	5293.04
4	2	27.6799	5475.7
5	1	26.8392	5668.49
6	.5	20.996	5774.04
7	.25	23.3661	5776.8
8	0	35.248	5846.59
9	0	32.6863	5838.13

b₁

Q FOR FRACTURE WIDTH ON CORE SAMPELS
SPECIMEN FILE : CAPQP8.2
SPECIMEN : STRIPA 88, FRAC.WIDTH: 5-0 MM, SAT, WINDOW:2E-6 SEC, P-WAVES   GROUND END SURFACES
STANDARD FILE : ALSPA3.1
STANDARD Q : 2000
STANDARD VEL : 6362
STANDARD LENGTH : .07622 M.
SMOOTHING OF Q-PLOT: 033 POINT RUNNING

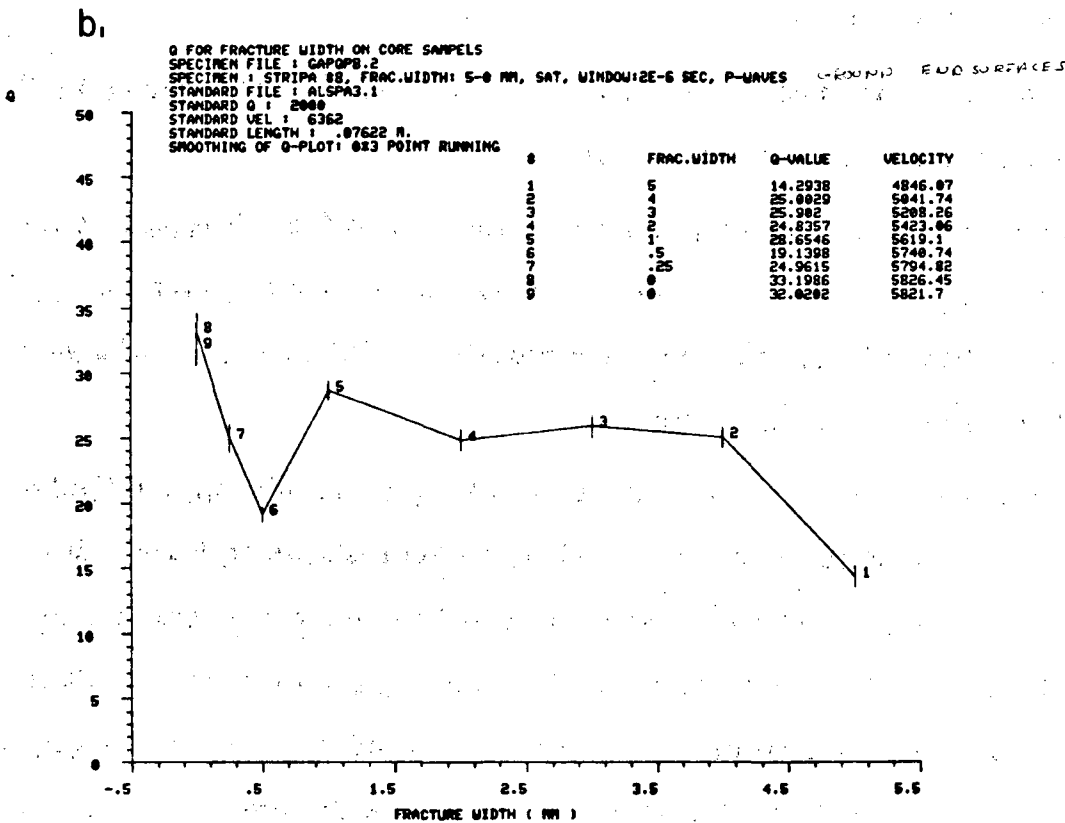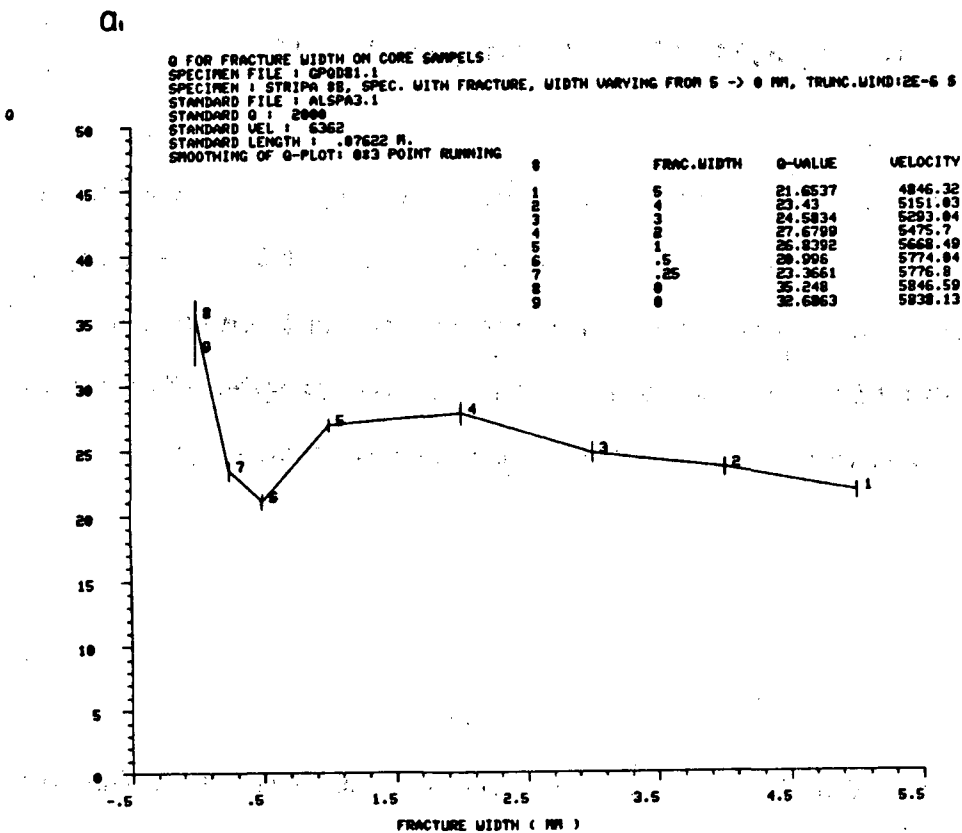| 8	FRAC.WIDTH	Q-VALUE	VELOCITY
1	5	14.2938	4846.07
2	4	25.0029	5041.74
3	3	25.982	5208.26
4	2	24.8357	5423.06
5	1	28.6546	5619.1
6	.5	19.1398	5740.74
7	.25	24.9615	5794.82
8	0	33.1986	5826.45
9	0	32.0202	5821.7

Fig. 8.11 a) Q-values as function of fracture width for a specimen with rough fracture surfaces. The specimen was broken in a tensile test. b) Q-values as function of fracture width for the specimen with smooth grounded fracture surfaces.

9. SUMMARY AND CONCLUSIONS

In this thesis a detailed field and laboratory project involving ultra-sonic wave propagation in a rock mass is described. It has been shown that it is possible to obtain much information about the behavior of a heated, cooled, and dewatered rock mass by transmitting high frequency ultrasonic seismic waves between boreholes in the heated zone.

9.1 Field work

Seismic velocities

The following is a point-by-point summary of the results of the field work in the Stripa mine.

1. Low-velocity zones can be located with a cross-hole seismic technique between two boreholes in the rock mass.

2. P-wave velocities provide a quantitative analysis of the fracture porosity in the medium. This is done by using the measured velocities and velocities obtained from the modal composition of the rock and the velocities of the individual minerals.

3. P-wave velocity variations upon dewatering provide a quantitative estimate of the effective porosity. This has been shown to have a directional component, i.e. the porosities so estimated vary systematically with direction of the cross-section. The total porosity of the Stripa quartz monzonite was found to be 1.5 %. The effective porosity varied between 0.16 % and 0.23 %, with the higher value obtained in the M8-M6 section, a direction which is roughly perpendicular to a large portion of the fractures in the rock mass.

4. By observing the time constant of the changing velocities and attenuation and the change in porosity, an estimate of the permeability of the rock mass can be obtained.

5. P- and S-waves can be used to monitor thermal processes by observing velocity increases due to thermal expansion of the rock. The P-wave velocity is seen to increase linearly with temperatures up to 130°C. The rate of change of velocity with temperature varies from $1.22 \frac{m}{s}\,^\circ C^{-1}$ to $4.00 \frac{m}{s}\,^\circ C^{-1}$ for mean temperatures up to $66\,^\circ$C. The largest velocity changes were found in the general direction of the minimum horizontal principal stress. The stress directions are inferred from geological evidence such as faulting and pegmatite dikes and *in situ* stress measurements.

6. P- and S-wave velocities can be used to assess thermal damage of a rock mass and the extent of the disturbed zone due to heating. Damage to the rock mass, is indicated by permanently reduced P-wave velocities, was observed as far as 2.1 m from the 3.6 kW H9 heater. The temperature increase at this distance was less than 35°C. An extensive zone with permanently lowered velocity was found over two paths which passed 0.2 and 0.3 m from the heater borehole wall. While the compressional velocities appeared to be responsive to effects from the thermal processes, the attenuation of P-waves proved sensitive in monitoring the associated process of fracture closure due to dewatering.

7. By using a set of data from independent laboratory measurements of static and dynamic moduli as well as theoretical moduli calculated from the modal composition of the rock, and unconnected porosity from seismic velocities, it was possible to calculate the decrease of the

effective stress with increasing temperature. The increase of the pore pressure minus the increase of the confining pressure is found to be 2.4 $bars°C^{-1}$. This pore pressure increase has been shown to hydrofracture the intact rock at a temperature of 77°C. However, fractures already existing in the rock have a much lower tensile strength and will open at lower temperatures. The effective stress in the direction of the minimum principal stress is shown to be zero for a temperature increase of 15°C. This temperature increase is found inside a radius of 3.5 m, at which distance fractures perpendicular to the minimum principal stress with zero tensile strength will open.

The cross-hole technique has proved to be useful because the velocity and the attenuation transmission characteristics of high-frequency waves contain information about different aspects of the status of the rock mass.

Attenuation

8. The field work shows that elastic waves are highly attenuated in a saturated crystalline rock mass which is extensively microfractured. The Q_α values found before the heater and the dewatering processes were activated ranged from 8 to 20. This is lower than commonly reported for granitic rocks in laboratory tests. It is also lower than values reported for other field tests in different rock types.

9. Attenuation does not appear to change across low velocity zones. Attenuation is much less sensitive to fractures which give rise to low velocity zones.

10. Attenuation is apparently not sensitive to different widths of water-filled fractures as long as the asperities on the pairs of surfaces do not

touch.

11. Attenuation characteristics change rapidly at some point during the process of closure of fractures. Laboratory tests indicate that a rapid decrease in attenuation occurs when the asperities first come into contact. This suggests that a locking mechanism between contacting asperities decreases attenuation. Attenuation should thus be a function of asperities which are locked.

9.2 Laboratory work

The uniaxial tests on the Stripa quartz monzonite show how laboratory data can be used together with the field data to gain a better understanding of the properties of the rock, as well as mechanisms for attenuation. The following is a summary and conclusions based on the laboratory work performed.

Seismic velocities

1. By observing waveforms as a function of applied stress, a combination of propagation and attenuation effects can be illustrated in one picture.

2. The compressional velocities reveal a fracture anisotropy in the Stripa quartz monzonite.

3. Both V_p and V_s are linear functions of saturation.

4. Both V_p and V_s are linear functions of the width of a water-filled fracture.

Attenuation effects

5. In the laboratory tests it was shown that changes in attenuation with uniaxial stress is related to the observed direction of microfractures. Q_α increases with stress when the direction of microfractures is perpendicular to the applied stress. Q_β changes less than Q_α with the application of unconfined uniaxial stress. The small changes, and in some cases even decreasing values, of Q_β with uniaxial stress indicates that fractures oriented parallel to the stress direction open with stress.

6. The laboratory values of attenuation reveal the level of the intrinsic attenuation for the rock in question. The low values found for the field data were confirmed by the laboratory test. The numberical values for Q_α ranges from 15-35 at low stresses to 27-80 for 50 MPa unixial stress. These values are lower than what is commonly reported for crystalline rock. Q_β vary between 14-30 for low axial stresses and 18-42 for axial stresses as high as 50 MPa.

7. For core taken from boreholes drilled prior to the heater experiment both the Q_α and Q_β values are higher for saturated specimens than for convection-oven-dried specimen which yield a saturation of approximately 20-40 %.

8. The attenuation is more sensitive than the velocities to the orientation of the fractures closing with the application of stress.

9. Tests on specimens recovered after the heater test show that the fracture porosity has not changed significantly. This is based on the observation that the change of velocities with stress has not changed in the heated specimen. The observation that the Q_α values increase from 20 to 242 with stress increasing from 2.3 to 51 MPa indicates that the aspect ratios for the existing fractures decrease because of increased

length of the fractures due to the heating process.

10. The laboratory tests on three specimens from the H10 area before and after heating provide evidence of microfracturing around this heater to a distance of at least 1.45 m, where the temperature had reached 130°C. From the large increase in Q_{α} with stress it is concluded that microfractures closed more easily in the heated samples. Based on this information it is concluded that the thermal process lowered the aspect ratios for fractures by extending them in the length direction. Thin-section analysis failed to detect any difference between heated core and core obtained before the heater experiment was started. This indicates that the attenuation properties of a specimen are sensitive to the extent and direction of induced microfractures.

11. Laboratory tests on outgassed samples provided information on attenuation mechanisms. Under low axial stress the $Q\alpha$ values are lower than for the saturated case, indicating that the frame attenuation is important for highly fractured crystalline rocks.

12. When the axial stress is increased on vacuum-dried specimens from 5 to 30 MPa, Q_{α} increased from 21 to 150. This decrease of attenuation in a dry specimen at high stresses suggests a locking mechanism for prevention of relative movement of fracture surfaces.

13. A large decrease in Q_{α} is observed when the saturation is reduced from 100 % to 65 %.

14. Q_{α} is minimum when the specimens are 65 % saturated.

15. Q_{α} increases when the specimen is vacuum-dried, if the fractures are oriented so that they close when stress is applied.

9.3 General

It has been shown in this report that a geophysical technique can be very effective in monitoring the status of, and changes in, a rock mass. The information obtained about the rock mass includes the location of fracture zones, the porosity, effective directional porosity, and to some extent, the permeability, by studying the time constant for the decrease in Q_α and V_p as functions of dewatering.

It has been shown that the Q values are affected by the presence of pore fluids, but that the Q values are very low even for the dry specimens. This suggests that extensive microfracturing lowers the Q values, suggesting further that the dominant mechanisms in a highly-fractured crystalline rock are related to thermoelastic processes which provide a high intrinsic attenuation.

A mercury porosimeter was used to obtain a fracture width spectrum as function of total fracture volume. To obtain the aspect ratio spectrum one has to have the length of the fractures as well. This can possibly be obtained from a SEM study of the rock.

9.4 Mechanism

The results from laboratory tests on a specimen from the H10 area show that thermal extension of fractures does not lower the Q at lower stress levels, despite the larger contact surfaces. The rapid increase in Q for this sample with applied stress indicates that the fractures close more easily. A possible model that would satisfy these requirements is a frame attenuation model for which energy is absorbed by a thermoelastic mechanism. An increase in Q with stress would result from a locking mechanism which causes the attenuation to decrease the more the

asperities become interlocked. The high attenuation at partial saturations tends to confirm the model of Winkler and Nur (1982) in that Q_α was observed to change more than Q_β with a change in the saturation.

The most important part of this thesis is the demonstration that a small scale field experiment can be used to obtain parameters of the rock which cannot be obtained by laboratory experiments. This experimental work will serve as a data base for building theoretical models and for guiding the implementation of ultrasonic monitoring systems in full-scale repositories.

10. RECOMMENDATIONS

10.1 Field work

The largest drawback with the data collected in the Stripa experiment is the limited S-wave data collected. By improving the quality of the S-waves transmitted and detected between boreholes a better understanding of the changes in the rock mass should be achieved. From the laboratory work performed it is clear that S-wave attenuation responds more to fractures oriented parallel to the transmission direction than do the P-waves. Thus, by observing the ratio Q_α / Q_β important information concerning the dominant fracture direction can be obtained.

Suggested directional permeability experiment

The increase of the Q values in the lower end of the cross-sections suggest that the attenuation is sensitive to fracture closure. This could be utilized in a determination of the porosity, directional porosity and in defining a directional permeability function. For example, this could be done by drilling eight boreholes in a quadratic configuration, and then dewatering the rock mass through the boreholes. The configuration suggested would effectively isolate the rock mass contained within the boreholes hydraulically. By including the capability of recording the water inflow as a function of depth in the boreholes it would be possible to achieve some control on the influence of larger fractures which are believed to provide the major permeability of a crystalline rock mass.

The result from the pore pressure calculations suggest that it is important to dewater the rock mass around radioactive canisters to avoid mechanical damage by the high thermal expansion of the pore fluids. A cross-hole technique monitoring velocity and attenuation can be used to determine when the dewatering has decreased the water content in the rock mass.

A cross-hole technique can be used together with artificially induced excess fluid pressure in boreholes to determine the location of the open fractures and the direction of the conducting fracture systems.

Changes in several aspects of data handling could greatly improve the quality of field data obtained. Use of an AM tape recorder made it impossible to retain absolute amplitude control. If the waveforms were digitized directly in field, the signal/noise ratio would improve by an order of magnitude for cross-hole data over a distance of a few meters.

Together with the active transmission of P- and S-waves a field experiment should include the collection of acoustic emission data to record micro-seismic event when fractures are extended or created in the rock mass.

The porosity and permeability of the host rock for disposal of radioactive waste is of great interest. The pore fluids are the potential carriers of the dissolved waste to the surface. By understanding the pore fluid movements in the rock mass means can be devised to prevent much of the movement of the fluid. Also, dewatering the rock mass results in a reduction in permeability through closure of fractures and a consequent retardation in water flow toward the repository. This results in a delayed contact between the surrounding pore fluids lying outside the immediate rock mass and the radioactive waste.

The aspect ratio spectrum for the rock mass can be obtained by monitoring the pore pressure concurrently with Q_α and Q_β, employing the relationship

$$P_c = \frac{\pi \, \alpha \, E}{4 \, (1 - \nu^2)}$$

where P_c is the effective pressure nessecary to close a fracture with aspect ratio α and ν Poisson's ratio. E is the Young's modulus.

10.2 Laboratory work

Any future laboratory work should include the capability of applying confining stress to the test specimen. Uniaxial tests alone made it difficult to assess any differences between the Q_α and Q_β for the different specimens. Transmission of signals in several different radial directions across the specimen would make it possible to utilize a tomography technique for a two-dimensional view of events in the cross section of the specimen. It would also be possible to obtain a two-dimensional lengthwise view of a specimen tested by putting several transducer at the same cylindrical angle along the length of a specimen with the second set of transducers 180° from the first.

By applying polyaxial stress on prismatic specimen the orientation of the microscopic fractures can be obtained by observing changes in Q_α and Q_β.

10.3 Implementation in an operational repository.

The monitoring program for a repository should be done on several different scales.

First it is important to understand the behavior of the rock in the immediate vicinity of a hot canister. This represents the smallest scale of monitoring. The heat load can be applied with electric heaters in this test, whose purpose is to obtain confirmation of the design parameters to which the rest of the repository is designed. The response of the rock to heating and dewatering is a complex combination of effects on the various mineral components, their distribution, mineral alterations and, of course, fractures on all scales. This can not be modeled at present due to the many parameters involved, so by performing the small-scale monitor test described above as the first stage, in the actual storage rock mass, necessary knowledge of the repository rock can be obtained. The scale of the first stage is over a few meters.

The scale of the second stage of monitoring is over 100 m. A monitoring program to assess the stability of the excavated drifts should performed. The loading time of a repository will probably extend over one or two decades, so the long term stability of the rock mass must be understood. This can be achieved by implementing a monitor program of the rock in or between drifts immediately after the drifts are excavated in order to get the base values.

The scale of the third stage of monitors is over one or two km. This monitor program should be implemented before excavation commences on either shafts or drifts. This program can be performed between deep boreholes from the surface. Thus it will be possible to monitor the large-scale influence of dewatering and heating, as well as the stress

readjustments associated with emplacement of the drifts. With the boreholes from the surface, changes in the rock mass can be followed and evaluated before, during and after commissioning of a nuclear waste repository.

Ultimately, such a moitoring program should be able to provide, at reasonably high resolution, a verification system for the mechanical integrity of the repository at the above scales.

REFERENCES

Adams, L.H., and E.D. Williamson. The Compressibility of minerals and rocks at high pressure, *J. Franklin Inst.*, 195, 475, 1923

Aki, K., M. Fehler, R. Aamodt, J. Albright, R. Potter, C. Pearson, and J. Tester, Interpretation of seismic data from the hot dry rock fracture experiment at Los Alamos Scientific Laboratories, *J. Geopys. Res.*, *87*, 936-944, 1982

Anderson, D.L., B. Minister and D. Cole, The effect of oriented cracks on seismic velocities, *J. Geophys. Res.*, *79*, 4011-4015, 1974

Andersson, B., and P.H. Halen, Mining methods used in the underground tunnels and test room at stripa, *Lawrence Berkeley Laboratory Report, LBL-7081,* SAC-8, 1979

Auld B. Cross-hole and down-hole Vs by mechanical impulse. *J. Geotech. Engin. Div.* ASCE *103*, GT 12, 1381-1398, 1977

Biot, M.A., General theory of three dimensional consolidation, *J.Appl.Phys.*, *12*, 155-164, 1941

Birgersson, L., and I. Neretnieks, Diffusion in the matrix of granitic rock. Field test in the Stripa mine. Draft report, *Royal Institute of Technology*, Stockholm, Sweden, 1982

Bonner, B.P., Vp/Vs in saturated granodiorite loaded to failure, *Pageoph*, Vol. 113, 1975

Brace W.F., Pore Pressure in Geophysics, *Flow and Fractures of Rocks*, Geophys. Mon. No. 16, John Wiley and Sons, New York, pp. 265-274, 1972

Carlsson, H. Stress measurements in the Stripa granite, *Lawrence Berkeley Laboratory Report, LBL-7078*, SAC-4, 1978

Carroll R.D., Rock Properties interpreted from sonic velocity logs. *J. Soil Mech. Found. Div.* ASCE *92*, SM2, 43-51, 1966

Carroll R.D., The determination of the acoustic parameters of volcanic rocks from compressional velocity measurements. *Int. J. Rock Mech. Min. Sci.*, 5, 557-579, 1969

Chan C., E. Binnall, P. Nelson, R. Stolzman, O. Wan, C. Weaver, K. Ang, J Braley, and M.McEvoy, Thermal and Thermomecanical data From *In Situ* Heater Experiments at Stripa, Sweden. *Lawrence Berkeley Laboratory Report, LBL-11477*, SAC-29, 1980

Chan, T., N. Littlestone, and O. Wan, Thermomechanical modeling and data analysis for heating experiments at Stripa, Sweden, *Proc. 21st U.S. Rock Mechanics Symposium, Rolla, Mo*, May, 1980

Cheng, C.H. and M. N. Toksoz, Inversion of seismic velocities for the pore aspect ratio spectrum of a rock, *J. Geophys. Res.*, *84B13*, 7533-7543, 1979

Cheng, C.H., M.N. Toksoz, and M.E. Willis, Determination of In Situ Attenuation From Full WAveform Acoustic Logs, *J. Geophys. Res.*, *87B7*, 5477-5484, 1982

Cook, N.G.W. and K. Hodgson, Some detailed Stress-strain curves for rock, *J. Geophys. Res.*, *70*, 2883-2888, 1965

Cook, N.G.W., Field measurement techniques: status and needs. *Proc. Workshop on the Thermochemical Modeling for a Hardrock Waste Repository* Berkeley, Ca. June 25-27, 1979

Cook, N.G.W., Mechanical and thermal design considerations for radioactive waste repositories in hard rock, part I: an appraisal of hard rock for potential underground repositories of radioactive waste. *Lawrence Berkeley Laboratory Report*, *LBL-7073*, SAC-10, 1978

Coon R.F., and Merritt A.H. Predicting *in situ* modulus of deformation using rock quality indexes. In Determination of the In Situ Modulus of Deformation of rock, *ASTM Publ.* STP 477, 154-173, 1970

Cratchley C.R., Grainger P., McCann D.M. and Smith D.I. Some applications of geophysical techniques in engineering geology with special reference to the Foyers hydro-electric scheme. *24th Int. Geological Congr. Section 13*, 163-175, 1972

Doe, T.W., K. Ingevald, L. Strindell, B.C. Haimson, and H. Carlsson, Hydraulic fracturing and overcoring stress measurements in a deep borehole at the Stripa test mine, Sweden. *Proceedings, 22nd U.S. Rock Mechanics Symposium*, Mass. Inst. Technology, p 373-378, 1981

Doe, T., Determination of the state of stress at the STripa mine, Sweden, *Earth Sciences Division Annual Report 1981*, *Lawrence Berkeley Laboratory*, 1981

Fehler M., Changes in P Wave Velocity During Operation of a Hot Dry Rock Geothermal System, *J. Geophys. Res.*, *86*, 2925-2928, 1981

Fehler, M., Using Dual-Well Seismic Measurements to Infer the Mechanical Properies of a Hot Dry Rock Geothermal System, *J. Geophys. Res.*, *87*, 5485-5494, 1982

Fehler, M., Interaction of Seismic waves wtih a viscous liquid layer, *Bull. Seismol. Soc. Am.*, *72*, 55-72, 1982

Flexer, S., H. Wollenberg, and D.E. Wedge, Petrologic changes and damage in the Stripa Quartz Monzonite in response to heater tests, *Lawrence Berkeley Laboratory Report*, *LBL-14929*, SAC-41, 1982

Forster, C.B. and J.E. Glae, A Filed assessment of the use of borehole pressure transients to measure the permeability of fractured rock masses, *Lawrence Berkeley Laboratory Report, LBL-11829*, SAC-34, 1981

Gale, J.E., A Numerical field and laboratory study of flow in rocks with deformable fractures, *Ph.D. Thesis*, 255 pp., University of Cal., Berkeley, 1975

Gale, J.E., P.A. Witherspoon, C.R. Wilson and A. Rouleau, Hydrogeological characterization of the Stripa site, Presented at workshop on *in situ* experiments in granite associated with geological disposal of radioactive waste, Stockholm, Sweden, October 25-27, 1982

Geyer, R.l. and Myung, J.I. The 3-D velocity log; a tool for *in situ* determination of the elastic moduli of rocks. *Proc. 12th Symp. Rock Mech.*, Rolla 71-107, 1971

Good, R.J., and R.SH. Mikhail, The contact angle in mercury intrusion porosimetry, *Powder Technology*, 29, 53-62, 1981

Gordon, R.B., and L.A. Davis, Velocity and attenuation of seismic waves in imperfectly elastic rock, *J. Geophys. Res.*, v. 73, p. 3917-3935, 1968

Gordon, R.B. and C.W. Nelson, Anelastic properties of the earth, *Rev. Geophysics*, 4, 457-474, 1966

Hadley, K., Comparison of calculated and observed crack densities and seismic velocities in Westerly Granite, *J. Geopys. Res.*, 81, 3484-3494, 1976

Hadley, K., Vp/Vs Anomalies in dilatant rock samples, *Pageoph*, Vol. 113, 1975

Ito, H., J. De Vilbiss, and A. Nur, Compressional and Shear waves in Saturated Rock during water-steam transition. *J. Geophys. Res.*, 84B9, 4731-4735, 1979

Jackson, D.D. and D.L. Anderson, Physical mechanisms of seismic waves, *Rev. Geophys. Space. Phys.*, 8, 1-63, 1970

Jaeger, J.C. and N.G.W. Cook, Fundamentals of Rockmechanics, *Chapman and Hall*, *Wiley and Sons*, New York, third edition, 1979

Johnson, B., S. Bauer, and A.F. Gangi, Effects of thermally induced microcracks upon permeability of Westerly granite as a function of effective pressure, abstract, *EOS Trans. AGU*, 6046, 943, 1979.

Johnston, D. H., and M. N. Toksoz, Ultrasonic P and S wave attenuation in dry and saturated rocks under pressure, *J. Geophys. Res.*, 85, 925-936, 1980

Johnston, D. H. and M.N. Toksoz, Thermal Cracking and Amplitude Dependent Attenuation, *J. Geophys. Res.*, *85*, 937-942, 1980

King, M.S., Static and dynamic moduli of rocks under pressure, In *Rock Mechanics : Theory and Practice, (Editor: W.H. Somerton), 19, 329-351, 1970*

King M.S., Pobran V.S., and McConnell B.V. Acoustic borehole logging system. *Proc. 9th Canad. Rock Mech. Symp.*, Montreal, 21-51, 1974

King M.S., Stauffer M.R., and Pandit B.I. Quality of rock masses by acoustic borehole logging. *Proc. III Int. Congress IAEG*, Madrid, SEc IV, 1. 156-164, 1978

Kjartansson, E., Constant Q-wave propagation and attenuation, *J.Geophys.Res., 84B9*, 4737-4748, 1979

Kloubek., J., Hysteresis in porosimetry, *Powder Technology*, 29, 63-73, 1981

La Port M., Lakshmanan J., Lavergne M., and Willm C., Seismic measurement by transmission-application to civil engineering. *Geophysical Prospecting 21*, 146-157, 1973.

Landau, I., and E. Lifshitz, *Thory of Elasticity*, translated from Russion by J. Sykes and W. Reid, 134 pp., Addison-Wesly, Reading, Mass., 1959

Leijon, B., Predicted rock stresses for the pilot heater test at Stripa mine. *Lawrence Berkeley Laboratroy Report, LBL-7086*, SAC-06, Appendix II, by Carlsson H., 1978

Lockner, D.A., J.B. Walsh, and J.D. Byerlee, Changes in Seismic velocity and attenuation during deformation of granite, *J. Geophys. Res.*, *82*, 5374-5378, 1977

Nadai, A., *Theory of Flow and Fracture of Solids*, 705 pp., McGraw-Hill, New York, 1963

Mason, W.P., K.J. Marfurt, D.N. Beshers, and J.T. Kuo, *J. Acoust. Soc. Am.*, 63, 1596-1603, 1978

McCann D.M., Grainger P. and McCann C. Inter-borehole acoustic measurements and their use in engineering geology. *Geophysical Prospecting 23*, 50-69, 1975

McDonal F.J., F.A. Angona, R.L Mills, R.L Sengbush, R.G. Van Nostrand, and J.E. White, Attenuation of shear and compressional waves in Pierre shale, *Geophysics, v.23*, p421-439, 1958

Morrow C., D. Lockner, D. Moore and J. Byerlee, Permeability if Granite in a Temperature Gradient, *J. Geophys. Res.*, *86B4*, 3002-3008, 1981

Myung J.I. and Baltosser R.W. Fracture evaluation by the borehole logging method. *Proc. 13th Symp. Rock Mech.*, Urbana, IL, 31-56, 1972

Nelson P., Paulsson B., Rachiele R., Andersson L. Schrauf T., Hustrulid W., Duran O., and Magnusson K.A. Preliminary report on geophysical and mechnical borehole measurements at Stripa, *Lawrence Berkeley Laboratory Report, LBL-8280*, SAC-16, 1979

Nelson, P.H., R. Rachiele, J.S. Remer, and H. Carlsson, Water inflow into boreholes during the Stripa heater experiments, *Lawrence Berkeley Laboratory Report, LBL-12574*, SAC-35, 1981

Nelson, P. and C. Wilson, Thermomechanical and macropermeability experiments in the Stripa granite - Status report, *Proceed. of workshop on thermomechanical, hydrochemical modeling fir a hard rock waste repository, LBL-11204*, CONF-800751, ONWI-164, 1980

Nur, A., Effects of Stress on Velocity Anisotropy in Rocks with Cracks, *J. Geophys. Res.*, 76, 2022-2034, 1971

Nur, A. and G. Simmons. Stress Induced Velocity Anisotrophy in Rocks: An Experimental Study, *J. Geophys. Res.*, 74, 6667-6674, 1969

Nur, A. and G. Simmons, The effect of saturation on velocity in low porosity rocks, *Earth and Planetary Letters* 7, 183-193, 1969, North-Holland Publishing Comp., Amsterdam

Nur, A., and J.D. Byerlee, An exact effective stress law for elastic deformation of rock with fluid, *J. Geophys. Res.*, 76, 6414-6419, 1971.

O'Connel, R.J., and B. Budiansky, Seismic velocities in dry and saturated cracked solids, *J. Geophys. Res.* 79, 5412-5426, 1974

O'Connell, R.J., and B. Budiansky, Viscoelastic Properties of Fluid-Saturated Cracked Solids, *J. Geophys. Res.*, 82, 5719-5735, 1977

Olkiewicz, A., J.E. Gale, R. Thorpe, and B. Paulsson, Geology and fracture system at Stripa, *Lawrence Berkeley Laboratory Report, LBL-8907*, SAC-21, 1979

Orr, Jr. C., Application of mercury penetration to material analysis, *Powder Technol.*, 3, 117-123, 1969/70

Palciauskas, V.V. and P.A. Domenico, Characterization of Drained and Undrained Response of Thermally Loaded Repository Rocks, *Water Resources Res.*, 18, 281-290, 1982

Pandit, B.I., and M.S. King, The variation of elastic wave velocities and quality factor Q of a sandstone with moisture content, *Can. J. of Earth. Sci.*, 16, 2187-2195, 1979

Paulsson B.N.P. and King M.S. A Cross-hole Investigation of a Rock Mass Subjected to Heating. *Proc. Rockstore 80* Stockholm, 1980

Paulsson B.N.P., Nelson P., and Kurfurst P.J. Characterization of the discontinuities in the Stripa granite -- the full scale experiment drift, *Lawrence Berkeley Laboratory Report, LBL-9063*, 1981

Price D.G., Malone A.W., and Knill J.L. The application of seismic methods in the design of rock bolt systems. *Proc. Int. Congress IAEG*, Paris, 2, 740-752, 1970

Rice, J.R., J.W. Rudnicki, and D.A. Simons, Deformation of spherical cavities and inclusions in fluid infiltrated elastic materials, *Int.J.Solids Struct.*, *14*, 289-303, 1978

Schrauf, T., H.Pratt, E. Simonson, W. Hustrulid, P. Nelson, A. Dubois, E. Binnall, and R. Haught, Instrument Evaluation, Calibration, and Installation for the Heater Experiments at Stripa, *Lawrence Berkeley Laboratory Report, LBL-8313*, SAC-25, Berkeley, California

Sears, F.M., and B.P. Bonner, Ultrasonic Attenuation Measurements by Spectral Ratios Utilizing Signal Processing Techniques, *IEEE transactions on Geophysical Remote Sensing*, Vol. GE - 19, No. 2 April 1981.

Simmons, G., and H. Cooper, DSA of the microcracks in the GT-core, Interpretaion and implications, report, *Mass. Inst. Technol.*, Cambridge Sept. 1976

Simmons, G., and H.W. Cooper, Thermal cycling in three igneous rocks, *Int. J. Rock Mech. Mining Sc. Geomech. Abstr.*, *15*, 145-148, 1978

Simmons G. and H. Wang, Single Crystal Elastic Constants and Calculated Aggregate Properties, *M.I.T. press*, Cambridge, 1972

Sjogren B., Ofsthus A., and Sandberg J. Seismic classification of rock mass qualities. *Geophysical Prospecting* 27, 409-442, 1979.

Spencer, Jr. J.W., Bulk and Shear Attenuation in Berea Sandstone: The Effect of Pore Fluids, *J. Geophys. Res.*, *84*, 7521-7523, 1979

Spitzer, Z., Mercury porosimetry and its applictation to the analysis of coal pore structure, *Powder Technology*, 29, 177-186, 1981

Stephansson O., Lande G., and Bodare A. A seismic study of shallow jointed rocks. *Int. Jour. Rock. Mech. Min. Sci.*, *16*, 319-327, 1979

Swan, G.. The mechanical properties of Stripa Granite, *Lawrence Berkeley Laboratory Report, LBL-7074*, SAC-03, 1978

Thorpe, R., Cahracterization of discontinuities in the Stripa Granite time-scale heater experiment, *Lawrence Berkeley Laboratory Report*, LBL-7083, SAC-20, UC-70

Timoshenko, S.P. and J.N. Goodier, Theory of elasticity, second edition, *McGraw Hill*, New York, 1951

Timur, A., Temperature dependence of compressional and shear wave Velocities in Rocks. *Geophysics*, Vol 425, 950-956, 1977

Toksoz, M.N., D.H. Johnston, and A. Timur, Attenuation of seismic waves in dry and saturated rocks; 1. Laboratory measurements. *Geophysics, v. 44*, no 4, 681-690, 1979

Toksoz, M.N., C.H. Cheng, and A. Timur, Velocities of Seismic Waves in Porous Rocks, *Geophysics, v. 41*, p.621-645, 1976

Tullos, F.N., and A.C. Reid, Seismic attenuation of Gulf coast sediments, *Geophysics, v.34*, p.516-528, 1969

Walsh, J.B., Seismic wave attenuation in rock due to friction, *J. Geophys. Res., 73*, 2209-2216, 1968

Walsh, J.B., The effect of cracks on the Uniaxial Elastic Compression of Rocks, *J. Geophys. Res., 70*, 1965

Walsh, J.B., The effect of cracks on the compressibility of rock, *J. Geophys. Res., 70*, 381-389, 1965

Walsh, J.B., Theoretical bounds for thermal expansion, specific heat, and strain energy due to internal stresses, *J. Geophys. Res., 78*, 7636-7647, 1973

Winkler, K.W. and A. Nur, Seismic attenuation: Effects of pore fluids and frictional sliding, *Geophysics*, v. 47, p.1-16, 1982

Winkler, K. and A. Nur, Pore Fluids and Attenuation in Rocks, *Geophys. Res. Letters, v6*, p.1-4, 1979

Winkler, K, A. Nur and M. Gladwin, Friction and seismic attenuation in rocks, *Nature*, 277, 528-531, 1979

Witherspoon P.A., and O. Degerman Swedish-American cooperative program on radioactive waste storage in mined caverns, *Lawrence Berkeley Laboratory Report, LBL-7049*, SAC-01, 1978

Witherspoon P.A., N.G.W. Cook, and J.E. Gale, Progress with field investigations at Stripa, *Lawrence Berkeley Laboratory Report, LBL-10559*, SAC-27, 1980

Witherspoon P.A., Gale J.E., Nelson P., Doe T., Thorpe R., Forster C., and Paulsson B. Rock mass characterization for storage of nuclear waste in granite. *Proc. 4th Congress Int. Soc. Rock Mech.*, Montreaux, 2, 711-718, 1979

Wollenberg, H., S. Flexer and L. Andersson Petrology and Radiogeology of the Stripa Pluton, *Lawrence Berkeley Laboratory Report*, *LBL-11654*, SAC-36, 1981

Wyllie, M.R.J., A.R. Gregory and G.H. Gardner, An experimental investigation of factors affecting elastic wave velocities in porous media, *Geophysics*, *v. 23*, 459-493, 1958